Influence of the Bulk Chemical Composition on the Microstructure Evolution of Irradiated Chemically-tailored Nuclear RPV Steels

Aidar Zakirov

Normandie Université

THÈSE

Pour obtenir le diplôme de doctorat

Spécialité PHYSIQUE

Préparée au sein de l'Université de Rouen Normandie

Influence of the Bulk Chemical Composition on the Microstructure Evolution of Irradiated Chemically-tailored Nuclear RPV Steels

Présentée et soutenue par
AIDAR ZAKIROV

Thèse soutenue le 02/11/2022 devant le jury composé de		
MME GRACE BURKE	, Université du Tennessee	Rapporteur du jury
MME MARTA SERRANO	, Centre Rech. Energétique, Environ. Tech.	Rapporteur du jury
M. RACHID CHAOUADI	, Centre d'Etude de l'Energie Nucléaire	Membre du jury
M. BERTRAND RADIGUET	MAITRE DE CONFERENCES, Université de Rouen Normandie	Membre du jury
M. ERICH STERGAR	, Université Catholique de Louvain (Belgique)	Membre du jury
MME INGE UYTDENHOUWEN	, Centre d'Etude de l'Energie Nucléaire	Membre du jury
M. ERIC VAN WALLE	, Centre d'Etude de l'Energie Nucléaire	Président du jury
M. PHILIPPE PAREIGE	PROFESSEUR DES UNIVERSITES, Université de Rouen Normandie	Directeur de thèse

Thèse dirigée par PHILIPPE PAREIGE (GROUPE DE PHYSIQUE DES MATERIAUX)

UNIVERSITÉ DE ROUEN NORMANDIE

ED 591 PSIME

GPM Groupe de Physique des Matériaux

Acknowledgements

Before acknowledging all the people who had directly contributed to the successful completion of my PhD thesis, I would like to start by thanking my family and friends for believing in me and providing all the necessary support during the stressful times, even being separated by the thousands of kilometres. It was especially important during the depressing times of covid-19 pandemic. All the time we spent meeting and having fun online helped me a lot.

To respect the time flow, I would like to give a sincere thanks to Nariman Enikeev, who helped to nucleate my interest in material science and paved the way to further achievements.

Any PhD study comes with the student and the supervisors. I was lucky to have Bertrand Radiguet and Philippe Pareige guiding me here, at GPM Rouen. Bertrand spent numerous afternoons explaining the basics of irradiation damage, APT, etc. The vast knowledge of Philippe aided tremendously, when I needed a broader view on my results. Thank you for giving me enough freedom to develop into a more independent scientist and guiding me when it was necessary. Special thanks for spending a lot of time correcting the manuscript to make it more pleasant to the reader. The same warm words are going to my supervisors from SCK CEN: Rachid Chaouadi, Erich Stergar and Inge Uytdenhouwen. Even though the time I spent at SCK CEN was short; every time we had a meeting, you were giving extremely useful feedback on the scientific side and also on how to develop into a better researcher.

I am sincerely thankful to my thesis committee: Pr. Eric van Walle, Pr. Marta Serrano and Pr. Grace Burke. It is a very encouraging feeling of knowing that such renowned specialists had reviewed my manuscript. Thank you for all the comments and corrections in the pursuit of making the final document better. It was especially pleasant to have a thorough discussion during the defence.

Obtaining the experimental results wouldn't been possible without numerous people who provided technical support during the PhD. Many thanks to Auriane Etienne and Beatrice Foulon for organising the workflow at GENESIS platform. Special thanks to Fabien Cuvilly, Ronan Henry and Ivan Blum for assisting with the SEM/FIB and APT instruments. Sincere thanks to Wouter Van Renterghem for helping with the sample preparation during the times of covid-19 limitations. Warmest thanks to Gerald Da Costa for always being willing to explain the intricacies of the APT data mining procedures.

Deepest thanks to Cristelle Pareige who was always ready to help me with the questions I was shy to ask my supervisors. Special thanks to Xavier Sauvage and Simona Moldovan who gave me various advice numerous times. My PhD was almost finished when I first met Ben Jenkins, but his different view on some scientific questions gave me a lot of things to reflect on. Another person who deserves many thanks is Nicolas Castin who was always happy to discuss and compare my observations with atomistic modelling.

Special words should be said to acknowledge the aid of the administration and ICT staff: Linda Widerowski, Christine Vurpillot, Caroline Jorry, Romain Vincent, Germain Martigny, Marie-Ange Derue and Griet Vanderperren.

Going a bit down memory lane, I cannot not to mention the professors and colleagues from USATU, who helped and guided me during my bachelor and master studies: Olga Kulyasova, Elena Bobruk, Maksim Murashkin, Marina Nikitina, Rinat Islamgaliev.

Last, but certainly, not least come the new friends I found here, so far away from home. My manuscript is already long enough so, unfortunately, I could not mention everyone I met. But the warmest thanks are going to Olya, Solene and Begona, who helped and guided me from day one, even though they never met me before. The four years of my PhD passed swiftly because I was surrounded by great people such as Andrey, Ben, Bence, Felix, Inna, Ivan and Mykola. Finally, the number of coffee breaks we took with Gilles and Maria goes far beyond the number of successful APT experiments I acquired.

As it was briefly mentioned before, my PhD occurred during the covid-19 outbreak, and the experimental part of the studies was delayed. I would like to thank the University of Rouen Normandy and SCK CEN for granting the financial means to prolong my PhD study and, furthermore, providing the additional project to continue the work. During this PhD research, the experiments were performed on GENESIS platform instruments supported by the Région Haute-Normandie, the Métropole Rouen Normandie, CNRS via LABEX EMC3 and French National Research Agency via “Investissements d’avenir” program (ANR-11-EQPX-0020). This work was partially supported by the CNRS Federation IRMA - FR 3095.

Contents

List of Acronyms and Abbreviations

3D	Three-dimensional
A	Austenite
ALARA	As Low As Reasonably Achievable
AKMC	Atomic Kinetic Monte Carlo
amu	Atomic Mass Unit
APT	Atom Probe Tomography
ASTM	American Society for Testing and Materials
bcc	Body Centred Cubic Lattice
BKS	Bacon-Kock-Scattergood
BR2	Belgian Reactor 2
BWR	Boiling Water Reactor
CALLISTO	Capability for Light Water Irradiation in Steady State and Transient Operations
CALPHAD	Calculation of Phase Diagrams
CANDU	Canada Deuterium Uranium Reactor
CCC	Chemical Composition Correction Model
CD	Cluster Dynamics
CD-P	Cluster Dynamics for Precipitation
CDS	Coherent Domain Size
CEC	Cu-enriched Cluster
CEF	Cu-enriched Feature
CoN	Cluster over Nominal
CRP	Cu-rich Precipitate
CRSS	Critical Resolved Shear Stress
CT	Chemically-tailored
CVN	Charpy V-notch test
DBH	Dispersed Barrier Hardening
DBTT	Ductile-to-brittle Transition Temperature
DFT	Density Functional Theory
DL	Dislocation Line
DLD	Delay Line Detector
dpa	Displacement per Atom
DR	Detection Rate of APT
EBSD	Electron Backscatter Diffraction
EDX (or EDS)	Energy-dispersive X-ray Spectroscopy
EONY	Eason, Odette, Nanstad, Yamamoto
fcc	Face Centred Cubic Lattice
FIB	Focused Ion Beam
FIM	Field Ion Microscope
FKH	Fridel-Kroupa-Hirsh
JEAC	Japan Electric Association Code

GB	Grain Boundary
GENESIS	Groupe d'Etudes et de Nanoanalyses des Effets d'Irradiations
GIS	Gas Injection System
GPM	Le Groupe de Physique des Matériaux
HAGB	High-angle Grain Boundary
HR	High Resolution
ICF	Image Compression Factor
IK	Inverse Kirkendall
IPM	Iso-position Method
KMC	Kinetic Monte Carlo
LAGB	Low-angle Grain Boundary
LE	Local Electrode
LEAP	Local Electrode Atom Probe
LMIS	Liquid Metal Ion Source
LWR	Light Water Reactor
M	Martensite
MAUD	Material Analysis Using Diffraction
MC	Monte Carlo
MCP	Micro-channel Plate
MD	Matrix Damage
MDC	Molecular Dynamics Calculations
MNS	Mn-Ni-Si
MNSF	Mn-Ni-Si Enriched Feature
MNSP	Mn-Ni-Si Precipitate
MR	Mass Resolution of APT
MSM	Maximum Separation Method
MTR	Material-test Reactor
NDT	Nil-Ductility Temperature
NPP	Nuclear Power Plant
NRC	Nuclear Regulatory Commission
OES	Optical Emission Spectroscopy
OKMC	Object Kinetic Monte Carlo
PAS	Positron-annihilation Spectroscopy
PD	Point Defect
PDC	Point Defect Cluster
PDSC	Point Defect-solute Cluster
PKA	Primary Knock-on Atom
PWR	Pressurised Water Reactor
RADAMO	Radiation Damage Modelling
RB	Russel-Brown
RED	Radiation Enhanced Diffusion
REP	Radiation Enhanced Precipitation

RIP	Radiation-induced Precipitation
RIS	Radiation-induced Segregation
ROI	Region of Interest
RPV	Reactor Pressure Vessel
SANS	Small Angle Neutron Scattering
SC	Solute Cluster
SCK CEN	Belgian Nuclear Research Centre
SCMF	Self-Consistent Mean Field
SEF	Solute-enriched Feature
SEM	Scanning Electron Microscopy
SFA	Shear Fracture appearance
SIA	Self-interstitial Atom
sqrt	Square Root
SRT	Standard Rate Theory
STEM	Scanning Transmission Electron Microscopy
TEM	Transmission Electron Microscopy
TOF	Time of flight
TTS	Transition Temperature Shift
V	Vacancy
WWER	Water-water Energetic Reactor
UMD	Unstable Matrix Defect
USE	Upper Shelf Energy
UTS	Ultimate Tensile Strength
XPD	X-ray Powder Diffraction
XRD	X-ray Diffraction
YS	Yield Strength

List of Main Terms

α_{obs}	Obstacle Strength
μ	Shear Modulus
σ	Yield Strength
$\Delta\sigma$	Yield Strength Increase
τ	Shear Stress
ϕ	Neutron Flux
ϕt	Neutron Fluence
Ω_{obs}	Obstacle Resistance
b	Burgers Vector
C	Concentration
d	Cluster Size (Diameter)
f_V	Volume Fraction
M	Taylor Factor
N_D	Number Density
R_{Eq}	Equivalent Spherical Cluster Radius
R_g	Guinier Radius
S	Shape Factor
Q	APT Detection Efficiency

Introduction

The growth of the global population and industrialisation request more and more energy production each year. At the same time, humanity is running out of fossil fuels, and there is a demand for a sustainable energy source to stop the detrimental climate changes. In this scenario, sources of electricity production with low carbon emission are essential.

Nuclear power is a source of energy with low CO_2 emission which contributes to around 10 % of the electricity supply worldwide by the fleet of 440 nuclear reactors [1]. Contrary to the general public perception, nuclear energy is the safest way of producing electricity used so far [2]. By 2020s almost 100 nuclear reactors will surpass 40 years from the day they started to produce electricity. Currently, almost 70% of the active reactors are over 30 years old [3]. The design of nuclear power plants (NPP) of the next generation is not finalised yet, and the first fusion reactor is still under development. Thus, the lifetime of contemporary pressurized water reactors (PWRs) should be safely prolonged.

One of the critical long-term operation issues of NPPs is the neutron irradiation embrittlement of reactor pressure vessel (RPV) materials. The RPV is a steel-made container of nuclear fuels, internal structures and coolant water maintained under high pressure (about 15 MPa) at high temperature (around 300 °C) [4]. The RPV is one of the most important parts of the NPP because it acts as a barrier between radioactive materials and the environment and cannot be replaced.

During the operation of NPP, neutrons produced by nuclear fission in the reactor core can interact with the RPV steel, resulting in the formation of self-interstitial atoms (SIA) and vacancies (V) which will enhance diffusion and lead to the formation of irradiation enhanced precipitates. Also, a continuous flux of these point defects can drag solute atoms resulting in the formation of irradiation-induced solute clusters or segregations. Precipitates and clusters act as barriers for dislocation motion resulting in the hardening and the consequent embrittlement of material [5]. Alloying elements such as Mn, Ni and Si, and impurities like Cu and P are often associated with the clusters and precipitates formed under irradiation.

Different parameters influence the magnitude of irradiation hardening. The most noteworthy ones are irradiation temperature and flux, accumulated dose and bulk chemical composition. The irradiation temperature (~290 °C) and flux (~10^{14} n/m^{2}s) are similar for most commercial nuclear

power plants [4]. The accumulated dose increases with the operation time. Finally, the bulk chemical composition significantly varies depending on the country and the time of NPP construction.

The main objective of this PhD research is to understand the influence of the bulk chemical composition (focusing on Mn, Ni, Cu and P) on the microstructure evolution and consequently its impact on the irradiation hardening of RPV steels.

To do so, seven chemically-tailored (CT) RPV steels, divided into four groups are selected. The first group aims to evaluate the effect of Mn, the second to account for the effect of Ni and Mn/Ni synergy, the third one to study the effect of P content and its synergy with Cu, and finally the fourth one to measure the effect of high bulk concentrations of Cu, P, Mn, Ni combined. These materials were irradiated at 290 °C inside the BR2 material test reactor (MTR) at high flux conditions (from 1 to 2.5 x 10^{17} n/m^2s, E > 1 MeV) [6]. In order to evaluate the evolution of solute cluster characteristics with irradiation dose, three distinct irradiation doses of about 0.06, 0.08 and 0.13 dpa, representing typical exposures for nearly 25, 30 and 50 years of operation in commercial NPPs are studied. Microstructural features are characterised by Atom Probe Tomography (APT) using a CAMECA LEAP 4000X HR with electrical pulses (GPM Rouen). The magnitude of irradiation hardening was measured using tensile specimens tested at room temperature, in hot cells at SCK CEN. The irradiation hardening due to solute cluster formation is estimated with several hardening models. Predicted values are compared with the experimental data measured by tensile tests.

The manuscript is composed of five chapters. In the first chapter, the literature review on the microstructure evolution and mechanical properties degradation of RPV steels under the effect of irradiation will be delivered. The irradiation related processes occurring at the atomic scale will be reported. The description of the radiation enhanced and radiation-induced mechanisms driving the microstructure evolution under irradiation will be given. The main metallurgical and irradiation parameters influencing the microstructure evolution will be listed. The correlation between microstructure evolution and detrimental irradiation hardening and embrittlement processes will be reported.

In Chapter II, definitive information about composition, thermo-mechanical treatment, irradiation conditions and irradiation hardening, of chemically-tailored RPV steels selected to study the effect of bulk chemical composition on microstructure evolution and irradiation hardening will be presented. A comprehensive description of the APT technique, selected to study the irradiation-

induced microstructure evolution on the nanoscale, its limitations and sample preparation procedure will also be described.

In Chapter III, the results of the microstructure investigation on chemically-tailored RPV steels at the micro- and nano-scales will be delivered. The results of the chemical composition measurements and cluster identification procedures in both reference and irradiated states will be reported. For the neutron irradiated materials, the number density, size and chemical composition of solute clusters evaluated by APT will be reported.

In the following Chapter IV, the discussion of the observed APT results will be delivered. Cross-comparison between chemically-tailored RPV steels to understand the effect of bulk solute concentration of Mn, Ni, Cu and P will be performed. The dose effect on the microstructure evolution will also be discussed. The more probable cluster / precipitates formation mechanisms will be proposed.

Further, in Chapter V, the obtained microstructural data will be compared with the results of tensile tests, to evaluate the effect of bulk chemical composition on the irradiation hardening in CT RPV steels.

Finally, the manuscript will be summarised by a general conclusion and the future perspective of this study.

References

1. S. Chu, A. Majumdar. Nature 488 (2012): 294–303. https://doi.org/10.1038/nature11475

2. B.W. Brook, A. Alonso, D.A. Meneley, J. Misak, T. Blees, J.B. van Erp. Sustainable Materials and Technologies 1-2 (2014): 8-16. https://doi.org/10.1016/j.susmat.2014.11.001

3. OECD and NEA. Report 'Legal Frameworks for Long-Term Operation of Nuclear Power Reactors '(2019). https://doi.org/10.1787/c7b6dbb2-en

4. N. Soneda (Ed.). Irradiation Embrittlement of Reactor Pressure Vessels (RPVs) in Nuclear Power Plants. Elsevier (2015). https://doi.org/10.1016/C2013-0-17428-4

5. G.S. Was. Fundamentals of Radiation Materials Science: Metals and Alloys. Springer, New York (2007). https://doi.org/10.1007/978-3-540-49472-0

6. R. Chaouadi. RADAMO Database: Available Irradiated RPV Materials for Advanced Microstructural Investigations, SCK CEN restricted report 27710469, T-0093

Chapter I: Theoretical background

1 Reactor of nuclear power plant

1.1 Nuclear power plants with pressurised water reactor

The first nuclear power plant (NPP) was connected to the electricity grid in the middle of the 20th century (1954) in the USSR. Starting from that point more and more countries had chosen nuclear power to be part of the electricity production industry, with more than 440 nuclear reactors running right now. Nuclear power contributes around 10% of electricity worldwide and takes an important place in electricity production mix. The leaders of the production of nuclear energy are the USA, France, China and Russia [1-7].

Nuclear power plants evolved in comparison with their first ancestors. Overall, we can divide nuclear power plants into five categories or generations (I, II, III, III+, IV) depending on their efficiency and safety. Generation one includes prototypes of nuclear reactors developed in the middle of the previous century. The second generation of NPP was designed to be used commercially. The typical representatives of the generation II reactors are the pressurised water reactor (PWR), the Canada deuterium uranium reactor (CANDU), the boiling water reactor (BWR) and the water-water energetic reactor (WWER). Both BWR and PWR are part of the so-called light water reactor (LWR) class [8].

The lifetime of generation II NPPs was originally aimed to be around 40 years of operation. The generation III is presented as an advanced LWR. They should reach 60 years of operation lifetime. The generation III+ is NPPs of the generation III with safety improvements. This generation is under construction nowadays. The IV generation which should be built in the coming decades will have at least the safety features of the generation III+ but will be based on new design and different fuel or coolant [1-4]. The time evolution of NPPs is presented on figure 1 [9].

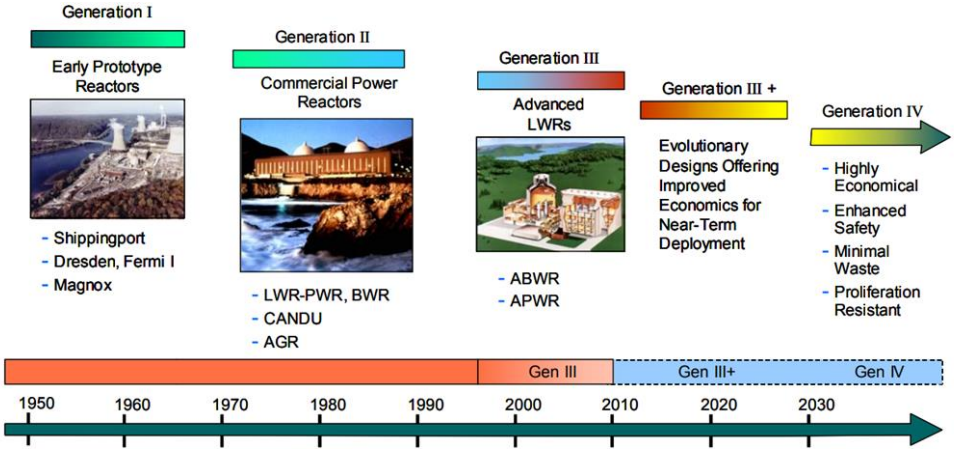

Figure 1. *Overview of nuclear power plant generations [9].*

The generations II, III, III+ NPPs are mainly running PWR system. The typical design of NPP with PWR is presented below (Fig. 2).

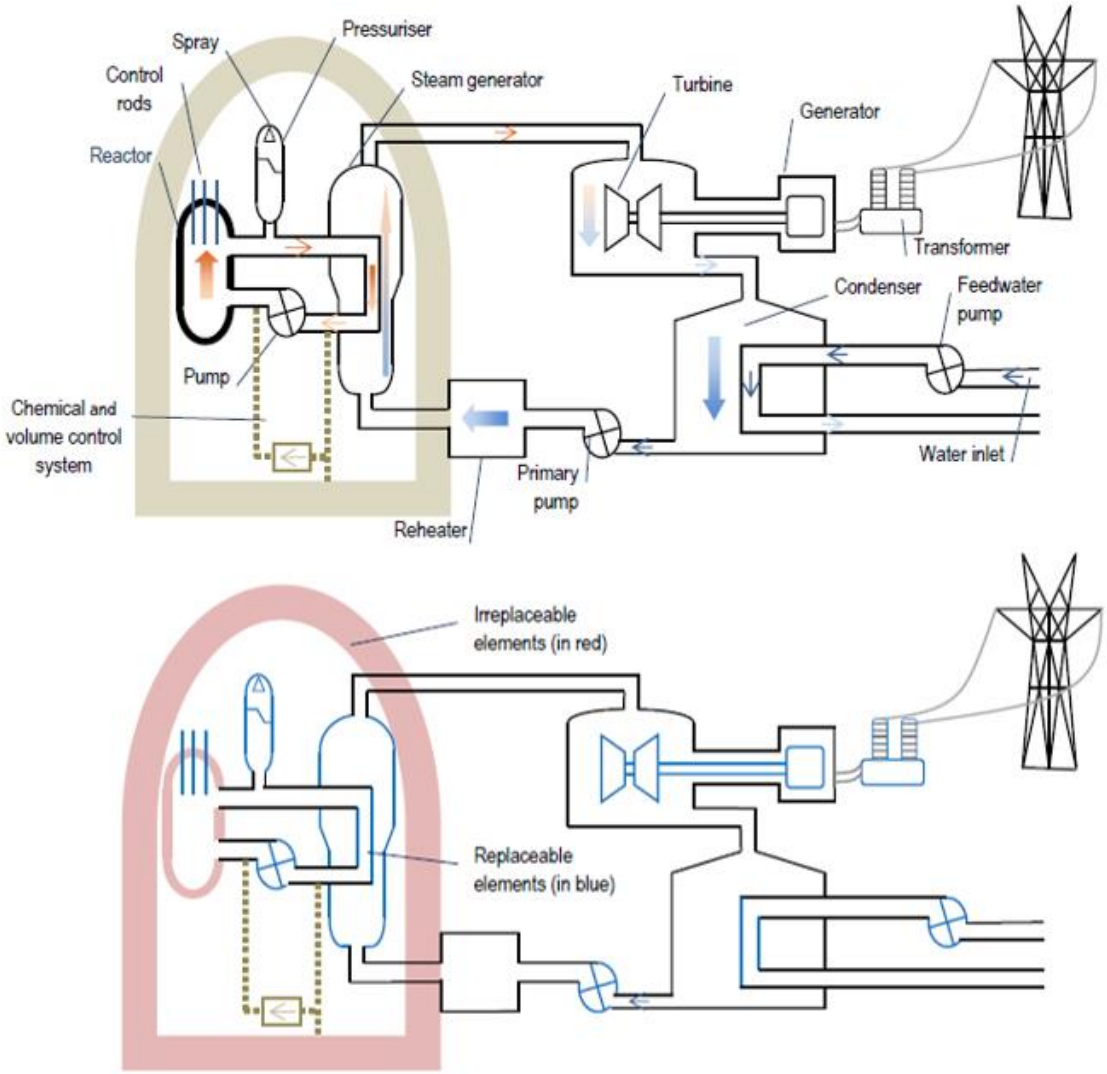

Figure 2. *General operation scheme of nuclear power plant with pressurised water reactor. Irreplaceable components such as reactor pressure vessel (RPV) and containment building are highlighted in red on the lower image [4].*

The safety of nuclear power plants is ensured by three barriers between radioactive elements and the environment. The first one is the fuel cladding. It is subjected to high doses of several dozens of displacements per atom (dpa) during operation, but it is possible to change the fuel assemblies if necessary. The second barrier is the vessel which acts as a container of the nuclear fuel and high temperature and high-pressure coolant water. The integrity of this barrier is crucial. In the case of RPV failure, the water maintained under high pressure and temperature will evaporate and expand causing a severe damage to the nuclear core with a probability of leaking of a highly active nuclear fuel. The third barrier is the containment structure which is designed to keep the radioactive products from the environment in the case of any failure.

From the whole NPP only two vital parts are irreplaceable - the containment structure and the vessel. Therefore, the integrity of these parts is necessary since they will not be changed during the whole NPP lifetime which is supposed to reach a minimum of 40 years. Since 2020, several nuclear power plants are over 50 years of operation and connected to the electricity grid. Currently, almost 70% of active nuclear reactors are over 30 years old. The designs of NPPs of the next generation (IV) are not finalised yet and the first fusion reactor is still under development. Thus, the lifetime of contemporary pressurised water reactors should be prolonged as much as it will be possible (up to 80 years) [1,3,4].

1.2 Reactor pressure vessel

In a PWR water is used as a neutron moderator and coolant for the heat transfer. To prevent water from evaporation at the high operating temperature of NPP (above 300 °C), it should be maintained under a high pressure of around 15 MPa.

The size of the vessel of a PWR is ranging between 10 and 15 meters in height and up to 5 meters in diameter, depending on the power capacity. To sustain the high pressure, the wall thickness of the vessel is about 20 to 25 cm thick. Due to its large size, it is impossible to make RPV from one cast. The conventional design consists of an assembly of formed plates made from base material A533B welded together by longitudinal and circumferential welds. The weld seams are a weakness of the structure and minimising the total length of weld seams was a goal for newer reactor designs. With the improvement of production technologies, it was possible to produce large forged rings which are welded together only with a circumferential weld (Fig .3). Typical examples are the American Society for Testing and Materials (ASTM) standard A508B steel and its French equivalent 16MND5.

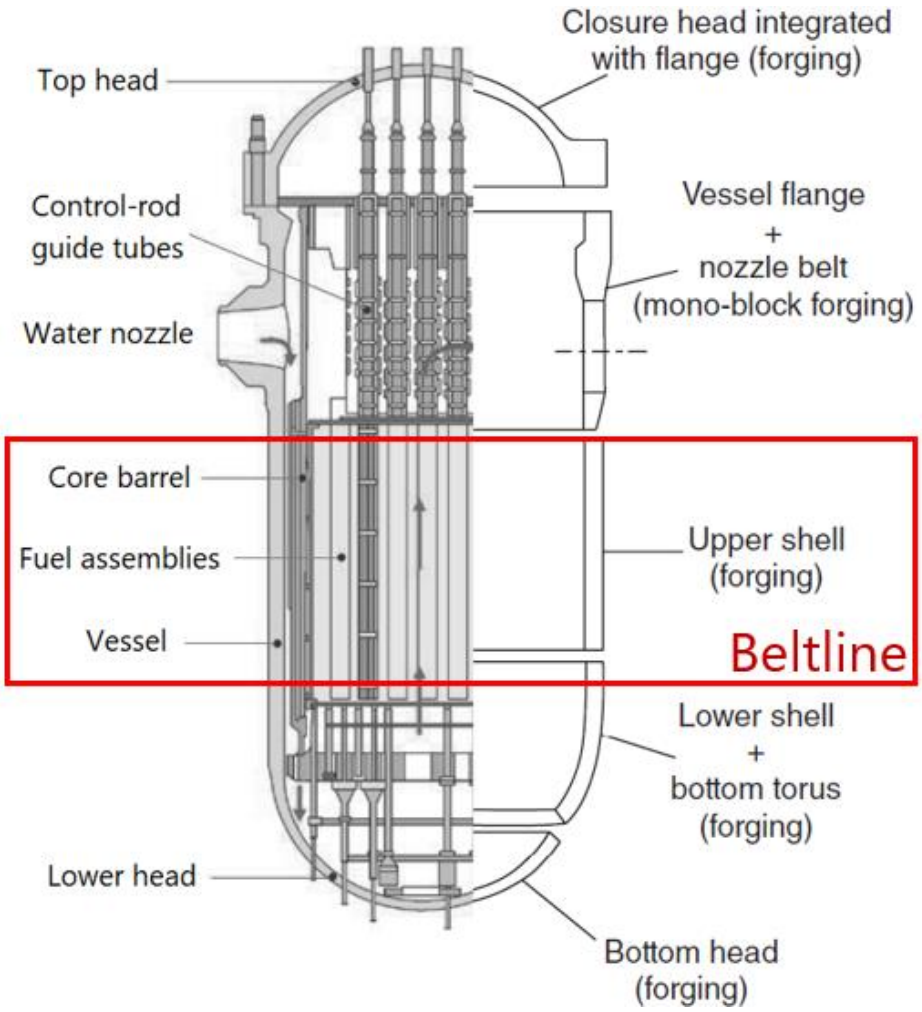

Figure 3. *Typical reactor pressure vessel made of forged rings [10,11]*

The typical material used for RPVs is low-alloyed ferritic steel. A typical chemical composition of steel plate (SA533B-1) is presented in Table 1.

Table 1. *Typical composition of western RPV steel. Balance is in Fe [8].*

[%]	Alloying elements						Residual elements		
	C	Mn	Mo	Ni	Cr	Si	P	Cu	S
weight	≤0.25	1.15-1.50	0.45-0.60	0.4 - 0.7	-	0.15 - 0.4	≤0.035	≤0.1	≤0.04
atomic	*≤1.2*	*1.2-1.6*	*0.27-0.36*	*0.4 - 0.7*	-	*0.3 - 0.8*	*≤0.06*	*≤0.1*	*≤0.07*

To reach the designated mechanical properties, a specific thermo-mechanical treatment is performed on the rings or plates. The optimized final microstructure is tempered bainite. The yield strength (YS) of RPV steels is around 450-500 MPa and the tensile strength is above 550 MPa [8].

2 Effect of neutron irradiation

2.1 Primary damage

In the current fleet of NPPs, the energy is produced from nuclear fission. A fissile isotope upon being bombarded by a neutron can split into two lighter nuclei while emitting additional neutrons and heat, due to the mass excess. The typical fuel for nuclear reactors is made of ^{235}U (Fig. 4).

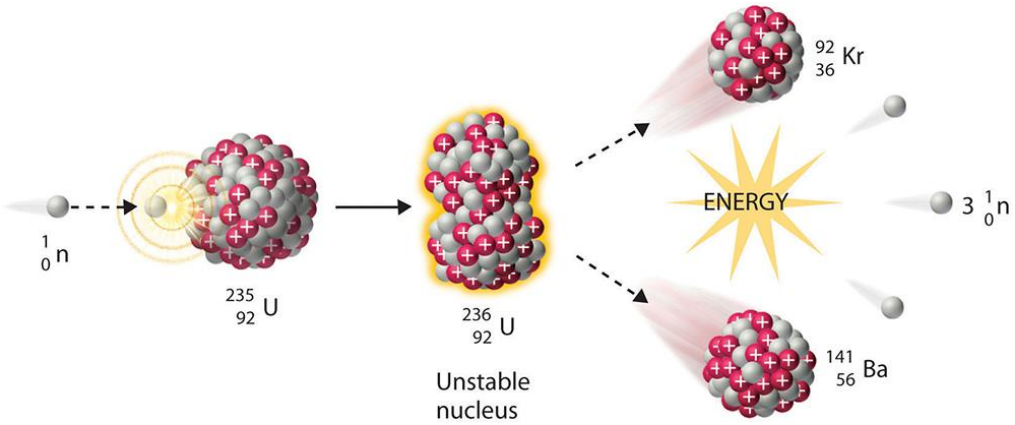

Figure 4. *Fission reaction of 235U utilised as fuel in commercial NPPs [3].*

Most of the emitted neutrons, with 1 MeV energy, are slowed down (moderated) and collide with other nucleus to maintain the chain reaction or are absorbed by control bars. In the case of PWR the moderator is light water. However, a small number of neutrons leave the reactor core and interact with the vessel atoms.

When a neutron knocks a lattice atom, it transfers a part of its initial energy (1 MeV) to the Fe atom. A frontal strike will transfer up to 70 keV to the Fe lattice atom. This energy is far superior to the energy needed to eject the Fe atom from its lattice site (displacement threshold energy, E_d is about 40 eV for Fe (ASTM value) [12]). When the atom is ejected from its lattice position it finishes as a self-interstitial atom, forming a dumbbell, and a vacancy is created at its initial position [13].

If the energy of the primary knock-on atom (PKA) is high enough it will move through the crystalline lattice colliding with other atoms and forcing them to leave their positions, resulting in the formation of a so called “displacement cascade” (also called damage cascade). In the displacement cascade, equal numbers of vacancies and self-interstitials are created. Each pair of vacancy and self-interstitial is called a Frenkel pair. The depth of the damage cascade is usually limited to around 10 nm. Mean free path of neutron in Fe lattice is on the level of few centimetres and one neutron can produce several damage cascades travelling through the RPV wall.

The time of formation and recombination of a damage cascade is extremely short. Therefore, it was never experimentally observed. Only numerical tools allow to recreate and visualize the defect creation and recombination processes. The simulation performed by Nordlund and co-workers illustrate the time evolution of a damage cascade (Fig. 5) [14].

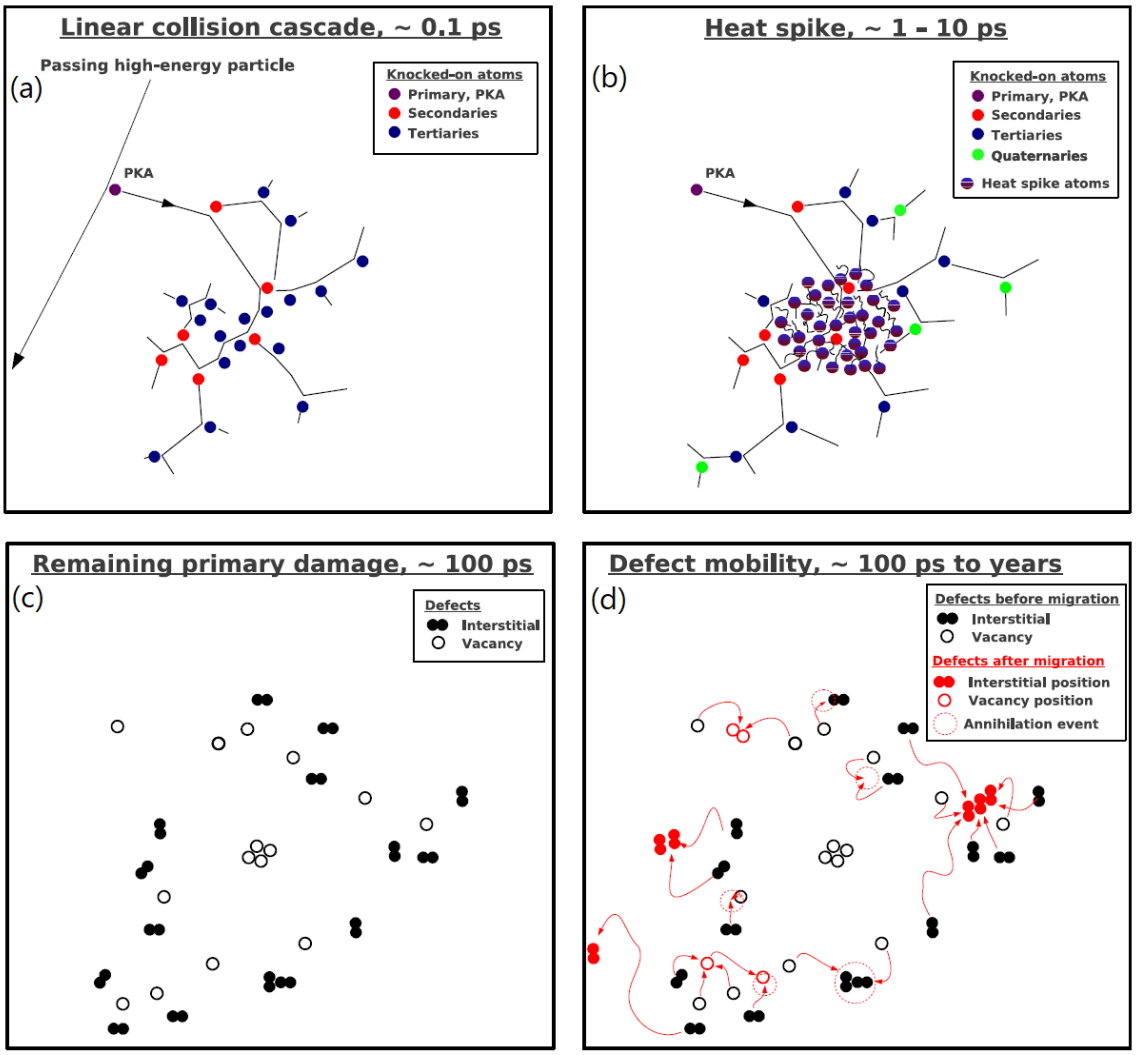

Figure 5. *The evolution of a damage cascade. (a) The initial event is the energy transfer from the neutron to PKA. (b) At 10 ps, a huge number of SIAs and Vs are created in the cascade. Most of them (more than 99%) will annihilate by mutual recombination. (c) After dozens of ps, few SIAs, vacancies and small SIA and vacancy clusters survive to the recombination process. (d) These PDs are mobile (SIA much more than V) and, after long range diffusion, can agglomerate into extended SIA and vacancy clusters, recombine or annihilate at sink [14].*

The high concentration of these PDs is the source of different process such as radiation enhanced diffusion (RED) and irradiation-induced segregation (RIS) which will be described in the next part.

2.2 Enhanced diffusion

Diffusion is the basic mechanism of atom transportation in metals. The diffusion coefficient can be written as: $D = D_0 exp\left(\frac{-Q}{k_B T}\right)$, where k_B is the Boltzmann's constant, T is the temperature, Q is the activation energy and $D_0 = \alpha_{v,i} a^2 \, v \, exp\left(\frac{S_f + S_m}{k_B}\right)$ is the temperature independent part, v is the Debye frequency (~10^{13}s^{-1}), S_f is the formation entropy and S_m is the migration entropy. In body centred cubic lattice (bcc) the coefficients α_v equals to 1 and α_i equals to 1/6 [13].

The total self-diffusion coefficient is given by the combination of vacancy and interstitial mechanisms $D_{th} = D_v X_v + D_i X_i$ with activation energy $Q = E_f + E_m$ and where E_f is formation and E_m is migration energies, X_v and X_i are the atom fractions of Vs and SIAs respectively. The energy to distort the lattice and create the self-interstitial atom (SIA) in Fe is around 5 eV [15], which is significantly bigger than the energy needed for a vacancy creation around 1.4 eV [16]. Therefore, without irradiation, the concentration of Vs is much bigger than the concentration of SIAs. Thus, the vacancy diffusion mechanism is the dominant one and diffusion is defined by a simple relation $D_{th} = D_v X_v^{eq}$.

As it was described in the previous subchapter, under neutron irradiation a high number density of vacancies and interstitials is created. The self-diffusion coefficient under irradiation is then given by the following equation $D_{rad} = D_v X_v^{rad} + D_i X_i^{rad}$. The operation temperature of PWR (around 290 °C) is high enough for the mobility of PDs, and low enough to observe $X_v^{rad} \gg X_v^{eq}$. Also, vast number of SIAs created under irradiation $X_i^{rad} \gg X_i^{eq}$ furthermore increases the magnitude of diffusion. Consequentially, irradiation diffusion coefficient is significantly higher than the thermal one $D_{rad} \gg D_{th}$. This phenomenon is called radiation enhanced diffusion. RED will promote the formation of thermodynamically favourable phases of super-saturated solutes. For example, Odette and co-workers have proposed the formation of Cu-rich precipitates (CRPs) in RPV steels containing more than 0.1 at. % of Cu by the radiation-enhanced precipitation (REP) [17].

The important note is that formation of precipitates of oversaturated solutes could be expected even without irradiation, for example in the case of long-term thermal aging. Yet in the case of ageing at RPV operation temperature formation of precipitates will take considerably more time since $D_{th} \ll D_{rad}$. Thermal diffusion for Cu atoms at operation temperature of PWR (290 °C) $D_{th}^{Cu} \sim$ 10^{-25} m^2/s which is more than two orders of magnitude lower than radiation-enhanced diffusion coefficient $D_{rad}^{Cu} \approx$ 2.5 x 10^{-23} m^2/s [17].

2.3 Induced clustering and segregation

In the previous paragraph, the enhanced precipitation phenomena due to neutron irradiation was described. But REP can't explain the formation of nanosized solute clusters of undersaturated elements. Hence, a different mechanism such as irradiation-induced segregation (RIS) should be accounted for. Contrarily to the irradiation-enhanced diffusion, this process will occur only under irradiation.

The phenomenon is based on the fact that under irradiation, the supersaturated point defects can annihilate on defect sinks such as grain boundaries (GBs), interfaces, dislocation networks, loops, voids and etc. Subsequently a point defect flux toward sinks is created. PDs may interact with solute atoms and drag them towards sinks with a magnitude depending on jump frequency and interaction energy values, thus resulting in the redistribution of solutes under neutron irradiation [13,18-20].

The first theories about flux coupling were proposed in the case of a binary alloy with A and B atoms. In the first case (Fig. 6.a) fluxes of both solutes are in the opposite direction from the vacancy flux. If atoms of species A are more diffusive than atoms of B ($D_A^V > D_B^V$), the vacancies flux will create a higher flux of A atoms in the opposite direction of the sink. This redistribution will result in the depletion of A atoms and the enrichment of B atoms at the sink. This process is called the Inverse Kirkendall (IK) effect.

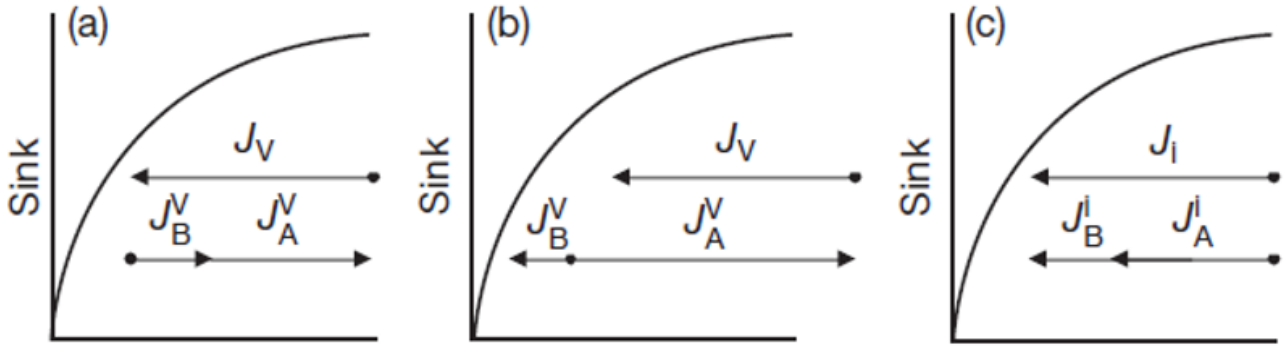

Figure 6. *Irradiation-induced segregation in a binary A-B alloy. (a) Fluxes of A and B solute atoms are in the opposite direction of vacancy flux. A atoms diffusing faster than B ones will result in the depletion of A and enrichment of B at sink. (b) Vacancies and B atoms are attracted. Vacancies flux will create the enrichment of B and depletion of A at the sink. (c) Both A and B atoms are transported by SIA towards the sink, enrichment in A and B elements will occur. Enrichment will depend on respective A and B nominal compositions [18].*

In some cases, the bonds between solute atoms and vacancies could be strong enough that the solute atom will be dragged towards the sink by the vacancy. In the proposed case (Fig. 6.b) we

will expect the enrichment of B at the sink for two reasons – the vacancies will transport B atoms towards the sink by the drag effect, and A atoms will be moved away by the IK effect, which will result in the additional enrichment of B atoms at the sink.

The interstitial mechanism (Fig. 6.c) is based on the fact that solute atoms may create interstitial-solute complexes, called mixed dumbbells. Therefore, solute atoms will be transported in the direction of the interstitial flux. Depending on relative diffusion rates ($D_A^I > D_B^I$) the faster specie will enrich at sinks.

RIS occurs when a significant flux of PDs towards sinks is created, which is possible in a finite temperature regime (Fig. 7). At the high temperature a big number of thermal vacancies is created $C_v^{eq} \gg C_v^{rad}$. Without PD oversaturation a flux towards sinks is not created and diffusion is controlled by the thermal process $D_{th} \gg D_{rad}$. If the temperature is too low, the vacancies will be immobile and would be annihilated by the mutual recombination with the mobile interstitials [18].

The second important parameter is the irradiation flux or defect production rate (Fig. 7). During irradiation with lower flux, RIS domain is shifted towards lower temperatures. PDs are created further away from each over and the probability of sink annihilation over mutual recombination increases. Contrary, if it the dose rate (dpa/s) is too high, a lot of PDs will be created in localised area and probability of mutual recombination increases [18].

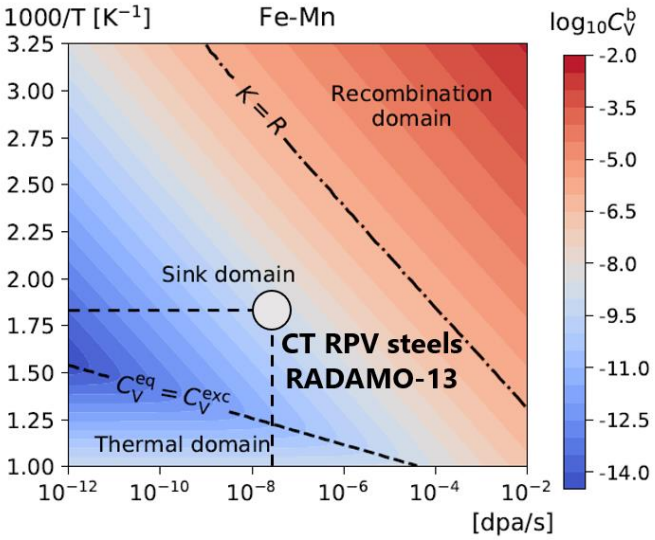

Figure 7. *Inverse temperature versus dose rate (dpa/s) graph defining different regimes for binary Fe-1Mn alloy. Same trends were observed for Fe-Ni, -Si, -P, -Cu, -Cr alloys [21]. Grey circle marks the Radiation Damage Modeling-13 (RADAMO) irradiation conditions which are inside the radiation-induced segregation domain.*

The development of modelling tools allows us to understand how different solutes will interact with vacancies and SIAs. The work of Messina and co-workers based on the combined *ab*

initio calculations with a mean field model, Density Functional Theory (DFT) and kinetic Monte Carlo (KMC) calculations is an example [21-29]. These data were further implemented by Castin and co-workers to predict the RIS with object kinetic Monte Carlo (OKMC) modelling [30,31].

When a V or SIA meet the solute atoms, they can form a stable V-solute pair or SIA-solute dumbbell. The pair considered stable when its migration energy (E_{mig}) is smaller than a dissociation energy (E_{dis}) $E_{mig} < E_{dis}$. This stable PD-solute pairs will move towards PDs sinks.

In the work of Messina and co-workers calculations showing the vacancy drag mechanism were performed in diluted (1 at .%) binary alloys for different typical solute elements (Mn, Ni, Si, P, Cu, Cr) playing major roles in irradiated RPV steels [22]. The vacancy-solute flux coupling was defined by the wind factor (G) (Fig. 8).

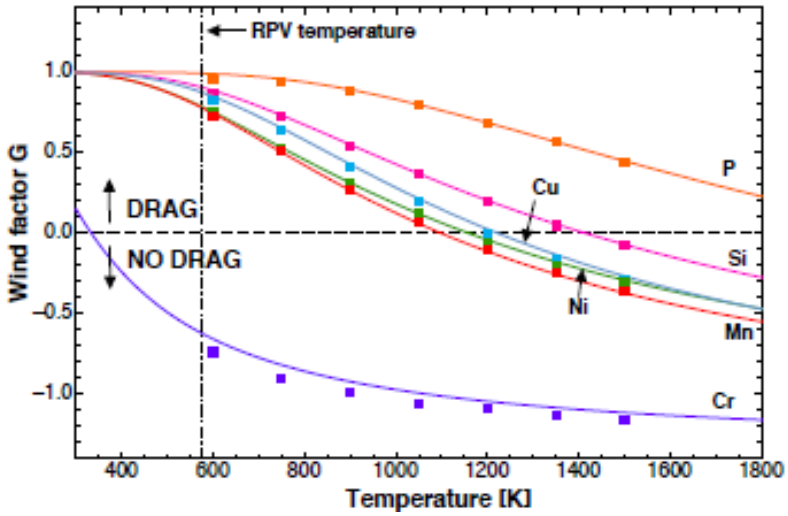

Figure 8. *Wind factor as a function of temperature calculated in a diluted Fe- binary alloys containing either P, Si, Cu, Ni, Mn or Cr. Vacancy-solute drag occurs for positive G values [22].*

It is evident that for the RPV operating temperature range, vacancies can drag P, Si, Cu, Ni and Mn atoms towards sinks, resulting in local enrichment and segregation. For chromium, the IK mechanism is dominant and results in the depletion of Cr at sinks.

In bcc Fe, the more stable SIA configuration is the <110> dumbbell. The Fe-solute mixed dumbbells are stable and allow transportation of solute atoms towards the sinks. The graph (Fig. 9) from [22] shows the comparison of mixed dumbbell mobility compared to the Fe-Fe one.

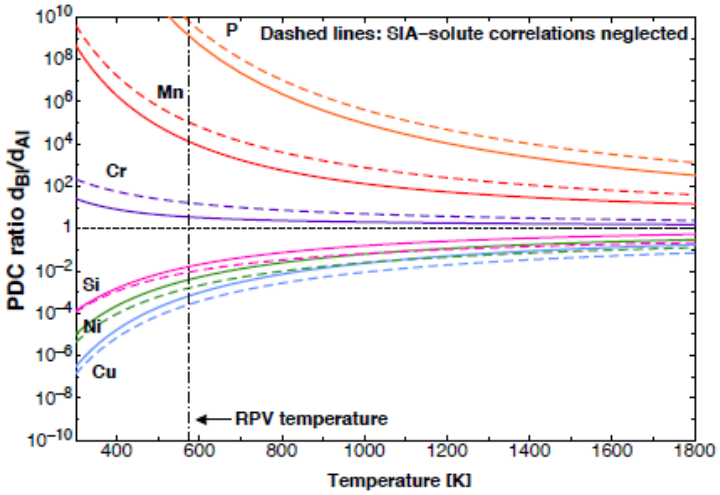

Figure 9. *Ratio of solute-to-solvent partial diffusion coefficients as a function of temperature. Solute diffusion is faster than self-diffusion for values greater than one [22].*

We can expect enrichment on sinks for more mobile atoms. Thus P, Mn and Cr atoms are concerned in irradiation and temperature conditions of RPV steel.

By combining both vacancy and SIA mechanisms we can predict the total effect of PD-solute flux coupling under irradiation (Fig. 10).

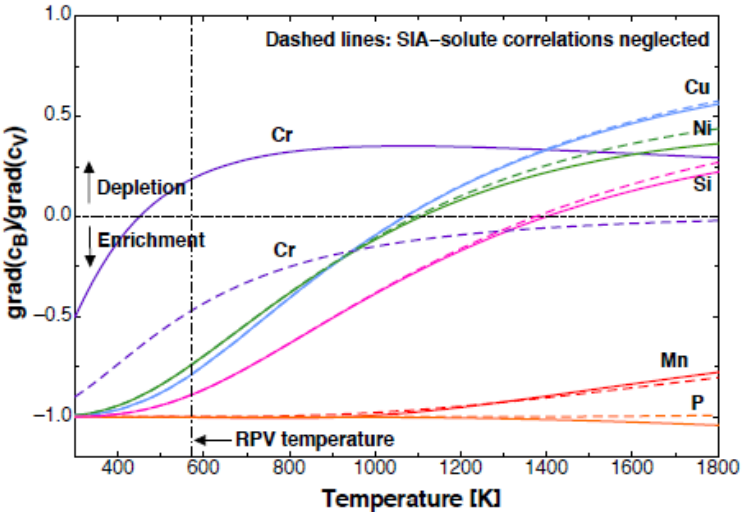

Figure 10. *Radiation-induced segregation profiles as a function of irradiation temperature. Solute enrichment on sinks occurs for negative values [22].*

For comprehensive understanding of RIS tendencies, the effect of solute atoms on pinning and immobilising the PD clusters (PDCs) should be defined. Small V and SIA clusters are extremely mobile in the absence of solute atoms. 3D migration energy of small SIA cluster is lower than 0.5 eV and in the case of 1D gliding of SIA loops is even lower and equals to around 0.1 eV. The small V cluster of around five vacancies has a higher migration energy of around 1 eV and can migrate in all directions [30].

In the case of RPV steel, these PDCs are rapidly becoming immobilised by the solute atoms surrounding them. With the increase of the bulk solute concentration the probability for PDCs to intercept solute atoms increases. With income of solute atoms small PDCs becoming more enriched in solutes and trapped with increased strength. The size of solute clusters will continuously grow if the substantial flux of PDs dragging solutes is created.

The composition of RPV materials is more complex than a binary alloy. There are numerous different solutes affected by the RIS and Kirkendall effect and having their independent behaviours, and the segregation tendencies could differ from the predicted in binary alloy ones. Yet comparison with atomistic modelling is important and useful to understand the mechanism at the origin of the formation of irradiation-promoted features. At the operating temperature of RPV steel (290 °C), we are anticipating the solute segregation of P, Mn, Si, Ni and Cu atoms. The summarised results of the RIS tendency for main solutes causing hardening in RPV steels are presented in Table 2.

Table 2. *RIS tendencies for solutes in RPV steel from [27].*

Solute	SIA dumbbell	E_{mig} [eV]	E_{dis} [eV]	V drag	E_{mig} [eV]	E_{dis} [eV]	Dominant mechanism
Cu	no	0.881	0.448	yes	0.693	0.908	V
Mn	yes	0.319	0.884	yes	0.623	0.805	SIA
Ni	no	0.674	0.355	yes	0.700	0.853	V
P	yes	0.213	1.290	yes	0.668	1.042	SIA
Si	yes	0.824	0.579	yes	0.720	0.965	both

3 Parameters influencing microstructural evolution

3.1 Neutron flux

The objective of NPP operation time increase up to 80 years raises the need to study materials irradiated up to higher doses (above 0.2 dpa), and the number of surveillance samples subject to such a high irradiation exposure is limited. Also, additional research on model alloys with composition different form commercial RPV steels to study specific effects of irradiation should be performed. To do so, material test reactors (MTRs) should be utilised. In MTR, high neutron flux is available and hence high accumulated doses could be achieved faster. One of them is the Belgian Reactor 2 (BR-2), reactor where materials studied in this work were irradiated.

For the actual RPV steel, irradiation flux ranges around 10^{14} to 10^{15} n/m^{2}s (E > 1 MeV). It is several orders of magnitude lower than the one observed in MTRs (above 5 x 10^{16} n/m^{2}s,

E > 1 MeV) [32]. This observation is important, meaning that MTR's conditions are not fully representative of RPV irradiation conditions. The flux effect must be considered.

As it was described in the previous chapter, RIS is possible only in specific irradiation flux/temperature conditions. Both in commercial NPP and MTR, the irradiation conditions lead to the same regime.

Odette and co-workers performed extensive research on the irradiation flux effect in the late 1990s and early 2000s, predicting the formation of unstable matrix defects (UMDs) in case of high flux conditions in MTR [33,34]. But this effect was experimentally not confirmed in the research performed by Chaouadi and Gerard [32]. In their study, UMDs in the high flux conditions were not observed. They concluded that kinetics of radiation hardening were the same whatever high or low fluxes were considered.

The effect of flux on RED was studied by Wells and co-workers [35]. They observed that a very high flux (above 10^{18} n/m^{2}s, E > 1 MeV) can result in the delay of precipitation and, hence shifting the hardening effect towards higher fluences. The explanation they gave was the following: increasing the flux results in an increase of the total defect formation and a decrease of the distance between each of them. In this condition a significant number of PDs will recombine. The term effective fluence (Φt_e) was proposed to perform the comparison between materials irradiated with a significantly different fluxes: $\phi t_e = \phi t(\phi_r/\phi)^p$, where Φt is the actual fluence, Φ is the actual flux, Φ_r is the reference flux and p is the scaling coefficient.

Another observed tendency is that the number density of irradiation promoted clusters is higher in the case of high flux MTR. Also, the size of these clusters is small. However, the total volume fraction of these clusters remains in the same range [36].

The study of the flux effect is out of the scope of this current work. The irradiation flux varies between around 1 to 2.5 x 10^{17} n/m^{2}s, E > 1 MeV [37], which represent insignificant variations. This flux is equivalent to dose rate of around 1.5 to 4 x 10^{-8} dpa/s.

3.2 Neutron fluence

The fluence can be defined by the number of neutrons interacting with the material or by the accumulated dose in terms of dpa. Increasing the irradiation dose will result in a higher transformation of the initial microstructure of the material. As an example, the number density and the size of irradiation-promoted features are usually presented as a function of accumulated dose.

The typical dose for RPV of PWR after 40 years of operation is around 0.1 dpa (one atom over ten is moved during 40 years). Reaching 60-80 years of operation will lead to a total accumulated dose of about 0.2 dpa.

Irradiation of RPV results in the formation of matrix damage (MD) features such as small point defect clusters (PDs), nanovoids and small dislocation loops [38-42]. These PDs, dislocation loops and nanovoids will act as point defect sinks and can therefore be decorated by solute atoms due to the PD-solutes flux coupling. At doses below 0.1 dpa, the effect of MD on hardening is negligible comparing to the effect of solute clusters and precipitates [43]. In RPV steel irradiated to higher doses of above 0.2 dpa (Φ = 0.2 to 0.5 x 10^{17} n/m^{2}s, E > 0.5 MeV) the small dislocation loops with a number density of 2 x 10^{22}m^{-3} and the average diameter of 4-5 nm were observed [44]. In another study of material irradiated up to around 1 dpa at a lower irradiation temperature of 275 °C (Φ = 0.2 x 10^{17} n/m^{2}s, E > 0.1 MeV) the small dislocation loops with a number density of 0.9 x 10^{22}m^{-3} and the average diameter of 7 nm were observed. In the same study nanovoids with a number density of 0.1 x 10^{22} m^{-3} and a mean diameter of 3.3 nm were found [45].

In the low-Cu RPV steels (~0.05 at. % Cu) solute clusters (SC) containing Mn, Ni, Si, P and Cu will be formed by RIS. With the increase of dose, the number density of these clusters will gradually increase up to 10^{24} m^{-3} [32]. These clusters will reach a size of around 3 nm in diameter and will no grow further. At higher levels of neutron irradiation, about 0.2 dpa, the formation of Mn-Ni-Si (MNS) enriched precipitates could be expected [35]. In the case of RPV steels with higher Cu content (above 0.1 at. %) the high mobility of Cu atoms arising from the large number of vacancies created under the irradiation will result in the rapid formation of Cu-enriched features (CEFs). Around the dose of 0.03 dpa, most of the Cu atoms will be inside the CEFs. Further, the matrix won't be supersaturated in Cu and the new CEFs won't be formed, and the microstructure evolution will be similar as in the low-Cu counterparts [38].

Generally, in the case of low-alloyed RPV steels, increasing irradiation fluence increases the number density of solute clusters and slightly increase the average size of the irradiation-induced features.

3.3 Bulk chemical composition

The irradiation temperature and neutron flux are similar for the RPV steels in the worldwide fleet of PWR nuclear power plants. Thus, the accumulated dose gradually increases with time in the same way for all commercial plants. The main parameter that varies is the nominal chemical composition of the steels.

For most RPVs, two types of steel are used for their production. A so-called base steel is used to produce the big plates and forged rings, that must be differentiated from the weld lines connecting these big parts together [8]. Usually, the weld is slightly more enriched with Mn and Ni (around 1.5 at. %) [47,48]. In the case of old welds, more Cu was introduced during the welding process [49,50]. The second difference comes from the origin of NPP. For example, in the eastern PWRs, a WWER steel is used, which has a higher Ni and Cr content than in its western counterparts [8].

Mn, Ni, Si, Cu and P are the elements defining the magnitude of irradiation hardening and embrittlement of RPV steels. The first two are the alloying elements added to increase the tensile properties and hardenability, and corrosion resistance. Silicon is used for deoxidization during steel production. The latter two are impurity elements from scrap and their presence is undesirable.

3.3.1 Copper

For the first NPPs of the second generation, the purity of RPV was not perfect and the Cu level was around 0.2 to 0.3 at. % [8]. It was fast discovered that Cu is one of the most or maybe even the most detrimental element concerning the hardening and embrittlement of irradiated RPV steels. In the acknowledged work by Hawthorne, the detrimental effect of Cu was proven, and synergy between Cu and other solute elements was studied [51].

The reason why Cu is so harmful is the fact that its solubility limit in the Fe matrix at the operating temperature of PWRs (300 °C) is very limited and about 0.007 at. % [52]. The formation of fully fcc (face centred cubic) ε-Cu precipitate is composed of several steps. The first is the formation of coherent bcc Cu-enriched cluster (CEC) with a diameter of below 5nm. Further, then the size grows above 5nm, the transformation to the faulted 9R fcc structure occurs. Finally, then the diameter surpasses 10nm, the large (diameter 10-20 nm) fully fcc ε-Cu precipitate is formed [53-56]. The latter ε-Cu precipitates were observed with STEM-EDS on the high-Cu RPV weld [53]. Their lattice structure is confirmed by TEM experiments and only these large fcc ε-Cu precipitates should be defined as true CRPs [54]. In the study by Styman and co-workers the thermal ageing on high-Cu (above 0.4 at. % Cu) was performed. The APT results showed the thermodynamically driven formation of small bcc CEFs, some of which further transformed into 9R Cu precipitates (Fig. 11) [57,58].

Yet, as it was noted in the section 2.2, the irradiation-enhanced diffusion coefficients are several orders of magnitude larger than the thermal ones. Also, the constant redistribution of PDs changes the kinetics of the CEFs evolution. Thus, under the effect of irradiation, within the typical for RPV steel fluxes, the CEFs are never grow large enough to transform to the fully fcc CRPs.

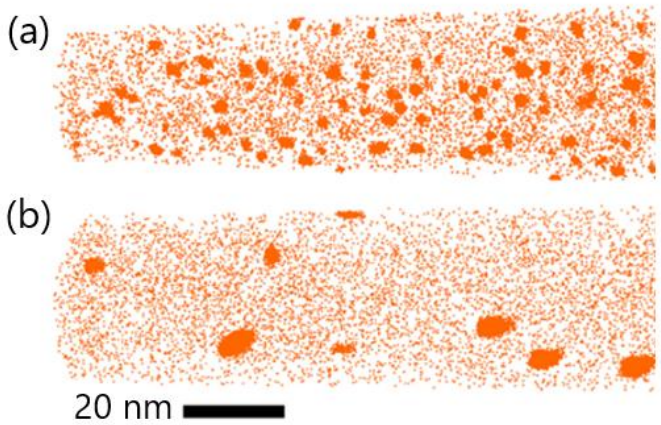

Figure 11. *Atom maps of typical Cu atoms distribution in high Cu/Ni RPV weld aged for 90,000 hours at (a) 330 °C and (b) 365 °C. The formation of CEFs is evident [57].*

CEFs were observed in numerous works on high-Cu RPV steels. Their diameter is usually on the order of 2 nm and their number density ranging between 10^{23} and 10^{24} m^{-3}. The core of CEFs is highly enriched in Cu (up to 80 at. %). Small amounts of Ni, Mn, Si, P and Fe atoms can be also associated to these features (Fig. 12) [32,50,59-67]. These features hinder the dislocation motion, resulting in hardening and consequentially in the embrittlement of RPV steel.

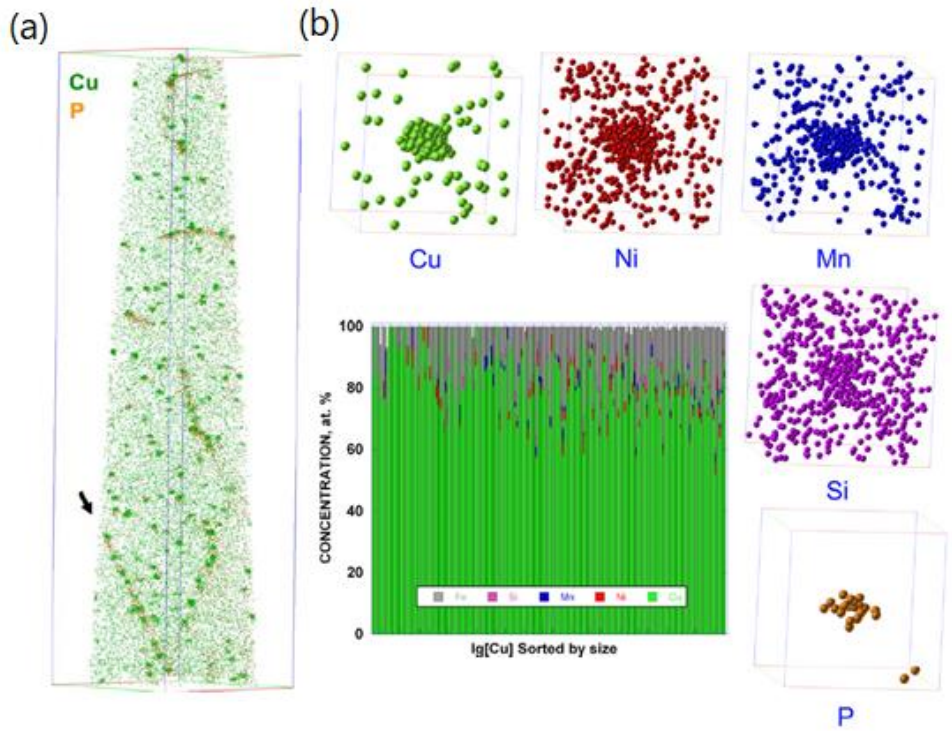

Figure 12. *APT observation by Miller and co-workers in a high-Cu RPV steel. (a) The high number density of CEFs and P segregations to dislocation lines are shown. (b) Atom maps of one CEF are presented, note that extents of Mn, Ni and Si atoms are larger than Cu ones. Clusters have around 80 at. % of Cu [50,63-66].*

In high-Cu steels the Cu-clustering, driven by irradiation enhanced diffusion, occurs swiftly. The modelling performed by Odette and co-workers predicts the formation of a high number of coherent to a bcc lattice Cu-rich features before reaching the dose of 0.03 dpa [17,60-62]. These CEFs act as barriers for dislocation lines (DLs) causing severe irradiation hardening. After these CEFs are formed, Cu in the matrix will be undersaturated and newer precipitates will not be formed, and the hardening effect will not increase further [17,60-62,68,69]. There is a saturation effect of this hardening mechanism.

Yet, in the studies on the steels with Cu content below 0.1 at. %, a more diluted Cu-enriched features containing up to 50 at. % of Fe have been observed [38,70-76]. Due to the lower Cu enrichment, they are usually defined as Cu-enriched clusters. Apart from the article by Fukuya and co-workers, in which it was defined as precipitate [76]. To understand more about the early stages of CEFs formation, electron and ion irradiations were utilised [77-79]. The conclusion was made that PDCs created at the damage cascade have an important role in CEFs formation acting as sites for heterogenous Cu clustering [77-79]. This is especially valid to the current fleet of wester PWRs, in which Cu content is maintained as low as 0.05 at. %. In that case, the supersaturation of Cu is not high enough to favour the formation of CEFs by radiation enhanced diffusion. In low-Cu steels, Cu is expected to segregate by radiation-induced mechanism via PDs flux coupling, same as other solutes (Mn, Ni, Si, P) [22].

3.3.2 Manganese, Nickel and Silicon

Mn and Ni, contrary to Cu and P, are alloying elements, so their presence is necessary to reach the desired mechanical properties of steel.

The strong effect of Ni on the hardening of RPV steels was observed in experimental study [32] and also predicted by modelling [49,80]. The influence of Mn was not so evident, and it was proposed that Mn acts alongside the Ni due to synergistic effect and will not result in severe embrittlement by itself [32,61]. The research of Meslin and co-workers on an ion irradiated model Fe-Mn alloy showed that Mn will form clusters even in the absence of Ni [81].

Overall, in the western commercial RPV steels both Mn (up to 1.5 at. %) and Ni (up to 1 at. %) are not oversaturated in the ferritic matrix at the operating temperature of PWR and should not precipitate [8,52]. Yet, formation of dilute solute clusters enriched in Mn and Ni is observed [74,82-92]. They contain up to 85 at. % of Fe and the formation mechanism of SCs is supposed to be irradiation-induced and is connected to the coupling between fluxes of PDs and solutes [74,83-86]. Other solutes are also associated with these clusters. They are highly enriched in Si (up to 20 to 30 relative percent of solute concentration) and to the lower extent by P and Cu [83,89]. So, Si has

similar to Mn and Ni an important role in solute cluster formation. The Si concentration in commercial RPV materials is maintained on the level of ~0.5 at. %. Solute clusters can pin dislocations and act as obstacles for their motion. Irradiation hardening due to formation of SCs linearly increases with the square root (sqrt) of irradiation dose [30,92].

Solute clusters are expected to be small and coherent to the Fe lattice [30], so they are hardly detectable with conventional TEM [93]. Yet, it became possible by the state of the art scanning transmission electron microscopy with energy dispersive spectroscopy (STEM-EDS) [94,95]. Solute clusters are usually studied by Small Angle Neutron Scattering (SANS) and Atom Probe Tomography. The typical number density of SCs is in the range of 10^{22} to 10^{24} m^{-3} and their size ranges from 1 to 3 nm in diameter (Fig. 13) [74,82-92]. More detailed information about solute cluster properties observed in literature is given in appendix A.1.

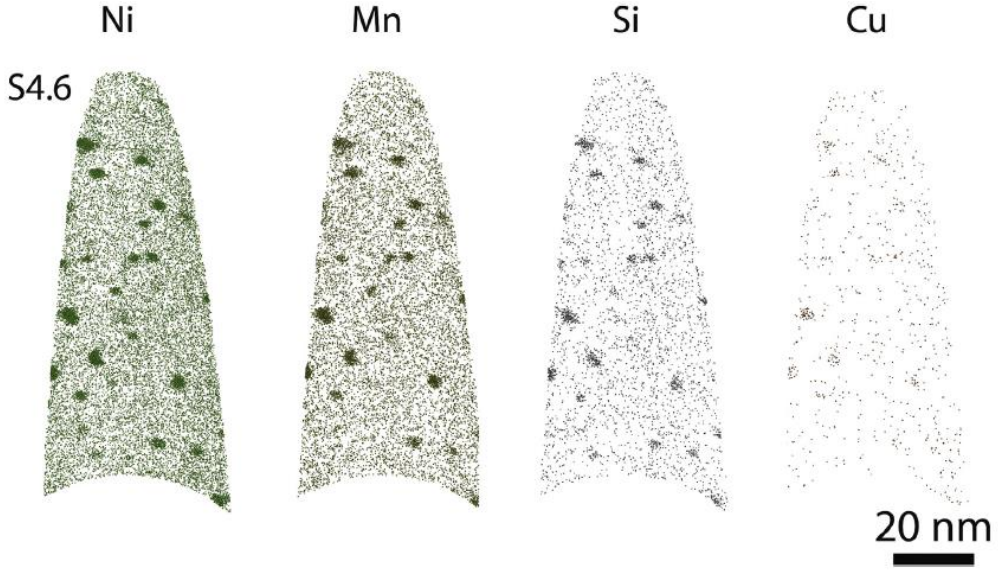

Figure 13. *Atom maps distribution of Ni, Mn, Si and Cu atoms in the 10nm cross-section slices from a surveillance RPV steel. Solute clusters enriched in Ni, Mn, Si and Cu are observed [89].*

The calculated hardening due to radiation-induced formation of SCs correlates well with the results of mechanical tests for surveillance materials irradiated up to 0.1 dpa (around 40 years of operation).

However, Odette and co-workers predicted the severe increase of irradiation hardening above the doses of 0.2 dpa due to radiation enchased formation of Mn-Ni-Si precipitates (MNSPs), also called “late-blooming phases” [60-63,96,97]. To explain the probable formation mechanism a new equilibrium thermodynamic model was developed based on Calculation of Phase Diagrams (CALPHAD) by Xiong and co-workers [98]. They predicted a wide range of Fe-free Mn-Ni-Si phases formed at the temperature 277 °C (Fig. 14).

Experimental studies on the "model" RPV materials with variable combinations of Mn (0.1-1.5 at. %), Ni (0.2-3.5 at. %), Si (0.1-1.3 at. %) and Cu (~0.00-0.25 at. %) concentrations were performed [35,99-107]. Most of materials were irradiated in the high flux MTRs up to doses of around 0.2 and 1.8 dpa at 290 to 320 °C [35,99-101,103-105]. In these studies, large volume fractions of solute features enriched in Mn, Ni and Si were identified. Important to note that around 50% of Fe was measured in the features core. Not to mix the Fe-free MNS precipitates predicted by modelling, and the Mn-Ni-Si enriched features (containing Fe) observed by APT, the term MNS-enriched features (MNSFs) will be utilised when describing the results obtained with APT.

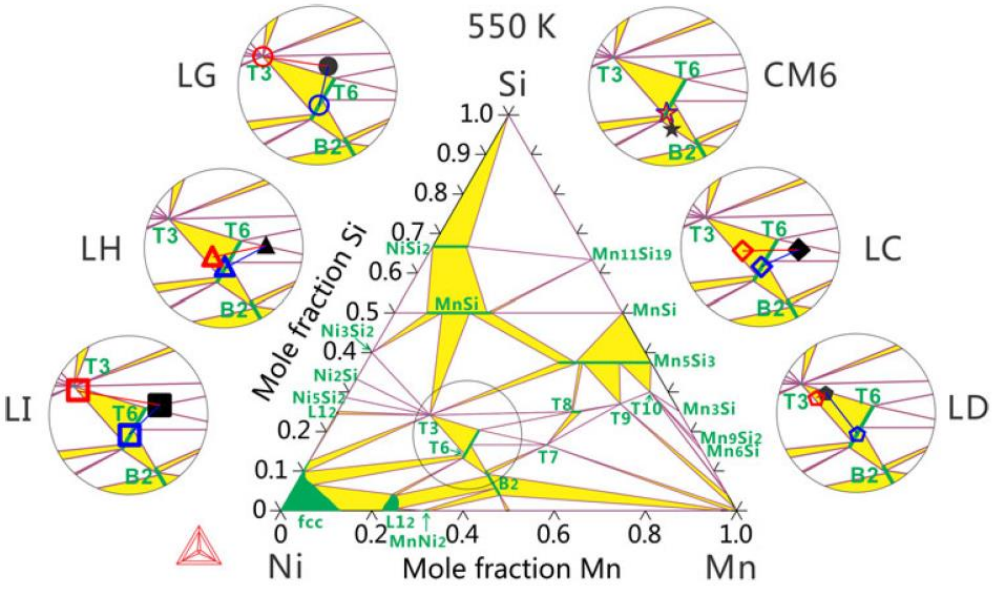

Figure 14. *Ternary phase diagram of Mn-Ni-Si system at 277 °C. Filled symbols represent the APT composition of MNSFs from experimental data on six RPV steels with different chemical compositions. Open red and blue symbols are the predictions from commercial and homemade CALPHAD databases [35,98,99].*

More detailed information about MNSFs properties observed in literature is given in appendix A.2. The summary of observed results is the following:

- High number density (10^{23} to 10^{24} m^{-3}) of MNSFs was observed. Average diameter of MNSFs ranges from 2 to 5 nm;
- High amount of Fe atoms was found inside MNSFs (50 to 60 at. %). US researchers considered Fe as APT artefact due to the high atomic density inside latter (several times above the matrix density). Therefore, they exclude Fe from the cluster composition measurements [35,94,104]. The exclusion of Fe is questionable and will be discussed in detail in chapter II.3.3.5;

- If Fe is removed as artefact, the results of APT experiments on model RPV steels irradiated up to 1.8 dpa correlate well with the thermodynamic model predictions of G (T3) and Γ_2 (T6) phases (Fig. 14) [98,99,102];
- In high-Cu materials CEFs can act as sites for heterogeneous MNSFs formation (Fig. 15) [99];
- In low-Cu materials MNSFs are heterogeneously forming on the dislocation network or small dislocation loops (Fig. 16) [100,102,107];
- Compositions of observed Mn-Ni-Si phases (if Fe is excluded from calculations as APT artefact,) do not always directly correspond to predicted phases and are dependent on the material bulk Mn, Ni and Si concentrations [100];
- In high-Ni (1.57 at. %) model RPV steel, some MNSFs grew after annealing at 425 °C for 29 weeks, which supports their thermal stability in the operation conditions of RPV steel [101].

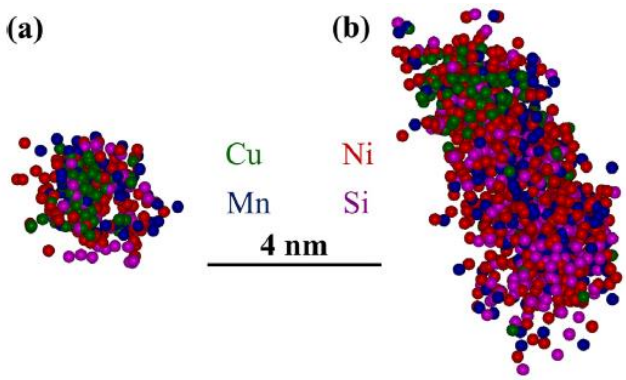

Figure 15. *Atom maps of Ni, Mn, Si and Cu distribution inside MNSFs. (a) CEF-core/MNS-shell structure observed in model RPV steel irradiated up to 0.2 dpa. (b) CEF with MNS-appendage structure observed in model RPV steel irradiated up to 1.8 dpa [35,99].*

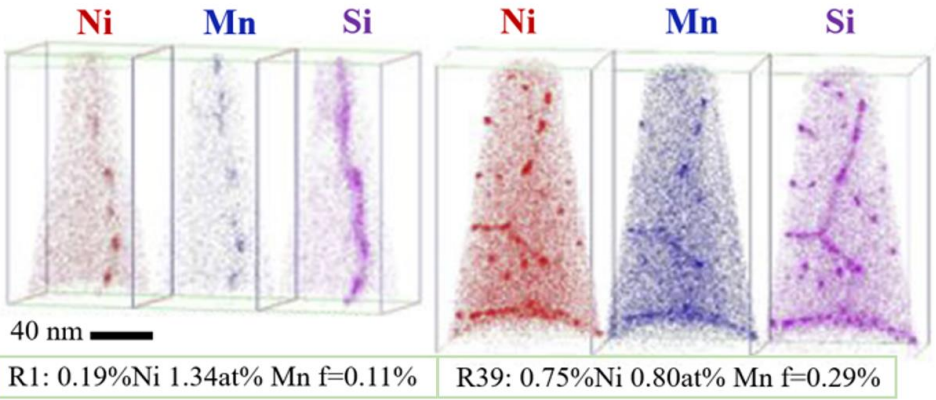

Figure 16. *Atom maps of Ni, Mn, Si distribution inside model RPV steel irradiated up to 0.21 dpa. Formation of MNSFs alongside dislocation lines is observed [100].*

In order to examine if MNSFs formation arises from precipitation, series of long-term aging experiments on model RPV steels were performed [53,55,108]. The number density of Mn-Ni-Si-enriched precipitates is significantly lower (~10^{22} m^{-3}) than observed in irradiated materials. A high amount of Fe atoms is associated with these precipitates (30 to 60 at. %) [53,55]. In the case where Fe was considered as APT artefact and removed from composition measurements, the composition of the thermodynamically formed MNS-precipitates after long-term ageing is in a good agreement with the predicted G- and Γ_2-phases [108]. But, in the study of Styman and co-workers, where model RPV steel was aged during 50000 and 90000 hours, different Fe concentration inside precipitates was observed (33 vs 39 at. %). If presence of Fe atoms inside precipitates arises from the APT artefacts, its concentration should had remained the same in both conditions. Since Fe precipitate concentration decreases with ageing time, the conclusion was made that Fe atoms were indeed present inside precipitates [53]. Latter observation questions the existence of predicted Fe-free Mn-Ni-Si phases.

G-phase is the ordered $Fm\bar{3}m$ structure and Γ_2-phase is a cubic lattice with $Fd\bar{3}m$ space group structure [109-111]. Due to the small size of MNSFs formed in RPV steels, the election diffraction data, which can resolve their lattice structure is not yet obtained [112]. The DFT study predicts that transformation from the coherent bcc MNS-enriched feature to the G- or Γ_2-phase becoming energetically preferable with Fe contents inside latter of below 20 at. % [111-113]. The Fe contents inside the MNSFs measured by APT are around 50 at. %, which is above the value needed for the transition. Therefore, the MNSFs observed in RPV steels by APT, are most likely the coherent bcc clusters, which could, theoretically, transform to G- or Γ_2-phases.

To conclude, the composition of small (around 2 to 3 nm in diameter) solute clusters enriched in Mn, Ni, Si, Cu and P observed in commercial RPV steels at the doses of around 0.1 dpa generally differs from the composition of predicted MNS-phases [76,83,86,88-91]. The formation mechanism is radiation-induced and driven by the flux coupling between PDs and solutes.

The mechanism of formation of Mn-Ni-Si solute-enriched features found at the doses above 0.2 dpa is still highly debatable. The probable explanation is the combination of radiation enhanced heterogeneous precipitation and radiation-induced solute segregation on the dislocation network, small PD clusters, and also on the CEFs in the case of high-Cu RPV steels.

3.3.3 Phosphorus

As Cu, P is an impurity and its presence in commercial RPV steel is undesirable. In the western RPV steels, P content is maintained below 0.05 at. % [8].

Compared to Cu, P has a different behaviour under neutron irradiation. P atoms are extremely diffusive and can migrate for long distances [22,27]. They will usually segregate at interfaces and grain boundaries (Fig. 17) [114-118]. Phosphorus GB segregation will not result in the increase of yield strength or hardening. However, it will weaken the GB energy cohesion and promote intergranular fracture [18,40]. The fracture will propagate by intergranular mechanism which requires less stress than the transgranular one. This process called non-hardening embrittlement and will be described in chapter IV.

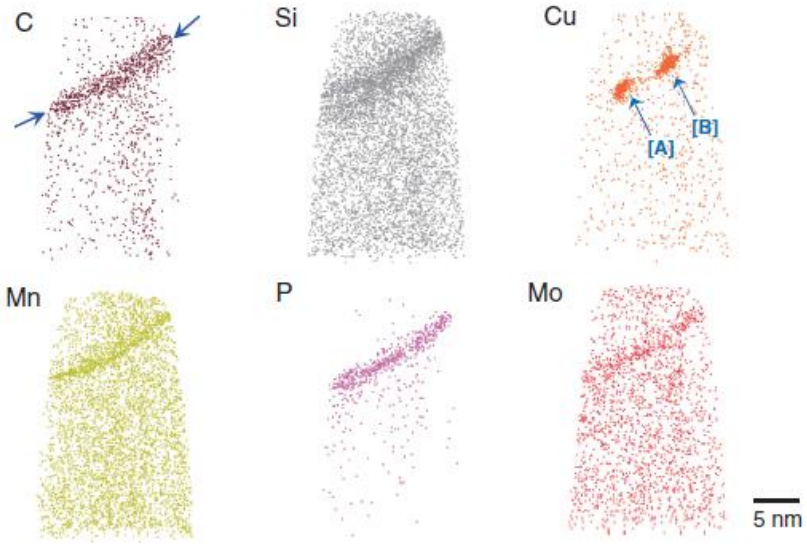

Figure 17. *Atom maps near GB region in Doel-2 RPV surveillance test specimen. Grain boundary enriched in C, Si, Mn, Mo and P is shown. Almost all P atoms from the surrounding area had segregated onto GB. Two CEFs on GB are also shown [118].*

Also, P segregation along dislocation lines (Cottrell atmosphere) was observed in the literature [66]. They result in the increase of energy needed for unpinning dislocations. The P segregation is due to the irradiation-induced dragging of solutes or impurities. As it was described earlier, Fe-P mixed dumbbells are extremely mobile and P atoms will be transported in a large amount towards the sinks such as dislocation lines (Fig. 18) [22,27].

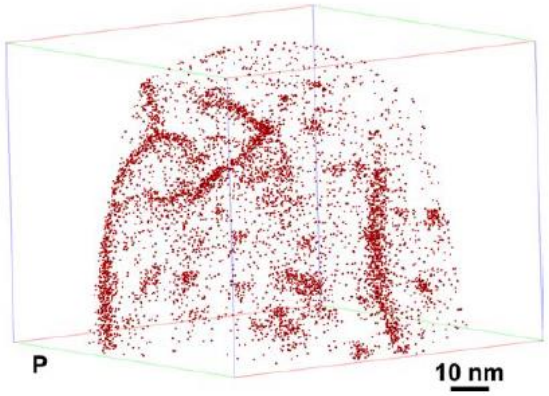

Figure 18. *Atom map showing the distribution of P atoms in neutron irradiated Fe-Ni-P model alloy. P segregations to dislocation lines are visible [66].*

The effect of P on the cluster formation was less extensively studied. However, highly mobile P atoms with a high binding energy with both V (1.29 eV) and SIA (1.04 eV) are the first candidates to intercept and trap PDCs, creating a PD sink for a further solute segregation [22,27]. For example, P-rich clusters were observed in Fe-P (~0.045 at. %) model alloy and in high-P (~0.06 at. %) WWER weld [119-122]. Same as in the case of CEFs and SCs, the P-rich clusters will impede the dislocation motion resulting in irradiation hardening. In addition, there is a synergetic effect between P and Cu. In the case of low-Cu and high-P steels, P can form spherical clusters on the dislocation lines [63-66].

4 Irradiation hardening

The evolution of the microstructure under neutron irradiation results in the hardening and, furthermore, embrittlement of RPV steel. The correct estimation of embrittlement magnitude is necessary for a safe operation and possible prolongation of NPP lifetime.

There are two main mechanisms for metal fracture: ductile and brittle. The brittle fracture happens with fast crack propagation and can result in complete failure of material when stress above critical point is applied. The ductile fracture is more stable and predictable. The fracture occurs with a plastic deformation of the material. A constantly increasing load is needed to maintain the crack propagation. Unirradiated RPV steels exhibit ductile fracture at operation temperature and brittle fracture at low temperature conditions below zero degrees Celsius [8]. The temperature when the material starts to exhibit mostly the brittle fracture is called ductile-to-brittle transition temperature (DBTT).

The DBTT is measured by the Charpy impact, also called Charpy V-notch (CVN), test. In Charpy impact test the notched bar of material of interest is broken in a wide range of temperatures and the absorbed energy is measured. Shear fracture appearance (SFA) and lateral expansion are also measured. From these data a graph showing absorbed fracture energy vs the test temperature is plotted. The minimum number of samples required to plot a Charpy curve is around 10 for a material exhibiting a low scatter and increases to about 18 for a non-homogeneous material. The transition temperature when material exhibits brittle fracture, also called nil-ductility temperature (NDT) is found to correlate well with the temperature at which the absorbed impact energy of CVN equals 41 J. The upward shift of DBTT quantifies the embrittlement (Fig. 19). Embrittlement results not only in DBTT shift but also in the decrease of the upper shelf energy (USE) which represents the maximum energy needed for fracture in the fully ductile region of selected material [116].

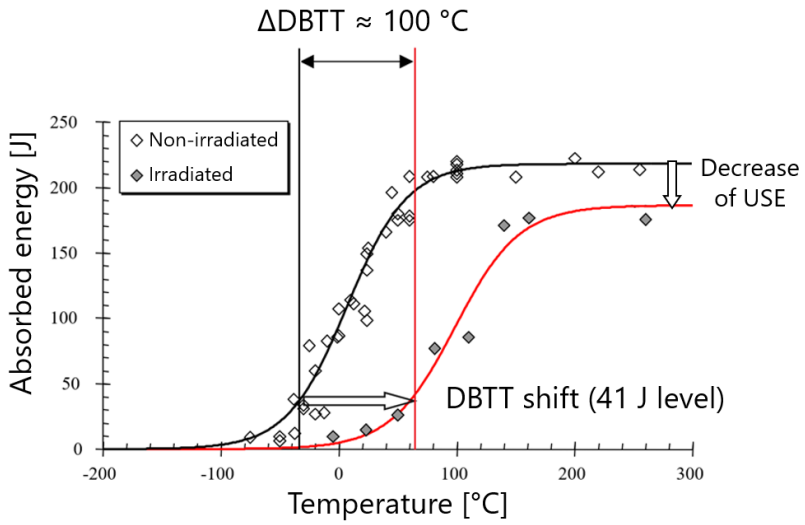

Figure 19. *Charpy curves for non-irradiated and irradiated RPV steel. The curve was plotted with the data of the Charpy impact test at different temperatures. DBTT is measured for 41 J of absorbed energy. A shift of DBTT of around 100 °C is observed [117].*

To evaluate the safety of commercial PWRs, surveillance capsules containing CVN and tensile test specimens are irradiated. These capsules are located closer to the reactor core. Due to the higher irradiation exposure the data form surveillance samples are used to estimate the anticipated embrittlement of the vessel itself. The data for more than 100 years of operation is available in surveillance databases. For the low-Cu RPV steels DBTT shift is below or equals to 50 °C at the doses of around 0.1 dpa [8].

There are two main mechanisms of embrittlement of RPV steels. The non-hardening and hardening embrittlement. The non-hardening embrittlement occurs mostly due to the P segregations at the GB. The non-hardening embrittlement is out of the scope of the current project. Hardening embrittlement is caused by the irradiation hardening of material. Irradiation hardening is measured as the yield strength increase from the tensile test curve. According to ASTM, three tensile tests are needed to obtain the proper yield strength increase. The yield strength of the material is proportional to the critical resolved shear stress τ_{crss} (CRSS) necessary to start the dislocation gliding [1122]. The yield strength of material is given by the sum of CRSS and grain size (Hall-Petch) contributions.

$$\sigma_y = M\tau_{rss} + \frac{K}{\sqrt{d_g}} \tag{1.1}$$

where M is the Taylor factor (3.06 in bcc Fe), K is strengthening coefficient (0.45 MPa $m^{1/2}$ in ferritic steels) and d_g is the average grain size. The ferrites grain in bainite have an elongated lath-like shape with a ratio between shortest and longest size of 1/10. In the current project to account for the grain shape the average grain size of ferrite for the irradiation hardening prediction was measured with the intercepts in the OIM Analysis software.

Since the grain size is not expected to evolve under irradiation, the Hall-Patch contribution will not change. Hence, the irradiation hardening is governed by the change of CRSS. Solute clusters, precipitates, matrix damage and solute segregations on the dislocation lines will lower the intragranular dislocation motion and will result in an increase of the critical resolved shear stress.

$$\Delta\sigma_{ir} = M\Delta\tau_{crss} \quad (1.2)$$

The increase of the yield strength will shorten the plastic deformation region and the fracture stress will be reached with a lower deformation level. With the constant fracture stress, the increase of the yield strength will result in the upward shift of the DBTT (Fig. 20) [8,13].

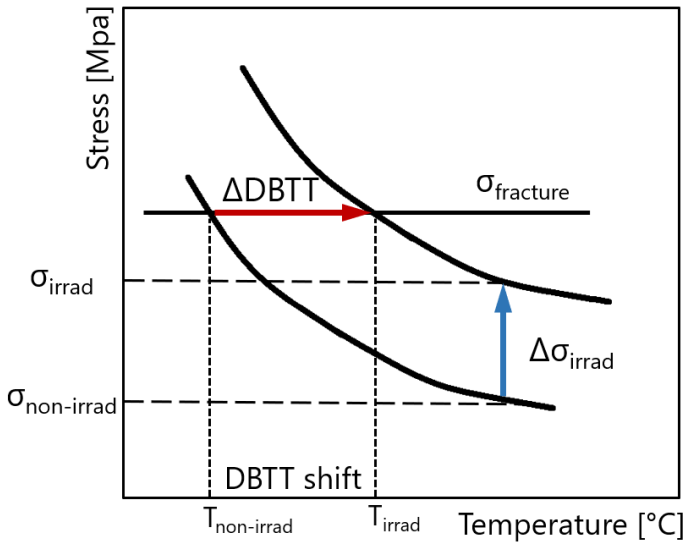

Figure 20. *The effect of irradiation hardening (increase of yield strength) on the upward shift of ductile-to-brittle transition temperature.*

There is no direct ratio between the irradiation hardening and embrittlement of RPV steels. The general empiric observations show that an increase of YS by 1 MPa roughly results in an upward shift of DBTT by 0.65 °C [123].

Correlation between microstructure evolution under irradiation and irradiation hardening is one of the main goals of the PhD project. To do so, tensile tests on the non-irradiated and irradiated specimens of chemically-tailored RPV steels were performed. Cross comparison of APT data and tensile test results were performed. Additionally, several hardening models were utilised to evaluate the influence of solute clusters number density and size on the irradiation hardening, and to find the dependence of solute cluster obstacle strength dependence to solute cluster chemical composition.

During the last half-century, several hardening models have been developed to correlate the microstructure evolution under the irradiation (formation of solute clusters, precipitates and matrix damage) with the irradiation hardening [124-128]. Solute clusters are the main contributors to the

increase of critical resolved shear stress and, accordingly, yield strength in RPV steels. The key parameters influencing the magnitude of solute clusters contribution to the critical resolved shear stress (τ_{sc}) are their obstacle strength (α_{obs}), their size (d) and their number density (N_D). The constant parameters are shear modulus, μ and the Burgers vector ($b=0.248$ *nm*). The shear modulus of different RPV steels was calculated with modelling simulations and experimental data and equals about 82-83 GPa [45,124,129].

One of the first models used for irradiation hardening calculations is the Dispersed Barrier Hardening (DBH) model. It can be used for both impenetrable and shearable obstacles [13]. In the DBH model, all obstacles with given N_D and d are considered to interact with the gliding dislocation with a given obstacle strength of α_{obs}. The contribution of obstacles to the CRSS is given by:

$$\tau_{sc} = \alpha_{sc}\mu b\sqrt{N_D d} \tag{1.3}$$

The Friedel-Kroupa-Hirsh (FKH) model was initially developed to calculate the hardening caused by small dislocation loops [125,126]. In the FHK model, the interparticle slip plane spacing L is increased because of the less pronounced dislocation line bowing during interaction with a small loop ($L = 1/dN_D^{2/3}$). The CRSS is calculated by the following equation:

$$\tau_{sc} = \frac{1}{8}\mu b d N_D^{2/3} \tag{1.4}$$

One of the most widely used models is the Russel-Brown (RB) model which was originally developed to estimate the hardening caused by Cu-precipitates [127]:

$$\tau_{sc} = \frac{0.8\mu b}{L}\left[1 - \frac{E_1^2}{E_2^2}\right]^{1/2} \qquad sin^{-1}\frac{E_1}{E_2} < 50° \tag{1.5}$$

$$\tau_{sc} = \frac{\mu b}{L}\left[1 - \frac{E_1^2}{E_2^2}\right]^{3/4} \qquad sin^{-1}\frac{E_1}{E_2} \geq 50° \tag{1.6}$$

where E_1 is the dislocation energy per unit length in the cluster/precipitate and E_2 is dislocation energy per unit length in the matrix and L is the obstacle spacing in the slip plane ($L = 1/\sqrt{N_D d}$). The ratio between these energies is dependent on the cluster/precipitates size:

$$\frac{E_1}{E_2} = \frac{E_1^{\infty} log\frac{r}{r_0}}{E_2^{\infty} log\frac{R}{r_0}} + \frac{log\frac{R}{r}}{log\frac{R}{r_0}} \tag{1.7}$$

where r is the average radius of solute cluster, r_0 is the inner cut-off radius ($r_0 = 2.5b$), R is the outer cut-off radius ($R=10^3 r_0$), the ratio of dislocation energy per unit length between infinite obstacle

(E_1^∞) and the matrix (E_2^∞) equals to $E_1^\infty / E_2^\infty = 0.6$ in Fe-Cu system and could be empirically calibrated for solute clusters [127].

The Bacon, Kocks and Scattergood (BKS) model considers the effect of free spacing between obstacles (both solute clusters and self-interaction with dislocations) on the increase of CRSS. The solute clusters contribution to the critical resolved shear stress is calculated in the following way [124,128]:

$$\tau_{sc} = \left(\frac{\Omega_{sc}}{\Omega_\infty}\frac{ln(2\,D/b)}{ln(l/b)}\right)^{3/2}\frac{ln(l/b)}{2\pi}\mu b\sqrt{N_D d} \tag{1.8}$$

where Ω_{sc} is the obstacle resistance of the solute clusters (weak obstacles), and Ω_∞ is the obstacle resistance above which the obstacle is impenetrable and cannot be sheared ($\Omega_\infty = 4.5\ GPa$), l is the free spacing between clusters in the dislocation slip plane $l = L - d$ and D is the effective obstacle diameter $D = dl/(d + l)$. In equation (1.8), the factor $\left(\frac{\ln(2D/b)}{\ln(l/b)}\right)^{3/2}$ accounts for the interaction of dislocation line with multiple randomly distributed obstacles and the factor $\frac{ln(l/b)}{2\pi}$ accounts for the effect of a single obstacle [130].

There are approaches to calculate the irradiation hardening. With the first one the contribution of different irradiation promoted obstacles (solute clusters, dislocation loops, voids…) are linearly summed. In the case of RPV steels the contribution of the matrix damage is expected to be negligible in comparison with solute clusters [43]. Therefore, the total irradiation hardening equals to:

$$\Delta\sigma_{ir} = M\tau_{sc} \tag{1.9}$$

With the second approach, the total irradiation hardening is calculated considering the effect of pre-existing before irradiation obstacles. These obstacles are the dislocation forest and the carbides. The contribution of the latter two obstacles is accounted for in the superposition method developed by Monnet and co-workers. The total irradiation hardening in RPV steels due to solute cluster formation is calcilutites with Eq. (1.10) [43,130].

$$\Delta\sigma_{ir} = M\left(\sqrt{\tau_{df}^2 + \tau_c^2 + \tau_{sc}^2} - \sqrt{\tau_{df}^2 + \tau_c^2}\right) \tag{1.10}$$

where τ_{df} is the contribution of the dislocation forest and τ_c is the contribution of carbides to the CRSS. Both τ_{df} and τ_c components will not be affected by the irradiation.

There is no “perfect" model to predict irradiation hardening. All the described above models have advantages and limitations. The DBH model works well with high strength obstacles [13,126]. The FKH model is suitable for weaker obstacles, such as solute clusters, with obstacle strength of

around the quarter (α_{obs} ~ 0.25) of impenetrable Orowan obstacle (α_{obs} = 1) [13,126]. The RB model was developed to treat the effect of Cu-precipitates, where due to a difference between the precipitate and Fe matrix shear modulus the energy of dislocation passing through a softer Cu-precipitate will be decreased, yet it is complicated to precisely evaluate the modulus for solute clusters. The BKS model is the more advanced one since it considers both self-interactions between dislocations, and the effect of different free spacing between obstacles on CRSS.

These four models will be used to calculate the irradiation hardening caused by solute clusters in CT RPV steels. The predicted results will be compared with the experimental values measured with tensile tests. By fitting the predicted values with the measured ones, the obstacle strength of solute clusters will be estimated. Also, by comparing different models, the more reliable one accounting for irradiation hardening caused by solute clusters in chemically-tailored RPV steels will be selected. Although, it should be noted that to simplify the calculations numerous parameters (initial microstructure, carbides spatial distribution, absence of PDCs not observed by APT…) are assumed to be the same in every steel, which are not the case in reality.

Summary

Neutron irradiation hardening and embrittlement of reactor pressure vessel steel is one of the critical safety issues of NPPs. With a goal to prolongate the operation time of the current PWR fleet, a correct embrittlement prediction is crucial. During the operation of NPP, neutrons produced by nuclear fission in the reactor core can interact with the RPV steel, resulting in formation of self-interstitial atoms and vacancies which will enhance diffusion and lead to the formation of irradiation enhanced precipitates. Also, continuous flux of these point defects drags solute atoms with them, resulting in the formation of irradiation induced solute clusters. These precipitates and clusters act as barriers for dislocation movement, resulting in the hardening and the embrittlement of material. Impurities such as Cu, P and alloying elements like Mn, Ni and Si are often associated to the clusters and/or precipitates formed under irradiation. The magnitude of irradiation hardening depends on bulk composition of these elements and on the synergies between them.

The main objectives of the current PhD research are the understanding of the influence of the bulk chemical composition (focusing on Cu, P, Mn and Ni) on the microstructural evolution and consequently its impact on the hardening and embrittlement of RPV steels. To do so, seven chemically-tailored RPV steels, divided into four groups were selected. The first group aims to study the effect of P content and its synergy with Cu, the second to evaluate the effect of Mn, the third to account for the effect of Ni and Mn/Ni synergy, and finally the fourth one to measure the effect of high concentration of Cu, P, Mn, Ni combined. These materials were irradiated at 290 °C inside the Belgian Reactor 2 (BR2) MTR at high flux conditions (from 1 to 2.5 x 10^{17} n/m^{2}s, E > 1 MeV). The additional focus will be on the synergy between solute cluster properties and the irradiation dose. To investigate the evolution of microstructure with the neutron exposure RPV steels were irradiated up to three doses of around 0.06, 0.08 and 0.13 dpa, which represent exposure typical for around 25, 30 and 50 years of operation in commercial NPPs. Besides, it is important to get additional information about the dominant mechanisms and the kinetics of cluster formation. The main parameters which will be tackled in this PhD project are summarised in Table 3 below.

Table 3. *Main properties influencing the effect of neutron irradiation.*

Effect of	Will it be studied?
Temperature	No
Flux	No
Fluence	Yes
Bulk chemical composition	Yes
Synergy between elements	Yes
Mechanism of cluster formation (RED or RIS)	Yes
Irradiation hardening	Yes

In the present research, the temperature effect won't be studied since the temperature of irradiation is the same for all studied steels and is equal to 290 °C, which is in the range of operating temperatures for the PWR. Also, the irradiation flux was of the same order of magnitude for all RPV steels used in the current project, so flux effect is out of scope.

From the literature review, we can already predict what should be the irradiation induced features that should be observed in the present research. A summary on the typical features is presented in Table 4.

Table 4. *Microstructure features formed under neutron irradiation.*

Type of features	Number density [m^{-3}]	Size [nm]	Influence on mechanical properties	Bulk CC effect	Will it be studied?
Cu-Mn-Ni-Si-P (solute) clusters	10^{22}-10^{24}	1-3	Hardening	Yes	Yes
Cu-enriched features	10^{23}-10^{24}	2-3	Hardening	Yes	Yes
Mn-Ni-Si-enriched features	10^{23}-10^{24}	2-4	Hardening	Yes	Yes
Matrix damage	10^{20}-10^{22}	< 1	Hardening	No	No
Segregation on dislocation lines	-	-	Hardening	Yes	Yes
Segregation on grain boundaries	-	-	Embrittlement	Yes	No

The formation mechanism of Mn-Ni-Si enriched features proposed by Odette and co-workers is still not well-defined, therefore, it is hard to predict the formation of these features, especially at low and medium doses of around 0.1 dpa studied in the current project. The matrix damage is usually observed at the much higher irradiation doses of several dpa and won't be studied in the current project. The segregation on the GBs is observed in the RPV steels irradiated to relatively low doses but it will not be studied in the current project.

The irradiation hardening due to solute cluster formation will the calculated with DBH, FKH, RB and BKS models. Predicted values will be compared with the experimental tensile tests results.

In the upcoming chapter II definitive information about composition, thermo-mechanical treatment, irradiation conditions and irradiation hardening, measured using tensile specimens tested

at room temperature inside hot cells at Belgian Nuclear Research Centre (SCK CEN), of chemically-tailored RPV steels selected to study the effect of bulk chemical composition on microstructure evolution and irradiation hardening is delivered. To observe microstructural features such as solute clusters and precipitates formed under neutron irradiation APT experiments on the CAMECA LEAP 4000X HR with electrical pulses are performed. Comprehensive description of APT technique, its limitations and sample preparation procedure is given in the following chapter.

References

1. OECD and NEA. Report 'Legal Frameworks for Long-Term Operation of Nuclear Power Reactors '(2019). https://doi.org/10.1787/c7b6dbb2-en

2. V. Ghetta, D. Gorse, D. Mazière, V. Pontikis (Eds.). Materials Issues for Generation IV Systems. Springer Netherlands (2008). https:// 10.1007/978-1-4020-8422-5

3. J. Treiner. Reflets de la Physique 50 (2016): 35-35. https://doi.org/10.1051/refdp/201650030

4. OECD and NEA. Report 'The Economics of Long-Term Operation of Nuclear Power Plants' (2012). https://doi.org/10.1787/9789264992054-en

5. S. Zinkle, G.S. Was. Acta Materialia 61 (2013): 735–58. https://doi.org/10.1016/j.actamat.2012.11.004

6. S. Chu, A. Majumdar. Nature 488 (2012): 294–303. https://doi.org/10.1038/nature11475

7. B. Brook, A. Alonso, D. Meneley, J. Misak, T. Blees, J. van Erp. Sustainable Materials and Technologies 1–2 (2014): 8–16. https://doi.org/10.1016/j.susmat.2014.11.001

8. N. Soneda (Ed.). Irradiation Embrittlement of Reactor Pressure Vessels (RPVs) in Nuclear Power Plants. Elsevier (2015). https://doi.org/10.1016/C2013-0-17428-4

9. A Technology Roadmap for Generation IV Nuclear Energy Systems. Issued by the U.S.DOE Nuclear Energy Research Advisory Committee and the Generation IV International Forum, (2002). http://www.gen-4.org/Technology/roadmap.htm

10. C. Ching-Hsin, H. Chou, C. Huang. International Journal of Pressure Vessels and Piping 167 (2018): 43–51. https://doi.org/10.1016/j.ijpvp.2018.10.007.

11. A. Bentaib, H. Bonneville, G. Cénérino. Nuclear Power Reactor Core Melt Accidents: Current State of Knowledge. EDP Sciences (2015). https://doi.org/10.1051/978-2-7598-1930-0

12. C. Erginsoy, G. Vineyard, A. Englert. Physical Review 133 (1964) A595. https://doi.org/10.1103/PhysRev.133.A595

13. G.S. Was. Fundamentals of Radiation Materials Science: Metals and Alloys. Springer, New York (2007). https://doi.org/10.1007/978-3-540-49472-0

14. K. Nordlund, F. Djurabekova. (2014). Journal of Computational Electronics 13 (2014): 122–141. https://doi:10.1007/s10825-013-0542-z

15. J.-M. Zhang, B. Wang, K.-W. Xu, V. Ji. Radiation Effects & Defects in Solids 164 (2009): 508–516. https://doi.org/10.1080/10420150802682595

16. S. Kim, W. Buyers. Journal of Physics F: Metal Physics 8 (1978): L103–8. https://doi.org/10.1088/0305-4608/8/5/001

17. G.R. Odette, T. Yamamoto, T.J. Williams, R.K. Nanstad, C.A. English. Journal of Nuclear Materials 526 (2019): 151863. ttps://doi.org/10.1016/j.jnucmat.2019.151863

18. M. Nastar, F. Soisson. Rudy J.M. (Ed). 'Radiation-Induced Segregation' In Comprehensive Nuclear Materials. Elsevier (2012): 471-496. https://doi.org/10.1016/B978-0-08-056033-5.00035-5.

19. A. Ardell, P. Bellon. Current Opinion in Solid State and Materials Science 20 (2016): 115-39. https://doi.org/10.1016/j.cossms.2015.11.001

20. R. Sizmann, (1978). Journal of Nuclear Materials 69-70 (1978): 386–412. https://doi:10.1016/0022-3115(78)90256-8

21.L. Huang, M. Nastar, T. Schuler, L. Messina. Physical Review Materials 5 (2021): 033605. 10.1103/PhysRevMaterials.5.033605

22. L. Messina, P. Olsson, M. Nastar, W. Gudowski. Proceedings of ICAPP 2015, Paper 15572. https://www.researchgate.net/publication/301232158

23. L. Messina, Luca, M. Nastar, T. Garnier, C. Domain, Pär Olsson. Physical Review B 90, (2014): 104203. https://doi.org/10.1103/PhysRevB.90.104203

24. L. Messina, Z. Chang, P. Olsson. Nuclear Instruments and Methods in Physics Research Section B: Beam Interactions with Materials and Atoms 303 (2013): 28–32. https://doi.org/10.1016/j.nimb.2013.01.049

25. L. Messina, M. Chiapetto, P. Olsson, C. Becquart, L. Malerba. Physica Status Solidi A 213, (2016): 2974–80. https://doi.org/10.1002/pssa.201600038

26. M. Chiapetto, L. Malerba, C.S. Becquart. Journal of Nuclear Materials 462 (2015): 91-99. https://doi.org/10.1016/j.jnucmat.2015.03.045

27. L. Messina, T. Schuler, M. Nastar, M. Marinica, P. Olsson. Acta Materialia 191 (2020): 166–185. https://doi.org/10.1016/j.actamat.2020.03.038

28. M. Chiapetto, C. S. Becquart, C. Domain, L. Malerba. Nuclear Instruments and Methods in Physics Research B 352 (2015): 56–60. https://doi.org/10.1016/j.nimb.2014.11.102

29. M. Nastar. Philosophical Magazine 85 (2005): 3767–94. https://doi.org/10.1080/14786430500228390

30. N. Castin, G. Bonny, A. Bakaev, F. Bergner, C. Domain, J.M. Hyde, L. Messina, B. Radiguet, L. Malerba. Materials Today Energy 17 (2020): 100472. https://doi.org/10.1016/j.mtener.2020.100472

31. Castin, N., G. Bonny, A. Bakaev, F. Bergner, C. Domain, J.M. Hyde, L. Messina, B. Radiguet, L. Malerba. SSRN Electronic Journal (2019). https://doi.org/10.2139/ssrn.3427540

32. R. Chaouadi, R. Gérard. Journal of Nuclear Materials 418 (2011): 137–42. https://doi.org/10.1016/j.jnucmat.2011.06.012

33. G.R. Odette, B. Wirth. Journal of Nuclear Materials 251 (1997): 157–71. https://doi.org/10.1016/S0022-3115(97)00267-5

34. G.R. Odette, G.E. Lucas, D. Klingensmith. MRS Proceedings 650 (2000): R6.4. https://doi.org/10.1557/PROC-650-R6.4

35. P. Wells. PhD Thesis 'The Character, Stability and Consequences of Mn-Ni-Si Precipitates in Irradiated Reactor Pressure Vessel Steels', (2016): 221. https://escholarship.org/uc/item/3vh4k9tf

36. A. Wagner, F. Bergner, R. Chaouadi, H. Hein, M. Hernández-Mayoral, M. Serrano, A. Ulbricht, E. Altstadt. Acta Materialia 104 (2016): 131–42. https://doi.org/10.1016/j.actamat.2015.11.027

37. R. Chaouadi, R. Gérard, E. Stergar, W. Van Renterghem. Journal of Nuclear Materials 519 (2019): 188–204. https://doi.org/10.1016/j.jnucmat.2019.03.030

38. C.A. English, J.M. Hyde. 'Radiation Damage of Reactor Pressure Vessel Steels' In Comprehensive Nuclear Materials. Elsevier (2012): 151–80. https://doi.org/10.1016/B978-0-08-056033-5.00087-2

39. E. Altstadt (Ed.). Report 'Treatment of long term irradiation embrittlement effects in RPV safety assessment' D1.9 (2014). https://cordis.europa.eu/docs/results/249/249360/final1-longlife-final-report.pdf

40. B. Radiguet, F. Vurpillot, G. Da Costa, C. Pareige, A. Etienne. P.D. Styman, H. Weekes, J.M. Hyde. Report 'APT Characterisation of Radiation Damage in RPV Steels: Experimental and Data Processing Uncertainties' D6.39 (2016): 88.

41. H. Watanabe, S. Arase, T. Yamamoto, P. Wells, T. Onishi, G.R. Odette. Journal of Nuclear Materials 471 (2016): 243-250. https://doi.org/10.1016/j.jnucmat.2015.12.045

42. B. Gurovich, E. Kuleshova, Ya. Shtrombakh. S. Fedotova. D. Erak. D. Zhurko. Journal of Nuclear Materials 456 (2015): 373-381. https://doi.org/10.1016/j.jnucmat.2014.09.080

43. G. Monnet. Journal of Nuclear Materials 508 (2018): 609–27. https://doi.org/10.1016/j.jnucmat.2018.06.020

44. B. Gurovich, E. Kuleshova, Y. Shtormbakh, D. Erak, A. Chernobaeva, O. Zabusov. Journal of Nuclear Materials 389 (2009): 490-496. https://doi.org/10.1016/j.jnucmat.2009.02.002

45. F. Bergner, F. Gillemot, M. Hernández-Mayoral, M. Serrano, G. Török, A. Ulbricht, E. Altstadt. Journal of Nuclear Materials 461 (2015): 37–44. https://doi.org/10.1016/j.jnucmat.2015.02.031

46. A. Wagner. Dissertation 'Long-term irradiation effects on reactor-pressure vessel steels', (2015): 131. https://www.hzdr.de/FWR/DOCS/Publications/Dissertation_Arne_Wagner.pdf

47. J.M. Hyde, M.G. Burke, R. Boothby, C.A. English. Ultramicroscopy 109 (2009): 510–17. https://doi.org/10.1016/j.ultramic.2008.10.018

48. M.K. Miller, K. Powers, R.K. Nanstad, P. Efsing. Journal of Nuclear Materials 437 (2013): 107–15. https://doi.org/10.1016/j.jnucmat.2013.01.312

49. P. Pareige, B. Radiguet, A. Suvorov, M. Kozodaev, E. Krasikov, O. Zabusov, J. Massoud. Surface and Interface Analysis 36 (2004): 581–84. https://doi.org/10.1002/sia.1705.

50. M.K. Miller, K.F. Russell, M.A. Sokolov, R.K. Nanstad. Journal of Nuclear Materials 320 (2003): 177–83. https://doi.org/10.1016/S0022-3115(03)00108-944

51. J.R. Hawthorne. Nuclear Engineering and Design 89 (1985): 223-232. https://inis.iaea.org/search/search.aspx?orig_q=RN:17039044

52. P. Auger, P. Pareige, S. Welzel, J-C. Van Duysen. Journal of Nuclear Materials 280 (2000): 331–44. https://doi.org/10.1016/S0022-3115(00)00056-8

53. P.D. Edmondson, C.P. Massey, M.A. Sokolov, T.M. Rosseel. Journal of Nuclear Materials 545 (2021): 152740. https://doi.org/10.1016/j.jnucmat.2020.152740

54. R. Monzen, M.L. Jenkins, A.P. Sutton. Philosophical Magazine A 80 (2000): 711-723. https://doi.org/10.1080/01418610008212077

55. P.D. Styman, J.M. Hyde, K. Wilford, D. Parfitt, N. Riddle, G.D.W. Smith. Ultramicroscopy 159 (2015): 292–298. https://doi.org/10.1016/j.ultramic.2015.05.013

56. G. Fourlaris, A.J. Baker, G.D. Papadimitriou. Acta Metallurgica et Materialia 43 (1995): 2589-2604. https://doi.org/10.1016/0956-7151(94)00474-V

57. P.D. Styman, J.M. Hyde, K. Wilford, A. Morley, G.D.W. Smith. Progress in Nuclear Energy 57 (2012): 86–92. https://doi.org/10.1016/j.pnucene.2011.10.010

58. P.D. Styman, J.M. Hyde, A. Morley, K. Wilford, N. Riddle, G. D.W. Smith. Materials Science and Engineering: A 736 (2018): 111–119. https://doi.org/10.1016/j.msea.2018.08.063

59. S. Shu, B. Wirth, P. Wells, D. Morgan, G.R. Odette. Acta Materialia 146 (2018): 237–52. https://doi.org/10.1016/j.actamat.2017.12.006

60. G.R. Odette, T. Yamamoto, D. Klingensmith. Philosophical Magazine 85 (2005): 779–97. https://doi.org/10.1080/14786430412331319910

61. G.R. Odette, G.E. Lucas. JOM 53 (2001): 18–22. https://doi.org/10.1007/s11837-001-0081-0

62. G.R. Odette, MRS Proceedings 373 (1994): 137. https://doi.org/10.1557/PROC-373-137

63. M.K. Miller, M.A. Sokolov, R.K. Nanstad, K.F. Russell. Journal of Nuclear Materials 351 (2006): 187–96. https://doi.org/10.1016/j.jnucmat.2006.02.013

64. M.K. Miller, K.F. Russell. Journal of Nuclear Materials 371 (2007): 145–60. https://doi.org/10.1016/j.jnucmat.2007.05.003

65. M.K. Miller, K.F. Russell, M.A. Sokolov, R.K. Nanstad. Journal of Nuclear Materials 361 (2007): 248–61. https://doi.org/10.1016/j.jnucmat.2006.12.015

66. M.K. Miller. Journal of Materials Science 41 (2006): 7808–13. https://doi.org/10.1007/s10853-006-0518-5

67. P.D. Edmondson, M.K. Miller, K.A. Powers, R.K. Nanstad. Journal of Nuclear Materials 470 (2016): 147–54. https://doi.org/10.1016/j.jnucmat.2015.12.038

68. A. Wagner, A. Ulbricht, F. Bergner, E. Altstadt. Nuclear Instruments and Methods in Physics Research Section B: Beam Interactions with Materials and Atoms 280 (2012): 98–102. https://doi.org/10.1016/j.nimb.2012.03.008

69. G.R. Odette, Radiation Effects and Defects in Solids 144 (1998): 189–231. https://doi.org/10.1080/10420159808229676

70. R.G. Carter, N. Soneda, K. Dohi, J.M. Hyde, C.A. English, W.L. Server. Journal of Nuclear Materials 298 (2001): 211–24. https://doi.org/10.1016/S0022-3115(01)00659-6

71. P. Auger, P. Pareige, M. Akamatsu, D. Blavette. Journal of Nuclear Materials 225 (1995): 225–30. https://doi.org/10.1016/0022-3115(94)00522-2

72. L. Liu, K. Nishida, K. Dohi, A. Nomoto, N. Soneda, K. Murakami, Z. Li, D. Chen, N. Sekimura. Journal of Nuclear Science and Technology 53 (2016): 1546–53. https://doi.org/10.1080/00223131.2015.1136902

73. B. Radiguet, PhD Thesis 'Etude de la formation d'amas diffus de solutés sous irradiation dans des alliages modèles ferritiques', (2004): 224. https://tel.archives-ouvertes.fr/tel-00510750

74. E. Meslin, B. Radiguet, P. Pareige, A. Barbu. Journal of Nuclear Materials 399 (2010): 137–45. https://doi.org/10.1016/j.jnucmat.2009.11.012

75. P. Pareige, K.F. Russell, M.K. Miller. Applied Surface Science 94–95 (1996): 362–69. https://doi.org/10.1016/0169-4332(95)00398-3

76. K. Fukuya, K. Ohno, H. Nakata, S. Dumbill, J.M. Hyde. Journal of Nuclear Materials 312 (2003): 163–73. https://doi.org/10.1016/S0022-3115(02)01675-6

77. B. Radiguet, P. Pareige, A. Barbu. Nuclear Instruments and Methods in Physics Research Section B: Beam Interactions with Materials and Atoms 267 (2009): 1496–99. https://doi.org/10.1016/j.nimb.2009.01.146

78. B. Radiguet, A. Barbu, P. Pareige. Journal of Nuclear Materials 360 (2007): 104–17. https://doi.org/10.1016/j.jnucmat.2006.09.007

79. P. Pareige, B. Radiguet, A. Barbu. Journal of Nuclear Materials 352 (2006): 75–79. https://doi.org/10.1016/j.jnucmat.2006.02.073

80. A. Krvukov, L. Debarberis, U. von Estorff. Int. J. Nuclear Knowledge Management 4 (2010). https://publications.jrc.ec.europa.eu/repository/handle/JRC58870

81. E. Meslin, B. Radiguet, M. Loyer-Prost. Acta Materialia 61 (2013): 6246–54. https://doi.org/10.1016/j.actamat.2013.07.008.

82. M.K. Miller, A. Chernobaeva, Ya. Shtrombakh, K.F. Russell, R.K. Nanstad, D. Erak, O. Zabusov. Journal of Nuclear Materials 385 (2009): 615–22. https://doi.org/10.1016/j.jnucmat.2009.01.299

83. T. Takeuchi, A. Kuramoto, J. Kameda, T. Toyama, Y. Nagai, M. Hasegawa, T. Ohkubo, T. Yoshiie, Y. Nishiyama, and K. Onizawa. Journal of Nuclear Materials 402 (2010): 93–101. https://doi.org/10.1016/j.jnucmat.2010.04.008

84. E. Meslin, M. Lambrecht, M. Hernández-Mayoral, F. Bergner, L. Malerba, P. Pareige, B. Radiguet, et al. Journal of Nuclear Materials 406 (2010): 73–83. https://doi.org/10.1016/j.jnucmat.2009.12.021

85. E. Meslin, B. Radiguet, P. Pareige, C. Toffolon, and A. Barbu. Experimental Mechanics 51 (2011): 1453–58. https://doi.org/10.1007/s11340-011-9476-1

86. H. Huang, B. Radiguet, P. Todeschini, G. Chas, P. Pareige. MRS Proceedings 1264 (2010): 1264-BB05-18. https://doi.org/10.1557/PROC-1264-BB05-18

87. M.J. Konstantinović, I. Uytdenhouwen, G. Bonny, N. Castin, L. Malerba, P. Efsing. Acta Materialia 179 (2019): 183–89. https://doi.org/10.1016/j.actamat.2019.08.028

88. K. Dohi. ASME Pressure Vessels and Piping Conference (2010): 95–102. https://doi.org/10.1115/PVP2010-25514

89. K. Lindgren, M. Boåsen, K. Stiller, P. Efsing, M. Thuvander. Journal of Nuclear Materials 488 (2017): 222–30. https://doi.org/10.1016/j.jnucmat.2017.03.019

90. K. Dohi, K. Nishida, A. Nomoto, N. Soneda, H. Matsuzawa, M. Tomimatsu. ASME Pressure Vessels and Piping Conference (2009): 403–9. https://doi.org/10.1115/PVP2009-77658

91. K. Fukuya, Journal of Nuclear Science and Technology 50 (2013): 213–54. https://doi.org/10.1080/00223131.2013.772448

92. J. May, H. Hein, E. Altstadt, F. Bergner, H. W. Viehrig, A. Ulbricht, R. Chaouadi, B. Radiguet, S. Cammelli, H. Huang, K. Wilford. Report IAEA-CN-194-041. https://inis.iaea.org/collection/NCLCollectionStore/_Public/43/070/43070846.pdf?r=1&r=1

93. M. Hernandez-Mayoral, D. Gomez-Briceno. Journal of Nuclear Materials 399 (2010): 146-153. https://doi:10.1016/j.jnucmat.2009.11.013.

94. P.D. Edmondson, C.M. Parish, R.K. Nanstad. Acta Materialia 134 (2017): 31–39. https://doi.org/10.1016/j.actamat.2017.05.043

95. M.G. Burke, M. Watanabe, D.B. Williams, J.M. Hyde. Journal of Materials Science 41 (2006): 4512–4522. https://doi.org/10.1007/s10853-006-0084-x

96. H. Ke, P. Wells, P. D. Edmondson, N. Almirall, L. Barnard, G.R. Odette, D. Morgan. Acta Materialia 138 (2017): 10–26. https://doi.org/10.1016/j.actamat.2017.07.021

97. J. Ke, H. Ke, G.R. Odette, D. Morgan. Journal of Nuclear Materials 498 (2018): 83–88. https://doi.org/10.1016/j.jnucmat.2017.10.008

98. W. Xiong, H. Ke, R. Krishnamurthy, P. Wells, L. Barnard, G.R. Odette, D. Morgan. MRS Communications 4 (2014): 101–5. https://doi.org/10.1557/mrc.2014.21

99. P. Wells, T. Yamamoto, B. Miller, T. Milot, J. Cole, Y. Wu, G.R. Odette. Acta Materialia 80 (2014): 205–19. https://doi.org/10.1016/j.actamat.2014.07.040

100. N. Almirall, P. Wells, T. Yamamoto, K. Wilford, T. Williams, N. Riddle, G.R. Odette. Acta Materialia 179 (2019): 119–28. https://doi.org/10.1016/j.actamat.2019.08.027

101. N. Almirall, P. Wells, H. Ke, P.D. Edmondson, D. Morgan, T. Yamamoto, G.R. Odette. Scientific Reports 9 (2019): 9587. https://doi.org/10.1038/s41598-019-45944-z

102. N. Almirall, P. Wells, S. Pal, P.D. Edmondson, T. Yamamoto, K. Murakami, G.R. Odette. Scripta Materialia 181 (2020): 134–39. https://doi.org/10.1016/j.scriptamat.2020.02.027

103. N. Almirall, P. Wells, T. Yamamoto, K. Yabuuchi, A. Kimura, and G.R. Odette. Journal of Nuclear Materials 536 (2020): 152173. https://doi.org/10.1016/j.jnucmat.2020.152173

104. B. Jenkins, J. Douglas, N. Almirall, N. Riddle, P. Bagot, J.M. Hyde, G.R. Odette, M. Moody. Materialia 11 (2020): 100717. https://doi.org/10.1016/j.mtla.2020.100717

105. D.J. Sprouster, J. Sinsheimer, E. Dooryhee, S.K. Ghose, P. Wells, T. Stan, N. Almirall, G.R. Odette, L.E. Ecker. Scripta Materialia 113 (2016): 18–22. https://doi.org/10.1016/j.scriptamat.2015.10.019

106. M. Mamivand, P. Wells, H. Ke, S. Shu, G.R. Odette, D. Morgan. Acta Materialia 180 (2019): 199–217. https://doi.org/10.1016/j.actamat.2019.09.016

107. G.R. Odette, N. Almirall, P. Wells, T. Yamamoto. Acta Materialia 212 (2021): 116922. https://doi.org/10.1016/j.actamat.2021.116922

108. B. Jenkins, P.D. Styman, N. Riddle, P. Bagot, M. Moody, G.D.W. Smith, J.M. Hyde. Scripta Materialia 191 (2021): 126–30. https://doi.org/10.1016/j.scriptamat.2020.09.029

109. X. Yan, A. Grytsiv, P. Rogl, V. Pomjakushin, X. Xue. Journal of Alloys and Compounds 469 (2009): 152-155. https://doi.org/10.1016/j.jallcom.2008.01.142

110. K.P. Gupta. Journal of Phase Equilibria and Diffusion 27 (2006): 529–534. https://link.springer.com/content/pdf/10.1007/BF02736466.pdf?pdf=button

111. Y. Matsukawa, T. Takeuchi, Y. Kakubo, T. Suzudo, H. Watanabe, H. Abe, T. Toyame, Y. Nagai. Acta Materialia 116 (2016): 104-113. https://doi.org/10.1016/j.actamat.2016.06.013

112. D.J.M. King, P.A. Burr, S.C. Middleburgh, T.M. Whiting, M.G. Burke, M.R. Wenman. Journal of Nuclear Materials 505 (2018): 1-6. https://doi.org/10.1016/j.jnucmat.2018.03.050

113. T.M. Whiting, D.M.J. King, M.R. Wenman. Journal of Nuclear Materials 542 (2020): 152429. https://doi.org/10.1016/j.jnucmat.2020.152429

114. Y. Nishiyama. Onizawa K, Suzuki M, Anderegg JW, Nagai Y, Toyama T, Hasegawa M, Kameda J. Acta Materialia 56 (2208) 4510-4521. https://doi:10.1016/j.actamat.2008.05.026

115. S. Fedotova, E. Kuleshova, D. Maltsev, M. Saltykov. Journal of Nuclear Materials 528 (2020): 151865. https://doi.org/10.1016/j.jnucmat.2019.151865

116. L. Zhang, B. Radiguet, P. Todeschini, C. Domain, Y. Shen, P. Pareige. Journal of Nuclear Materials 542 (2020): 152531. https://doi.org/10.1016/j.jnucmat.2020.152531

117. T. Toyama, Y. Nagai, A. Al Mazouzi, M. Hatakeyama, M. Hasegawa, T. Ohkubo, E. Van Walle, R. Gerard. Materials Transactions 54 (2013): 2119–24. https://doi.org/10.2320/matertrans.M2013133

118. B. Gurovich, E. Kuleshova, Ya. Shtrombakh, O. Zabusov, E. Krasikov. Journal of Nuclear Materials 279 (2000): 259–72. https://doi.org/10.1016/S0022-3115(00)00007-6

119. E.D. Eason, G.R. Odette, R.K. Nanstad, T. Yamamoto (Eds). A Physically Based Correlation of Irradiation-Induced Transition Temperature Shifts for RPV Steels. Report ORNL/TM-2006/530 (2007): 250. https://info.ornl.gov/sites/publications/files/Pub2592.pdf

120. M.K. Miller, R. Jayaram, K.F. Russell. Journal of Nuclear Materials 225 (1995): 215-224. https://doi.org/10.1016/0022-3115(94)00667-9

121. M.K. Miller, K.F. Russell. Applied Surface Science 94/95 (1996): 378-383. https://doi.org/10.1016/0169-4332(95)00400-9

122. R.E. Stoller, S.J. Zinkle. Journal of Nuclear Materials 283–287 (2000): 349–52. https://doi.org/10.1016/S0022-3115(00)00378-0

123. R.K. Nanstad, M.A. Sokolov, D.E. McCabe. Journal of ASTM International 5 (2008). https://doi.org/10.1520/JAI101346

124. G. Monnet, L. Vincent, L. Gélébart. Journal of Nuclear Materials 514 (2019): 128–38. https://doi.org/10.1016/j.jnucmat.2018.11.028

125. F. Kroupa, P. B. Hirsch. Discussions of the Faraday Society 38 (1964): 49. https://doi.org/10.1039/df9643800049

126. S.J. Zinkle, Y. Matsukawa. Journal of Nuclear Materials 329–333 (2004): 88–96. https://doi.org/10.1016/j.jnucmat.2004.04.298

127. K.C. Russell, L.M. Brown. Acta Metallurgica 20 (1972): 969-974. https://doi.org/10.1016/0001-6160(72)90091-0

128. D.J. Bacon, U.F. Kocks, R.O. Scattergood. Philosophical Magazine, 28 (1973): 1241–1263. https://doi.org/10.1080/14786437308227997

129. G. Gosh, G. Olson. Acta Materialia 50 (2002): 2655-2675. https://doi.org/10.1016/S1359-6454(02)00096-4

130. C. Sobie, N. Bertin, L. Capolungo. Metallurgical and Materials Transactions A 46 (2015): 3761–72. https://doi.org/10.1007/s11661-015-2935-z

Chapter II: Materials and techniques

1 Materials

As it was described in the 1st chapter the chemical composition has a strong effect on the microstructure evolution, hardening and embrittlement of RPV steels under irradiation. The goal of this PhD project is, therefore, to focus on the correlation between microstructural changes, irradiation hardening and the material bulk composition. To study the effect of the bulk chemical composition, a set of materials with different solute contents should be used. The materials for the present research are samples from the RADAMO-13 program. The RADAMO test program had started in early 2000 within the SCK CEN. The main goal was to predict irradiation hardening and embrittlement of the different types of commercial and model RPV steels [1].

1.1 Bulk chemical composition

Most commercial RPV materials are produced within a narrow range of chemical compositions. The heat treatment procedures, and therefore, the final microstructure can also slightly vary between different countries. The precise study on the effect of the chemical composition of specific elements and their synergy is not possible only looking at commercial grades. To solve that issue, the RADAMO-13 program was initialised. As part of the RADAMO-13 program, 23 chemically-tailored (CT) steels were fabricated following the commercial RPV steel fabrication procedure. Their reference compositions are close to the ASTM A533B Cl.1 standard [2]. All 23 CT RPV steels have the same C, Si, S and Mo contents. Among elements known to have a detrimental effect on the evolution of the mechanical properties of RPV steels are Cu, P, Ni and Mn. Therefore, their concentrations were systematically varied to study their individual and synergistic effects on the microstructure and mechanical properties evolution of the CT RPV steels under neutron irradiation [1].

From 23 available materials irradiated as part of RADAMO-13 program, seven chemically-tailored RPV steels were selected [1]. The tensile tests on the non-irradiated materials were performed. The yield strength (YS or σ_y) and ultimate tensile strength (UTS or σ_{uts}) are presented alongside the chemical composition of CT RPV steels in Table 1.

Table 1. *Chemical composition in weight and atomic (highlighted by grey colour) percent, Fe in balance. The initial tensile properties of the chemically-tailored RPV steels selected for this PhD are also shown [2].*

ID	C	S	Mo	Al	Cu	P	Ni	Mn	Si	σ_y [MPa]	σ_{uts} [MPa]
D	0.20	0.005	0.51	0.02	0.05	0.009	0.74	0.04	0.24	417	542
	0.94	0.009	0.30	0.05	0.045	0.017	0.71	0.04	0.48		
E	0.21	0.005	0.48	0.02	0.05	0.013	0.67	0.80	0.26	483	604
	0.99	0.009	0.29	0.04	0.045	0.024	0.65	0.83	0.53		
F	0.20	0.007	0.51	0.03	0.04	0.011	0.69	1.73	0.24	535	647
	0.94	0.013	0.30	0.06	0.036	0.020	0.67	1.77	0.49		
I	0.21	0.008	0.51	0.02	0.04	0.010	1.68	1.78	0.26	492	792
	1.01	0.015	0.31	0.04	0.037	0.019	1.65	1.86	0.54		
N	0.20	0.008	0.50	0.03	0.05	0.020	0.69	1.46	0.25	548	653
	0.95	0.014	0.30	0.05	0.045	0.037	0.67	1.51	0.51		
O	0.21	0.006	0.51	0.02	0.05	0.029	0.68	1.45	0.27	544	656
	0.99	0.011	0.31	0.04	0.045	0.054	0.66	1.50	0.55		
W	0.20	0.008	0.52	0.03	0.30	0.028	1.64	1.78	0.25	514	801
	0.97	0.015	0.32	0.07	0.276	0.053	1.61	1.86	0.52		

The chemical compositions were measured by the steel manufacturer with optical emission spectroscopy (OES) at four different positions to evaluate the homogeneity. The reported results were presented in weight percentage (wt. %) and were converted into atomic (at. %) to allow direct comparison with the APT data. The tensile tests on non-irradiated samples were performed at room temperature on the set of 12 specimens for each of seven selected CT RPV steels at SCK CEN [1]. The results of the tensile test show the homogeneity of mechanical properties of the plates of chemically-tailored RPV steels. The average uncertainty of the tensile tests was estimated to be about 25 MPa [1-3].

The selected materials are divided into four categories to study the synergetic effects between different elements. The first group of materials is presented by steels D, E and F. They are low-Cu, low-P, medium-Ni steels. Only the Mn content varies, starting from low-Mn steel D (0.04 at. % Mn), to medium-Mn steel E (0.83 at. % Mn) and finally to high-Mn steel F (1.77 at. % Mn).

The second group allows to investigate the Mn/Ni synergy. It consists of the two low-Cu, low-P, high-Mn steels F and I which have a difference only in Ni content. F is the medium-Ni steel (0.67 at. % Ni), and I is the high-Ni (1.63 at. % Ni) steel.

Three steels were selected to study the effect of the P content in the low-Cu, medium-Ni, and moderate-Mn material. Steel F has a low P content (0.02 at. %), steel N has a medium P content

(0.037 at. %) and steel O has a high one (0.054 at. %). It has to be noticed that steel F contains a little bit less Cu and a little bit more Mn than the two others.

Finally, steel W is a high-Cu, high-P, high-Ni, and high-Mn material. It was selected to investigate the cluster formation kinetics. The big difference of steel W from the other materials is the significantly higher Cu content (0.28 at. %).

1.2 Thermal treatments of steels

To obtain the bainitic microstructure, typical for commercial RPV materials, the chemically-tailored RPV steels were fabricated following the ASTM standard of A533B RPV steel [2]. Each steel ingot, with a size of 125 x 125 x 90 mm^3, was hot rolled to get a plate of 25 mm thick. To obtain the bainitic microstructure typical of commercial RPV steels, the following heat treatment was applied (Fig. 1) [2]:

- Austenisation at 900 °C for four hours with water quenching;
- Tempering at 665 °C for four hours with air cooling;
- Stress relief annealing at 640 °C for eight hours with furnace cooling;
- Air cooling below 400 °C.

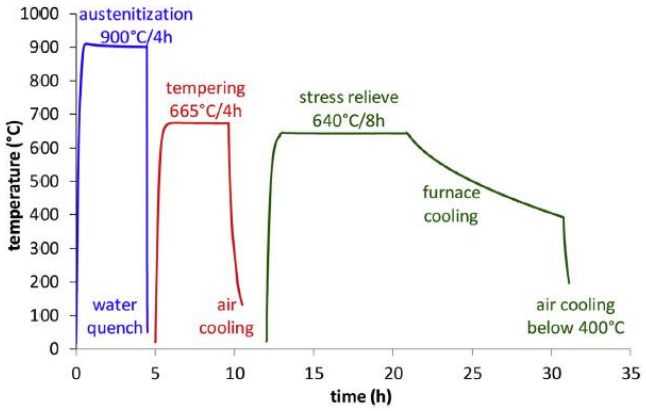

Figure 1. *Heat treatments applied to chemically-tailored RPV steels to obtain the bainitic microstructure [2].*

Depending on the cooling rate, tempering temperature and chemical composition, several types of bainitic microstructure can be formed (Fig. 2) [4-7]. Bainite is a complicated microstructure and should be identified with care. The final structure could be composed of polygonal (Fig. 2.a) or lath (Fig. 2.b-e) ferrite grains. The other significant difference is in the presence of retained martensite (M) and austenite (A) constituents (Fig. 2.b, e). The internal structure of M/A features is composed of martensite needles separated by layers of residual austenite [4]. Another important variable is the carbides or M/A spatial distribution. In the case of upper bainite, the carbides and M/A constitutes are distributed between ferrite laths (Fig. 2.b, c). In the case of lower bainite the precipitates are located inside the ferrite laths (Fig. 2.d, e).

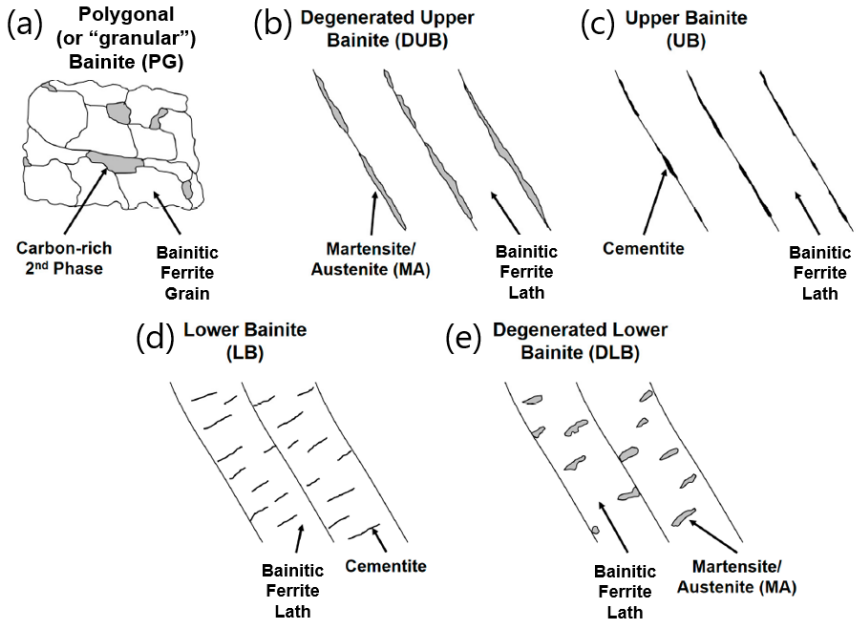

Figure 2. *Schematic image of different types of bainitic microstructure that can be formed after tempering [5,6].*

In the case of commercial RPV steels, due to the big size of ingots (vessel rings), the cooling rate is not homogeneous at the different thicknesses of the RPV wall. Therefore, both upper and lower bainite can be observed in commercial RPV steels [8].

The specimens for the microstructure investigation in the shape of rods with a diameter of around 8 mm and length of 35 mm were prepared. After the thermal treatment the microstructure of several steels was characterised with optical and electron microscopy by SCK CEN (Fig. 3.a). Also, optical microscopy study on steel W was performed at Le Groupe de Physique des Matériaux (GPM) Rouen (Fig. 3.b). The results showed that the tempered lath-like bainitic microstructure was formed. To confirm that bainitic microstructure was formed in every material, a dedicated EBSD study will be performed.

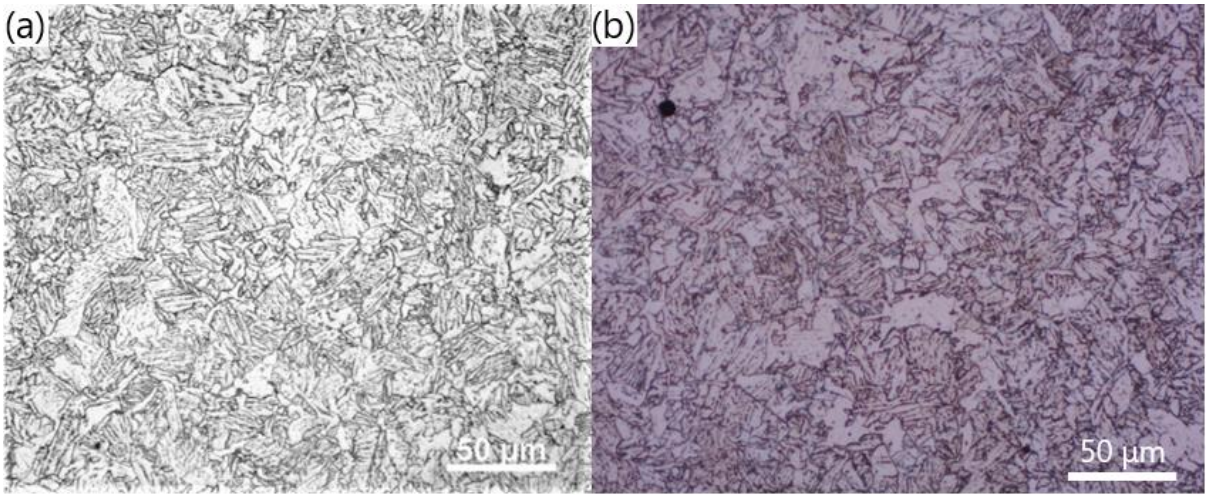

Figure 3. *Microstructure of CT RPV steels. (a) Steel D [2]. (b) Steel W.*

The transmission electron microscopy (TEM) observations on as-received steels I and W were performed at SCK CEN by Dr. Wouter Van Renterghem [3]. Big spherical elongated M_3C (Fe-Mn-C) with a size of several hundreds of nanometres were identified (Fig. 4.a). Also, the M_2C (Mo-Fe-C) carbides were found. They are needle shaped with a length of 50 to 100 nm and width of around 10 nm (Fig. 4.b). Carbides formed both inside and in-between ferrite laths were observed. Additionally, the M/A features were observed between the ferrite laths (Fig. 4.c). The final microstructure of steels I and W in composed of the mixture of lower, upper and degenerated upper bainite (Fig. 2.b, c, d).

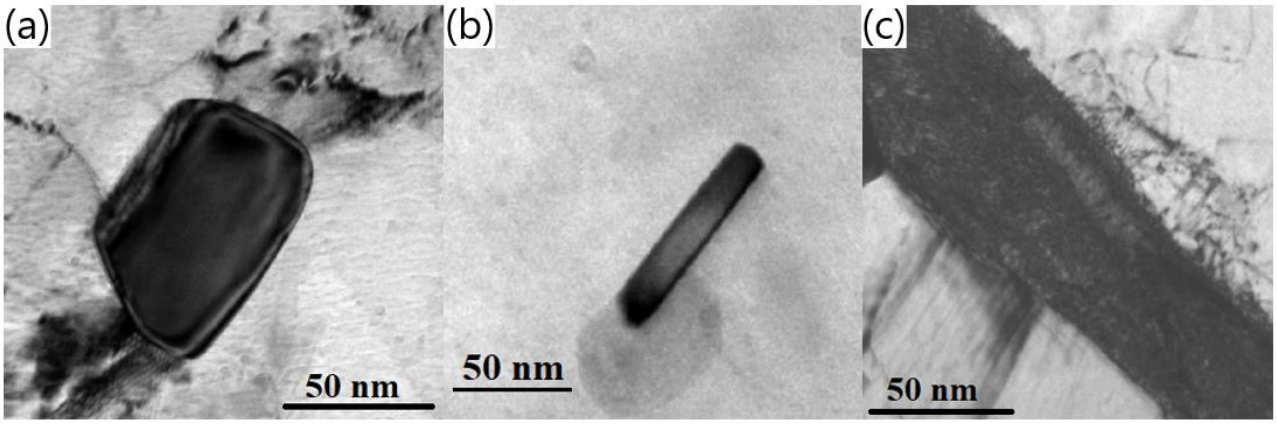

Figure 4. *Bright field TEM images of chemically-tailored RPV steel I. (a) M_3C carbide. (b) M_2C carbide. (c) M/A features observed between ferrite laths [3].*

The TEM study on other steels (D, E, F, N, O) was not performed. Yet, since the C and Mo bulk contents are the same for all studied materials, the formation of the carbides is also expected. At the same time, the significant difference between the latter steels and I, W is the lower Mn and Ni bulk concentrations. The combine Mn plus Ni content in steels D, E, F, N and O is below 2.5 at. %, and is ~3.5 at. % in the case of I and W. Mn and Ni are known to be the austenite stabilisers and their high concentration could be connected to the presence of M/A constitutes [2]. Therefore, to evaluate the presence of M/A features the dedicated EBSD study on CT RPV steels will be performed.

Since the tempered bainitic structure was observed, the dislocation density is expected to the on the level of RPV steels, which is around 10^{14} m^{-2} [3,9].

1.3 Neutron irradiation

Microstructure specimens in a shape of rods from seven chemically tailored RPV steels were irradiated as a part of the RADAMO-13 program in the material testing reactor BR2 at SCK CEN (Fig. 5.a). The irradiation was performed inside the Capability for Light Water Irradiation in Steady State and Transient Operations (CALLISTO) loop in October 2015. The CALLISTO loop was

specifically designed to imitate the PWR conditions, namely the high pressure (15.5 MPa) and high temperature (290 °C) [10,11]. RPV steels from the current project were irradiated simultaneously for the same period. The accumulated fluence varies due to the variation of the neutron flux at the different positions relative to the reactor core (Fig. 5.b). The irradiation dose is modelled by a Monte Carlo N-Particle code and confirmed by the mechanical tests on the reference samples with a well-known evolution of properties under the effect of irradiation.

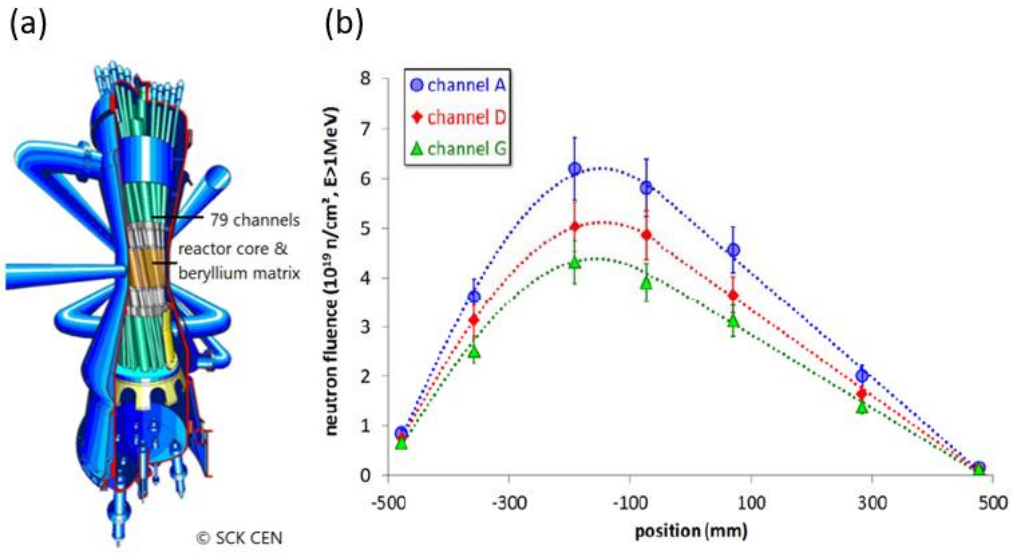

Figure 5. *(a) The schematic view of BR2. CALLISTO loop had occupied 3 from 79 channels in BR2 [10,11]. (b) Distribution of accumulated neutron fluence at the different specimen locations [1].*

Since the direct measurements of mechanical properties on microstructure samples cannot be performed, a set of tensile specimens was irradiated during the same campaign. For each CT RPV steel 12 tensile test specimens were simultaneously irradiated. Due to their small size, (24 mm in length and diameter of 2.4 mm) three specimens can be loaded at the specific position, hence four different doses were reached. The detailed information about irradiation of tensile specimens is given in appendix A.3.

Due to different axial positions during irradiation a wide range of accumulated doses was obtained for microstructure specimens. Five steels, namely D, E, F and W were irradiated up to the dose of around 0.06 dpa, we will further refer to this condition as “low” dose. Five steels: D, E, F, I, N and O were irradiated up to the dose of around 0.08 dpa, we will further refer to this condition as “medium” dose. More detailed irradiation of microstructure specimens is given in appendix A.3.

Unused tensile test of several steels, namely E, F and I were additionally irradiated as a part of RECALL-0 irradiation campaign up to around 0.13 dpa. RECALL-0 irradiation was also performed in BR2 at 290 °C. We will refer to these samples as “high” dose.

The accumulated dose, in dpa, was calculated using the cross section of the 1440 barns (10^{-28} m^2) for the high energy neutrons (E > 1 MeV). Irradiation conditions and accumulated dose for studied CT RPV steels is presented in Table 2.

Table 2. *Irradiation conditions CT RPV steels used in this PhD project. Values of RADAMO-13 irradiation are in regular font. Values of RECALL-0 irradiation are in italic font.*

ID	T_{irrad} [°C]	Fluence [10^{23} n/m^2]	Flux [10^{17} n/m^2s]	dpa/s [10^{-8}]	Dose [dpa]
D	290	6.29	2.60	3.74	0.091
E Low	290	4.78	1.98	2.85	0.069
E Medium	290	6.37	2.63	3.79	0.092
E High (T)	290	9.59	2.58; *1.18*	3.71; *1.70*	0.138
F Low	290	2.79	1.69	2.43	0.056
F Medium	290	4.09	2.23	3.21	0.078
F High (T)	290	9.34	2.48; *1.18*	3.57; *1.70*	0.134
I Medium	290	5.72	2.36	3.40	0.082
I High (T)	290	9.14	2.46; *1.13*	3.54; *1.62*	0.132
N	290	5.21	2.15	3.10	0.075
O	290	4.38	1.81	2.61	0.063
W	290	4.25	1.76	2.53	0.061

Thin disks which had been cut out from microstructure specimens were shipped to the GPM laboratory to perform microstructural investigations. The transfer of these active materials between Belgium and France takes time and need to be organised following the legislation procedures. To overcome these time constraints, an alternative procedure was implemented. Some of the lift-outs on active samples (both microstructure and tensile in the case of "high" dose condition) were performed inside the hot cells at SCK CEN by Dr. Wouter Van Renterghem. The pre-tips of active CT RPV steel were welded on APT coupons. The volume of active material was then limited to several cubic micrometres (μm^3), and the dose rate (<100 nSv) and activity (~kBq) levels are below the background level.

1.4 Tensile tests

The magnitude of irradiation damage on mechanical properties of commercial RPV steels is usually reported as embrittlement of material. The embrittlement is usually estimated by the change of ductile-to-brittle transition temperature. DBTT is measured by Charpy impact test curves. With the Charpy test the combined effect of both non-hardening and hardening embrittlement can be

evaluated. The drawbacks of the Charpy test are the big size of the specimen and the high number of specimen (around 10 to 12) required to be tested [2].

In the present work, the main focus is on the irradiation hardening. Therefore, tensile tests, which provide the information about YS and UTS, were used. For each steel, 12 tensile specimens were irradiated up to four different doses. For each dose, tensile tests on two samples were performed, and the third one was saved to perform experiments with additional annealing later on. Tensile tests were performed (prior to this project) inside SCK CEN hot cells, at room temperature with a strain rate of around 10^{-4} s^{-1}. Trend curves of yield strength increase as a function of neutron fluence were plotted to fit experimental data points. Example for CT RPV steel W is presented in figure 6. The average uncertainty margin of tensile test experiments was estimated with a large database by Chaouadi and co-workers and equals to around 25 MPa, which is close to other values presented in literature [1,12]. More detailed information about measured yield strength increase is given in appendix A.3.

Direct irradiation hardening measurements could not be performed on the microstructure specimens. Therefore, to attribute the irradiation hardening value to each microstructure bar the interpolation of the tensile data trend curve as a function of neutron exposure was made (Fig. 6).

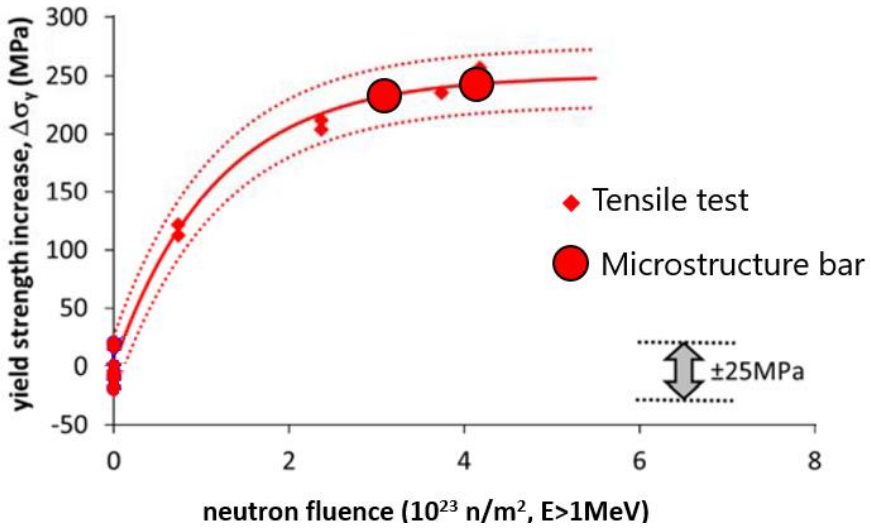

Figure 6. *Yield strength increase as a function of neutron fluence for CT RPV steel W. Small diamond points are the results of the tensile test experiments. From the tensile test data the trend curve of irradiation hardening vs neutron fluence was plotted. The values of irradiation hardening for the microstructure specimens (big circle points) were interpolated as a function of neutron exposure. The default uncertainty margin of tensile tests of 25 MPa is shown [1,12].*

The interpolated irradiation hardening values attributed to the CT RPV steel microstructure specimens plotted by the increase of yield strength ($\Delta\sigma_y$) as a function of irradiation dose are presented in figure 7.

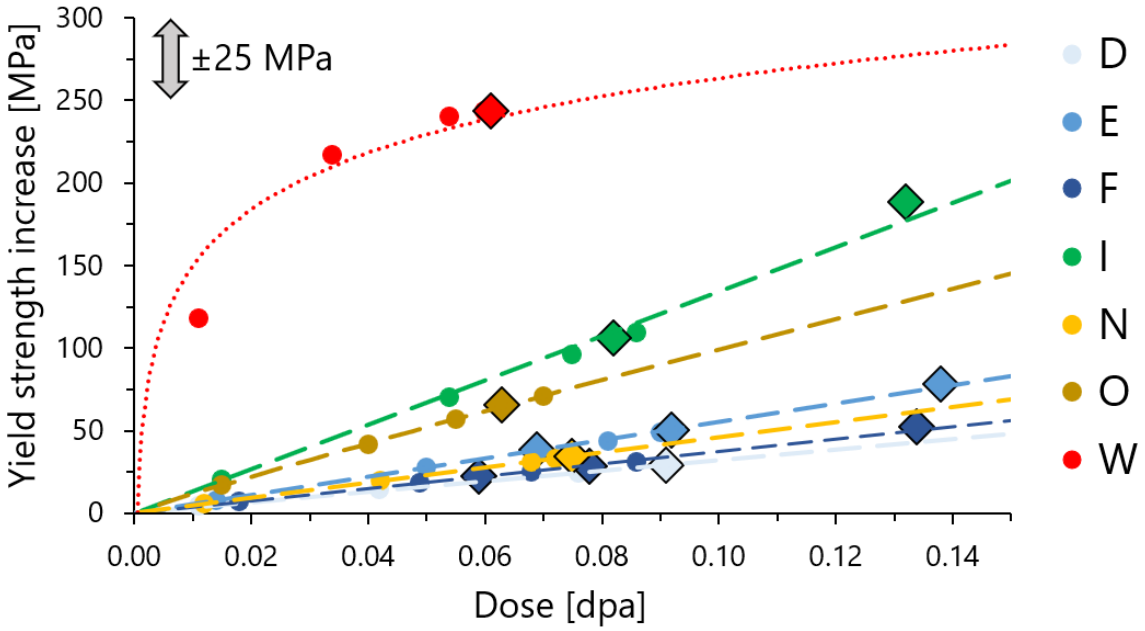

Figure 7. *Yield strength increase as a function of accumulated dose for seven chemically-tailored RPV steels. Circle symbols represent the results of the tensile test. From these values trends were plotted. Big diamond symbols represent the specimens studied in the current PhD project. The default uncertainty margin of 25 MPa is also shown.*

We can clearly see that those materials follow several distinct trends. The CT RPV steels D, E, F, and N exhibit a low hardening effect, which increases almost linearly with dose. CT RPV steel O, also exhibit almost a linear trend of yield strength increase with dose, but the hardening effect is stronger. Even stronger linear-like hardening trend in observed for CT RPV steel I. High-Cu steel W has a completely different hardening tendency than other materials. As typical for high-Cu commercial RPV steels, strong (similar to square root trend) hardening tendency is observed. The severe hardening effect is observed at the low doses, and with increase of dose becomes linear-like, same as for the low-Cu steels.

The results of the tensile test are the cornerstone of the current PhD research. They will be used to draw a comparison between microstructure evolution and the hardening effect under neutron irradiation. Also, experimentally measured hardening will be compared with the yield strength increase calculated with the different hardening models [13,14].

2 Sample preparation

During irradiation, neutrons can interact with the nuclei of the atoms resulting in transmutation and formation of unstable isotopes (activation). These unstable isotopes will decay emitting alpha particle ($^4_2\alpha$), beta particle (β^- or β^+), gamma ray photon (γ). These radiation emissions are detrimental to human health. Therefore, strict safety measures should be followed while handling the active materials.

2.1 GENESIS platform

The GENESIS (abbreviation for Groupe d'Etudes et de Nanoanalyses des Effets d'Irradiations) platform was constructed (2013 to 2016) as a part of the GPM laboratory. The research performed within the platform focuses on irradiation effects on nuclear materials, mainly the characterization of the microstructure evolution, at the atomic scale. Therefore, GENESIS platform was developed following safety regulations to handle radioactive samples (beta and gamma emitters only).

In the case of RPV steels, typically activated isotopes with a long half-life are ^{55}Fe, ^{54}Mn, ^{63}Ni and ^{60}Co. Two main risks for the handling of the active materials are internal and external exposure. To limit the external exposure and prevent internal contamination “As Low As Reasonably Achievable” (ALARA) principles are mandatory. Several protective measures are implemented. To limit the exposure, active sample handling is performed using long tweezers and special β-protective gloves. Dose rate at the distance of 10 cm is measured and recorded before and at the end of session. Sample transfer from lead storage towards the microscope is performed inside a lead container (Fig. 7.a). During all manipulations the operator should position the movable lead shield between himself and the active specimen (Fig. 7.b). The sample placement onto the microscope specimen holder is performed inside a glovebox equipped with a protective lead shield to limit exposure and minimise potential contamination (Fig. 7.c). The sample transfer from the glovebox to the microscope is performed with a special trolley inside a protective lead container (Fig. 7.d).

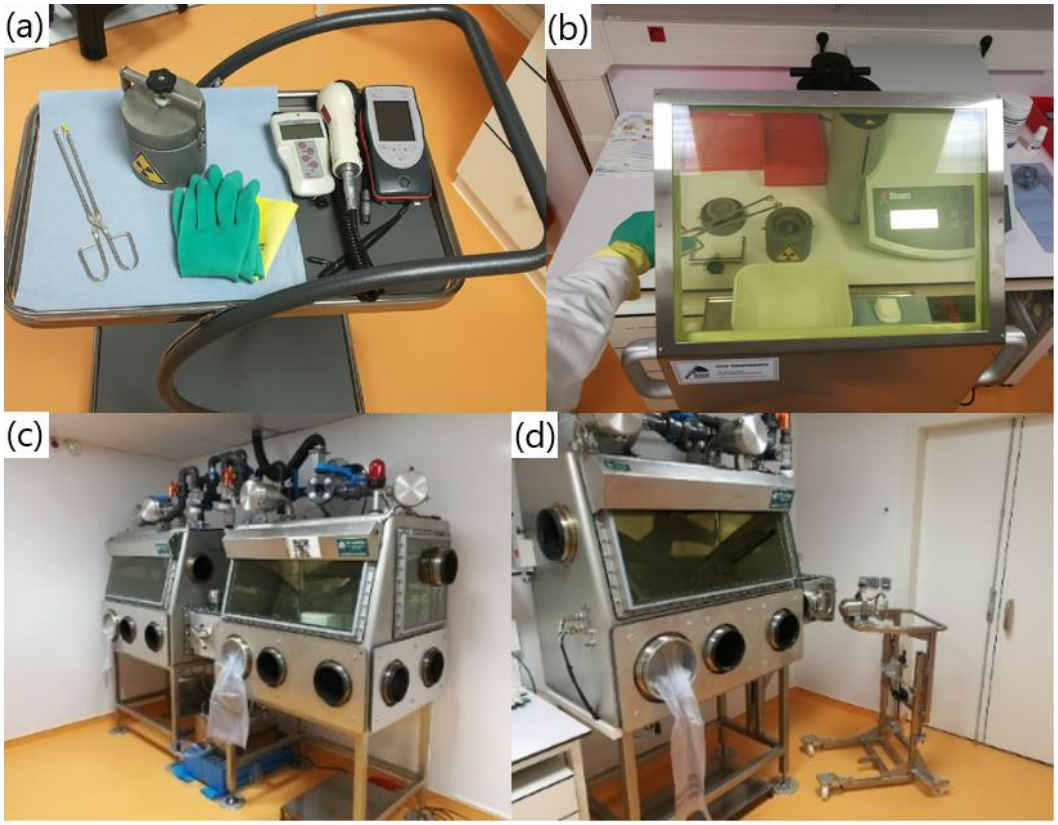

Figure 7. *(a) Set of instruments to handle the active materials: β-protective gloves, lead container, long tweezers, radiometers and contamination probe. (b) Sample transfer to the lead contained behind the movable lead shield. (c) The two-glovebox setup for sample preparation (mechanical polishing). (d) Glovebox and the trolley with the lead container for sample transfer towards the microscope.*

To ensure that nothing was contaminated at the end of the session, wipe tests on all the instruments and surfaces which have been in contact with active sample should be performed. To prevent the contamination of the laboratory outside from the dedicated zone of the GENESIS platform, the contamination control with the Sirius^{TM}-5 detector must be performed.

2.2 Focused Ion Beam tool

In order to perform APT experiments, a very sharp (few nanometres) tip shaped specimen is needed. This specific sample need to be extracted from thin disks of active material which was beforehand cut inside the hot cells at SCK CEN. Specimen preparation using the electro-polishing method was not convenient due to the small size of samples (disks with thickness of ~0.2 mm). Thus, sample preparation with focused ion beam (FIB) was used.

A focused ion beam is the part of SEM/FIB setup. A detailed explanation of FIB instrument can be found in references [15,16]. The GENESIS platform is equipped with the ZEISS Crossbeam 540 (XB540) instrument with a modified airlock chamber to perform the introduction of radioactive

samples. It uses Ga as liquid metal ion source (LMIS). The ion beam column is located at 54° away from the SEM column. The XB540 is also equipped with a Pt gas injection system (GIS), and an Omni Probe 400 micromanipulator to perform the local sample handling. To perform microstructure characterisation, the XB540 setup is also equipped with EBSD and energy dispersive X-ray spectroscopy (EDS) detectors (Fig. 8).

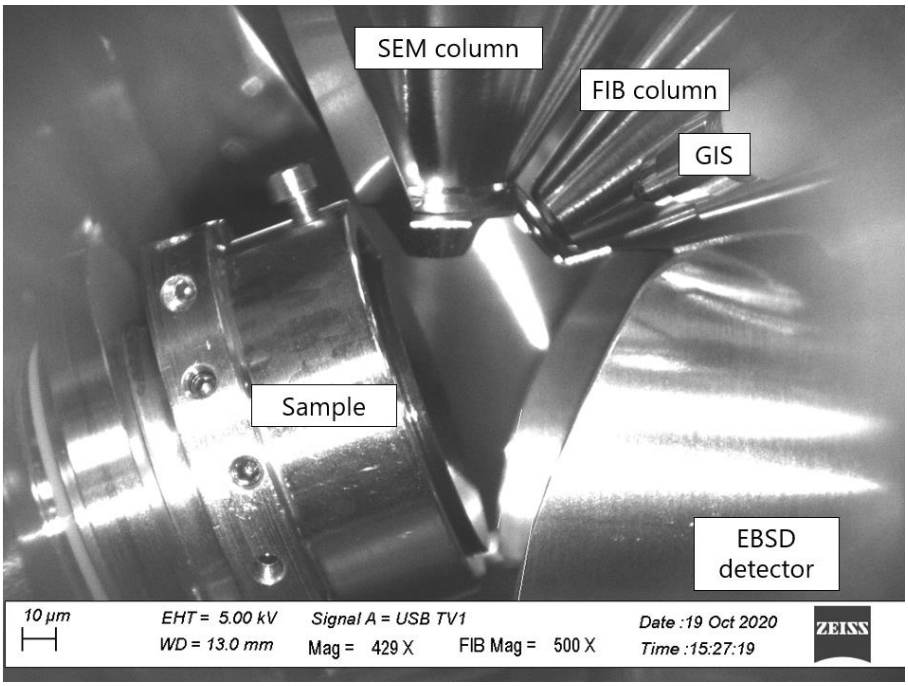

Figure 8. *The main chamber of the XB540 setup. The FIB column, GIS and EBSD detectors are located at the right side of the chamber to allow three-axis specimen stage movement at the tilted setup.*

The use of the FIB limits the human body exposure to the radioactive materials. Indeed, the sample preparation is performed inside the SEM/FIB chamber, several meters away from the operator. The volume of active material transferred to APT or TEM is very limited (down to cubic micrometres (μm^3)). An additional advantage is the possibility to perform the specific-site lift-out after utilising the EBSD technique.

The FIB needle preparation follows the procedure described below. The region of interest (ROI) was selected from SEM imaging or EBSD map. In our case, ferrite laths were generally selected. A 0.2-0.5 µm layer of Pt was deposited with GIS to protect the ROI during the first steps of milling with high-energy ions (30kV; 15 nA). The milling of a parallelepiped, the so-called chunk, was performed. The chunk with a size of 20 x 2 x 4 μm^3 was lifted out from the specimen using the micromanipulator. From one chunk, five or six APT tips were prepared. They were transferred to Si coupons (with 22 or 36 pre-tips) and welded by Pt deposition.

The next step is to form the final shape of the APT tip. This process is called annular milling. The milling with a set of circular masks is performed to refine the radius of the needle. The ion beam current and the inner radius of the patterns are continuously decreasing (Fig. 9). The last step is performed with the 30 kV, 20 pA ion beam and the mask radius of 50 nm. The known drawback of the FIB sample preparation is the Ga contamination of the tip surface [17]. The final cleaning procedure with the low energy ion beam (2 kV, 90 pA) is performed to remove the top 250 nm contaminated with the implanted Ga ions.

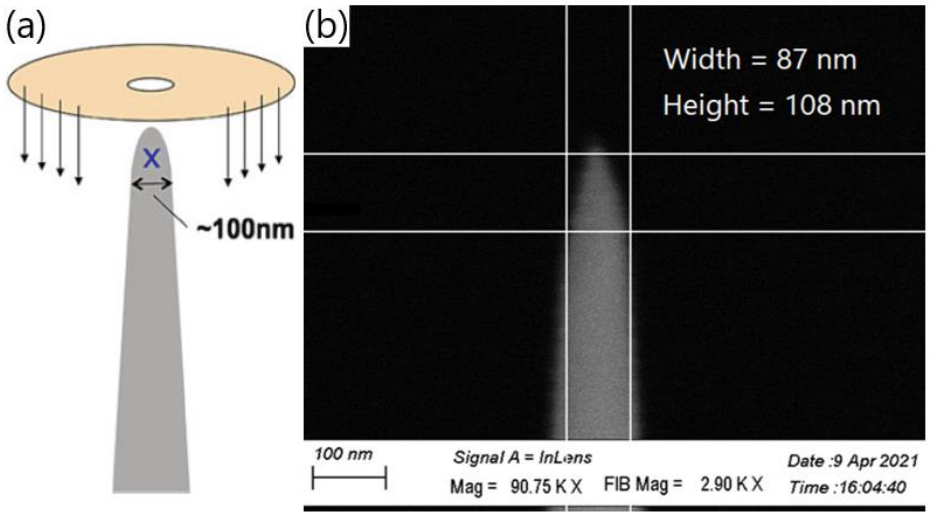

Figure 9. *(a) Schematic view of the annular milling procedure. A donut shape pattern is used to refine the radius of the needle [15]. (b) SEM image of the APT tip prepared with FIB. A radius of around 40 nm at the distance of about 100 nm from the tip apex is achieved.*

2.3 Electron Backscatter Diffraction technique

Electron backscatter diffraction (EBSD) is a non-destructive microstructural analysis technique which allows to identify the crystal lattice, the grain orientation, the phase identification of materials [18]. To perform EBSD, the specimen should be tilted to around 70° and face the phosphor detector introduced inside the SEM chamber. During the experiment, phosphor screen will be fluoresced by the electrons scattered from the sample and Kikuchi patterns will be formed (Fig. 10).

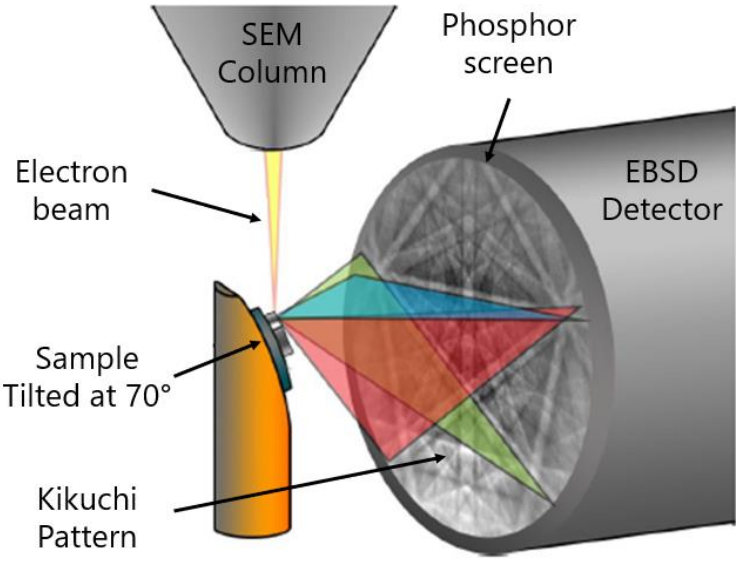

Figure 10. *Schematic view of an EBSD experiment. The electrons backscattered for the specimen tilted at 70° are projected toward the phosphor screen of ESBD detector [19].*

At the angle of 70° degrees and high voltage (above 20kV), backscattered electrons are diffracted by specimen atomic planes and projected towards the detector. Electron are scattering from the atomic planes by the Bragg's law:

$$n\lambda = 2d \sin\theta \qquad (2.1)$$

where n is the order of diffraction, λ in the electron wavelength, d is the reticular distance and θ is the angle of diffraction. For each atomic plane fulfilling the Bragg condition, two diffraction cones are formed. Intersections of these cones with the detector are seen as two bright Kikuchi lines, delimiting a Kikuchi band (Fig. 11.a). One Kikuchi band represents an atomic plane family and Kikuchi band intersections correspond to the zone axis. The reflection from different atomic planes results in the formation of the Kikuchi pattern. A Hough transform is performed to identify the Kikuchi bands. Hough transform maps each pixel of the image, as a sinusoidal curve in a Hough space. The curves of the pixels belonging to the same line intercept in the same Hough cell, creating a spot with a high intensity. These pixels are attributed to the same Kikuchi line. The indexing is performed by the comparison of measured interplanar angles (angles between Kikuchi bands) and interplanar spacings (band width) with the theoretical values for the studied crystal lattice (Fig. 11.b) [20].

The depth resolution of EBSD technique depends on the quality of sample preparation, on the atomic number of the identified element and on the incident beam voltage and angle. For the Fe-based alloys, it is limited to below 20 nm [20]. Hence, it is generally accepted that EBSD provides information about the surface microstructure of the sample.

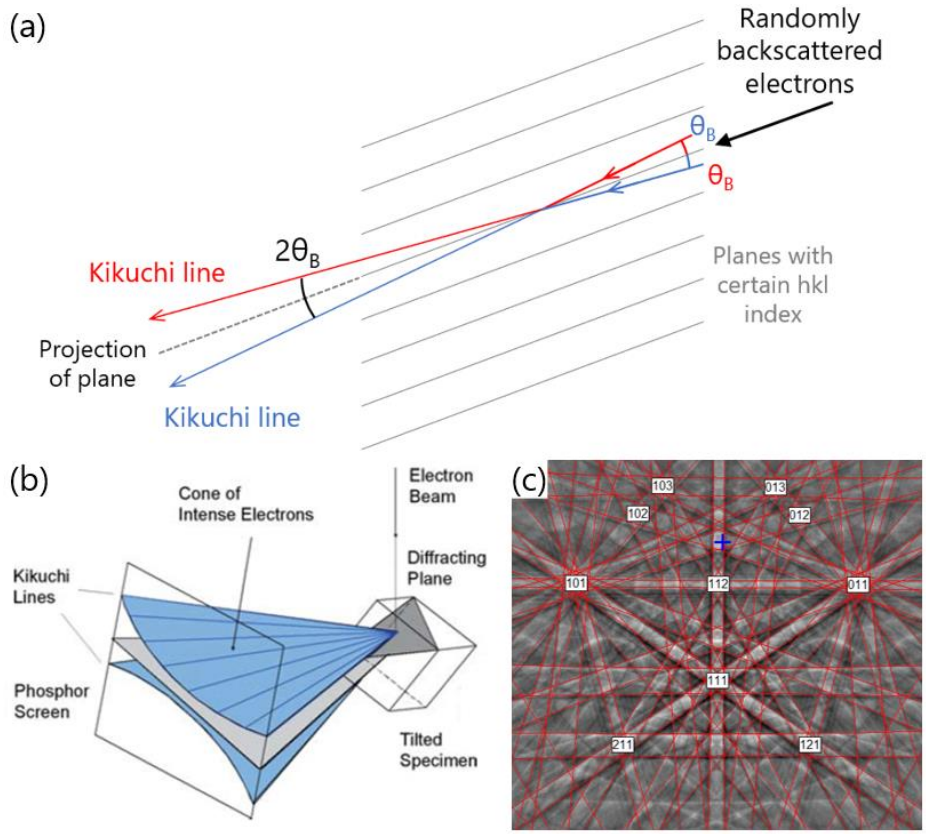

Figure 11. *(a) Diffraction of backscattered electrons travelling towards hkl planes with the fulfilling the Bragg condition angle. (b) Formation of two diffraction cones (Kikuchi band) by the backscattered electrons on the phosphor screen [20]. (c) The indexed diffraction pattern. Several crystallographic plans and zone axes are observed [21].*

A typical way to represent the EBSD data is the inverse pole figure (IPF) map (Fig. 12), where a given colour defines one grain orientation. In the present work, EBSD was utilised to get information about ferrite laths size, misorientation angles and parent austenite grain size. The presence of carbides and austenitic phase was also studied with the EBSD technique. Since no texture was observed, the information about the surface phase fraction was estimated to be representative of the volume fraction.

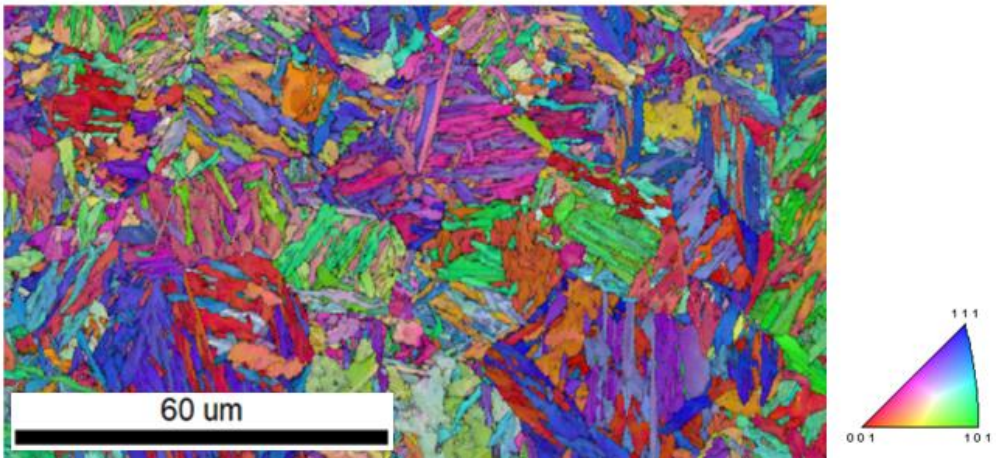

Figure 12. *IPF orientation EBSD map of the CT RPV steel I.*

3 Atom Probe Tomography

As it was mentioned earlier, the size of the solute clusters is so small, that only very high resolution techniques can be utilised for their characterization. One of them is Atom Probe Tomography.

Atom Probe Tomography is a destructive quantitative material analysis technique. It provides a three-dimensional reconstruction of the chemically analysed volume, at the atomic level. Size, morphology, number density and chemical composition of nm-size chemical heterogeneities can be quantified. The size of analysed volume is rather small ($< 5 \times 10^{-4}$ cubic micrometres). Yet, the precision of size and chemical composition measurements is better than of the most material analysis techniques. The additional advantage is the possibility of a three-dimensional (3D) reconstruction of analysed volume. The reconstruction of the microstructure at the atomic level allows to directly see atoms inside solute clusters, therefore giving the possibility to observe complex features like Cu-rich radiation-enhanced precipitate, with a Mn-Ni-Si shell, formed by the irradiation induced mechanism.

In this work, APT technique is used to study the neutron irradiated chemically-tailored RPV steels. APT principles, experimental procedures, advantages and limitations will be described in detail further. This chapter is based on the books written by Gault, Larson, and Miller [25-28].

3.1 Principle

Atom probe tomography is a destructive material analysis technique based on the field evaporation effect and the time of flight (TOF) mass spectrometry using a position sensitive detection. Schematic view of the APT setup is presented in figure 13.

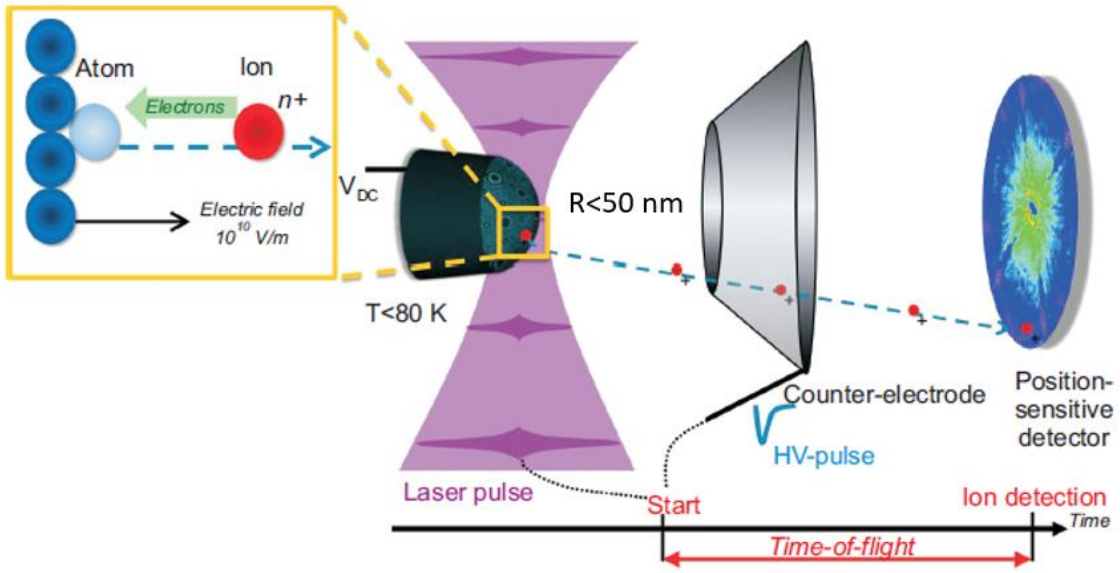

Figure 13. *Schematic view of the local electrode equipped APT setup. Sharp needle-like specimen with radius below 50 nm is cooled to cryogenic temperatures and subjected to high voltage. Atoms are progressively field evaporated by the virtue of high voltage or laser pulses. These pulses onset the time-of-flight measurements. Projected atoms (also referred as ions) are collected by the position-sensitive detector [29].*

In order to field evaporate atoms from the surface of the tip shaped specimen, a high electric field E (10-60 V/nm) is required. E is given by:

$$E = \frac{V}{R_{tip}\, k_f} \tag{2.2}$$

where k_f is the geometric shape factor (or field factor), V is the total applied voltage and R_{tip} is the radius of the tip apex. The field factor of a perfect sphere is equal to one. In the case of a needle specimen with a more elliptic end shape, the value ranges from two to eight. To keep the applied voltage in a reasonable range (up to 10 kV), the tip radius should be refined below 50 nm. The specimen is cooled down to cryogenic temperature (several dozens of K) in order to decrease the thermal vibration of the atoms. The APT experiments are performed under high vacuum (around 10^{-7} Pa) to prevent collisions between ions and residual gas atoms and to prevent surface pollution.

Practically, the standing voltage applied to the sample generates an electric field lower than the evaporation field. High voltage (HV) or laser pulses are added to the standing voltage to provoke field evaporation of surface atom at controlled time (Fig. 14). The ion is positively charged and projected towards the detector following electrical field lines.

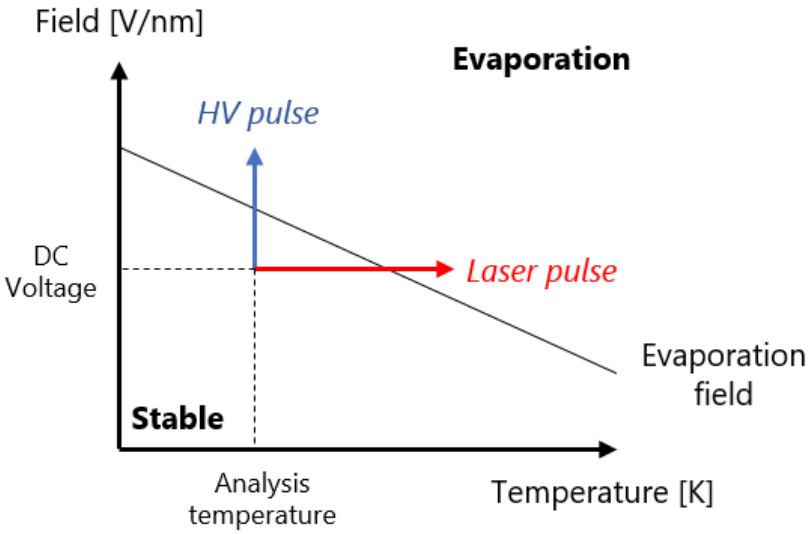

Figure 14. *Two mechanisms to provoke the field evaporation are presented. High voltage pulse is presented with blue arrow. By increase of the total applied voltage, the electric field increases above evaporation limit. Laser pulse is presented with red arrow. Temperature of specimen is increased due to absorption of laser light up to the region where, generated by standing voltage, field is above the evaporation field.*

The time between HV or laser pulses and the ion impact on the detector is measured. Using energy conservation, this measurement allows to calculate the mass over charge ratio of the ions, so its chemical nature. The ion evaporated from the surface has the following potential energy:

$$E_P = neV \tag{2.3}$$

where n is the charge state, e is the elementary electric charge and V the total voltage (equal to the sum of standing voltage (V_{DC}) and the pulse voltage (V_P)).

The assumption that an ion has no initial velocity and that its potential energy is fully converted into kinetic energy (E_k) is made. Hence, E_k at the moment of the impact will be written as:

$$E_k = E_P = \frac{1}{2}mv^2 \tag{2.4}$$

where m is the mass of the ion, and final velocity v is deduced from the equation:

$$v = \frac{L}{t} \tag{2.5}$$

where L is the flight length and t is the measured time of flight.

Combining the previous formulas, the final equation for the mass-over-charge ratio is expressed as:

$$M = \frac{m}{n} = 2eV\left(\frac{t}{L}\right)^2 \tag{2.6}$$

The mass-over-charge ratio for every detected ion is recorded and presented in the form of mass-over-charge ratio spectrum in atomic mass units (a.m.u.) or Daltons (Da) (Fig. 14).

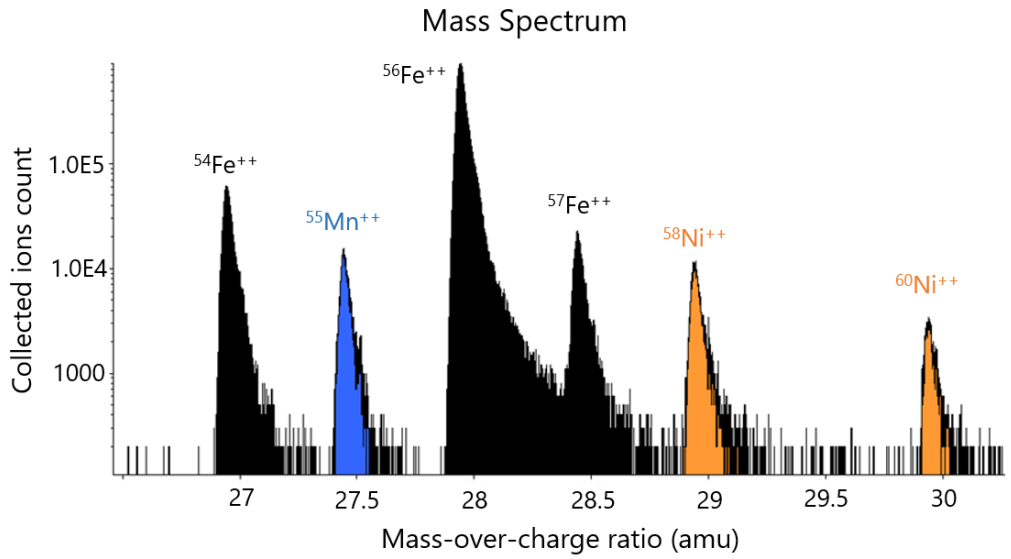

Figure 15. *Mass-over-charge ratio spectrum from the commercial IVAS software. From the mass spectrum several isotopes of Fe, Ni and Mn are identified.*

The detector of the APT instrument is used not only to measure the time of flight but also to collect information about the position of the impact. In a modern APT instrument, the system consisting of two micro-channel plates (MCPs) and a delay line detector (DLD) is used [26]. MCPs are utilised to amplify the signal of the ions. When the ion collides with MCP, it creates an electron cloud towards the DLD (Fig. 16.a).

Further, the electron cloud is hitting the DLD, creating signals to both ends of delay line anodes. Deepening on time for a signal to reach the end of the wires, the initial position of the impact (X', Y') is identified (Fig. 16.b). There are three delay lines in CAMECA LEAP instruments which allows to reach the detection efficiency of almost 95 % [26].

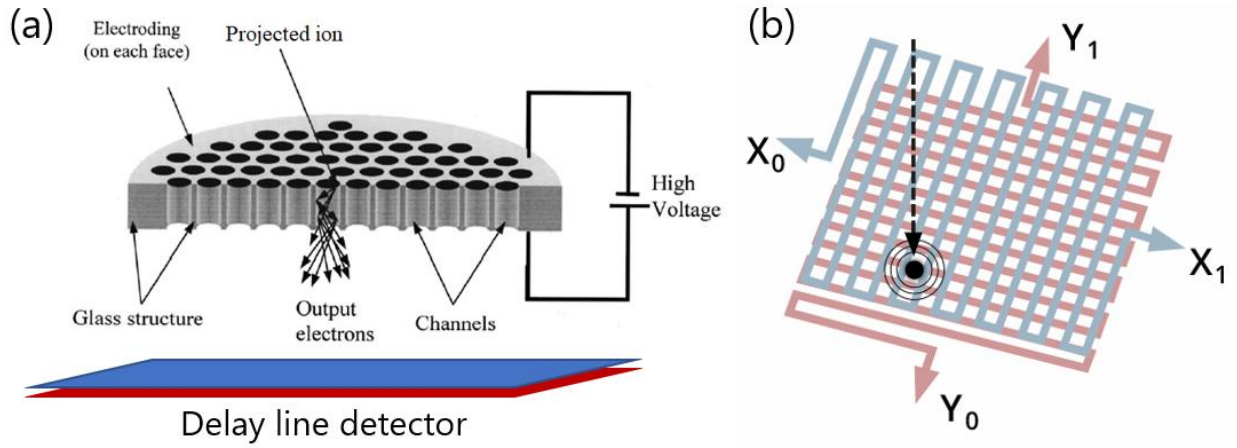

Figure 16. *(a) Cross section view and the operation principle of the MCP [30]. (b) Identification of the impact position of the ion (X', Y') with the delay line detector. Only two delay lines are shown for the image simplicity [31].*

Yet, the final detection efficiency of the MCP-DLD system is up to 60 % and has no preferential dependency on the nature of the ion. This limitation arises from the limited effective surface of the MCPs [26].

The main instrument used in the current study is the commercial Local Electrode Atom Probe (LEAP) 4000X HR. The "HR" is the abbreviation for the high resolution, meaning that this instrument has a reflectron setup. The "X" means that it can be used either in electrical or laser modes.

The reflectron is an electrostatic lens that sets the ions with lower energy to fly via a shorter path and the high energy one to take a longer one (Fig. 17). Hence, the average time of flight is equalised. As the trade-off, the utilisation of the reflectron results in the loss of some ions and the final detection efficiency of the LEAP 4000 HR instrument is around 36 %, in comparison with 57 % for the straight path LEAP 4000 Si ("Si" means straight-flight-path instrument).

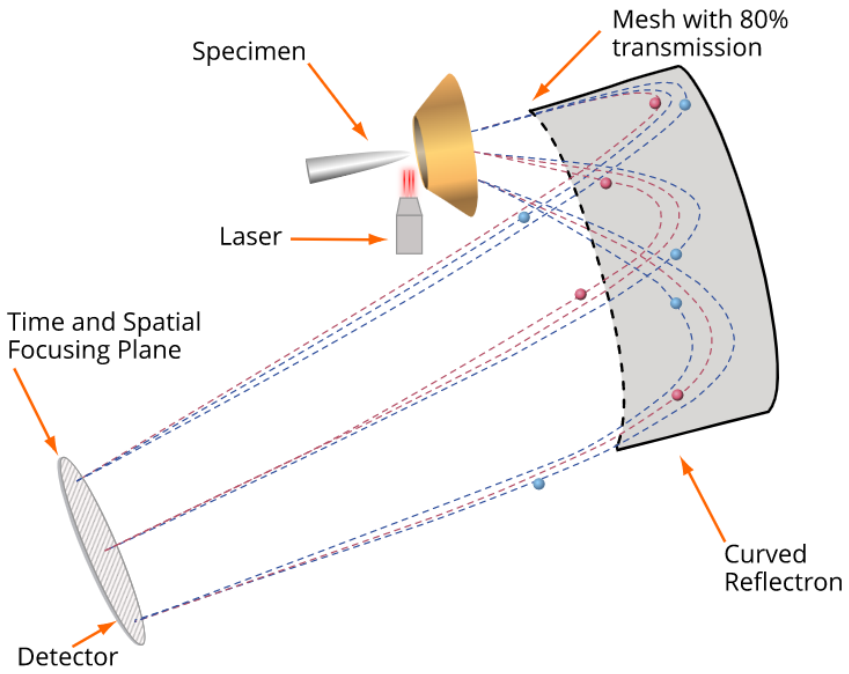

Figure 17. *Schematic view of the atom flight path on the reflector equipped APT setup [31].*

To understand the importance of the reflectron, we should refer to mass resolution (MR). MR is the ability to identify two neighbour peaks on the mass spectrum. The MR is given at the 1 and 10 % maximum of the main $^{56}Fe^{++}$ peak (Fig. 18). The longer time of flight will result in the overestimation of the mass over charge ratio and therefore the peaks will have a "tail". The use of a reflectron provides high mass resolution measurements

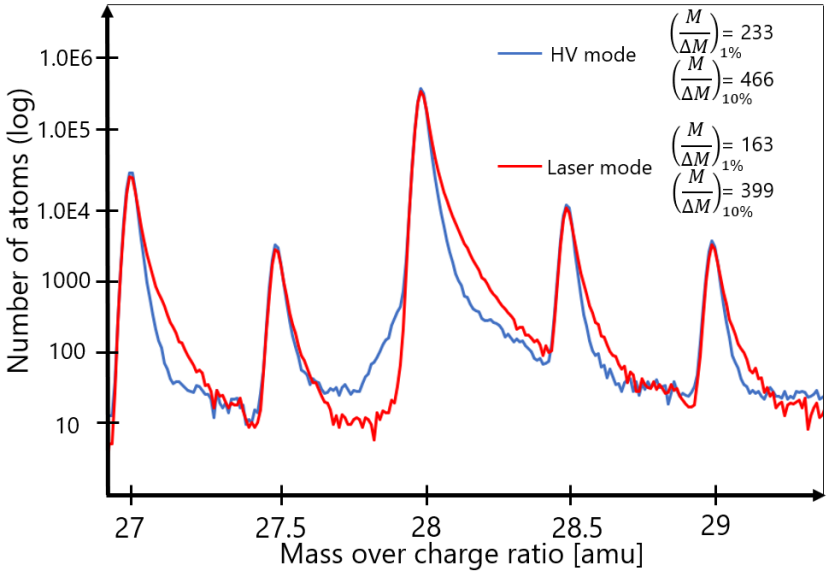

Figure 18. *The mass spectrum from APT experiments on CT RPV steel E with HV and laser modes. The mass resolution at 1 and 10 % is indicated. MR is better in the case of HV mode. The number of atoms in the analysed volumes is 3 million.*

The APT in the laser-assisted mode limits the total applied voltage to the specimen to the standing one (V_{DC}). With a lower total applied voltage and without repetitive HV pulses, the probability of sample fracture decrease, and the yield of the APT experiment is improved. The trade-offs of the laser mode are the surface diffusion (will be described in 3.3.4), complexity of mass spectrum decomposition (will be described in 3.3.1) and, in some cases, the lower mass resolution. Laser-assisted heating of the APT specimen subjected to cryogenic temperature is a complicated process. After application of laser pulse, a finite time is needed for heat to spread until specimen will be cooled down to the analysis temperature. A prolonged cooling time results in a longer interval when ions are probable to be emitted from the surface, which consequently increases the measured time-of-flight and hence forms a longer tail to the associated pick on the mass spectrum. Regardless, in the case of HV experiments, the lower MR arises from a longer time of flight of some ions which have less energy since they were evaporated before or after the HV pulse maximum. Slightly larger peak tails in the experiments performed in laser than in the case of HV mode were observed on the mass spectrum (Fig. 18). Yet, in the case of the modern APT instruments, the MR on both HV and laser modes is sufficient to perform precise chemical composition measurements.

To summarise APT principle, atoms are field evaporated and projected towards a position sensitive detector (MCP-DLD system). The information about the chemical nature of ions is collected in the form of the mass over charge ratio. Experimental conditions are important for the quality of the acquired data and furthermore the correct interpretation of observed features. The experimental parameters are described in the following sub-chapter.

3.2 Experimental conditions

The correct determination of the experimental condition of an APT experiment defines the quality and reliability of acquired data. For example, wrong experimental parameters can result in the preferential evaporation of specific chemical species brining artificial bias in the data treatment.

Preferential evaporation occurs when specific atoms have a lower evaporation field evaporate under the standing voltage, between the HV or laser pulses (Fig. 19.a). If an atom is evaporated between the pulses, the TOF is not measured and therefore the mass over charge ratio cannot be calculated, and the information about the chemical nature of this ion is lost [32-36].

In the case of RPV steels, Cu plays a major role in the formation of the clusters and precipitates. Cu is in supersaturation in the Fe matrix. Cu has a lower evaporation field (30 V/nm) than Fe (33 V/nm) and the preferential evaporation of Cu was observed in the experiments performed with both HV and laser pulses [33-36]. Yet, the phenomenon is more pronounced in experiments using laser pulses [33]. To limit the preferential Cu evaporation, APT experiments were performed in the voltage mode. However, as mentioned before, preferential Cu evaporation still exists in this later case. There are two ways to mitigate this problem: by increasing the pulse fraction or/and by decreasing the temperature of analysis. The significant increase of the pulse fraction will result in the total applied field being significantly higher than the evaporation field of low-field elements (Fig. 19.b). This will promote the simultaneous evaporation and detection of multiple events, which will decrease the quality of analysis. The second option is to decrease the temperature of the analysis (Fig. 19.c). Yet, this option is also not ideal since at the lower temperature the probability of fracture of the specimen significantly increases.

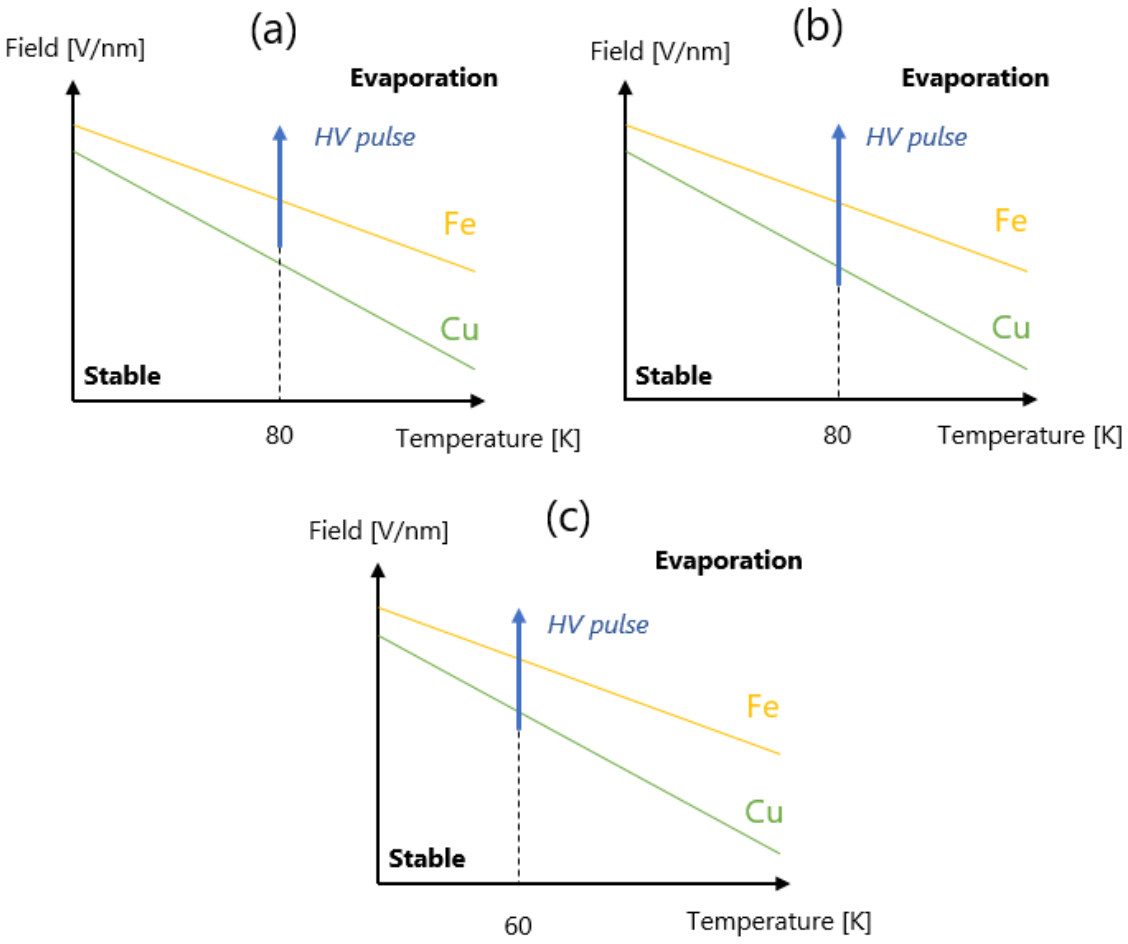

Figure 19. *Schematic view of evaporation fields for Cu and Fe as a function of temperature and effect of pulse for 3 analysis conditions. (a) The pulse fraction is too low and preferential evaporation occurs. (b) With the increase of HV pulse, the Cu preferential evaporation is reduced, yet the probability of multiple events is increased. (c) With a decrease in the analysis temperature, the preferential Cu evaporation is alleviated.*

To test the effect of temperature on the preferential evaporation of Cu, a set of experiments on non-irradiated low-Cu RPV steels from the current project was performed. During these experiments, the temperature at the beginning of the analysis was 80 K and after collecting half a million atoms (Mat) the temperature of analysis was successively decreased by 10 K steps. The total temperature range of the experiment was from 80 to 30 K. Three experiments were performed, but only two tips survived until 30 K and one fractured at 40 K. The results are presented as a ratio between measured with APT Cu content and the reference one (black line), measured by optical emission spectroscopy [1] (Fig. 20). The second plot (gold line) is the ratio of Cu^+ over the total amount of collected Cu atoms (Fig. 20). It is observed that portion of Cu^+ increases with the increase of the analysis temperature [36].

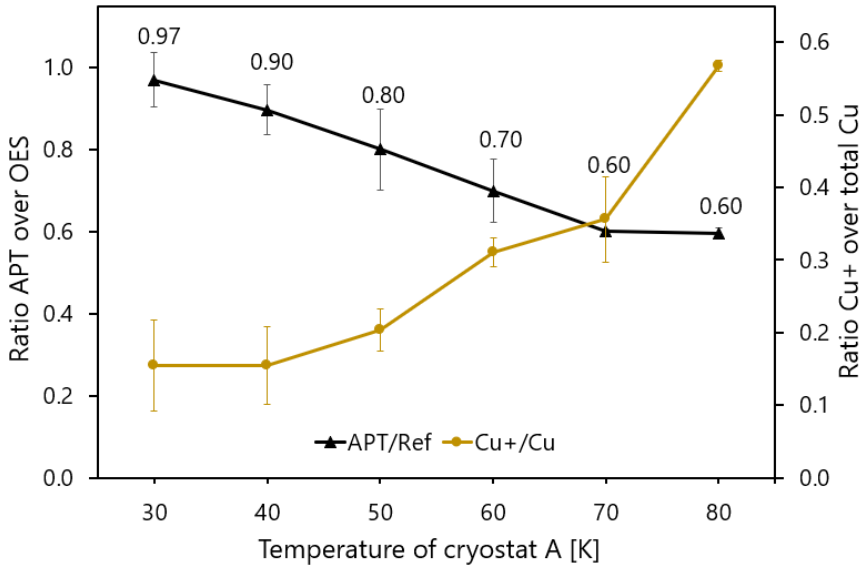

Figure 20. *Ratio of APT vs OES Cu concentration measurements as a function of APT analysis temperature (black line). Also, ratio of Cu+ over the total amount of Cu collected by the APT as a function of analysis temperature (gold line).*

The CT RPV steels have a bainitic structure that exhibits a high number of interfaces between ferrite laths and carbides. Each interface is a possible place for stress accumulation and fracture of the tip. As it was described earlier, SEM/FIB setup was utilised for APT specimen preparation. The specimen made by FIB has a welding part which is an additional interface for a possible fracture. Therefore, at the low analysis temperatures of 40 and 50 K the success/failure ratio of APT experiments was too low and the temperature of 60 K was selected as the optimal experimental conditions. The correction of bulk Cu composition due to preferential evaporation is systematically performed for data treatment.

Pulse frequency (pulse repetition rate) defines the number of HV pulses per second. The higher it is, higher is the speed of data acquisition. The higher pulse frequency shortens the time between HV pulses and hence increases the time of the specimen being under the higher electric field. At higher electric field, residual gas atoms are ionised further from the surface of the specimen and are not detected, resulting in a decrease of the background noise and improve quality of analysis [26]. The maximum pulse frequency is limited by the time of flight of ions since the time between the pulses should be sufficient enough to measure the time of flight. In recent APT instruments, voltage pulse fraction reaches 200 kHz.

Pulse fraction is a portion of the standing voltage. During the pulse, the total applied voltage is increased and hence the electric field is higher, and the process of field evaporation occurs. In the LEAP 4000X HR, the HV pulse is applied to the local electrode (LE) and it has a maximum voltage limit of 1.7 kV [26]. As it was mentioned before, lower pulse fraction will increase the number of

low-field elements evaporated between the pulses, and excessive pulse fraction will promote the simultaneous evaporation and multiple events. To account for preferential Cu evaporation a pulse fraction of 20% was selected for these experiments on RPV steels [33]. Few APT experiments in the laser-assisted mode were performed. The pulse energy of around 20 pJ was selected to reach the 20% pulse fraction.

The analysis temperature, repetition rate and pulse fraction are set before the analysis and are not adjusted during acquisition.

The only adjustable parameter is the detection rate (DR). The detection rate is the number of atoms detected per HV pulse. Typical detection rate for APT experiments on RPV steel is in the range from 0.1 to 0.5 % (detected atoms per one pulse). Detection rate of 0.1 % means that instrument is set to detect one atom every one thousand HV pulses. A high DR decreases the duration of analysis and lowers the background noise. During APT experiment atoms are progressively removed (destructive technique) and the shape of specimen tip evolves (increase of radius). With increase of specimen size, if the total number of detected atoms per one pulse remains the same (constant DR), the flux of atoms evaporated from the needle unit area is decreasing. Therefore, it is recommended to maintain a constant evaporation flux by continuously increasing the DR. Yet, increasing the DR results in a higher field applied to the specimen and, therefore, increases the probability of fracture. To conclude, the adjustment of DR is the balance between the quality of data and the experiment yield. Since RPV steel was proven to be brittle under electric field, the DR was controlled in the range of 0.1 to 0.2 % to maintain the evaporation flux in the range of 0.1 ion/s/nm^2.

The selection of most APT analysis parameters presents the choice between the quality and speed of acquisition versus the yield of the experiment [37]. The typical parameters for the APT experiments on the chemically-tailored RPV steels used in the current research are presented in Table 3.

Table 3. *The set of APT parameters used in the current research.*

Pulse mode	High voltage
Temperature (T_A)	60 K
Pulse frequency	200 kHz
Pulse fraction	20 %
Evaporation flux	~ 0.1 i/nm^{2}s
Detection rate	0.1 – 0.2 %
Detection efficiency	36 %

3.3 Data treatment

Data treatment of APT results requires specific software. In the present research commercial software IVAS version 3.8.0 from CAMECA was utilised for the specimen shape reconstruction. Further, more powerful and flexible GPM 3D software was used for the chemical composition measurements and cluster identification.

3.3.1 Mass spectrum indexation

As it was described earlier, the information about the chemical nature of ions is represented in the form of mass over charge ratio (*M*) spectrum. The spectrum represents the number of detected ions for a certain *M* range. In the case of RPV steels, the spectrum ranges from 1 to 100 a.m.u. covers the most common isotopes. The initial spectrum is not indexed and the operator should define peak ranges manually. For these materials, H and H_2O peaks are considered to be artefacts and are not further identified.

The peak identification is rather straightforward since it is dependent on the mass of the element (which is known) and its charge state. The challenging part is when two isotopes of different elements have the same mass over charge ratio and are overlapping (Fig. 21). In that case, it is impossible to identify to which element the single atom from the selected range originally refers. Yet, for the chemical composition measurements it is usually possible to resolve the peak overlapping and precisely identify the initial composition.

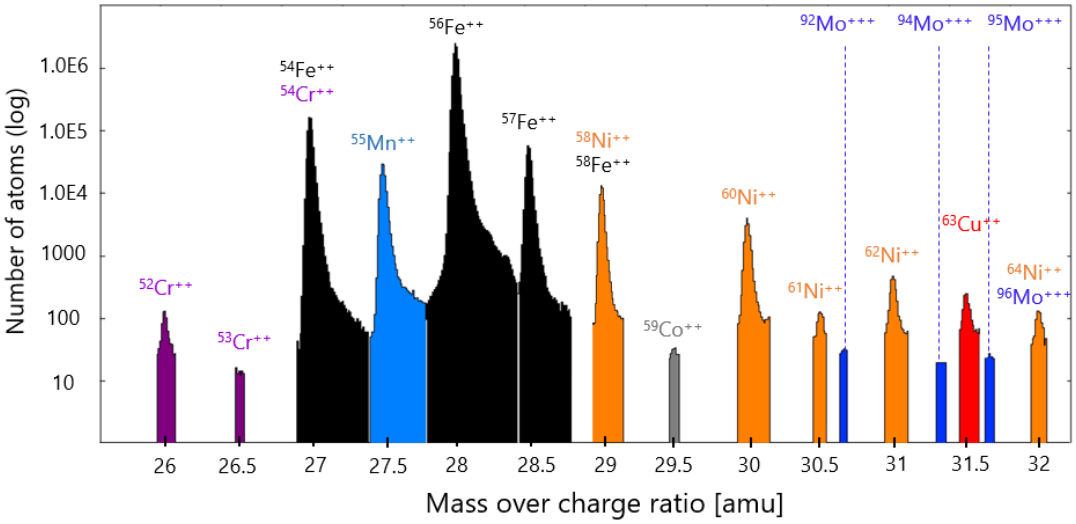

Figure 21. *Mass spectrum exported from the GPM software. The background noise is excluded. The mass spectrum peaks with isotope overlapping are shown.*

The peak decomposition was performed by comparing the ratio between a number of atoms of the isotope in the selected mass spectrum range, and the expected number of atoms in the same range, calculated with the natural isotope abundance. The following ranges were concerned by isotopic overlap and peak decomposition in the current research:

14 a.m.u. => $^{28}Si^{++}$ and $^{14}N^{+}$

27 a.m.u. => $^{54}Fe^{++}$ and $^{54}Cr^{++}$

29 a.m.u. => $^{58}Ni^{++}$ and $^{58}Fe^{++}$

32 a.m.u. => $^{64}Ni^{++}$ and $^{96}Mo^{+++}$

The peak decomposition for S was not possible. The main isotope of $^{32}S^{++}$ has the same mass over charge ratio as the main isotope of O^{+} and equals to 16 a.m.u.. The second most common isotope of $^{34}S^{++}$ has a mass over the charge ratio of 17 a.m.u., but the number of atoms for the given S composition was too low and below detectability. Since S/O peak decomposition was an unreachable task, and some oxygen is always present in steel, all the atoms at 16 a.m.u. range were evaluated to be O^{+}.

Some molecular ions formed with metal and oxygen, nitrogen or carbon were detected: FeO, AlO, AlOH, CrO, MoN, C_2, C_3 and FeC. The $^{36}C_3^{++}$ can overlap with $^{18}H_2O^{+}$ and with $^{72}FeO^{++}$. In that case, if in the 3D reconstruction, atoms were located on the surface of the volume – they were considered $^{18}H_2O^{+}$ and excluded from the analysis. If the atoms were distributed around pole figures – they were identified as $^{36}C_3^{++}$. Finally, if atoms were mostly randomly distributed inside the volume they were defined as an iron oxide $^{72}FeO^{++}$. In the case of $^{56}Fe^{+}$ and $^{56}MoN^{++}$ if there were no other MoN peaks, the 56 mass over charge peak was identified as $^{56}Fe^{+}$. If other MoN peaks were present, it was identified as $^{56}MoN^{++}$.

Using the laser-assisted atoms probe, a higher number of ions are evaporated with a one-charged state $^{56}Fe^{+}$, $^{57}Fe^{+}$, $^{58}Fe^{+}$, $^{58}Ni^{+}$, $^{60}Ni^{+}$, and complex ions such as $^{44}AlOH^{+}$ are observed, making the peak decomposition a tedious task.

When all mass spectrum ranges were identified and the peak decomposition was performed, the Cu correction due to preferential evaporation was performed. The final concentration value in the atom probe analysis was given in atomic percent (at. %). The concentration of the element i (C_i) is given by the ratio:

$$C_i = \frac{n_i}{n_{tot}} \tag{2.7}$$

where n_i is the number of atoms i and n_{tot} is the total number of atoms inside the volume.

The uncertainty on concentration measurements for a single APT experiment is given by two standard deviations from the number of atoms:

$$2\sigma_i = 2\sqrt{\frac{C_i(1-C_i)}{n_{tot}}} \quad (2.8)$$

Due to the high total number of atoms (several Mat), this variation for a single APT experiment is rather low. The more important value is the uncertainty between several APT experiments performed on the same CT RPV steel. For the global and matrix concentrations the uncertainty value for a single CT RPV steel is given by two standard deviations between average values measured in each condition:

$$2\sigma_{g,m} = 2\sqrt{\frac{\sum_{i=1}^{n}(C_i-\bar{C})^2}{n-1}} \quad (2.9)$$

where $\bar{C}$ is the mean concentration of given steel, *n* is the number of performed experiments.

Number of atoms for cluster core concentrations measurements is usually limited to hundreds of atoms. Concentration measurements with erosion and concentration profiles are performed inside small boxes containing dozens of atoms. For the latter three cases the uncertainty margins are calculated as two standard deviations from the number of identified atoms (Eq. 2.8).

Uncertainty of cluster number density is calculated as average number density (N_D^{Av}) divided by the square root of the number of identified clusters (n_{clust}):

$$2\sigma_{ND} = 2N_D^{Av}/\sqrt{n_{clust}} \quad (2.10)$$

In the case of cluster size (radius), the error margin is presented by one standard deviation between all identified clusters:

$$\sigma_r = \sqrt{\frac{\sum_{i=1}^{n}(R_i-\bar{R})^2}{n-1}} \quad (2.11)$$

3.3.2 Reconstruction parameters

The reconstruction of the initial position of the atom in the 3D-reconstruction is performed with an inverse projection model. It is known that the electric field between the specimen and the local electrode (LE) has an impact on the ion trajectories. Basically, evaporated ions will follow the electric field lines between the tip and the LE independently of the chemical nature of the ion.

To define the ions flight path, the point projection model is used. It assumes that ions are flying in straight lines ordinated from the projection point. This point is located behind the centre of hemispherical needle apex. To precisely reconstruct the initial position of atom the magnification of APT experiment (*G*) should be evaluated:

$$G = \frac{L}{(m+1)R_{tip}} \tag{2.12}$$

where L is the flight length, R_{tip} is the tip radius and $(m+1)$ or (ξ) is the image compression factor (ICF) [25].

The correlation between the initial position of the ion and the position of impact with a detector is dependent on the magnification, and equals:

$$X = \frac{X'}{G}; Y = \frac{Y'}{G} \tag{2.13,2.14}$$

where X' and Y' are the impact positions, and X and Y are the initial position of the atom on the tip. The depth coordinate Z is defined by the arrival order of ions on the detector. For each collected ion, a depth increment, ΔZ, is adjusted from the following equation:

$$\Delta Z = \frac{G^2 V_{at}}{Q S_d} \tag{2.15}$$

where V_{at} is the volume of one atom (1.17×10^{-29} m^3 for Fe), Q is the detection efficiency of the APT (36 % in the case of the LEAP 4000X HR), and S_d is the surface of the detector. The simplified scheme of the point projection model is presented in figure 22.

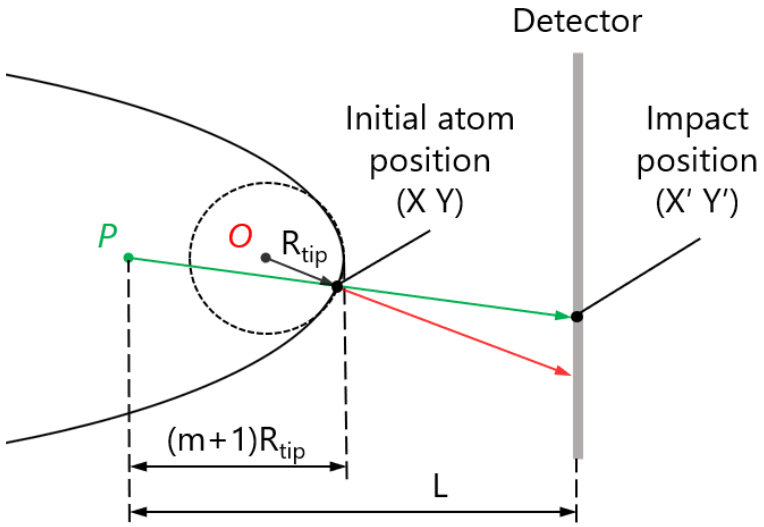

Figure 22. *The schematic view of the point projection model. O is the centre of the hemisphere cap. P is the projection point. The initial atom position (X Y) is identified from the impact point (X′ Y′) with the point projection model.*

The average flight length (L) is known for the selected APT instrument, 382 mm in the case of LEAP 4000X HR. The unknown parameters are the projection point position (P), which is set by the ICF, and the R_{tip} which can be derived from the voltage necessary to reach the suitable evaporation field:

$$R_{tip} = \frac{V}{E\ k_f} \tag{2.16}$$

E value for the RPV steel, which mostly contain Fe, equals 33 V/nm. The evaporation voltage for each ion is recorded. Therefore, only two parameters, ICF (ξ) and the field factor (k_f), need to be adjusted.

If no site-specific procedure was utilised, the analysis direction of the APT needle will have a random crystallographic orientation. The so-called ball model was proposed by Müller to explain the field ion microscope (FIM) images (Fig. 23.a). As we can see, the sharp APT sample exhibits facets and atomic planes with certain orientation, that can be identified. Since the APT detector is flat, the crystallographic orientations are represented in the form of quasi-stereographic projections. The poles can be identified with the desorption maps on the detector (Fig. 23.b). On desorption map of multiple events, high density of events on the poles and terraces are observed, the detailed reasoning of this phenomenon will be described further.

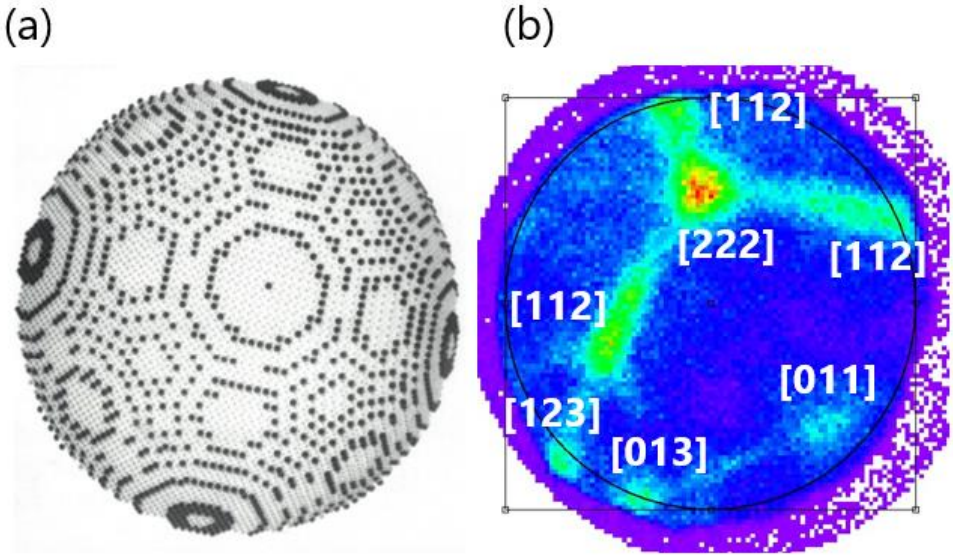

Figure 23. *(a) Ball model of the FIM or APT tip [28]. (b) The detector desorption map with multiple events shown. Crystallographic orientations can be identified.*

The image compression factor can be calculated by comparing the experimental and theoretical values between two crystallographic directions.

$$\xi = \frac{\theta_{theoretical}}{\theta_{observed}} \tag{2.17}$$

To determine the observed values, two poles on the detector map should be identified.

$$\theta_{obs} = arctan\frac{D}{L} \tag{2.18}$$

where *D* is the distance between two poles on the detector map and *L* is the distance between the tip and APT detector. The theoretical values are available in literature [25]. The average calculated value ξ for the RPV steels (prepared with FIB) is 1.73. In the case where only one pole was identified, the ICF = 1,65 reference mean value in the case of LEAP 4000X HR was utilised.

The next step is to evaluate the field factor k_f. The field factor expresses the tip shape and electrostatic environment imperfectness in comparison with the perfect hemisphere. In the present research it ranges from 4 to 7 in case of HV APT experiments, and around 3.5 for the experiment performed in the laser mode. If the k_f is wrong, the analysis volume will become elongated or compressed. If the volume is elongated or compressed, the interplanar distance will change. The interplanar spacing in specific Miller orientations for bcc iron lattice is well known. The most common poles observed are along [011], [002] and [222], with the following interplanar distances d_{011} = 0.203 nm, d_{002} = 0.143 nm, and d_{222} = 0.083 [25]. If k_f is correct, the measured interplanar spacing will be we same as the theoretical one (Fig. 24).

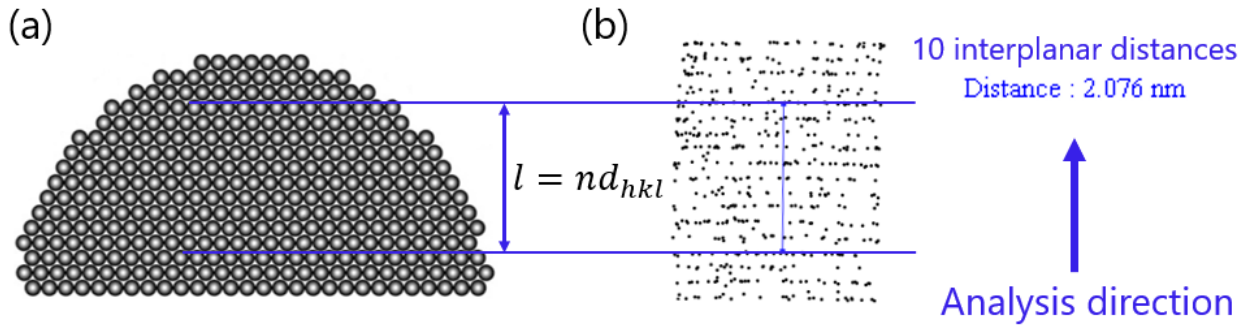

Figure 24. *(a) The schematic cross-section view of APT specimen. The atomic planes are visible [28]. (b) The section of APT volume from the RPV steel with [011] orientation. The interplanar distance of around 0.2 nm was measured.*

The shape factor is proportional to the square root of the interplanar distance. If the estimated shape factor value is wrong, the correct one can be calculated with this proportion:

$$k_f = k_{wrong}\sqrt{\frac{d_{hkl}^{theor}}{d_{hkl}^{wrong}}} \tag{2.18}$$

The average value of the field factor for the needles of RPV steel prepared with FIB equals 5.3. If the field factor was not possible to calculate, like in the case of carbide, this mean value was utilised for the reconstruction.

3.3.3 Cluster identification

The main focus of this part of the data treatment subchapter is the description of solute cluster identification and characterisation procedures. Thus, the first step is to identify these clusters.

Solute cluster formed during irradiation RPV steels could have rather low number density (~10^{22} m^{-3}), small size (diameter < 2 nm) and high Fe concertation (~80 at. %), and the cluster identification procedure in not straightforward. During cluster identification procedure all atoms at 14 a.m.u. range were identified as the main isotope of $^{28}Si^{++}$ which has an abundance of 92.2%. The peak at 29 a.m.u. was defined as main isotope of $^{58}Ni^{++}$. which has an abundance of around 68 %.

Solute clusters are expected to be enriched in Mn, Ni, Si, P and Cu. Initially, the cluster data treatment was performed separately for each of these solutes. In that case only small clusters containing about 5 solute atoms were found. Usually, these clusters had uncharacteristic elongated shape, and it was not possible to define if they were real ones or the APT artefacts (will be described in 3.3.4). Yet, as it was described in chapter I these solutes (Mn, Ni, Si, P, Cu) are segregating simultaneously driven by the flux of PDs. Therefore, all these elements were merged together and defined as new, "solute cluster" (SC) element (Fig. 25).

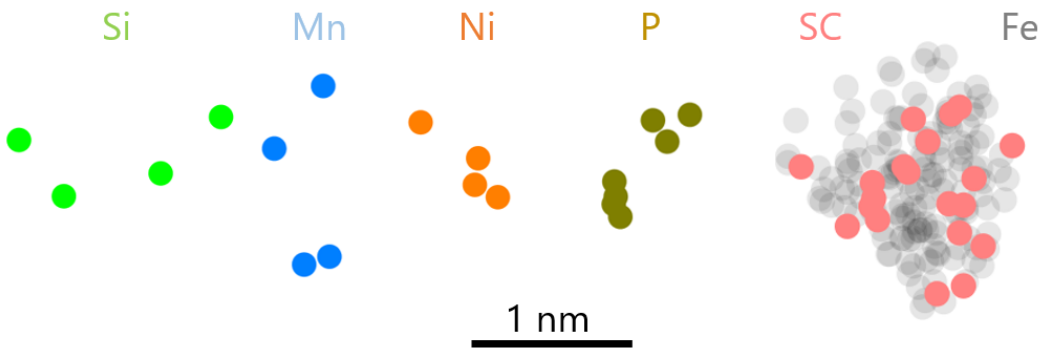

Figure 25. *Atom maps of solute cluster observed in CT RPV steel O. Si, Mi, Ni and P are combined as SC. Fe atoms assigned to cluster are also shown.*

In the case of high-Cu CT RPV steel W, Cu and Al were also found inside the clusters and were added as part of SC element for the cluster data treatment. The cluster identification procedure on the SC element was performed further.

There are two main methods for cluster identification: the maximum separation method (MSM) and the iso-position method (IPM). The latter one was employed. The method is capable to identify the local regions enriched in solutes. These regions could be the segregations on GBs or dislocation lines, solute clusters and precipitates. The detailed explanation of the iso-position method is derived in book written by Lefebvre, Vurpillot and Sauvage [38].

First, a 3D mesh with a step of 1 nm is created and the local chemical composition is calculated in each voxel (Eq. 7). Using a delocalization value of 0.5 nm and a tri-linear interpolation, a local composition is assigned to each atomic position. The same procedure is performed on the

volume with the same atom positions but a randomly assigned chemical nature. For the solute of interest, the distribution of concentrations in actual and randomised dataset are plotted (Fig. 26).

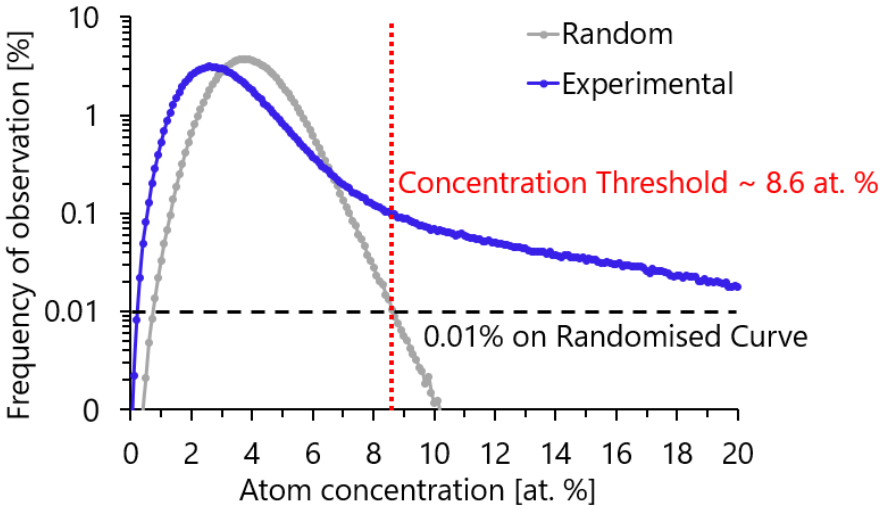

Figure 26. *The atom concentration histogram. Blue points are the actual volume. Grey points are the randomised dataset. The concentration threshold is selected from the data of the randomised dataset curve.*

The concentration threshold (C_{th}) corresponds to the concentration with a relative occurrence equal to 0.01% in the randomised dataset (Fig. 26). This approach allows to limit considering statistical fluctuation as potential cluster. The atoms with higher concentration than this threshold are filtered for further data treatment (Fig. 27). Concentration threshold is directly related to the global composition of solute elements. In CT RPV steels with higher global solute composition, C_{th} is higher. Also, C_{th} can slightly vary between several volumes of the same material due to local chemical heterogeneity.

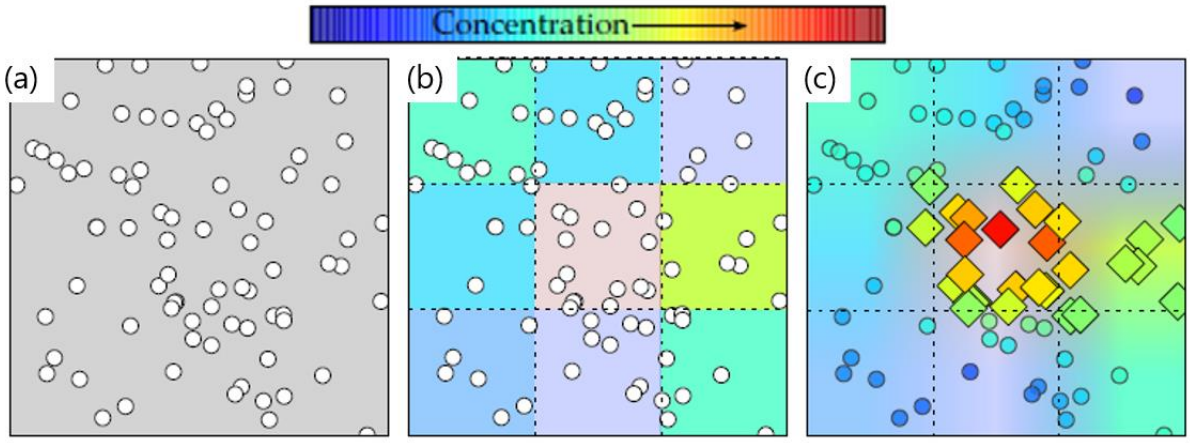

Figure 27. *The 2D schematic representation of the iso-position method. (a) White symbols are the solute atoms distributed in a volume. (b) The volume is divided into small boxes and concentration of each element inside each box is calculated. (c) These concentrations are assigned to each atom position. The positions with a concentration of given solutes above a user defined threshold (diamond symbols) are filtered for further analysis [24].*

Then, filtered atoms should be assigned to the clusters. The atomic distance or the envelope methods are utilised. In the atomic distance, the filtered atoms located closer than d_{max} to each other belong to the same cluster. In the envelope method, the volume is once again divided in a small grid and, if two neighbour boxes contain filtered solute atoms, atoms from these boxes are assigned to the same cluster. The following step for both methods is to select only the clusters with a total number of solute atoms above a user define number, N_{min} for further data treatment.

The last step is to define the interface between cluster and matrix, in order to calculate the cluster size, and the interface of the cluster core to measure the chemical composition (core composition). To do so, an erosion procedure is applied, in which cluster atoms at a distance larger than d_{ero} from the cluster / matrix interface are assigned to the matrix (Fig. 28). The d_{ero1} for the first erosion is set at the half-maximum value of the solute concentration in the cluster core. The d_{ero2} for the second erosion is set at the region where cluster composition saturates (plateau) [39,40]. To evaluate the half-maximum and plateau region precisely both erosion procedures should be performed on the clusters of the same size range. To do so, clusters are separated by the size classes and treated separately.

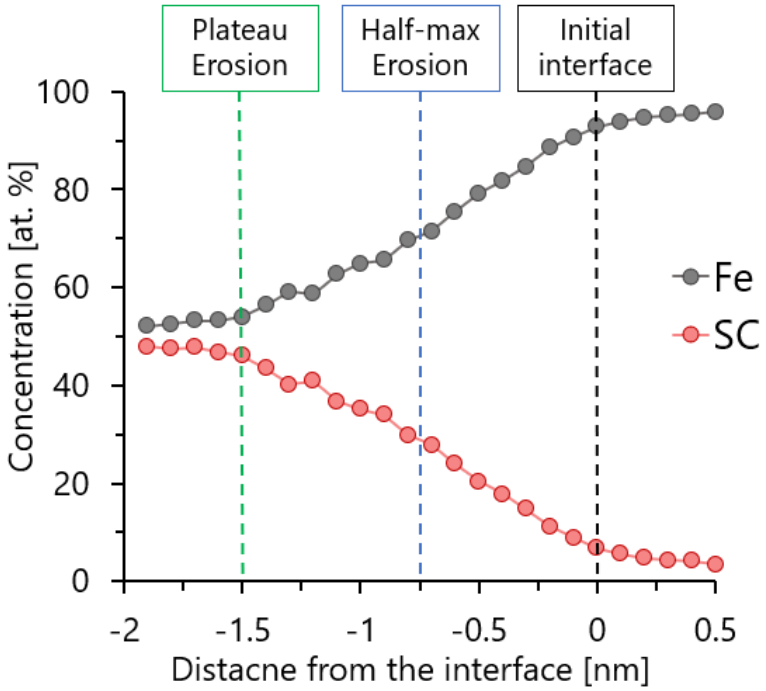

Figure 28. *Erosion profiles on clusters from steel W exported from GPM software. The black dashed line represents the matrix-cluster interface directly after identification. The blue dashed line sets the cluster interface to measure the cluster size. The green dashed line defines the cluster core for composition measurements.*

The results of cluster data mining are represented as:

- Number of clusters: N_c;
- Number of atoms in a single cluster: n_i;
- Total number of atoms in the clusters: n_c;
- Total number of atoms in the volume: n_{tot};
- Guinier radius: $R_g = \sqrt{\frac{5}{3}} R_{gyr}$; (2.20)
- Mass spectrum of the cluster cores.

With these data it is possible to calculate the following values:

- Equivalent spherical radius of the cluster: $R_{Eq} = \sqrt[3]{\frac{3 n_i V_{at}}{4\pi Q}}$; (2.21)
- Cluster number density: $N_D = \frac{N_c Q}{n_{tot} V_{at}}$; (2.22)
- Cluster volume fraction: $f_V = \frac{n_c}{n_{tot}}$; (2.23)
- Cluster core composition – with the peak decomposition procedure.

If the surface of identified solute cluster was in contact or cut by the border (edge) of APT volume it was defined as “edge cluster”. Edge clusters were excluded from the equivalent radius and core chemical composition measurements. Yet they have been included in the number density calculation as a half of a cluster and to the mole fraction calculations.

There is no ideal parameters for the cluster identification procedure. The variables are changing not only between different materials and irradiation conditions but also between two APT experiments from the same sample. The integrity of the cluster identification procedure is dependent on the set of these parameters and defined by the user. To be able to compare the results obtained by the various researches utilising different methods, a series of benchmarks were performed. From these benchmarks, the recommended guidelines for cluster identification procedure were created [40-45].

The parameters for the solute cluster identification procedure in RPV steels used in the current research are shown in the Table 4.

Table 4. *The set of parameters used for cluster identification.*

Filtering algorithm	Iso-position
Clustering method	Atomic distance
Clustering solutes in low-Cu steel	Mn, Ni, Si, P
Clustering solutes in high-Cu steel	Mn, Ni, Si, P, Cu, Al
Concentration threshold	5 – 9 %
d_{max} for atomic distance procedure	0.5 nm
N_{min} inside the cluster	8 – 12 solute atoms
d_{ero1} (for cluster size)	Up to 0.5 nm
d_{ero2} (for core composition)	Up to 1 nm

3.3.4 Artefacts

As shown previously, the reconstruction of the analysed volume is not straightforward and needs models and user-dependant parameters. Additionally, several artefacts can be observed, and if not treated properly can result in a wrong interpretation of the results.

One of the most common artefacts is the trajectory aberration or the local magnification effect. This process arises from the inhomogeneous distribution of the electric field at the vicinity of the tip surface. As we saw earlier with the ball tip model, the surface of the specimen consists of facets defined by the crystallography of the material. The electric field on the sample surface will be higher on the edges of the atomic rows since the kink atoms will protrude above the surface and have their own, lower radius of curvature, oriented not normal to the tip surface (Fig. 29). The local increment of electric field is express as the field enhancement factor ($\gamma = F_{local}/F$) as a ratio of a higher local field over the average field for the given radius of tip.

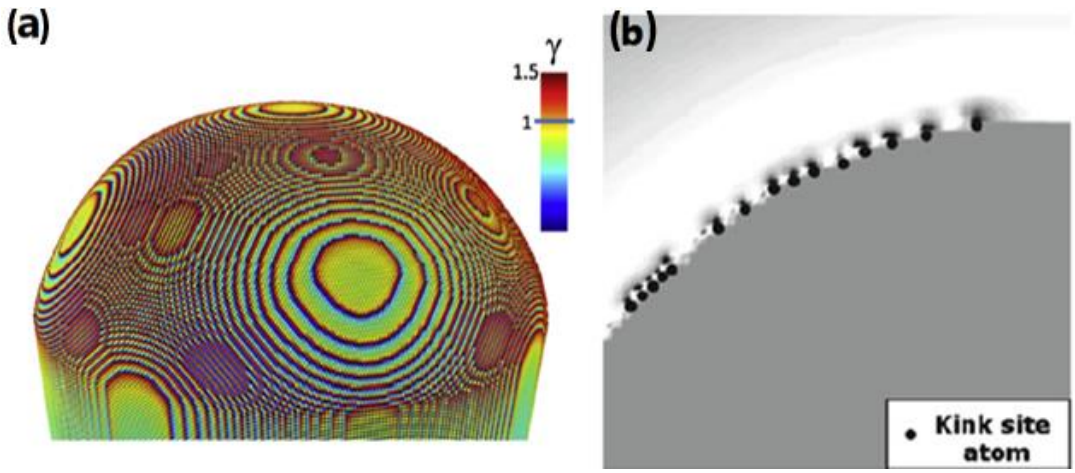

Figure 29. *(a) Distribution of the surface enhancement factor. Maximum enhancement factor of 1.5 is found above the atoms on the edge position of the crystalline terraces. (b) A simulation of the electric field around the kink atoms around the apex of the tip. Dark regions represent the higher field above the kink atoms [38].*

Because of the local variation of radius at the tip surface and orientation, the initial projection point will not be the same. And the ion trajectory will be modified. On the APT reconstruction, these artefacts are observed as zones with low atom density around the poles and zone lines.

The other type of artefacts is preferential evaporation or retention due to the different evaporation fields of different elements. The preferential evaporation of Cu in the case of RPV steel was already addressed earlier. In the case of preferential retention, the evaporation field of the elements is significantly higher than the average evaporation field applied to the tip (E_{Fe} = 33 V/nm in the case of RPV steel). Atoms of these elements will be partially retained at the surface and are susceptible to surface migration by the thermally assisted process. Usually, atoms will migrate on the surface upon reaching the pole or the zone lines, where the higher local evaporation field is observed, and further evaporate (Fig. 30). Typical elements subjected to the surface migration are small atoms like C, P, Si and S [46-49].

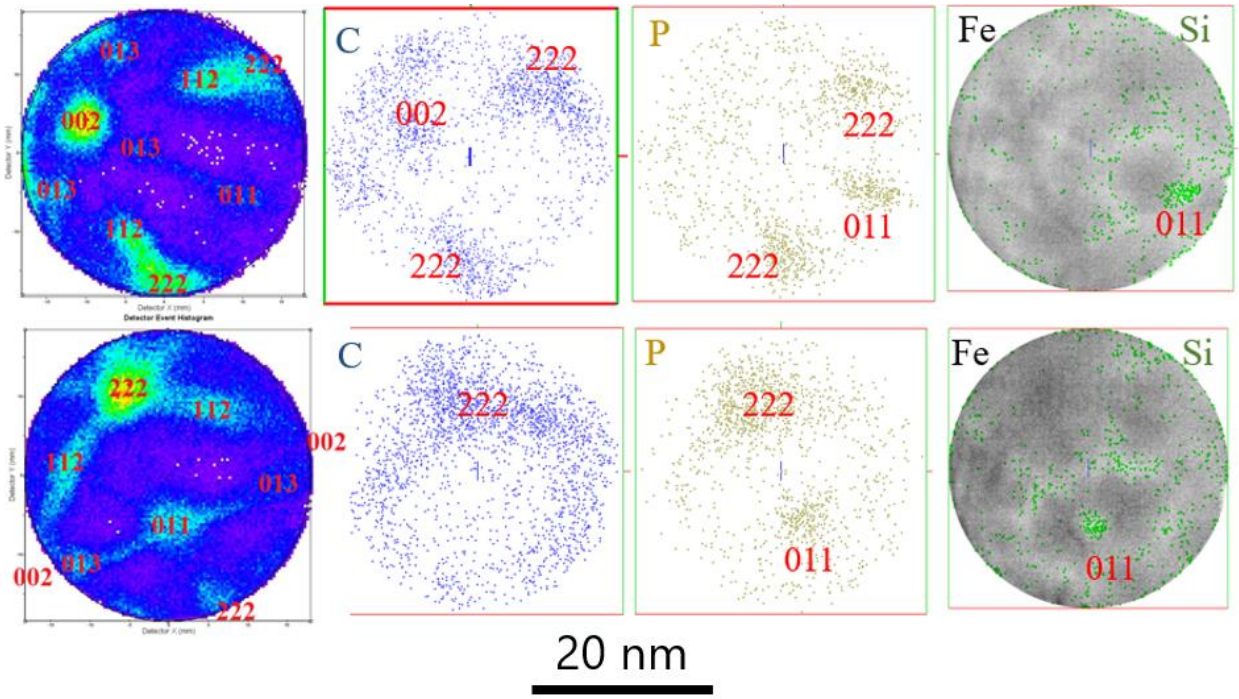

Figure 30. *The atom maps showing the high density of C, P and Si atoms at the poles and zone axis. The low-density regions on Fe maps on the right image are also evident. These APT experiments were performed on non-irradiated RPV steels.*

Si and P are known to form solute clusters in RPV steels under irradiation. Therefore, the spatial distribution of these elements should be measured as precisely as possible. In the case of APT experiments in the laser mode, the phenomenon of surface migration is more pronounced due to heat up of the specimen [46]. Hence, to limit the possible artefacts, the HV mode was preferred. Still, surface migration of Si and P is observed and complicates the cluster identification procedure.

Both Si and P were found as a part of Mn-Ni-Si-P clusters. Si and P atoms are combined into the SC elements for the cluster data treatment and their presence brings bias to cluster identification procedure, even though Mn and Ni are not taking part in surface migration. The artificial high density of these elements around the poles can be identified as cluster by the cluster identification algorithms (Fig. 31) [48]. These clusters should be manually removed during data treatment.

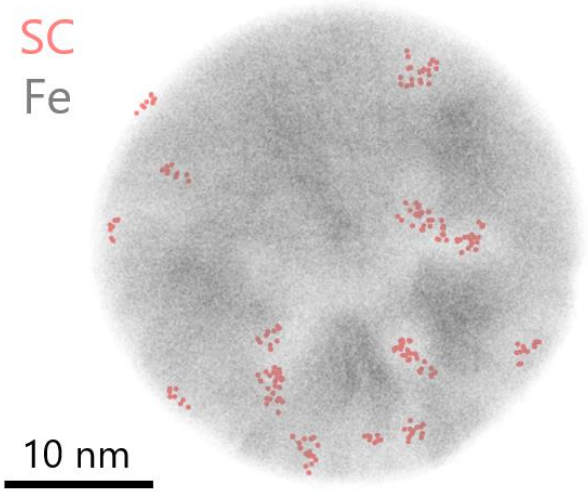

Figure 31. *Artefact Mn-Ni-Si-P cluster identified alongside the poles and zone lines in the non-irradiated steel O. C_{th} = 6.6 %, N_{min} = 8 SC atoms. The low Fe density at poles and zone lines is evident.*

The last but not least artefact is the local magnification due to the difference in the evaporation field between cluster or precipitate and the matrix [50-52]. In the case of low evaporation field clusters, trajectory focusing occurs. Atoms of the low field feature will evaporate before the matrix ones, resulting in the flattering on the surface and in the change on the local shape of the tip. The trajectory atoms into clusters or their close vicinity will be modified. They will be projected towards the centre of the particle. The result is that cluster will appear compressed in directions perpendicular to the analysis one, and some matrix atoms can be artificially introduced into the cluster. Both phenomena result in a higher atomic density inside the particle (Fig. 32.a). In the case of the high field features, the defocusing effect is observed. Atoms will retain on the surface and the cluster will protrude on top of the sample almost like the kink atoms. The ion trajectory of the cluster atoms will be directed out from the cluster centre and the atomic density inside the cluster will be reduced (Fig. 32.b).

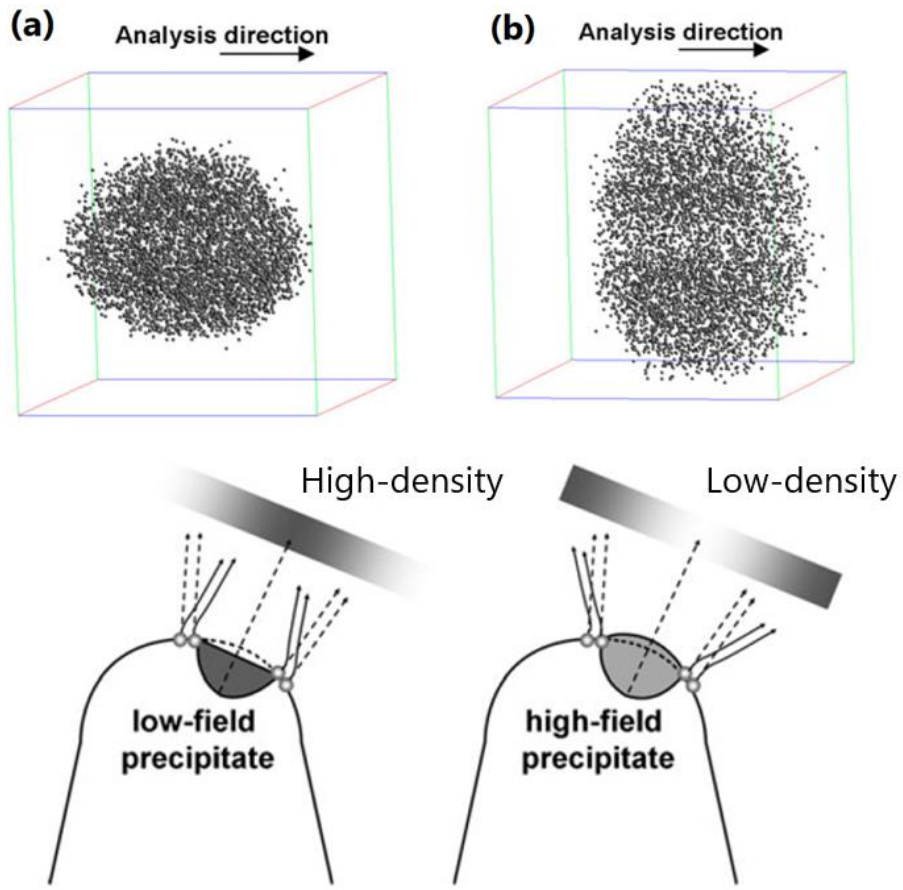

Figure 32. *(a) Simulated reconstruction of a low field precipitate. The lateral compression (X and Y dimensions) is observed. (b) Simulated reconstruction of the high field precipitate. The precipitate is dilatated in the directions normal to the analysis direction [25, 51].*

For example, CEFs observed in irradiated RPV steels are low field features. To avoid size miscalculation, the equivalent spherical radius of solute clusters was calculated.

3.3.5 Chemical composition of solute clusters

One of the highly debatable questions inside the APT community is the presence of Fe inside the solute clusters or precipitates. Japanese [53,54] and French [55,56] researchers are counting Fe atoms as a part of solute clusters. Researchers from USA are usually identifying Fe atoms as an APT artefact and exclude them form the chemical composition measurements [57-59].

A chemical composition correction (CCC) model to quantify the bias in the chemical composition measurement due to the local magnification effects was developed by Hatzoglou and co-workers [60-62]. In the CCC model the APT bias is evaluated by changes of cluster shape and atomic density inside the cluster. CCC model was successfully utilised on the cubic and spherical clusters.

To account for the local magnification effect of low-field features, such as CEFs in the case of RPV steels, the shape factor (S) should be calculated:

$$S = \frac{XY}{Z^2} \tag{2.24}$$

Where Z is the dimension of cluster in the evaporation direction and X and Y are the dimensions oriented normal to the evaporation direction. The depth resolution (below 0.1 nm) in APT experiments is more precise than the lateral one (0.5 to 1 nm) and shall not be affected by the local magnification effects. The shape factor represents the artificial compression or dilution of cluster. The shape factor of perfect spherical cluster equals to one. If $S > 1$ cluster is dilated in the directions normal to the evaporation direction and if $S < 1$ cluster is compressed.

The next step is to evaluate the reduced density inside the cluster (ρ). To do so a cylindrical concentration profile with a radius (R_p) should be plotted through the cluster. N_b is the total number of atoms evaluated as part of cluster, d_p is the thickness of one slice of the cylinder, for the depth concentration measurements, N is the total number of slices through the cluster (Fig. 33). The reduced density is given by:

$$\rho = \frac{V_{at}}{Q} \mathrm{x} \frac{N_b}{N d_p \pi R_p^2} \tag{2.25}$$

If the calculated reduced density is bigger than one ($\rho > 1$), the atomic density inside the cluster is bigger than in the surrounding matrix, if contrary ($\rho < 1$), the density is lower than the matrix one.

There are two possible APT artefacts caused by the local magnification effect, the focusing of the atom trajectories and the mixing of the cluster and matrix atoms. If both artefacts affect the solute cluster, the composition bias can be evaluated with the following equation:

$$\rho = \frac{1}{S}\left(1 + \frac{C_{APT} - C_{Real}}{C_{Mat} - C_{APT}}\right) \tag{2.26}$$

where C_{APT} is the measured solute concentration by APT, C_{Mat} is the matrix one and C_{Real} is the cluster solute concentration without bias. If cluster is affected by only atom trajectory focusing, with no matrix mixing, C_{APT} will be equal to C_{Real}, and equation 2.26 becomes:

$$\rho = \frac{1}{S} \tag{2.27}$$

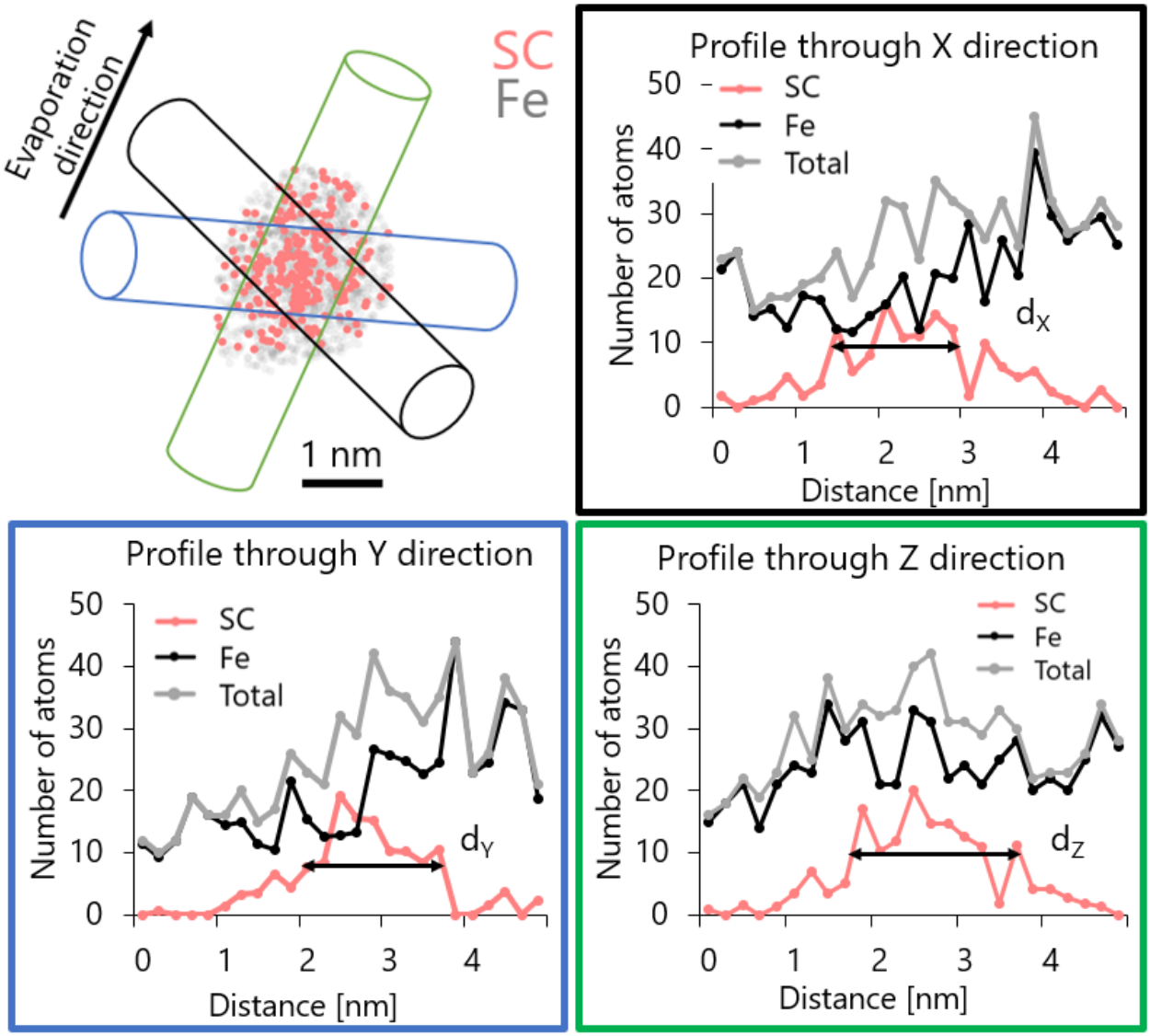

Figure 33. *The cylindrical profiles plotted through the cluster to estimate the size of cluster and reduced density in each direction (X, Y, Z). Radius of the cylinder for selected volume is 0.7 nm, d_p is 0.2 nm. The charts outline colours are representing to which cylinder graph is referred. The cluster size in each direction was calculated at the half-maximum of solute concentration.*

The reduced density and shape factor were calculated for 22 clusters from several RPV steels in which ellipsoidal cluster shape was observed. Cylinders with a radius of 0.7 nm were used. From the cylindrical profiles, the precise size of clusters in each direction was evaluated at the half-maximum of solute concentration. Results are presented in Table 5 and in figure 34.

Table 5. *The shape factor (S) and reduced density (ρ) of the solute clusters found in the chemically-tailored RPV steels. The uncertainty values are given by two standard deviations.*

ID	Number of clusters	S	ρ	ρS
F28	10	0.6 ± 0.4	1.8 ± 0.8	1.0 ± 0.7
I19	6	0.6 ± 0.3	1.7 ± 0.6	0.8 ± 0.4
W28	8	0.5 ± 0.3	2.0 ± 0.8	1.0 ± 0.6

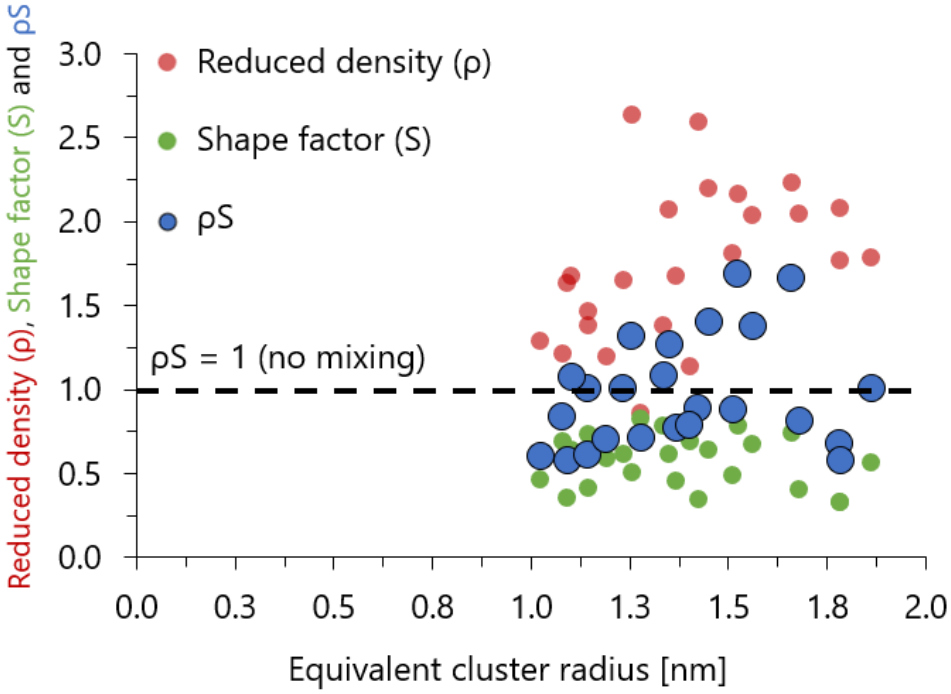

Figure 34. *Result of CCC model on CT RPV steels. The shape factor (S) is presented in green, reduced density (ρ) is presented in red and their multiplication (ρS) is presented in blue. Clusters on the ρS = 1 line are affected only by the atom focusing with no composition bias. Clusters above and below the ρS = 1 line are affected by both focusing and mixing.*

The results obtained with CCC model on the RPV steels studied in the current project have a dispersion and show that most of solute clusters are affected by only trajectory focusing and some clusters are affected by both trajectory focusing and atom mixing. Applying the composition correction from Eq. 2.27 resulted in decrease of Fe concentration inside the clusters by only ~4 at. %. Due to complexity of correction procedure and the small difference in obtained values, the initial cluster composition including Fe will be presented. Equivalent cluster size will be calculated including Fe atoms as a part of solute clusters.

Summary

During the operation of NPP, neutrons produced by nuclear fission in the reactor core can interact with RPV steel, resulting in formation of solute clusters and precipitates. These precipitates and clusters act as barriers for dislocation movement, resulting in the hardening and the embrittlement of material. To study these detrimental processes seven chemically-tailored RPV steels with various compositions divided into four groups were selected. First group to study the effect of P content and its synergy with Cu. Second to evaluate the effect of Mn. Third to account for the effect of Ni and Mn/Ni synergy. Finally, fourth one to measure the combined effect of high concentrations of Cu, P, Mn, Ni. These steels were irradiated at 290 °C inside the BR2 MTR at high flux conditions (from 1 to 2.5 x 10^{17} n/m^{2}s, E > 1 MeV) up to three doses of around 0.06, 0.08 and 0.13 dpa, which represents doses obtained during 25, 30 and 50 years of operation in commercial NPPs.

The irradiation hardening was measured with tensile tests at room temperature. The experiments on the irradiated specimens were performed inside hot cells at the Belgium Nuclear Research Centre SCK CEN at Mol.

Solute clusters and precipitates formed under neutron irradiation were studied and characterised by Atom Probe Tomography. The typical number density of SCs range from 10^{22} to 10^{24} m^{-3} and their sizes range from 1 to 3 nm in diameter. The APT experiments were performed inside controlled area within the GENESIS platform at GPM laboratory. Strict safety measurements to prevent contamination and to limit exposure were developed and utilised.

APT was proven to be the best analysis technique to characterise the small solute clusters, however great care should be taken to account for limitations of the technique. APT allows to obtain the following information about solute clusters: number density, size and chemical composition. The following issues and experimental artefacts were acknowledged and corrected:

- Correction of chemical composition (mass spectrum deconvolution);
- Cu concentration correction (due to preferential evaporation);
- Wrong cluster identification (due to surface migration);
- Cluster chemical composition measurements (CCC model).

APT experimental results collected on the chemically-tailored RPV steels are presented and described in Chapter III.

References

1. R. Chaouadi. RADAMO Database: Available Irradiated RPV Materials for Advanced Microstructural Investigations, SCK CEN restricted report 27710469, T-0093

2. R. Chaouadi, R. Gérard, E. Stergar, W. Van Renterghem. Journal of Nuclear Materials 519 (2019): 188–204. https://doi.org/10.1016/j.jnucmat.2019.03.030

3. W Van Renterghem, E. Stergar, R. Chaouadi. Effect of Nickel–Manganese Concentration on the Microstructure of Chemically-Tailored RPV Steels, SCK CEN restricted report 26724015, R-6490

4. H. K. D. H. Bhadeshia. Bainite in Steels: Theory and Practice. Third edition. Leeds, UK: Maney Publishing, 2015. ISBN 9781909662742

5. S. Zajac, V. Schwinn, K. H. Tacke. Materials Science Forum Vols. 500-501 (2005): 387–394. https://doi:10.4028/www.scientific.net/msf.500-501.387.

6. M. Müller, D. Britz, L. Ulrich, T. Staudt, F. Mücklich. Metals 10 (2020): 630. https://doi:10.3390/met10050630

7. A. Stahlkrantz, P. Hedstrom, N. Sarius, H. Sundberg, S. Kahl, M. Thuvander. Metallurgical and Materials Transactions A 51 (2020): 6470-6481. https://doi: 10.1007/s11661-020-06030-6

8. N. Soneda (Ed.). Irradiation Embrittlement of Reactor Pressure Vessels (RPVs) in Nuclear Power Plants. Elsevier (2015). https://doi.org/10.1016/C2013-0-17428-4

9. H. Liu, Q. Li. Materials Science and Engineering 490 (2019): 022019. doi:10.1088/1757-899x/490/2/022019

10. L. Vermeeren, J. Dekeyser, P. Gouat, S. Kalcheva, E. Koonen, V. Kuzminov, A. Veowimp, M. Weber. SCK CEN Reports, No. BLG-1006. https://publications.sckcen.be/portal/files/279253/BLG1006.pdf

11. S. Van Dyck, E. Koonen, M. Verwerft, M. Wéber. IAEA-TM-38728 (2010). https://www-pub.iaea.org/MTCD/Publications/PDF/SupplementaryMaterials/TECDOC_1713_CD/template-cd/datasets/Personnel/VanDyck.html

12. G.R. Odette, G.E Lucas. The Effect of Nickel on Irradiation Hardening of Pressure Vessel Steels. United States: ASTM (1990).

13. M. Ghiath. Journal of Nuclear Materials 508 (2018): 609–27. https://doi.org/10.1016/j.jnucmat.2018.06.020

14. S. Queyreau, G. Monnet, B. Devincre. Acta Materialia 58 (2010): 5586–95. https://doi.org/10.1016/j.actamat.2010.06.028

15. L. Giannuzzi, F. Stevie (Eds.). Introduction to Focused Ion Beams: Instrumentation, Theory, Techniques, and Practice. New York: Springer, (2005). ISBN 9780387233130

16. N. Yao (Ed.). Focused Ion Beam Systems: Basics and Applications. Cambridge: Cambridge University Press (2007). https://doi:10.1017/CBO9780511600302

17. K. Thompson, D. Lawrence, D. J. Larson, D. Olson, T. Kelly, B. Gorman. Ultramicroscopy 107 (2007): 131–139. https://doi.org/10.1016/j.ultramic.2006.06.008

18. A. Ul-Hamid. A Beginners' Guide to Scanning Electron Microscopy. Springer International Publishing (2018). https://doi.org/10.1007/978-3-319-98482-7

19. S. Kalacska, Z. Dankhazi, G. Zilahi, X. Maeder, J. Michler, P. Ispanovity, I. Groma. Materials Science and Engineering A 770 (2020): 138499. https://doi.org/10.1016/j.msea.2019.138499

20. A. Schwartz, M. Kumar, B. Adams, D. Field (Eds.). Electron Backscatter Diffraction in Materials Science (2009). https://doi.org /10.1007/978-0-387-88136-2

21. Website of the Oxford Instruments, EBSD Explained. http://www.ebsd.com/10-ebsd-explained

22. M. Hernandez-Mayoral, D. Gomez-Briceno. Journal of Nuclear Materials 399 (2010): 146-153. https://doi.org/10.1016/j.jnucmat.2009.11.013

23. P.D. Edmondson, C.M. Parish, R.K. Nanstad. Acta Materialia 134 (2017): 31–39. https://doi.org/10.1016/j.actamat.2017.05.043

24. A. Wagner. Dissertation 'Long-term irradiation effects on reactor-pressure vessel steels'. (2015): 131. https://www.hzdr.de/FWR/DOCS/Publications/Dissertation_Arne_Wagner.pdf

25. B. Gault, M. Moody, J. Cairney, S. Ringer. Atom Probe Microscopy, Springer Series in Materials Science, Springer New York (2012). https://doi.org/10.1007/978-1-4614-3436-8

26. D.J. Larson, T. Prosa, R. Ulfig, B. Geiser, T. Kelly. Local Electrode Atom Probe Tomography, Springer New York (2013). https://doi.org/10.1007/978-1-4614-8721-0

27. M.K. Miller. Atom Probe Tomography. Springer US (2000). https://doi.org/10.1007/978-1-4615-4281-0

28. M.K. Miller, R. G. Forbes. Atom-Probe Tomography, Springer US (2014). https://doi.org/10.1007/978-1-4899-7430-3

29. B. Gault. Applied Microscopy 46 (2016): 117-26. http://dx.doi.org/10.9729/AM.2016.46.3.117

30. W. Yi. Journal of Vacuum Science & Technology B 19 (2001): 2247. https://doi.org/10.1116/1.1420206

31. MyScope Online Microscopy Training. Microscopy Australia. https://myscope.training/

32. C. Hatzoglou, S. Rouland, B. Radiguet, A. Etienne, G. Da Costa, X. Sauvage, P. Pareige, F. Vurpillot. Microscopy and Microanalysis 26 (2020): 689–98. https://doi.org/10.1017/S1431927620001749

33. J.M. Hyde, M.G. Burke, B. Gault, D. Saxey, P.D. Styman, K. Wilford, T. Williams. Ultramicroscopy 111 (2011): 676–682. https://doi.org/10.1016/j.ultramic.2010.12.033

34. J.M. Hyde, G. Sha, E.A. Marquis, A. Morley, K. Wilford, T. Williams. Ultramicroscopy 111 (2011): 664–71. https://doi.org/10.1016/j.ultramic.2010.12.030

35. M. Perez, F. Perrard, V. Massardier, X. Kleber, A. Deschamps, H. de Monestrol, P. Pareige, G. Covarel. Philosophical Magazine 85 (005): 2197–2210. https://doi.org/10.1080/14786430500079645

36. J. Takahashi, K. Kawakami. Surface and Interface Analysis 46 (2014): 535–43. https://doi.org/10.1002/sia.5555

37. T. Prosa, S. Strennen, D. Olson, D. Lawrence, and D.J. Larson. Microscopy and Microanalysis 25 (2019): 425–37. https://doi.org/10.1017/S1431927618015258

38. W. Lefebvre-Ulrikson (Ed.). Atom Probe Tomography: Put Theory into Practice. London, Academic Press (2016). ISBN 9780128047453

39. D. Vaumousse, A. Cerezo, P. Warren. Ultramicroscopy 95 (003): 215–21. https://doi.org/10.1016/S0304-3991(02)00319-4

40. B. Radiguet - Atom probe tomography benchmark on RPV steels: synthesis of obtained results, Technical note. 6125-4501-2019-02130-EN

41. R. Kolli, and D. Seidman. Microscopy and Microanalysis 13 (2007): 272–84. https://doi.org/10.1017/S1431927607070675

42. P.D. Styman, J.M. Hyde, K. Wilford, G. Smith. Ultramicroscopy 132 (2013): 258–64. https://doi.org/10.1016/j.ultramic.2012.12.003

43. J.M. Hyde, G. DaCosta, C. Hatzoglou, H. Weekes, B. Radiguet, P. D. Styman, F. Vurpillot, et al. Microscopy and Microanalysis 23 (2017) 366–75. https://doi.org/10.1017/S1431927616012678

44. E.A. Marquis, V. Araullo-Peters, Y. Dong, A. Etienne, S. Fedotova, K.Fujii, K.Fukuya, et al. The Minerals, Metals & Materials Series (2019) 2097–2113. https://doi.org/10.1007/978-3-030-04639-2_141

45. Y. Dong, A. Etienne, A. Frolov, S. Fedotova, K. Fujii, K. Fukuya, C. Hatzoglou, et al. Microscopy and Microanalysis 25 (2019) 356–66. https://doi.org/10.1017/S1431927618015581

46. B. Gault, M. Müller, A. La Fontaine, M. Moody, A. Shariq, A. Cerezo, S. Ringer, G. D. W. Smith. Journal of Applied Physics 108 (2010) 044904. https://doi.org/10.1063/1.3462399

47. L. Yao, B. Gault, J. Cairney, S. Ringer. Philosophical Magazine Letters 90 (2010) 121–29. https://doi.org/10.1080/09500830903472997

48. L. Stephenson, M. Moody, P. Liddicoat, S. Ringer. Microscopy and Microanalysis 13 (2007) 448–63. https://doi.org/10.1017/S1431927607070900

49. B. Gault, F. Danoix, K. Hoummada, D. Mangelinck, H. Leitner. Ultramicroscopy 113 (2012) 182–91. https://doi.org/10.1016/j.ultramic.2011.06.005

50. D, Blavette, F. Vurpillot, P. Pareige, A. Menand. Ultramicroscopy 89 (2001): 145–53. https://doi.org/10.1016/S0304-3991(01)00120-6

51. T. Philippe, M. Gruber, F. Vurpillot, D. Blavette. Microscopy and Microanalysis 16 (2010): 643–48. https://doi.org/10.1017/S1431927610000449

52. E.A. Marquis, J.M. Hyde. Materials Science and Engineering R 69 (2010): 37–62. https://doi.org/10.1016/j.mser.2010.05.001

53. T. Takeuchi, A. Kuramoto, J. Kameda, T. Toyama, Y. Nagai, M. Hasegawa, K. Onizawa et al. Journal of Nuclear Materials 402 (2010): 93–101. https://doi.org/10.1016/j.jnucmat.2010.04.008

54. L. Liu, K. Nishida, K. Dohi, A. Nomoto, N. Soneda, K. Murakami, Z. Li, D. Chen, N. Sekimura. Journal of Nuclear Science and Technology 53 (2016): 1546–53. https://doi.org/10.1080/00223131.2015.1136902

55. H. Huang, B. Radiguet, P. Todeschini, G. Chas, P. Pareige. MRS Proceedings 1264 (2010): 1264-BB05-18. https://doi.org/10.1557/PROC-1264-BB05-18

56. E. Meslin, B. Radiguet, P. Pareige, A. Barbu. Journal of Nuclear Materials 399 (2010): 137–45. https://doi.org/10.1016/j.jnucmat.2009.11.012

57. N. Almirall, P. Wells, T. Yamamoto, K. Yabuuchi, A. Kimura, and G.R. Odette. Journal of Nuclear Materials 536 (2020): 152173. https://doi.org/10.1016/j.jnucmat.2020.152173

58. P. Wells, T. Yamamoto, B. Miller, T. Milot, J. Cole, Y. Wu, G.R. Odette. Acta Materialia 80 (2014): 205–19. https://doi.org/10.1016/j.actamat.2014.07.040

59. P.D. Edmondson, C.M. Parish, R.K. Nanstad. Acta Materialia 134 (2017): 31–39. https://doi.org/10.1016/j.actamat.2017.05.043

60. C. Hatzoglou, B. Radiguet, G. Da Costa, P. Pareige, M. Roussel, M. Hernandez-Mayoral, C. Pareige. Journal of Nuclear Materials 522 (2019): 64–73. https://doi.org/10.1016/j.jnucmat.2019.05.022

61. C. Hatzoglou, B. Radiguet, P. Pareige. Journal of Nuclear Materials 492 (2017): 279-291. https://doi.org/10.1016/j.jnucmat.2017.05.008

62. C. Hatzoglou, B. Radiguet, F. Vurpillot, P. Pareige. Journal of Nuclear Materials 505 (2018): 240-248. https://doi.org/10.1016/j.jnucmat.2018.03.057

Chapter III: Microstructure characterisation of chemically-tailored steels

In the present chapter, the results of microstructure investigation on chemically-tailored RPV steels at the micro and nano scales are described. Microstructure investigation was performed in non-irradiated state (reference materials) and after neutron irradiation up to doses ranging from 0.06 to 0.14 dpa. Irradiation doses represent values accumulated during 20 to 50 years in commercial RPV steels. EBSD analyses were performed on the reference materials. Global and matrix chemical compositions were measured with APT. Cluster identification procedure was performed on materials in both reference and irradiated states. Number density, size and chemical composition of solute clusters were evaluated from APT experiments.

To evaluate the effect of irradiation, the nominal solute concentration will be represented by the matrix values measured by APT in the non-irradiated state. The amount of solutes at grain boundaries and carbides is excluded since atoms from these regions are not expected to take part in intragranular solute cluster formation under irradiation.

Several (4) experiments were performed in the laser-assisted APT mode to increase the yield of experiments and to obtain more data. Cluster number density and size measured in these experiments are in good agreement with results obtained by APT in HV mode. Yet, lower P global concentration was measured. Also, a more pronounced effect of Si and P surface migration is known in the experiments in laser mode. To limit these biases, only the information about cluster number density and size from the experiments in laser mode is utilised. Composition measurements from these four experiments are not included.

Detailed information about every APT experiment performed on the irradiated materials is given in appendix B.3. In the present chapter, results of APT study on chemically-tailored RPV steels are presented. Therefore, to simplify the text, term “chemically-tailored RPV” won’t be written.

1 Microstructure characterisation in non-irradiated state

An accurate description of the initial microstructure (reference materials) is essential to identify the irradiation ageing mechanisms. Data collected on the reference materials are compared with microstructure observed in irradiated states. Two main techniques were used to fulfil this goal. EBSD was utilised to study microstructure at the microscale, and APT was utilised to study microstructure at the nanoscale.

1.1 Microstructure characterisation at the microscale

Structural characteristics at the microscale, such as grain size, grain shape, phase composition, dislocation density contribute to mechanical properties of metals. Chemically-tailored RPV steels were forged following the ASTM standard of A533B RPV steel. Microstructure was studied with optical microscopy at SCK CEN and with EBSD at GPM Rouen. The bainitic microstructure was identified [1]. It is composed of ferrite laths and carbides distributed inside and between grains. EBSD maps on steels in the reference state are reported in figure 1.

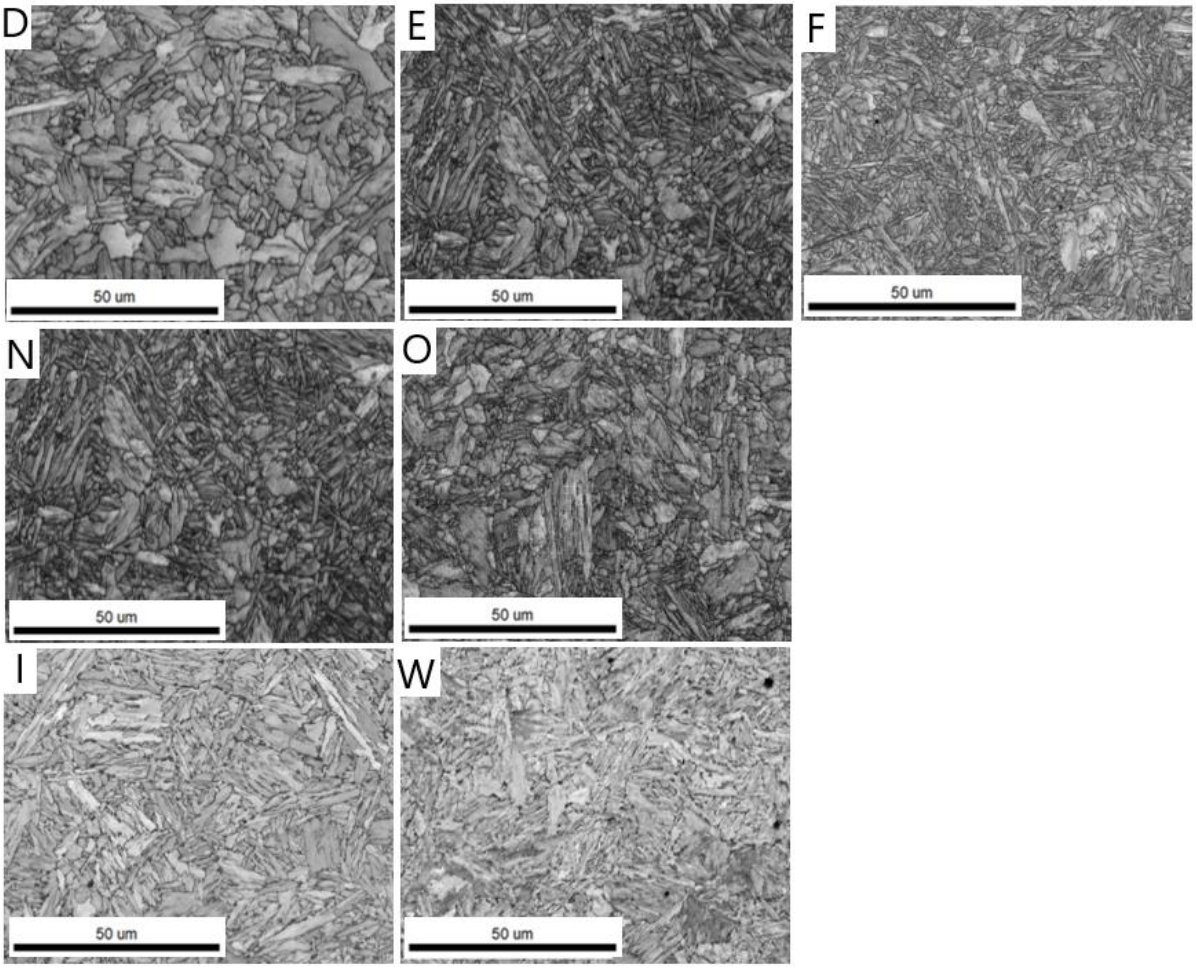

Figure 1. *Typical microstructure of steels D, E, F, I, N, O and W presented with image quality (IQ) EBSD maps. Bright areas are thin ferrite laths. Dark areas are GBs and carbides distributed in between and inside laths [2].*

As it was described in chapter II.1.2, a structure called degenerated bainite can form during thermomechanical treatment of low-alloyed ferritic steels. In that case, additionally to carbides, a second feature, called M/A (martensite/austenite) constituents, can form [3,4]. To identify the presence of M/A constitutes, EBSD analysis on ferrite, martensite and austenite phases was performed. Mostly ferritic phase was observed with EBSD phase identification. In most of the studied materials (D, E, F, N, O), ferrite has an acicular or lath morphology, typical for bainitic materials [5,6]. Yet, EBSD analysis on high-Ni/high-Mn steel I, revealed the presence of austenite (Fig. 2).

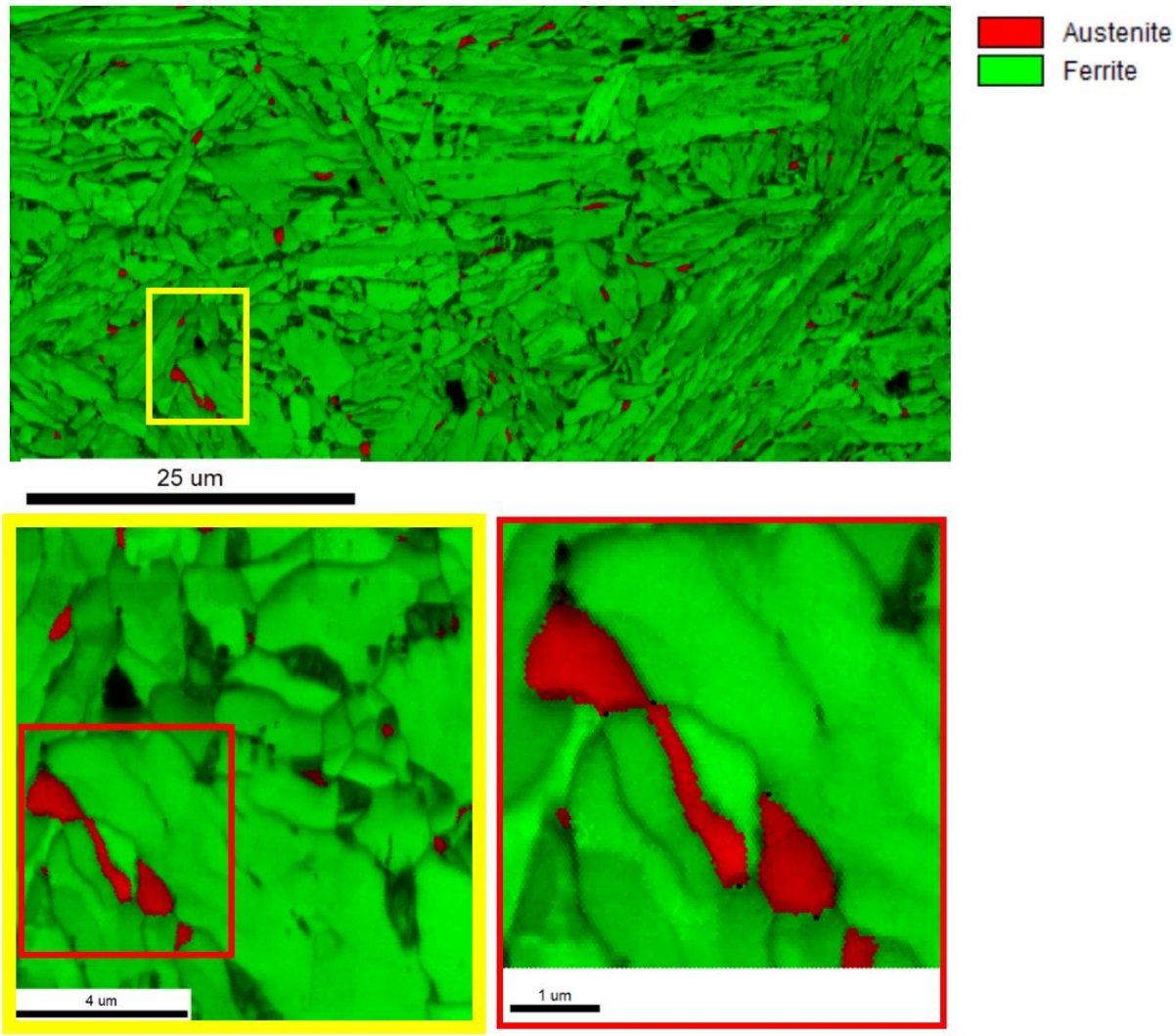

Figure 2. *Phase map of high-Mn/Ni steel I. Red areas are austenite phase. Green areas are ferrite phase. Step size of EBSD map is 50 nm.*

In the high-Cu, high-P, high-Ni, high-Mn (high-solutes) steel W, austenite phase is also observed (Fig. 3). In the separate TEM study on steels I and W performed at SCK CEN by Dr. Wouter Van Renterghem, austenitic phase was also identified [7].

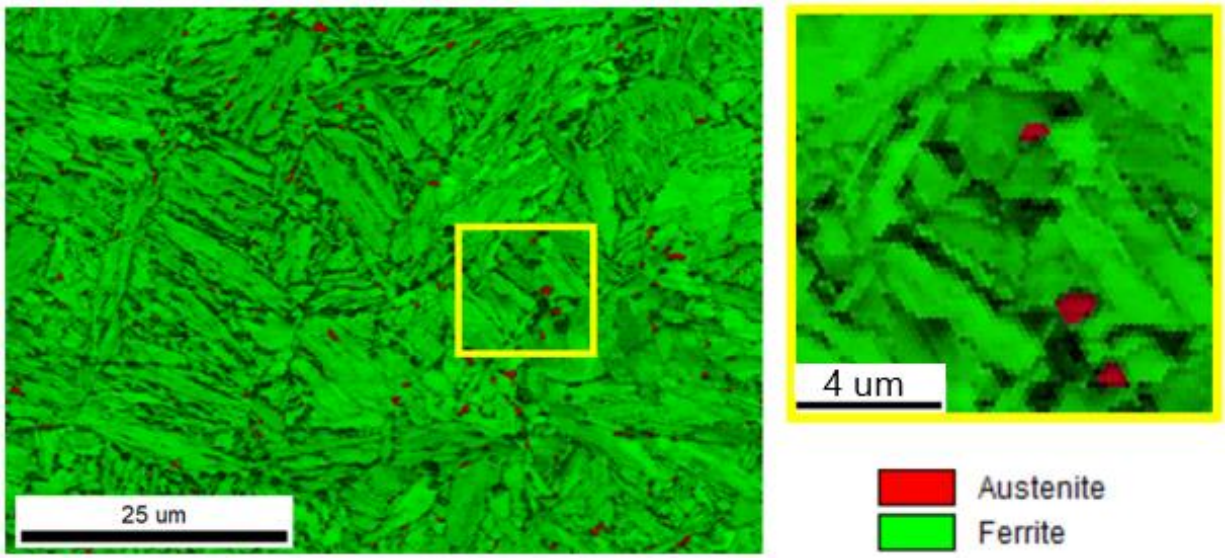

Figure 3. *Phase map of high-solutes steel W. Red areas are austenite phase. Green areas are ferrite phase. Step size of EBSD map is 300 nm.*

Due to the presence of a small fraction of austenitic phase, the conclusion was made that steels I and W have a partially degenerated bainitic structure. The significant difference of steels I and W from other steels studied here is the high concentration of Ni and Mn, which are austenite stabilisers. Unfortunately, information about the cooling rate during quenching procedure was not recorded, therefore it is complicated to understand what resulted in the presence of residual austenitic phase in these materials. The probable explanation is that the selected tempering temperature (665 °C) is too close to eutectoid temperature (A_1 ~ 730 °C), which in reality could be even lower due to the high Mn (~1.8 at. %) and Ni (~1.6 at. %) contents (austenite-stabilisers) [1]. The austenite volume fraction measured with EBSD is low (~0.7 %), and both steels I and W mostly exhibit ferritic lath structure.

Microstructure of steels is mostly composed of upper bainite which is formed by ferrite laths with interlath carbides. Information about grain orientation was also collected with EBSD. The distribution of misorientation angles in steel E, F, I, N, O and W follows the tendency for the upper bainite observed in the literature (Fig. 4.a) [5,6]. In the case of steel D, the misorientation angle distribution is similar to the one observed in granular bainite (Fig. 4.b).

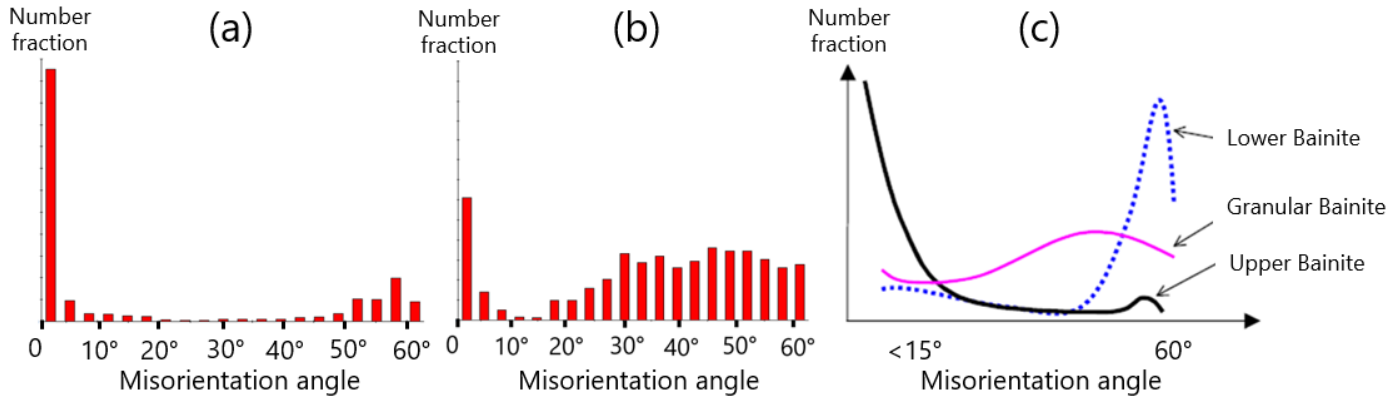

Figure 4. *Misorientation angles evaluated with EBSD on steels I (a) and D (b). The angles below 1° were removed to limit an error from wrongly identified areas. (c) Typical misorientation angles in the different types of bainite were observed in the literature [2,3].*

The thickness of ferrite laths is measured from EBSD maps by the intercept tool and equals to around 2 µm. On few IPF EBSD maps of steel I, the parent austenite grains are distinguishable (available in appendix B.1). Their size is estimated to be above 50 µm.

To evaluate the dislocation density, X-Ray diffraction (XRD) experiments were performed (methodology is explained in appendix B.2). Dislocation density measured with XRD is on the range of 10^{14} m^{-2} which is in good agreement with TEM measurements on steel I and on the typical dislocation density in commercial RPV steels [5,7].

Microstructure at this mesoscale is not expected to evolve after neutron irradiation at 290 °C. On the contrary, microstructure changes at the atomic scale, such as formation of nanosized solute clusters and solute segregations are expected. To study the microstructure of reference materials on the atomic level, Atom Probe Tomography was utilised.

1.2 Atom Probe Tomography experiments

Atom probe tomography is a powerful analysis technique that allows to resolve microstructure at the atomic level. The size of the analysed volume in a single APT experiment is on the level of 10^{-4} cubic micrometres. Therefore, number density and size of micrometre sized features such as carbides cannot be measured accurately. Chemical composition provided by APT experiments represents global composition inside the ferrite matrix, including dislocation lines but excluding GB regions. Carbides observed in APT experiments were studied separately.

APT was used to perform composition measurements at the nanoscale to evaluate the composition homogeneity of steels. A local (volume of μm^3) chemical heterogeneity will not be detected by the microscale techniques like X-Ray diffraction (XRD) and EDS, or macroscale technique like OES, but can be seen with APT experiments. To account for the local chemical

heterogeneity, APT needles were produced from at least two different areas of specimens. From each lifted-out chunk, two or three APT needles were analysed. The summary of successful APT experiments on steels in reference state is presented in Table 1.

Table 1. *Summary on APT experiments performed on the reference CT RPV steels.*

RPV steel	Number of experiments	Number of collected atoms [10^6]	Analysed volume [10^{-4} µm^3]
D	4	12.7	4.1
E	4	7.7	2.5
F	4	9.6	3.1
I	6	6.9	2.2
N	4	10.4	3.4
O	4	9.7	3.2
W	5	9.8	3.2

Si, Mn, Ni, P and Cu are the main elements known to take part in solute cluster formation under irradiation in RPV materials. Their concentrations measured with APT and OES techniques are presented in Table 2.

Table 2. *Concentration of Si, Mn, Ni, P and Cu in steels measured with OES and APT in the reference state. Values are given in at.%. "nd" means not detected. Uncertainty margins are represented by two standard deviations between APT experiments on a given steel. Cu concentration is corrected with the ratio described in chapter II.3.2. For steel I, ferrite phase is marked as (F) and austenite phase as (A).*

ID	Method	Si	Mn	Ni	P	Cu
D	OES	0.48	0.04	0.71	0.017	0.045
	APT	0.51±0.02	0.02±0.01	0.70 ±0.09	0.013 ±0.009	0.051 ±0.006
E	OES	0.53	0.83	0.65	0.024	0.045
	APT	0.56 ±0.06	0.59±0.02	0.66±0.07	0.024±0.003	0.048±0.008
F	OES	0.49	1.77	0.67	0.02	0.036
	APT	0.54±0.05	1.26±0.05	0.69±0.06	0.017±0.003	0.046±0.002
I (F)	OES	0.53	1.84	1.63	0.019	0.036
	APT	0.53±0.07	1.1±0.1	1.6±0.2	0.019±0.004	0.046±0.008
I (A)	OES	-	-	-	-	-
	APT	0.4±0.1	3.9±0.7	2.9±0.7	0.007±0.003	0.08±0.004
N	OES	0.51	1.51	0.67	0.037	0.045
	APT	0.47±0.02	1.05±0.03	0.62±0.02	0.030±0.002	0.039±0.007
O	OES	0.55	1.5	0.66	0.054	0.045
	APT	0.52±0.02	0.99±0.05	0.63±0.02	0.047±0.004	0.043±0.003
W	OES	0.52	1.86	1.61	0.053	0.276
	APT	0.49±0.04	1.18±0.07	1.5±0.1	0.040±0.01	0.27±0.02

Values measured with APT are in good agreement with data measured by OES. One exception is Mn global concentration, which is around 30 % lower than measured by OES. Mn is known to contribute to carbides, which could explain the depletion measured in the matrix by APT. This point will be detailed further. P global concentration measured by APT is slightly lower than measured with OES. The reason is likely that P atoms had segregated on GBs during thermomechanical treatment at 665 °C [8,9]. The austenite phase observed in steel I is enriched in Mn (3.9 at. %) and Ni (2.9 at. %). The observed enrichments of the second phase correlates well with values measured by TEM-EDS (Mn – 3.5 vs 3.9 at. %, Ni – 2.5 vs 2.9 at. %) [7].

It is important to note that in the austenitic phase, crystallographic orientations cannot be identified from the APT detector desorption maps (Fig. 5). If EBSD data was not collected prior to the APT experiment, the austenite can still be successfully identified with detector map.

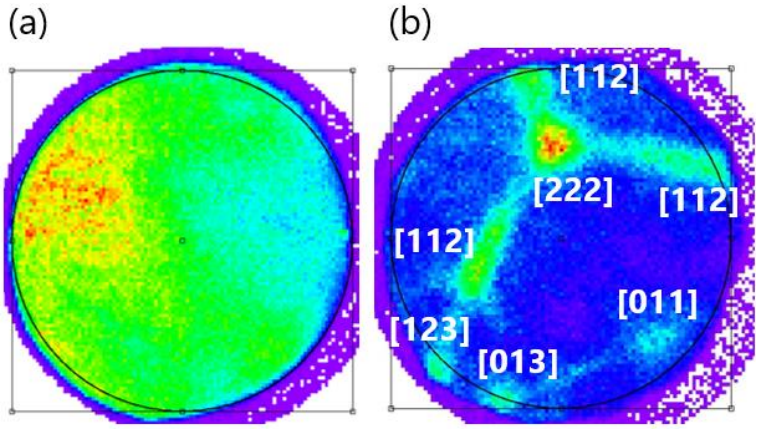

Figure 5. *Detector desorption maps of multiple events are shown. (a) Austenite grain. (b) Ferrite grain.*

Austenite volume fraction is calculated from the APT data using the following equation:

$$f_V = (C_B - C_F)/(C_A - C_F)$$

where C_B is the bulk concentration measured by OES, C_F is the concentration inside the ferritic matrix measured with APT, and C_A is the concentration inside the austenitic phase measured with APT. The calculation is performed with Ni, since it is not known to take part in carbide formation and should be randomly distributed in solid solution. The austenitic phase volume fraction equals ~1.5 %, which is above results measured by EBDS (~0.7 %). Anyway, the fraction of the austenitic phase remains low.

Three steels (D, E and F), with low (0.02 at. %), medium (0.6 at. %) and high (1.3 at. %) concentrations of Mn (respectively) were selected to study the Mn effect on solute cluster formation. APT atom maps of RPV steels D, E and F are shown in figure 6. The difference in Mn concentration is visible with a naked eye.

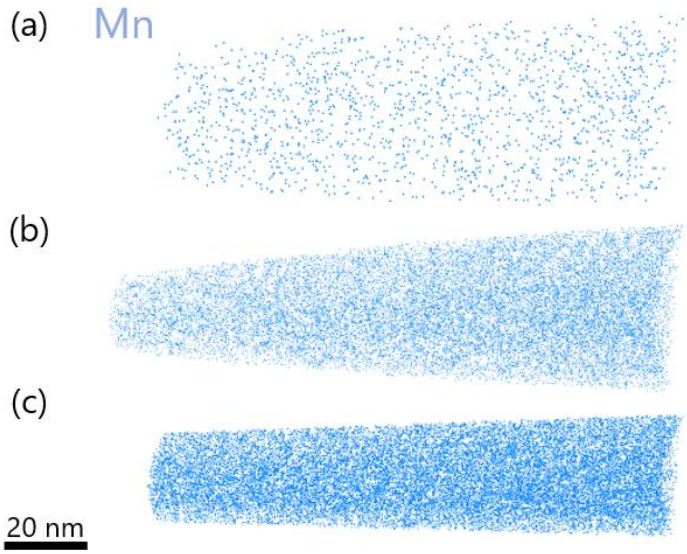

Figure 6. *Atom maps of non-irradiated steels. (a) Low-Mn steel D. (b) Medium-Mn steel E. (c) High-Mn steel F. Difference in Mn concentration is evident.*

To study the effect of P on solute cluster formation, two steels N and O with medium (0.03 at. %) and high (0.047 at. %) P concentrations were selected. The difference in P concentration between materials is evident on the atom maps (Fig. 7). Strong P migration towards [222] and [011] pole axes is also observed in medium-P and high-P steels N and O (low-P steel F added for comparison).

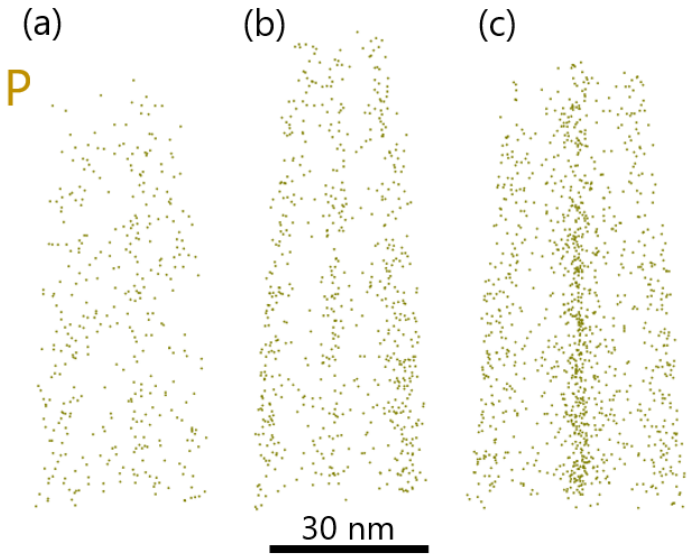

Figure 7. *Atom maps of non-irradiated steels. (a) Low-P steel F. (b) Medium-P steel N. (c) High-P steel O. Difference in P content is visible.*

Two steels F and I with medium (0.7 at. %) and high Ni (1.5 at. %) concentrations were selected to study the effect of Ni and Mn/Ni synergy. The difference in Ni concentrations between two steels is visible on atom maps (Fig. 8.a,b). High-solutes (0.27 at. % Cu; 0.04 at. % P; 1.6 at. % Ni; 1.2 at. % Mn) steel W is the only high-Cu material studied in the current project (Fig. 8.d).

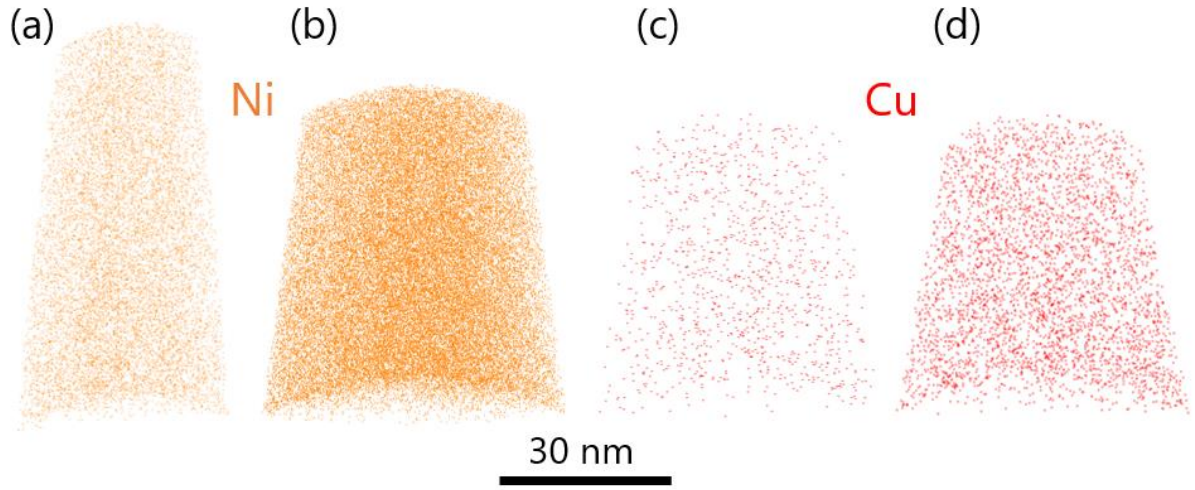

Figure 8. *Atom maps of non-irradiated steels. (a) Medium-Ni steel F. (b) High-Ni steel I. Difference in Ni concentration between RPV steels F and I is evident. (c) High-Ni steel I with low Cu content. (d) High-solutes steel W with high Cu content. The difference in Cu concentration is visible.*

Other solute elements such as C, Mo, Al and S are not known to have a significant role in solute cluster formation in RPV steels. C, Mo and Al were added by the manufacturer to get the microstructure and solid-solution of chemically-tailored RPV steels similar to the commercial RPV materials. C is the most important alloying element, and its concentration determines steel microstructure and properties. S is an impurity element which is also present in commercial RPV materials. As it was described in chapter II.3.3.1, S concentration cannot be measured with APT since its position on mass spectrum overlaps with O. C, Mo and Al concentrations measured by APT and OES are presented in Table 3.

Table 3. *Concentration of C, Mo, Al and S in steels measured with OES and APT at the reference state. Values are given in at. %. "nd" means not detected. Uncertainty margins are represented by two standard deviations between APT experiments on given steel. For steel I ferrite phase is marked as (F) and austenite phase as (A).*

ID	Method	C	Mo	Al
D	OES	0.94	0.30	0.05
	APT	0.12±0.04	0.16±0.03	0.05±0.01
E	OES	0.99	0.29	0.04
	APT	0.17±0.03	0.19±0.01	0.02±0.01
F	OES	0.94	0.30	0.06
	APT	0.12±0.07	0.18±0.03	0.04±0.01
I (F)	OES	1.00	0.31	0.05
	APT	0.1±0.1	0.22±0.07	0.04±0.04
I (A)	OES	-	-	-
	APT	2.0±1	0.2±0.2	0.03±0.02
N	OES	0.95	0.30	0.05
	APT	0.06±0.02	0.18±0.03	0.04±0.01
O	OES	0.99	0.31	0.04
	APT	0.08±0.02	0.21±0.01	0.05±0.01
W	OES	0.97	0.32	0.07
	APT	0.16±0.07	0.2±0.02	0.06±0.01

C concentration was set to around 0.2 wt. % that roughly equals to 0.9 at. %. Significant depletion of C and 30 % depletion of Mo in the ferrite, compared to bulk concentrations is observed. The reason is that, as already said for Mn, C and Mo take part in carbide formation. Mo and C form Mo_2C carbides which were observed by TEM [7]. Mn, Fe and C form M_3C carbides. Typical composition observed in literature is $Mn_{0.6}Fe_{2.4}C$ [10]. Carbide with the same composition was found in APT experiment on reference steel F (Fig. 9).

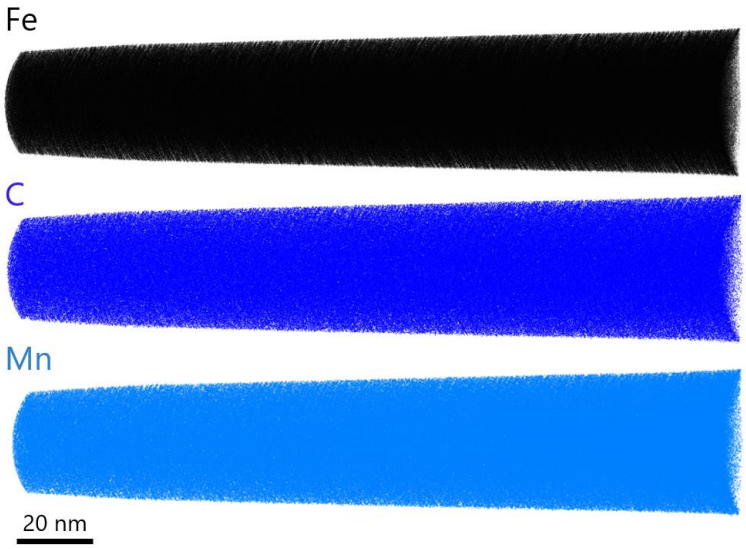

Figure 9. *Atom maps of M_3C carbide. High enrichment in C and Mn is observed.*

Additionally, GB segregation of C, P, Mo and Mn was observed in the literature after heat treatment at ~600 °C, which is close to the tempering temperature of CT RPV steels (665 °C) [9]. GB enriched in solutes was intercepted in one of APT experiments and will be described further.

Low concentrations (below 0.03 at. %) of Co, Cr, N and O are measured with APT. Co and Cr are not known to have a strong effect on solute cluster formation in RPV steel and are not studied in the current PhD project. N and O are introduced into steel during production. Due to low concentrations, these elements were not detected by OES. Concentrations of Co, Cr, N and O measured by APT are presented in Table 4.

Table 4. *Concentrations of Co, Cr, N and O in steels measured with APT at the reference state. Values are given in at. %. "nd" means not detected. Uncertainty margins are represented by two standard deviations between APT experiments on given steel. For steel I ferrite phase is marked as (F) and austenite phase as (A).*

ID	Co	Cr	N	O
D	0.001±0.001	0.001±0.001	0.01±0.01	0.01±0.01
E	0.001±0.001	0.015±0.003	0.03±0.02	0.03±0.02
F	0.001±0.001	0.011±0.002	0.03±0.03	0.02±0.01
I (F)	0.001±0.001	0.012±0.001	0.01±0.01	0.01±0.01
I (A)	nd	0.023±0.002	nd	0.002±0.01
N	0.002±0.001	0.009±0.001	0.03±0.02	0.01±0.01
O	0.001±0.001	0.027±0.006	0.06±0.03	0.03±0.02
W	0.001±0.001	0.009±0.001	0.03±0.03	0.02±0.01

Overall, APT chemical composition measurements show a good correlation with reference values obtained by OES. Ferrite matrix is depleted in C, Mn and Mo since these elements take part in carbide formation and GB segregation. P matrix concentration is lower due to P GB segregation during thermomechanical treatments. Co, Cr, N and O with low matrix concentration were not detected by OES measurements but measured with APT.

Another important reason to perform APT experiments on non-irradiated state is to ensure that atoms are randomly distributed inside the ferritic matrix, and no clustering or precipitation before irradiation is observed. Atom maps of reference steel N are presented in figure 10.

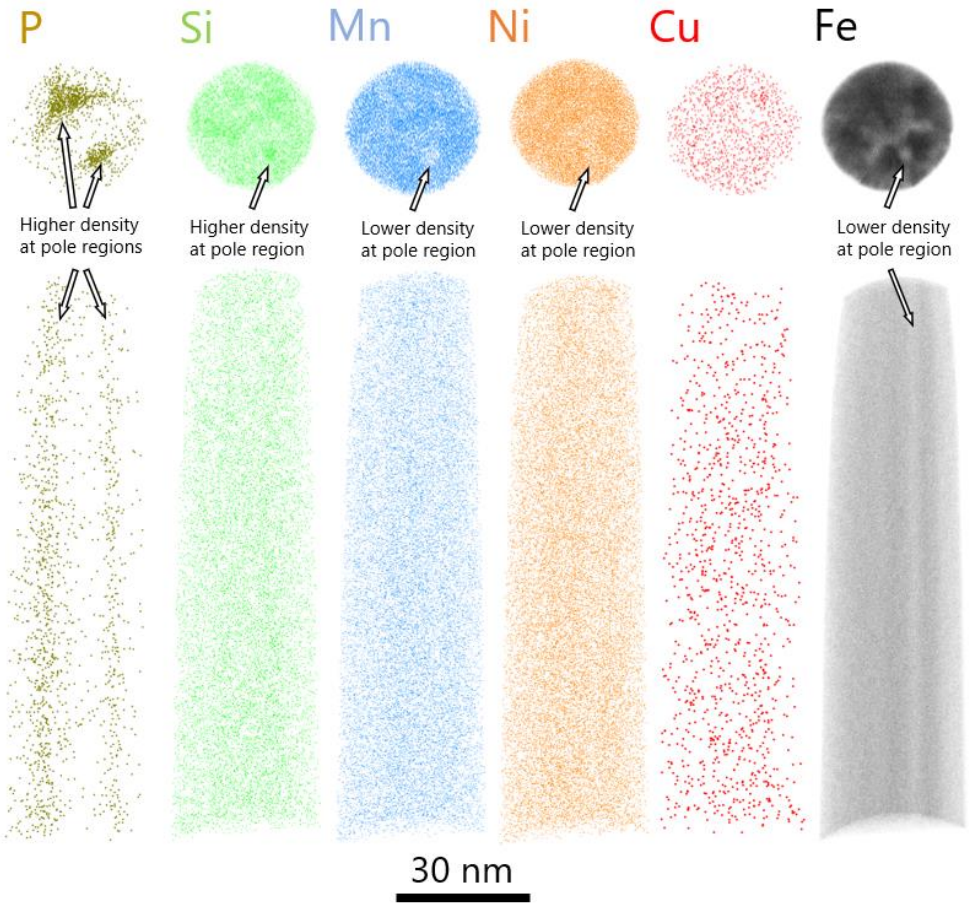

Figure 10. *Atom maps of steel N. Distribution of typical clustering elements in RPV steels, namely, P, Si, Mn, Ni, Cu is shown. Fe atoms are also presented.*

Lower density of Fe, Mn and Ni atoms alongside [011] crystallographic pole and zone lines is observed (Fig. 10). Alongside [002] pole slightly lower Fe and higher Mn density is measured. Contrary, a high-density of elements with the high evaporation field such as P, Si and C (not shown in figure 10) is found. High density of P atoms is visible alongside [222] and [011] poles. In the case of C, the migration towards [222] and [002] poles is observed. High number of Si atoms is found alongside [222], [011] and [002] poles. These are APT artefacts (described in chapter II.3.3.4) and the spatial distribution of atoms (especially in the case of P, Si and C) does not represent the real

state inside material. Apart from the latter three solutes, artificial redistribution of other species is insignificant, and atoms are randomly distributed in the volume. It is confirmed by the first nearest neighbour (1NN) distribution of Mn atoms, which follows the random curve (Fig. 11.a). The random 1NN curve is plotted with the following equation [11]:

$$F^r = 4\pi {d_s}^2 Q C_B \exp(-\frac{4}{3}\pi Q C_B {d_s}^3) \quad (3.1)$$

where Q is detection efficiency of 36%, C_B is the bulk solute concentration and d_s is the sampling step.

Cluster identification procedure on solute cluster (SC) element composed from combined Si, Mn, Ni, P and Cu atoms was performed (Fig. 11.b). No solute clusters are observed in steels D, E, F, I, N and O in the non-irradiated state. If any clusters are present, their highest possible number density is below 3 x 10^{21} m^{-3}. Or, the size of clusters is below resolution limit of APT. In the present research, the limit of the iso-position cluster identification procedure was evaluated and equals to around 8 detected solute atoms (detected by APT considering detection efficiency of ~36%). The total size of cluster containing 8 solutes is estimated to be around 40 atoms (considering average solute cluster enrichment of around 20 at. %). Taking into account the APT detection efficiency, the cluster of 40 detected atoms in reality contained ~110 atoms and had a radius of ~0.7 nm.

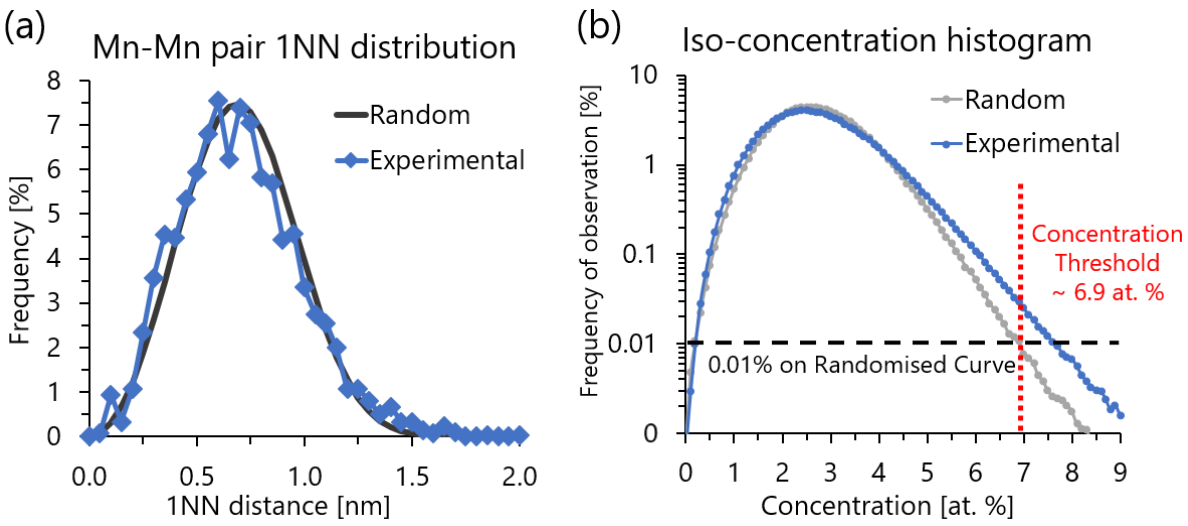

Figure 11. (a) *First nearest neighbour distribution of Mn atoms in the non-irradiated steel F. (b) Iso-concentration histogram for "SC" element in nor-irradiated steel F.*

In one of the APT experiments on steel N, a planar defect enriched in solutes is found and studied (Fig. 12). Due to the homogeneity of solute segregation is it assumed that a grain boundary (GB) is intercepted.

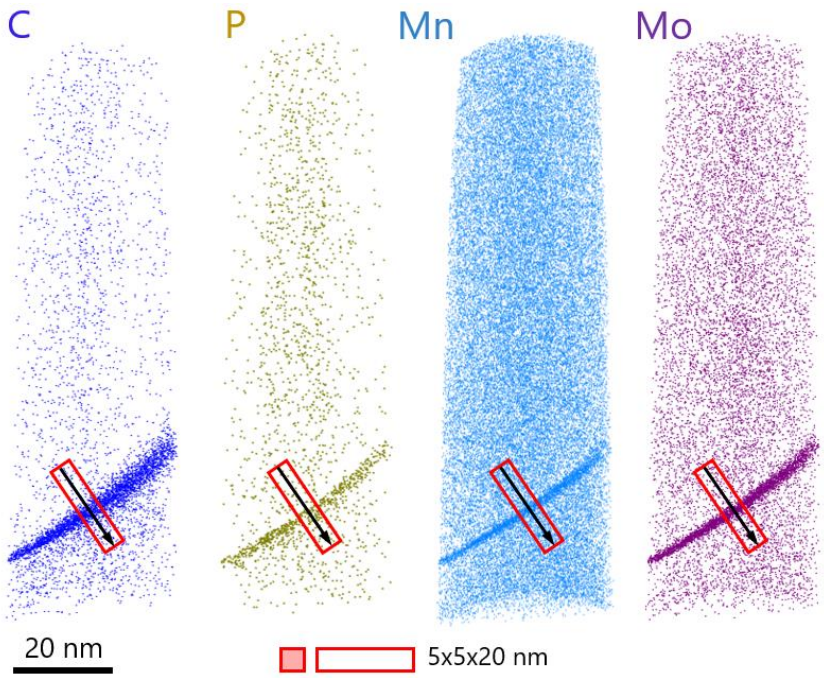

Figure 12. *Atom maps of GB segregation in non-irradiated steel N. Enrichment in C, P, Mn and Mo was observed. Concentration profile through GB is plotted and represented by red rectangle*.

APT detector maps of both grains are presented in figure 13. On the APT detector desorption maps, [011] crystallographic orientation was identified on both sides of GB. To identify both rotation and translation angles the information about additional poles is needed. Since the latter information is not available in the case of grain 'b", only the misorientation angle between [011] directions of these grains will be calculated. The measured from detector angle between [011] direction in grains "a" and "b" is 10.2°. Considering the image compression factor (~1.76), the misorientation angle between [011] directions is estimated to be around ~18°.

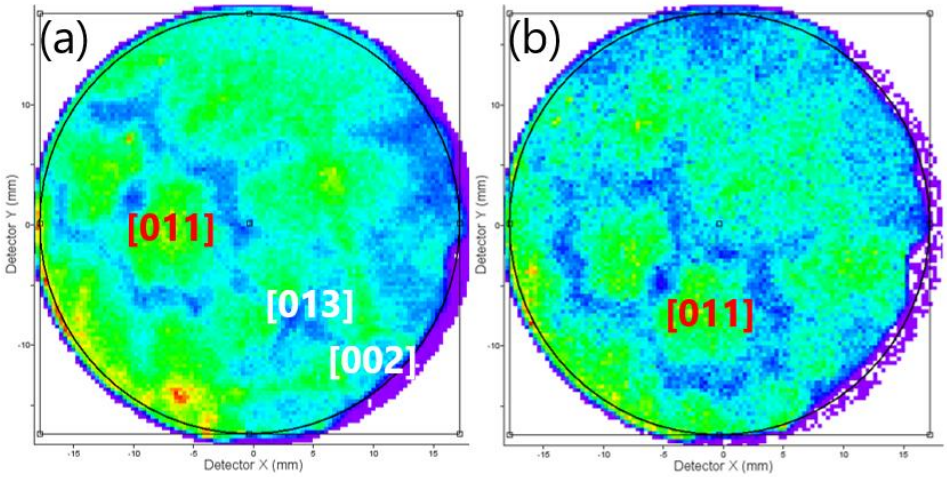

Figure 13. *Detector desorption maps of all events. (a) Grain above GB. (b) Grand below GB.*

The concentration profile plotted through GB is presented in figure 14.

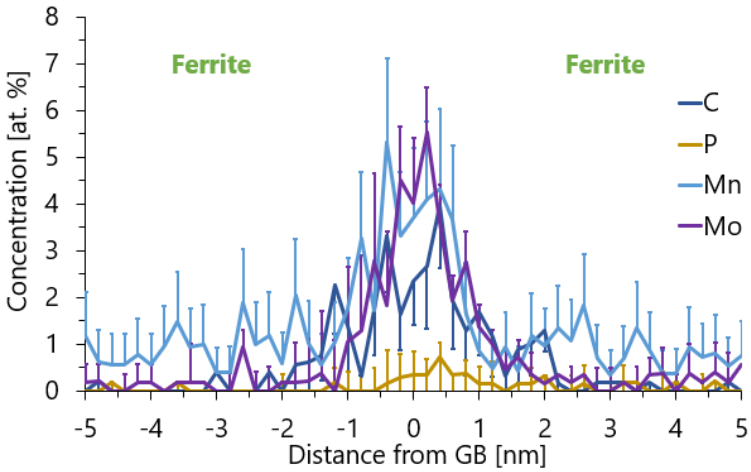

Figure 14. *Concentration profile plotted through GB. Enrichment in C, P, Mn and Mo atoms was observed. Uncertainty margins are represented by two standard deviations. For visual simplicity error margins only in one direction are presented.*

Only C, P, Mn and Mo appear to be enriched at this boundary. Solute concentration at GB was measured in the region at half-maximum of concentration peak. The concentrations and enrichment factors of these elements at the boundary are presented in Table 5.

Table 5. *Solute concentration at GB segregation region. Uncertainty margins are represented by two standard deviations.*

Element	Average concentration at GB region [at. %]	Nominal concentration [at. %]	Enrichment factor
C	2.1 ± 0.3	0.06 ± 0.02	35.0
P	0.7 ± 0.2	0.03 ± 0.002	23.3
Mn	3.4 ± 0.4	1.05 ± 0.03	3.2
Mo	3.5 ± 0.6	0.18 ± 0.03	19.3

High enrichment in C, P, Mo and Mn correlates well with lower matrix (than in bulk) concentration values measured by APT.

In high-solutes steel W, Cu-enriched features are observed (Fig. 15). Cu could have precipitated during a thermomechanical treatment, since the global Cu concentration (0.27 at. %) is much larger than its solubility limit in Fe at 300 °C (around 0.007 at. %) [12]. CEFs number density is around (6 ± 4) x 10^{21} m^{-3} with the average radius of 1.1 ± 0.1 nm. They are enriched in Cu (15 ± 5 at. %) and Mn (6 ± 3 at. %) with concentration of other solutes of 3 ± 2 at. % and Fe in balance. Due to their small size and the moderate Cu enrichment, the conclusion was made that the latter features are not the fcc ε-Cu precipitates observed with STEM-EDS in the high-Cu RPV weld, but rather a coherent bcc Cu-enriched clusters [13]. Yet, no diffraction data was collected to support that conclusion.

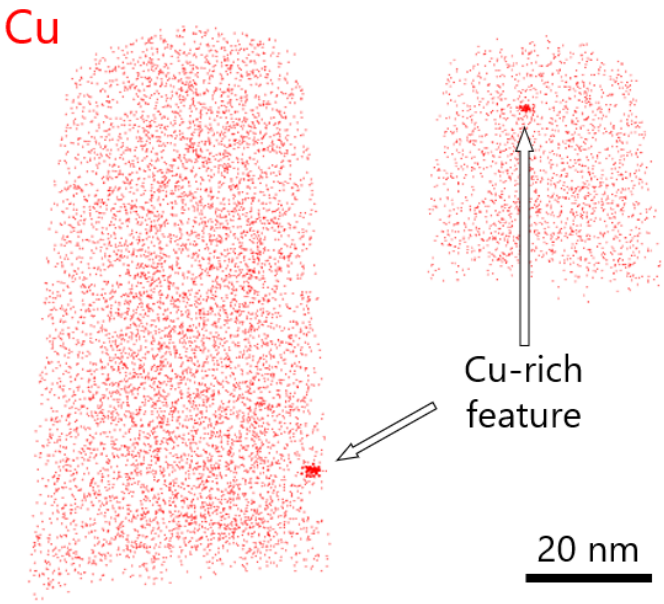

Figure 15. *Atom maps of reference high-solutes steel W. Small Cu-rich features are observed.*

Eason and Odette evaluated that during the typical for RPV steels tempering and stress relieve heat treatments (at 600-700 °C for ~10 hours) only around 0.25-0.3 at. % of Cu can remain in solid solution. If the nominal Cu content is higher, the excess of Cu atoms will result in extensive formation of Cu-enriched features even during rather short interval of 10 hours [14,15]. In the case of steel W, the nominal Cu content (0.276 at. %) is on the level of the limit predicted in the latter study, and the formation of large volume fraction of CEFs during tempering is not expected. The estimated volume fraction of Cu-rich features in steel W is below 0.01 %, which is coherent with the low Cu matrix depletion in comparison with bulk (0.27 vs 0.276 at. % Cu).

APT experiments of reference chemically-tailored RPV steels were performed. Chemical composition measured with APT shows a good correlation with results obtained with OES. Lower global concentrations for several solutes, namely C, Mn, Mo and P were observed. C, Mn and Mo take part to carbide, and C, Mn, Mo and P were found on segregation along a GB in medium-P steel N. M_3C carbides were observed with APT. Carbides Mn enrichment was directly related to the bulk Mn concentration. Cu-rich precipitates formed during thermomechanical treatment were found in high-solutes steel W. Apart from Cu-rich features in steel W (also enriched in Mn), no solute clusters enriched in Si, Mn, Ni, P and Cu were found (possible number density below 3×10^{21} m^{-3}) in the reference chemically-tailored RPV steels.

2 Microstructure characterisation in irradiated state with Atom Probe Tomography

Structure of bainitic RPV steel is not expected to evolve at the mesoscopic level (grain size, carbide volume fraction…) in operation conditions. The changes will occur at the nanometric level: nanosized solute clusters and solute segregations are formed under irradiation. Atom Probe Tomography was used to study the microstructure evolution at this scale.

The results obtained on each chemically-tailored RPV steel are presented in separate sections. For each material, matrix and global (composed of matrix, clusters and dislocation segregations) compositions calculated by APT are presented. Number density of solute clusters is given separately for clusters formed inside the ferrite matrix and along dislocation lines. Cluster size is calculated from number of atoms after the half-maximus erosion. Core chemical composition of solute clusters after the plateau erosion is also given.

2.1 Steel D: 0.05 at.% Cu, 0.017 at.% P, 0.71 at.% Ni, 0.04 at.%

The low-Cu (0.05 at. %), low-P (0.017 at. %), medium-Ni (0.71 at. %), low-Mn (0.04 at. %) steel D[1] is the first material selected to study the effect of Mn bulk concentration on solute cluster formation under neutron irradiation. Steel D was irradiated up to low (0.06 dpa) and medium (0.09 dpa) doses.

The global concentrations of solutes of interest measured in reference state and after irradiation at the highest dose are presented in Table 6. For reference steels, where clustering and segregation on dislocation lines were not observed, global composition represents the matrix one.

Table 6. *Concentration of Si, Mn, Ni, P and Cu measured by APT (at. %). Uncertainty margins are represented by two standard deviations between APT experiments on a given material.*

Dose	Volume		Si	Mn	Ni	P	Cu
Reference	Global/Matrix		0.51	0.02	0.68	0.013	0.05
		±	0.05	0.01	0.14	0.007	0.02
0.09 dpa	Global		0.48	0.02	0.69	0.004	0.05
		±	0.09	0.01	0.07	0.008	0.01

APT concentration measurements show a strong decrease (from 0.013 to 0.004 at. %) in the global P concentration. Also, a high dispersion between APT experiments (0.001 to 0.013 at. %) is

[1] It is important to keep in mind that these values are the bulk ones, including Mn into carbides. The Mn remaining in matrix in reference state, measured by APT is 0.02 at. %.

observed. Atomistic DFT and Self-Consistent Mean Field (SCMF) modelling predict that the mean free path of P-SIA mixed dumbbell could exceed 1 μm [16]. Hence, the mean free path of P atoms could be bigger than the size of APT volume. Consequently, a proposition is made that P atoms could have segregated onto GBs and dislocation lines which were not intercepted during analysis (Fig. 16). Depending on the presence of dislocations and GBs in the vicinity of APT volumes, lower or larger P content is measured.

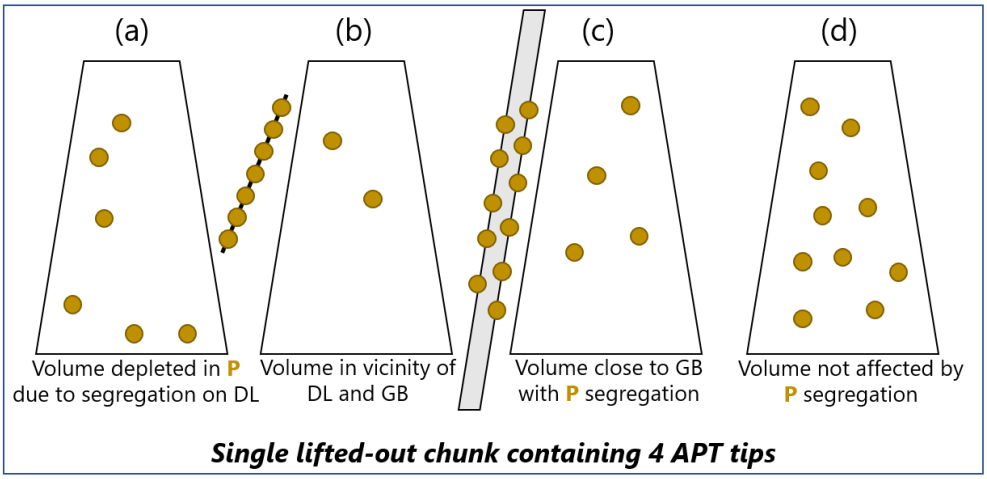

Figure 16. *Possible distribution of P atoms between APT specimens lifted-out from the same area. (a) Volume depleted in P due to its segregation on DL. (b) Volume depleted in P due to its long-range migration towards DL and GB. (c) Volume depleted in P due to its segregation on GB. (d) Volume with nominal P concentration.*

Additionally, as it was noted in the previously, P atoms can migrate towards [011] and [222] poles. Here we should note that the studied by APT volume represents only the central part of initial needle-shaped specimen (Fig. 17). The peripheral part of the tip is evaporated, but not detected. Main crystallographic orientations facing the APT detector are different for each specimen.

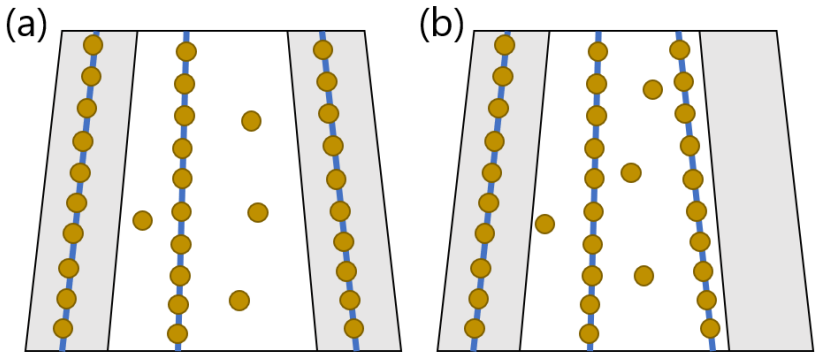

Figure 17. *Possible distribution of P atoms between APT specimens. Grey areas are the initial APT specimen. White areas are the detected by APT volume. Blue lines represent [222] and [011] poles. (a) Volume where only one crystallographic pole is located inside the detected volume. Lower P concentration is measured. (b) Volume where two crystallographic poles are inside the detected volume. Higher P concentration is measured.*

Consequentially, lattice could be oriented in a way where different number of crystallographic poles are located inside the studied part of the APT needle. If [222] and [011] poles are located outside of the detected volume, the P surface migration towards these poles could result in the lower measured P content. The two latter issues are resulting in high dispersion of P concentration measurements

Atom maps of the D steel, irradiated up to 0.09 dpa are shown in figure 18.

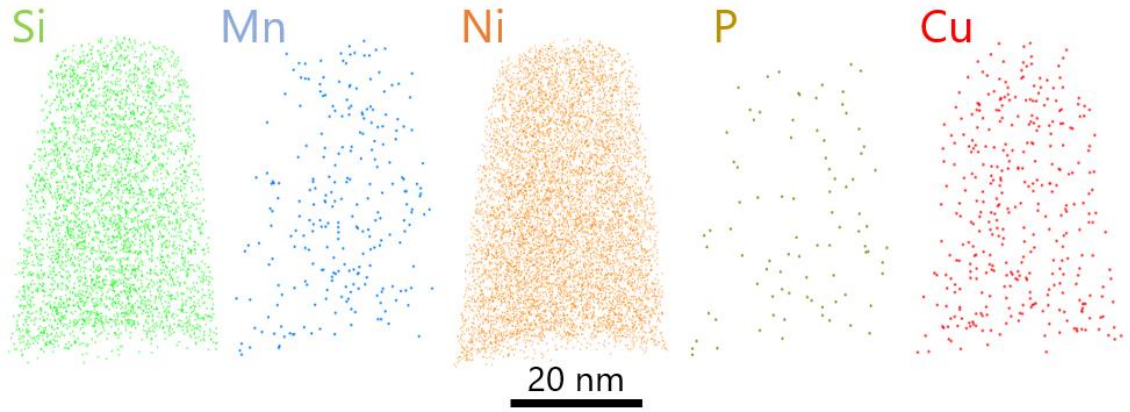

Figure 18. *Atom maps of low-Mn steel D. Si, Mn, Ni, P and Cu atoms are randomly distributed inside volume (apart from lower/higher density at crystallographic poles due to APT artefacts).*

No solute clusters are observed with a naked eye. With cluster identification procedure performed with SC, only small clusters of around five solute atoms were observed. The same type of clusters was observed in a volume with randomly distributed atoms, hence these clusters were identified as random fluctuations of concentration and removed.

Due to the low Mn content (0.02 at. %) steel D differs from the most of the commercial RPV materials and direct comparison is complicated. However, Burke and co-workers performed the study on the several types of ASTM A508 Gr 4N steel [18,19]. One of them, named “superclean” is in particular interest to compare with steel D. The former has a high Ni (3.5 at. %), low Si (0.01 at. %), low Mn (0.02 at. %) contents. It was irradiated under the high flux (~10^7 dpa/s) at 239 °C up to the low dose of ~0.02 dpa. No well-defined solute clusters were identified in this steel with the APT experiments. Yet, solute fluctuations (non-random distribution) of Ni and Mn atoms was identified with statistical analysis.

To evaluate if the similar solute fictions are present in steel D, the concentration distributions in reference and irradiated states were plotted (Fig. 19).

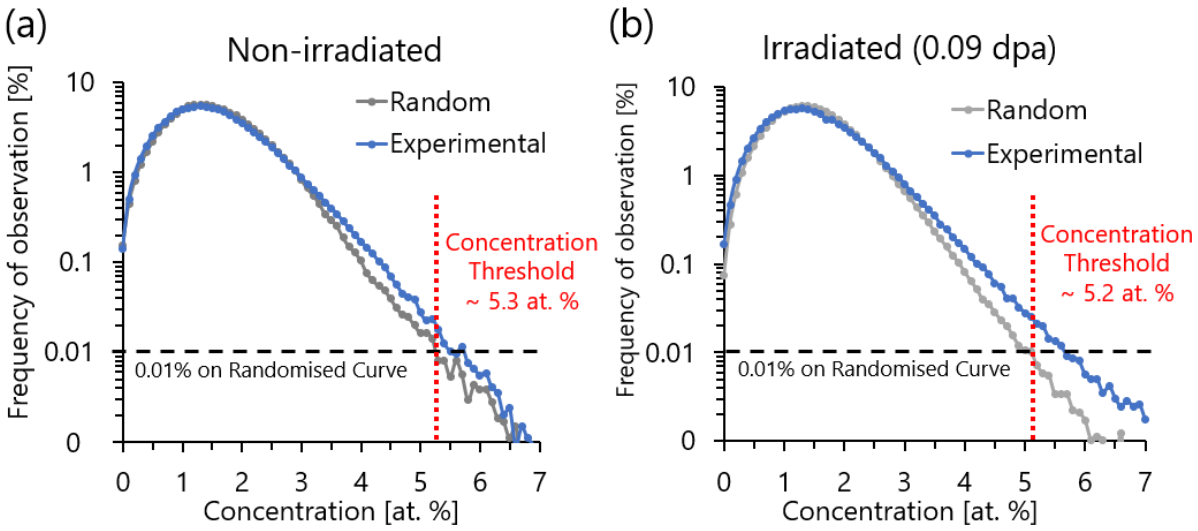

Figure 19. *Iso-concentration curves for SC atoms in steel D. (a) In reference state. (b) Irradiated up to 0.09 dpa. No significant evolution between reference and irradiated conditions is observed.*

Additionally, first nearest neighbour distributions are plotted to compare the randomness of solute atoms distribution in reference and irradiated steel D. To limit the bias from trajectory aberrations 1NN calculations are performed in a selected volume excluding low-density areas in vicinity of crystallographic poles. Mn concentration in RPV steel D is too low (0.02 at. %) to have statistically correct results. Several Ni peaks (including the main one at 29 amu) overlap with Fe, P and Mo atoms also found at 29, 31 and 32 amu ranges respectively. Main peak of Si (~92 % abundance) at 14 amu overlaps with N, yet the N concentration (~0.01 at. %) is expected to be too low to have an effect on the measurements. Therefore, the 1NN distribution for Si atoms is plotted (Fig. 20).

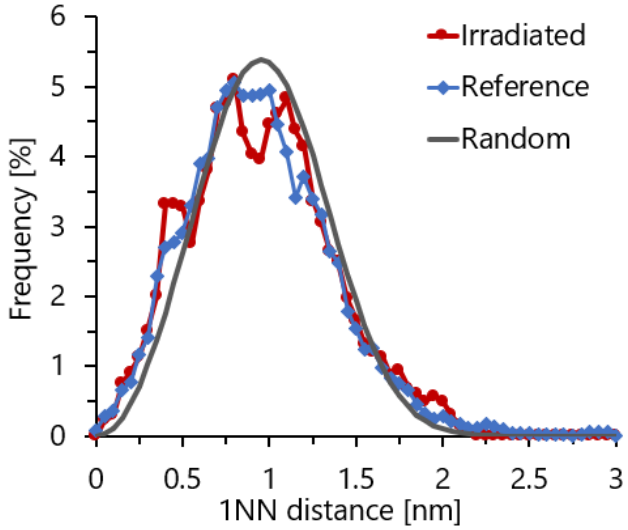

Figure 20. *First nearest neighbour distribution for Si atoms in reference and irradiated up to 0.09 dpa steel D. The random curve is obtained from Eq. 3.1. Curves are smoothed over 3 points.*

The curves are smoothed over 3 successive points and normalised to 100%. Further, the *V* parameter to evaluate the difference between experimental and theoretical curves is calculated: $V = \sum_i |F_i^e - F_i^r|$, where F^e and F^r are experimental and random observation frequencies normalised to 1 [11]. Hence, the *V* parameter equals 0 for the random distribution of atoms and equals to 2 for the case where experimental curve doesn't overlap with the random one at all. The 1NN distribution of Si atoms in both reference and irradiated states are slightly shifted from the random curve. *V* parameter equals to 0.17 in the reference state and to 0.19 after irradiation up to 0.09 dpa. The insignificant evolution of *V* parameter confirms the absence of extensive clustering in this material. Yet, this slight shift could indicate the first step of clustering (solute fluctuation). Or, for example, formation of clusters with a size smaller than the resolution limit of APT.

Altogether, the results of the cluster identification procedures allow to conclude that solute clusters hadn't formed in the low-Mn steel D irradiated up to 0.09 dpa. If such clusters are present, their number density should be below 4 x 10^{21} m^{-3}, which is on the level of the higher possible number density in reference materials. Besides, results of APT analysis cannot exclude formation of small (~10 monomers) SIA or V clusters which cannot be resolved with the APT, yet the latter ones were observed in commercial RPV steels by the PAS [17].

In one of the APT experiments, solute segregation on a planar defect (identified as GB) is intercepted, and concentration profile through GB is plotted (Fig. 21, 22). The concentration profile with only C, P and Mo atoms is available in appendix B.1.

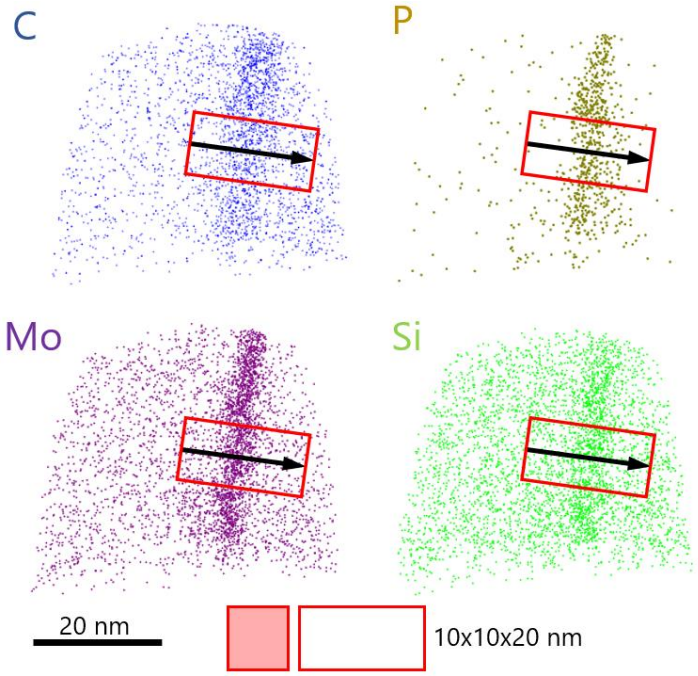

Figure 21. *Atom maps of segregation on the GB in steel D. Enrichment in C, P, Mo and Si atoms is observed.*

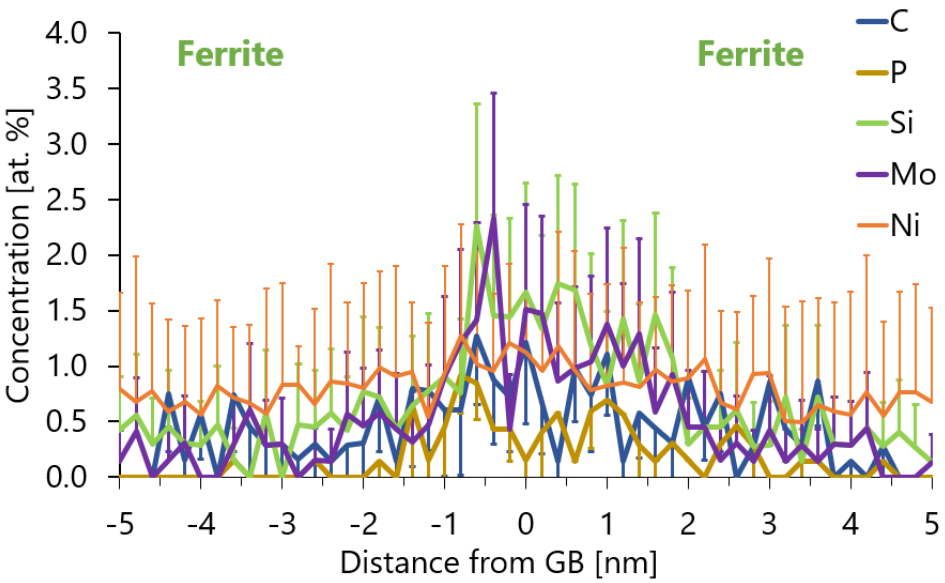

Figure 22. *Concentration profile plotted through the GB. Enrichment in C, P, Si and Mo atoms is observed. Error margins are represented by two standard deviations. For visual simplicity, only positive uncertainty margins are presented for Si, Ni and Mo, and negative fop C and P atoms.*

Results of the concentration measurements are presented in Table 7.

Table 7. *Solute concentration at GB segregation region. Uncertainty margins are represented by two standard deviations.*

Element	Average concentration at GB region [at. %]	Nominal concentration [at. %]	Enrichment factor
C	0.9 ± 0.2	0.12 ± 0.04	7.3
P	0.5 ± 0.1	0.01 ± 0.01	35.8
Mo	1.2 ± 0.2	0.16 ± 0.03	7.3
Ni	1.3 ± 0.2	0.70 ± 0.10	2.0
Si	1.3 ± 0.2	0.51 ± 0.05	2.6

The APT detector map showing both grains called “a” and “b” is presented in figure 23. Since in grain “b” only [222] direction is identified, the misorientation angel between these grains cannot be precisely evaluated.

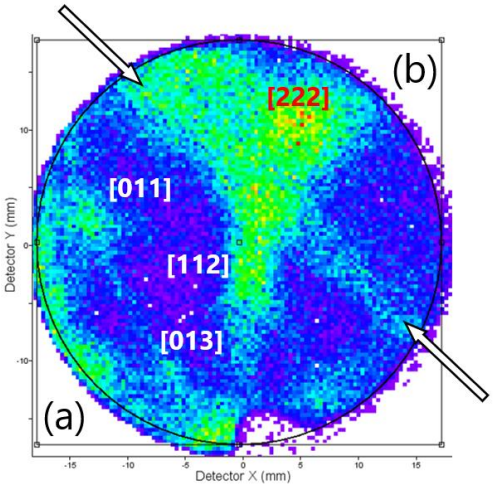

Figure 23. *Detector desorption map of multiple events. Grain boundary between grains "a" and "b" is shown by white arrows.*

Since no information about GB misorientation angles in non-irradiated steel N and irradiated steel D are collected, and since materials have a different composition, the direct comparison has to be considered carefully. However, it can be reasonably assumed that C, P, and Mo atoms had segregated onto GB during thermomechanical treatment in steel D, as in steel N. Additionally, Si and Ni enrichment which was not observed in reference steel N but is measured in irradiated steel D. These solutes could have segregated due to the radiation-induced mechanism, dragged by the flux of PDs towards the GB, which acts as a sink for point defects.

Since no clusters have been observed in the low-Mn RPV steel D irradiated to the dose of 0.09 dpa, APT study on material irradiated up to a lower dose of 0.06 dpa was not performed.

2.2 Steel E: 0.05 at.% Cu, 0.024 at.% P, 0.65 at.% Ni, 0.83 at.% Mn

Low-Cu (0.05 at. %), low-P (0.024 at. %), medium-Ni (0.65 at. %), medium-Mn (0.83 at. %) steel E[2] is the second material selected to study the effect of Mn concentration on the solute cluster formation. Steel E was irradiated at low (0.07 dpa), medium (0.09 dpa) and high (0.14 dpa) doses.

At all irradiation doses, decrease in Si, Mn, Ni and Cu matrix concentrations is on the level of APT uncertainties in a single volume (~0.01 at. %) and significantly smaller than the dispersion between APT experiments on a given condition (up to 0.1 at. %). Therefore, this matrix depletion is concluded to be not statistically meaningful (Table 8). Matrix P content (~0.01 at. %) is significantly lower than the nominal one (~0.02 at. %). Same as in the case of steel D, high

[2] It is important to keep in mind that these values are the bulk ones, including Mn into carbides. The Mn remaining in matrix in reference state, measured by APT is 0.83 at. %.

dispersion of P concentration can be due to long-range P diffusion towards defects (GBs, dislocations) outside of APT volumes.

Table 8. *Concentration of Si, Mn, Ni, P and Cu measured by APT (at. %). Uncertainty margins are represented by two standard deviations between APT experiments on a given material.*

Dose	Type		Si	Mn	Ni	P	Cu
Reference	Global/Matrix		0.56	0.59	0.66	0.024	0.048
		±	0.11	0.04	0.15	0.006	0.016
0.07 dpa	Global		0.58	0.56	0.73	0.028	0.054
		±	0.09	0.07	0.13	0.033	0.013
	Matrix		0.57	0.55	0.72	0.014	0.050
		±	0.09	0.07	0.13	0.022	0.014
0.09 dpa	Global		0.50	0.59	0.63	0.017	0.046
		±	0.06	0.03	0.03	0.040	0.005
	Matrix		0.49	0.58	0.62	0.007	0.043
		±	0.06	0.03	0.04	0.015	0.011
0.14 dpa	Global		0.51	0.54	0.60	0.012	0.043
		±	0.04	0.03	0.08	0.004	0.008
	Matrix		0.49	0.53	0.58	0.007	0.042
		±	0.06	0.03	0.07	0.013	0.007

Phosphorus is strongly depleted in the ferritic matrix because most of the P atoms had segregated along dislocation lines (DLs) and/or took part in solute clustering. The observed solute clusters are located inside the ferritic matrix or along dislocation lines. Apart from the clusters located on dislocation lines and in the ferrite, in one of the volumes collected on steel E irradiated at 0.07 dpa, solute clusters located on the dislocation network of a low-angle GB (LAGB) are observed (Fig. 24). An enrichment in Si, Mn, Ni, P and Mo is measured (Fig. 24.a). The combined concentration of these elements together is represented by the pink SC element (Fig. 24.b). Concentration profile (sampling box of 0.5 nm, step size 0.1 nm) is plotted alongside the dislocation line (Fig 24.c). Small regions (few nm) with higher solute enrichment are found. These regions are identified as solute clusters. The dislocation line between solute clusters is also enriched in Si, Mn, Ni, P and Mo (concentration profile with the separate representation of solutes is available in appendix B.1).

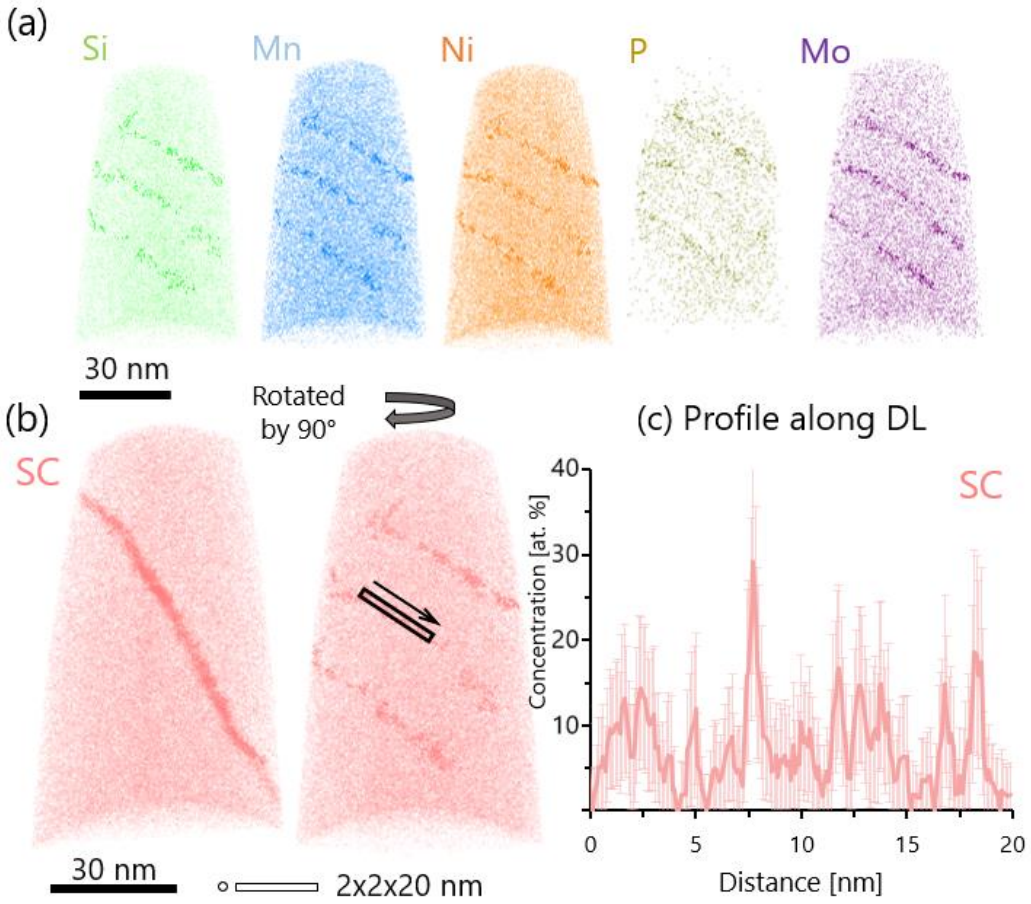

Figure 24. *(a) Atom maps of steel E irradiated at 0.07 dpa. Solute clusters enriched in Si, Mn, Ni, P and Mo are observed on the dislocation lines. (b) Atom maps of the same APT volume represented with SC element. Small cylindrical concentration profile is plotted alongside the dislocation line. (c) Concentration profile alongside dislocation line. The pink line represents a combined concentration of Si, Mn, Ni, P and Mo atoms.*

After irradiation at 0.07 dpa, solute clusters inside the ferritic matrix have a number density of (3 ± 2) x 10^{22} m^{-3} and a radius of (1.3 ± 0.3) nm. Concerning the ones observed on dislocation lines, the number density measured directly can be biased since it depends on the presence or not of dislocations in the analysed volume. Thus, the linear density along dislocation is calculated for each volume where dislocation lines are observed. Further, the mean dislocation line length was attributed to each volume assuming that dislocation density is around 10^{14} m^{-2} (from TEM and XRD measurements). From the mean length of dislocation lines and their linear density, number density of clusters formed on dislocation lines was calculated. The average number density of clusters formed on dislocation lines is around (2 ± 1) x 10^{22} m^{-3} with a radius of (1.9 ± 0.3) nm. Finally, the solute clusters found on the dislocation lines on the low-angle GB (tilt boundary with edge dislocations) were treated separately. To evaluate the total number density of clusters formed on the dislocation lines of the LAGBs, the surface density from this APT experiment was calculated ~(2.3 ± 0.5) x 10^{15} m^{-2}. Further, the total surface of lath-boundaries (~1.05 x 10^{6} m) in the volume of one

cubic meter was calculated assuming lath dimensions of 2x2x20 µm [4,20]. Finally, the number density of clusters formed on LAGB is calculated and equals (0.24 ± 0.05) x 10^{22} m^{-3} with the average radius of 1.2 ± 0.3 nm. It is also possible to calculate the misorientation angle (θ) between two grains using the following equation: $tg(\theta/2) = b/2h$, where b is Burgers vector (0.248 nm) and h is the distance between dislocations measured from APT reconstruction [21,22]. In the present case distance between dislocations is ~17 nm and the misorientation angle equals ~0.8 °.

In the samples irradiated at the medium dose (0.09 dpa), solute clusters are also observed in the ferritic matrix and along dislocation lines (Fig. 25). Number density of clusters inside the ferritic matrix equals to around (3 ± 2) x 10^{22} m^{-3} with a radius of (1.5 ± 0.3) nm. The number density of clusters formed on dislocation lines equals to (2 ± 1) x 10^{22} m^{-3} with a radius of around (2.0 ± 0.3) nm.

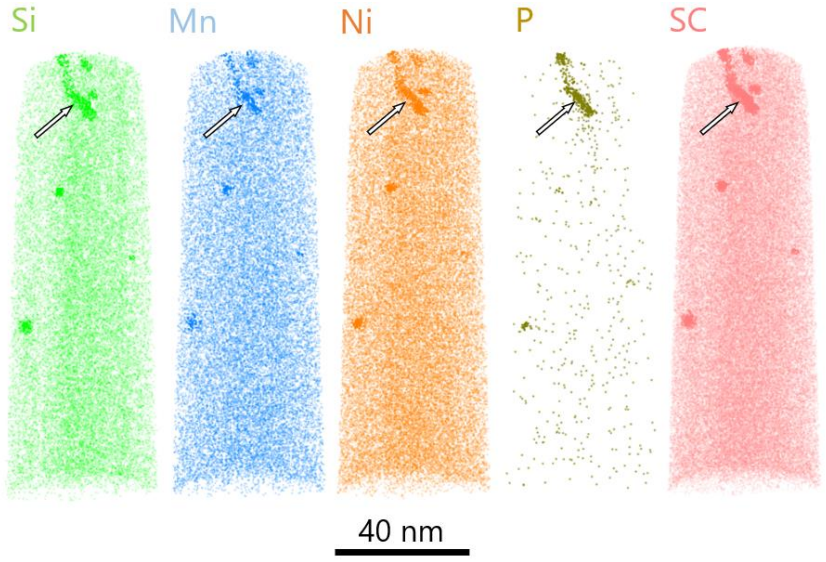

Figure 25. *Atom maps of steel E irradiated up to 0.09 dpa. Solute clusters enriched in Si, Mn, Ni and P are observed. Arrows indicate solute clusters on the dislocation line.*

In the material irritated up to the highest dose of 0.14 dpa, the number density of clusters formed inside the ferritic matrix equals to (9 ± 3) x 10^{22} m-3 with a radius of (1.4 ± 0.3) nm. Number density of clusters formed on dislocation lines equals to (2 ± 1) x 10^{22} m^{-3} with the radius of around (1.5 ± 0.2) nm.

The results about solute clusters number density as a function of irradiation dose are summarised in figure 26. Variation of number density of clusters formed on dislocation lines does not vary significantly between APT experiments (~0.5 x 10^{22} m^{-3}). To simplify the visual representation here and further, only the average density of clusters formed on dislocation lines will be represented on graphs. The number density of clusters inside the ferritic matrix is similar at 0.07 and 0.09 dpa (~3 x 10^{22} m^{-3}) and further increases up to 9 x 10^{22} m^{-3} at 0.14 dpa. The number density

of clusters formed on dislocation lines is slightly higher at the lower dose, yet in all cases it is on the level of around 2 x 10^{22} m^{-3}. With increase of irradiation dose and number density, the ratio of clusters formed on dislocation lines over total clusters decreases (from ~50% at 0.07 dpa to ~20% at 0.14 dpa). Number density of formed on low-angle GB clusters is by a factor of 6 smaller (0.5 vs 3) x 10^{22} m^{-3} than the lowest number density of clusters formed inside the ferritic matrix.

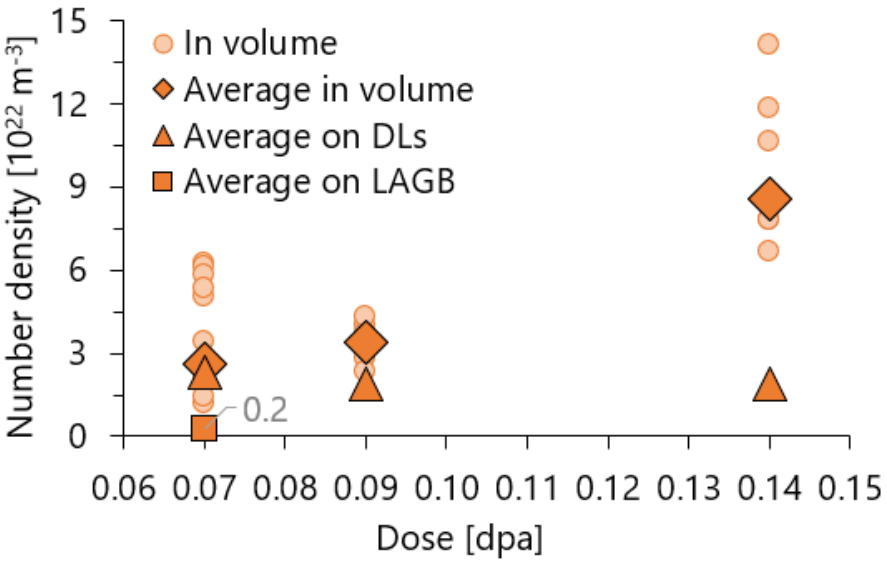

Figure 26. *Number density of solute clusters in steel E as a function of irradiation dose. Pale circles represent the number density of clusters inside ferritic matrix for each APT experiment. Diamonds represent the average number density of clusters inside ferritic matrix. Triangles represent the average number density of clusters formed on dislocation lines. Square (with grey data label) represents the number density of clusters formed on low-angle GB.*

Equivalent radius of clusters formed inside ferritic matrix is calculated from the number of atoms after first (half-maximum of solute concentration) erosion, assuming that clusters are spherical. Further, the observation frequency for each class size is reported in figure 27 (number of studied clusters for each condition is given in brackets within the legend). Additionally, number density for each class size is reported on the same graph.

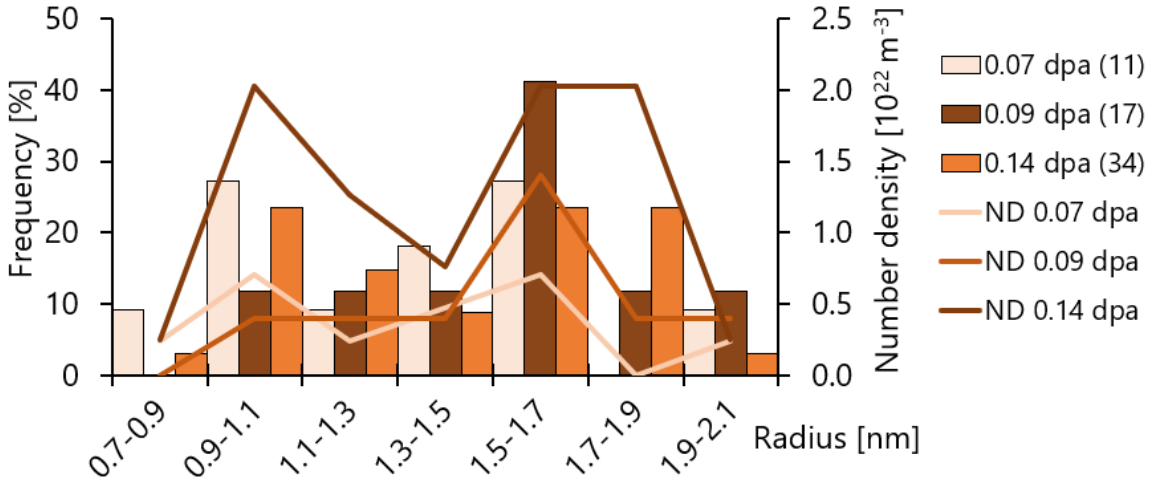

Figure 27. *Size distribution chart for clusters formed inside ferrite matrix.*

Due to a low number density at the low and medium dose conditions, only 11 and 17 clusters were studied respectively, it is complicated to evaluate the trends in cluster size distribution. High dispersion of cluster radii (from ~1 to ~2 nm) is observed and the average cluster radius increases from 1.3 to 1.5 nm (from 0.07 to 0.09 dpa). In the high dose condition information about 34 clusters was collected. Here a bimodal-like cluster radius distribution is observed. The average cluster radius is lower (1.4 vs 1.5 nm) than in the medium dose condition. The possible explanation is the formation of smaller (radius ~1 nm) clusters during irradiation above 0.1 dpa. This issue will be discussed in detail in chapter IV. Cluster size distribution chart for clusters formed on DLs and LAGB is shown in figure 28.

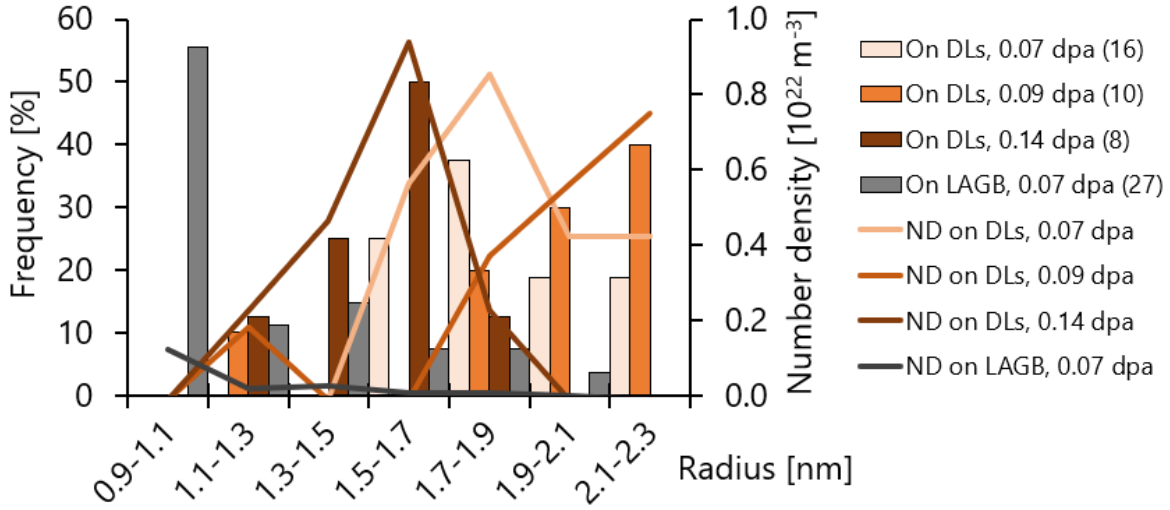

Figure 28. *Size distribution chart for clusters formed on dislocation lines and low-angle grain boundary.*

At all irradiation doses, clusters formed on dislocation lines are bigger than the ones in the matrix (~1.8 vs ~1.4 nm). The reason is that dislocations are the stronger sinks for SIA atoms.

Therefore, more SIA atoms annihilate on dislocations, resulting in the increase of the net number of transported solute atoms, and also, as it will be shown further, in the higher Fe cluster content. Same as for clusters located in the ferrite, with an increase of irradiation dose above 0.1 dpa, a decrease in the radius of clusters formed on dislocation lines is observed (from ~1.9 to 1.5 nm).

Clusters observed on the dislocation lines at the low-angle GB are smaller than the clusters observed inside the ferritic matrix and clusters formed on dislocation lines (1.2 vs ~1.5 and ~1.9 nm respectively).

The core composition of solute clusters, calculated after the second erosion is presented in Table 9. At all irradiation doses formed inside ferritic matrix clusters are enriched in Si (6-8 at. %), Mn (3-4 at. %), Ni (8-11 at. %), and P (2-4 at. %). With increase of irradiation dose, enrichment in Si, Mn and Ni progressively increases (all these solutes have nominal content above 0.5 at. %). Simultaneously, Fe cluster content decreases from 79.1 to 77.7 and further to 72.8 at. %. Also, a significant Mo enrichment (4.1 at. %) is observed on the clusters formed one dislocation lines in the high dose condition.

Table 9. *Composition of solute clusters in steel E (at. %)."nd" means not detected. The uncertainty margins are given by two standard deviations from APT data on a given condition.*

Type	Dose		Si	Mn	Ni	P	Cu	C	Mo	Fe
In volume	0.07		5.7	3.2	9.6	2.1	0.3	nd	nd	79.1
	dpa	±	1.3	1.0	1.7	0.8	0.3			2.3
	0.09		5.7	4.2	8.1	3.7	0.1	nd	0.4	77.7
	dpa	±	0.9	0.8	1.1	0.8	0.1		0.3	1.7
	0.14		8.2	4.2	11.3	2.7	0.2	nd	0.3	72.8
	dpa	±	0.8	0.6	0.9	0.4	0.1		0.2	1.2
On dislocations	0.07		2.1	1.5	3.5	5.5	nd	0.5	0.8	86.1
	dpa	±	0.6	0.5	0.8	1.0		0.3	0.4	1.5
	0.09		4.3	3.1	6.8	5.5	nd	nd	0.8	79.5
	dpa	±	1.8	1.5	2.2	2.0			0.8	3.6
	0.14		4.2	3.9	6.4	5.3	nd	1.9	4.1	73.2
	dpa	±	1.0	1.0	1.3	1.1		0.7	1.0	2.3
On LAGB	0.07		2.4	4.3	4.7	1.2	nd	0.5	1.6	85.8
	dpa	±	0.7	0.9	0.9	0.5		0.3	0.5	1.5

At all irradiation doses clusters formed on dislocation lines are more enriched in P (~5 vs ~3 at. %). At the same time, they are less enriched in Si (~4 vs ~6 at. %), Mn (~3 vs ~4 at. %) and Ni (~6 vs ~9 at. %). Also, higher Fe cluster content is measured. Clusters formed on LAGB have lower

P (1.2 vs 5.5 at. %), but higher Mn (4.3 vs 1.5 at. %), Ni (4.7 vs 3.5 at. %) and Mo (1.6 vs 0.8 at. %) enrichment than cluster formed at the dislocation lines at the same irradiation dose of 0.07 dpa. However, clusters formed inside ferritic matrix are the main focus of the research and will be discussed further.

Significant dispersion in solute concentrations for clusters formed inside ferritic matrix is observed between APT experiments on the same condition. For example, Ni cluster content ranges from 6 to 15.1 at. %. The same is observed for Mn (2.1 to 5.7 at. %), Si (1.3 to 9 at. %) and P atoms (0 to 3.8 at. %) for 0.07 dpa condition (detailed information is presented in appendix B.3). A proposition is made that the cluster composition could be correlated with the composition of APT volume (global composition excluding GBs and carbides). To evaluate the latter proposition, the evolution of relative cluster solute content (excluding all chemical species except Si, Mn, Ni, P and Cu and normalised to 1) as a function of relative global solute content (also excluding all elements apart of Si, Mn, Ni, P and Cu and normalised to 1) for each APT experiment is plotted (Fig. 29).

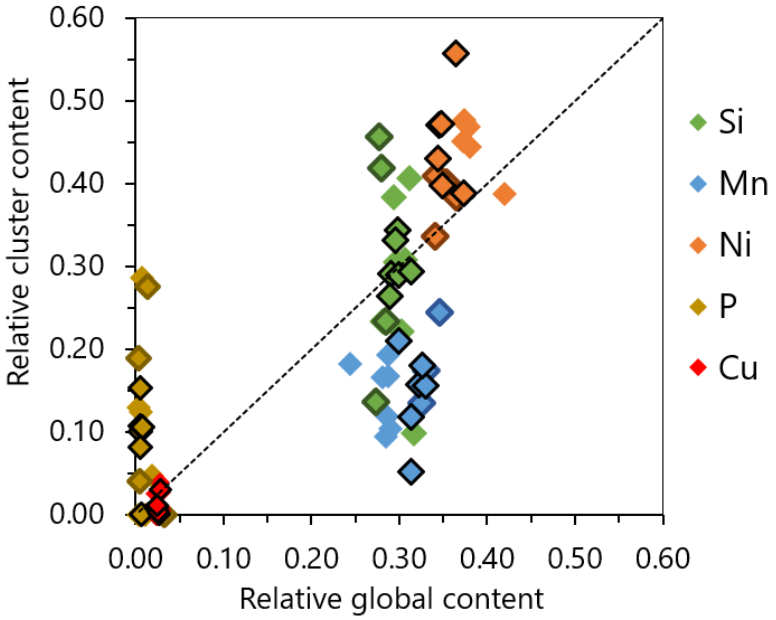

Figure 29. *Evolution of relative cluster solute content as a function of relative global solute content in steel E. Each diamond represents the results obtained in one APT experiment. Low dose represented by symbols without borders, medium dose by symbols with darker border and high dose by symbols with black border. 1:1 trend line is also plotted.*

At every irradiation dose a high dispersion of relative cluster solute contents is evident. Yet, in general, the tendency with a higher cluster solute enrichment in experiments with a higher global solute content is observed. Symbols located above 1:1 line correspond to the strong clustering tendency, since the relative solute ratio inside the clusters is higher than the relative global ratio of the given solute. Contrary, symbols below 1:1 show a less extensive clustering. Symbols

representing Ni are above 1:1 line and the significant Ni cluster enrichment is observed. The opposite tendency is evaluated for Mn atoms. Si symbols are distributed above and below 1:1 line. A tendency of strong P cluster enrichment is also evident.

Apart from the results presented above, in a several volumes, ferrite / carbide interfaces are intercepted. One of the cases was steel E irradiated up to 0.09 dpa (Fig. 30).

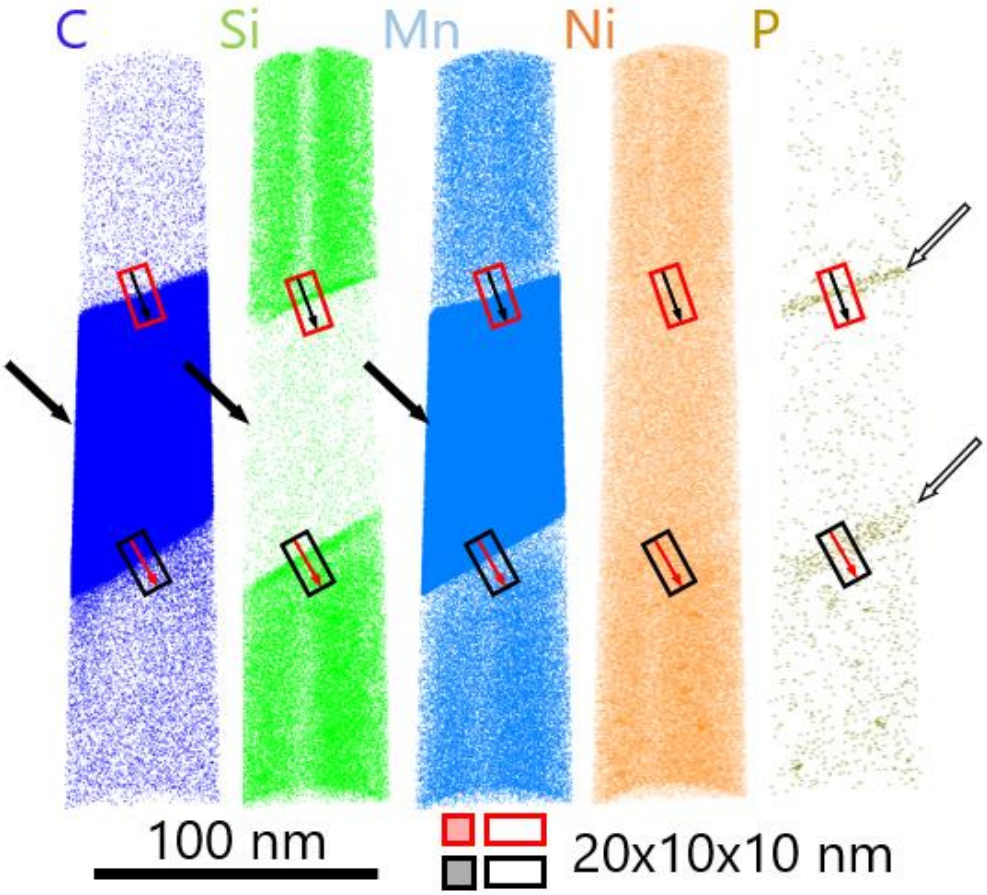

Figure 30. *Atom maps of steel E irradiated up to 0.09 dpa. Black arrow indicated the M_6C carbide enriched in C and Mn and depleted in Si. White arrows indicate ferrite /carbide and carbide / ferrite interfaces.*

The concentration profiles are plotted thought both top (left side on chart) and bottom (right side on chart) interfaces. The concentration profiles for elements with high concentration inside the carbide (C, Mn and Fe) and for other elements (P, Si, Ni and Mo) are presented in figures 31 and 32 respectively. Concentration profile plotted only for P atoms is available in appendix B.1.

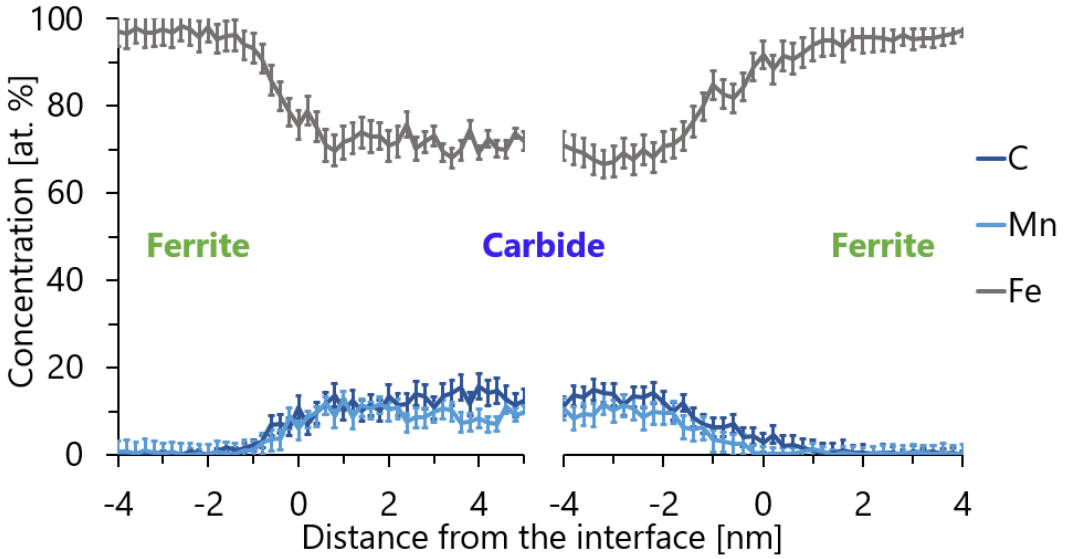

Figure 31. *Concentration profiles of ferrite / carbide interfaces for C, Mn and Fe atoms. Error margins are represented by two standard deviations.*

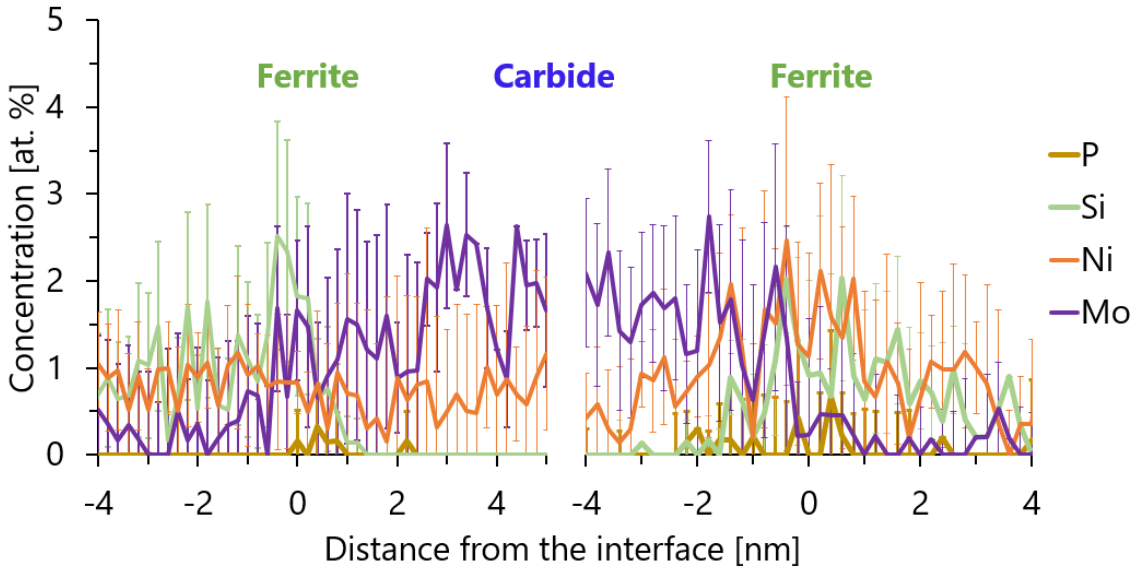

Figure 32. *Concentration profiles of ferrite / carbide interfaces for P, Si, Ni and Mo atoms. Error margins are represented by two standard deviations.*

The measured carbide composition is Fe-15C-8Mn-2Mo and refers to composition of M_6C carbide. In the case of C, Mn and Mo atoms, no interface enrichment is measured. These solutes have high-carbide and low-matrix concentrations, and the concentration profiles in the interface consist in a gradient with no interfacial enrichment. Enrichments in P, Si and Ni atoms are estimated from the half-maximum concentration are on the profile and reported in the Table 10.

Table 10. *Solute concentrations at ferrite / carbide interfaces. Uncertainty margins are represented by two standard deviations.*

Element	Average concentration [at. %]		Nominal concentration [at. %]	Enrichment factor	
	Top interface	Bottom interface		Top interface	Bottom interface
P	0.2 ± 0.1	0.2 ± 0.1	0.024 ± 0.003	6.5	7.0
Si	1.5 ± 0.4	1.2 ± 0.4	0.56 ± 0.06	2.7	2.2
Ni	0.7 ± 0.2	1.4 ± 0.4	0.66 ± 0.07	1.0	2.2

In another APT experiment, this time in the high dose condition, a M_3C carbide / ferrite interface is studied (Fig. 33). Concentration profiles for C, Mn, Fe and for P, Si, Ni, Mo atoms are presented in figures 34.a and 34.b respectively.

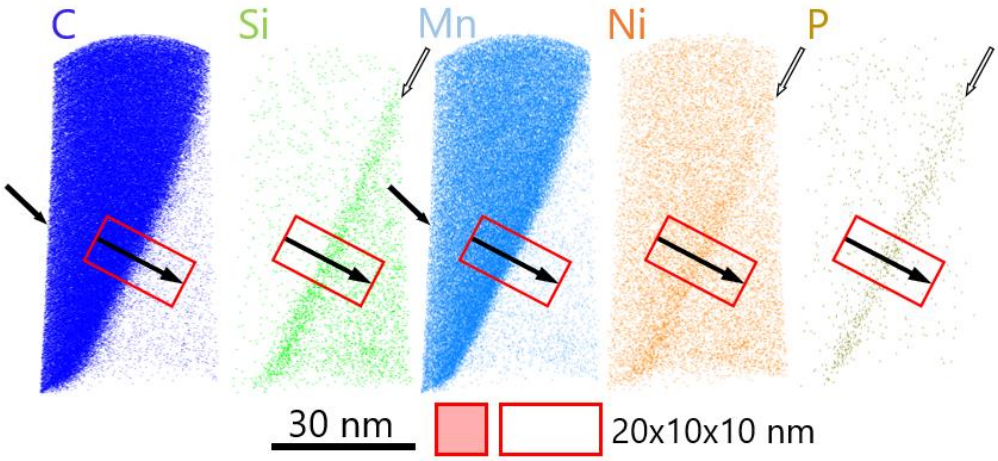

Figure 33. *Atom maps of steel E irradiated up to 0.14 dpa. Black arrows indicate the M_3C carbide enriched in C and Mn and depleted in Si. White arrows indicate ferrite /carbide interface.*

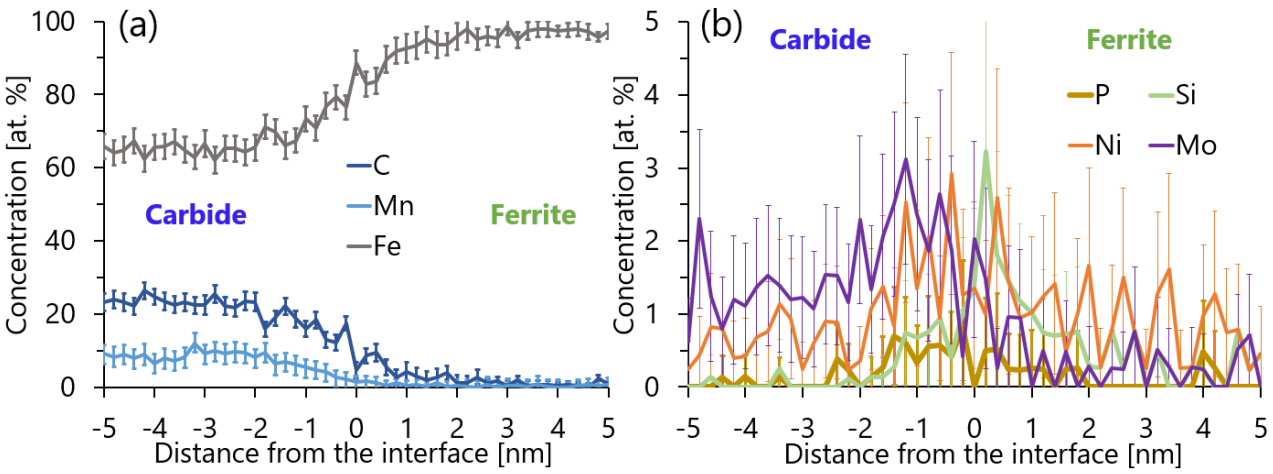

Figure 34. *Concentration profiles of carbide / ferrite interface. (a) For C, Mn and Fe atoms. (b) For P, Si, Ni and Mo atoms. Error margins are represented by two standard deviations.*

Additional profile with only P atoms is available an appendix B.1. The high concentration on the interface was measured for P, Si and Ni atoms (Table 11).

Table 11. *Solute concentrations at carbide / ferrite interface. Uncertainty margins are represented by two standard deviations.*

Element	Average concentration at GB region [at. %]	Nominal concentration [at. %]	Enrichment factor
P	0.5 ± 0.2	0.024 ± 0.003	21.2
Si	1.1 ± 0.3	0.56 ± 0.06	2.0
Ni	1.4 ± 0.3	0.66 ± 0.07	2.1

With increase of irradiation dose from 0.09 to 0.14 dpa, similar Si (~2) and Ni (~2), and higher P (21 vs ~7) enrichments on ferrite / carbide interfaces are measured. However, since we have no information about the interface structure, it is difficult to conclude that this observation is due to the different doses.

To conclude, solute clusters formed inside the ferritic matrix, on dislocation lines and on low-angle GB were observed. Number density and solute enrichment of clusters formed inside the matrix grows with increase of irradiation dose. Their average size increases from low to medium doses, and further decreases due to the formation of new, smaller clusters.

2.3 Steel F: 0.04 at.% Cu, 0.020 at.% P, 0.67 at.% Ni, 1.77 at.% Mn

Low-Cu (0.04 at. %), low-P (0.020 at. %), medium-Ni (0.67 at. %), high-Mn (1.77 at. %) steel F[3] is the last material selected to study Mn effect on solute cluster formation. Steel F was irradiated up to low (0.06 dpa), medium (0.08 dpa) and high (0.13 dpa) doses.

Matrix is slightly depleted in P at the medium (0.007 at. %) and high (0.009 at. %) irradiation doses. Excepted for P, the difference between global and matrix concentrations is insignificant (~0.02 at. %) whatever the irradiation dose is (Table 12).

[3] It is important to keep in mind that these values are the bulk ones, including Mn into carbides. The Mn remaining in matrix in reference state, measured by APT is 1.25 at. %.

Table 12. *Concentration of Si, Mn, Ni, P and Cu measured by APT (at. %). Uncertainty margins are represented by two standard deviations between APT experiments on a given condition.*

Dose	Type		Si	Mn	Ni	P	Cu
Reference	Global/Matrix		0.54	1.25	0.69	0.017	0.047
		±	0.09	0.09	0.06	0.006	0.006
0.06 dpa	Global		0.48	1.23	0.65	0.020	0.043
		±	0.06	0.16	0.07	0.040	0.011
	Matrix		0.48	1.22	0.64	0.017	0.043
		±	0.06	0.15	0.06	0.045	0.011
0.08 dpa	Global		0.50	1.26	0.69	0.018	0.047
		±	0.03	0.13	0.04	0.017	0.016
	Matrix		0.49	1.25	0.67	0.011	0.046
		±	0.03	0.13	0.03	0.015	0.007
0.13 dpa	Global		0.53	1.24	0.69	0.024	0.042
		±	0.06	0.24	0.09	0.018	0.007
	Matrix		0.51	1.22	0.66	0.015	0.041
		±	0.06	0.23	0.09	0.010	0.007

In the steel F, solute clusters in the ferritic matrix, along dislocation lines and on dislocation lines of LAGB are found. It has to be noticed that the majority of them are located in the matrix.

An example of atom map after irradiation at low dose (0.06 dpa) is given in figure 35. Solute clusters enriched in Si, Mn, Ni and P are visible on the combined (SC) atom map (Fig.35.a). The number density of clusters inside ferritic matrix is around $(6 \pm 2) \times 10^{22}$ m^{-3} with a radius of around (1.6 ± 0.2) nm. The number density of clusters formed on dislocation lines is around $(1.4 \pm 0.6) \times 10^{22}$ m^{-3} and the average radius is (1.6 ± 0.2) nm. Solute clusters found on low-angle GB are presented in figure 35.b (Separate concentration profiles for Si, Mn, Mo, Ni and P atoms are available in appendix B.1).

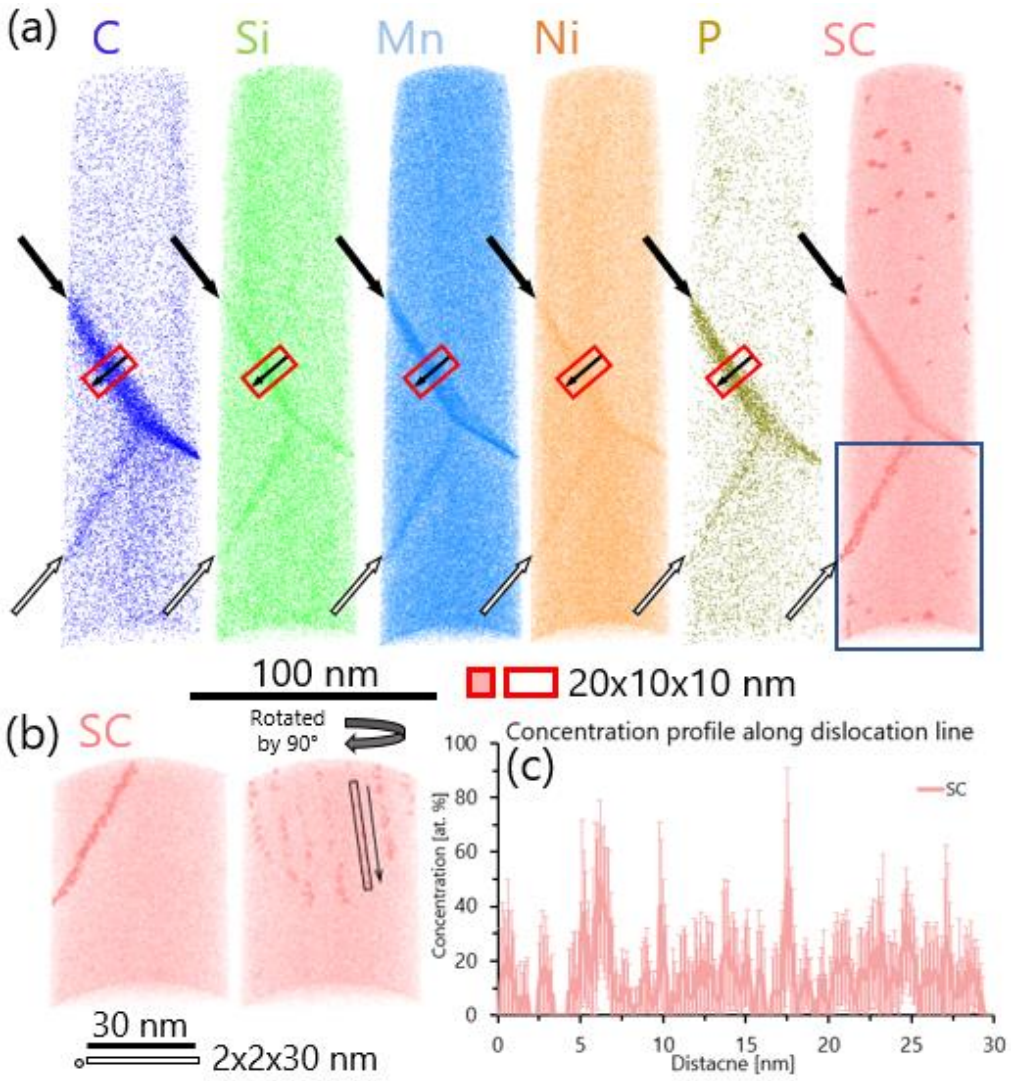

Figure 35. *Atom maps of steel F irradiated up to 0.06 dpa. (a) Solute clusters enriched in Si, Mn, Ni and P are observed. High-angle and low-angle GBs are shown by the black and white arrows respectively. (b) Selection of volume (blue rectangle) where clusters on LAGB were identified. (c) Concentration profile plotted alongside dislocation line of LAGB for SC atoms. This volume was obtained in laser mode.*

Estimated number density equals to (0.58 ± 0.08) x 10^{22} m^{-3} and the average radius is (1.0 ± 0.2) nm. Number density of clusters formed at LAGB in steel F is around 2 times larger than in steel E (0.58 ± 0.08 vs 0.24 x 10^{22} m^{-3}). It can be explained by the difference between misorientation angles (1.6° in steel F and 0.8° in steel E). Hence, the distance between dislocations is smaller (9 vs 17 nm), thus the surface density and consequentially the total calculated cluster density is higher.

In the same APT experiment, the second grain boundary exhibit a homogeneous segregation. Hence it is assumed to be a high-angle grain boundary (HAGB). Concentration profile plotted through this GB shows enrichments in C, P, Mn, Mo, Ni and Si (Fig. 36). Additional profile with only Si, Mo and P atoms is available in appendix B.1.

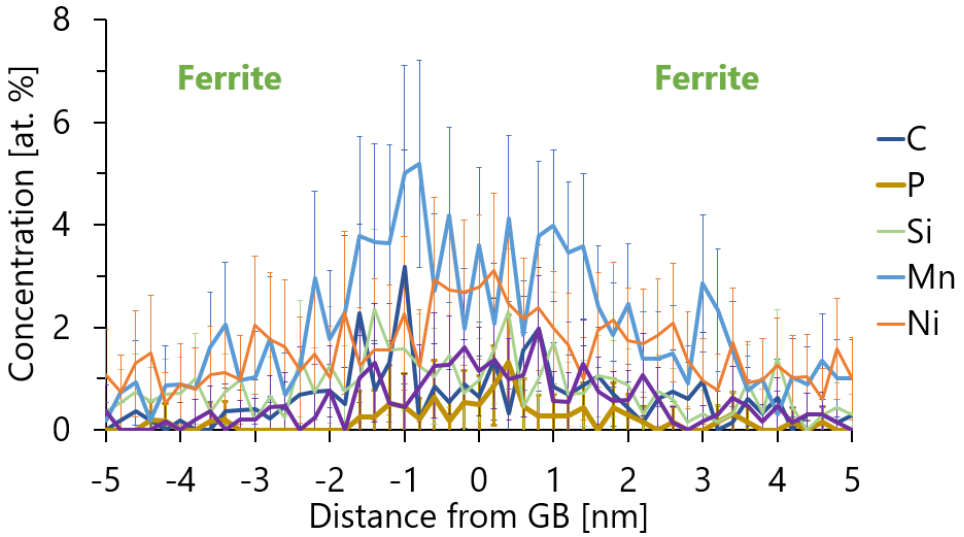

Figure 36. *Concentration profile plotted through the GB. Enrichment in C, P, Mn, Mo, Ni and Si atoms is observed. Error margins are represented by two standard deviations.*

The enrichment of solutes on GB is calculated from region of the half-maximum concentration and reported in Table 13.

Table 13. *Solute concentration at GB segregation region. Uncertainty margins are represented by two standard deviations.*

Element	Average concentration at GB region [at. %]	Nominal concentration [at. %]	Enrichment factor
C	1.1 ± 0.2	0.12 ± 0.07	9.2
P	0.5 ± 0.2	0.017 ± 0.03	31.2
Mn	3.5 ± 0.4	1.26 ± 0.05	2.8
Mo	1.2 ± 0.2	0.18 ± 0.03	6.4
Si	1.2 ± 0.2	0.54 ± 0.05	2.2
Ni	2.0 ± 0.3	0.69 ± 0.06	2.9

Similar to the case of steel D irradiated up to 0.09 dpa, high C (~8), P (~30) and Mo (~7) enrichment factors are measured. Close levels of Ni and Si (around 2) enrichments are also observed. The only difference is the higher Mn enrichment (2.8), which was not observed in the low-Mn steel D, yet it correlates well with we value of ~3.2 measured in the non-irradiated steel N.

With an increase of the irradiation dose up to 0.08 dpa, the number density of solute clusters inside ferritic matrix grows up to around (8 ± 3) x 10^{22} $m^{-3,}$ whereas the radius remains nearly the same, (1.7 ± 0.3) nm. Number density of clusters formed on dislocation lines almost does not evolve with dose (1.2 ± 0.9) x 10^{22} m^{-3}. Their average radius is around (1.8 ± 0.2) nm.

After irradiation up to 0.13 dpa, the number density of solute clusters reaches (20 ± 3) x 10^{22} m^{-3} (Fig 37). On the contrary, the average radius decreases and is around (1.4 ± 0.3) nm. Increase

of irradiation dose has small effect on clusters formed along dislocation lines. Their number density is (1.7 ± 0.5) x 10^{22} m^{-3} with an average radius of (1.8 ± 0.3) nm.

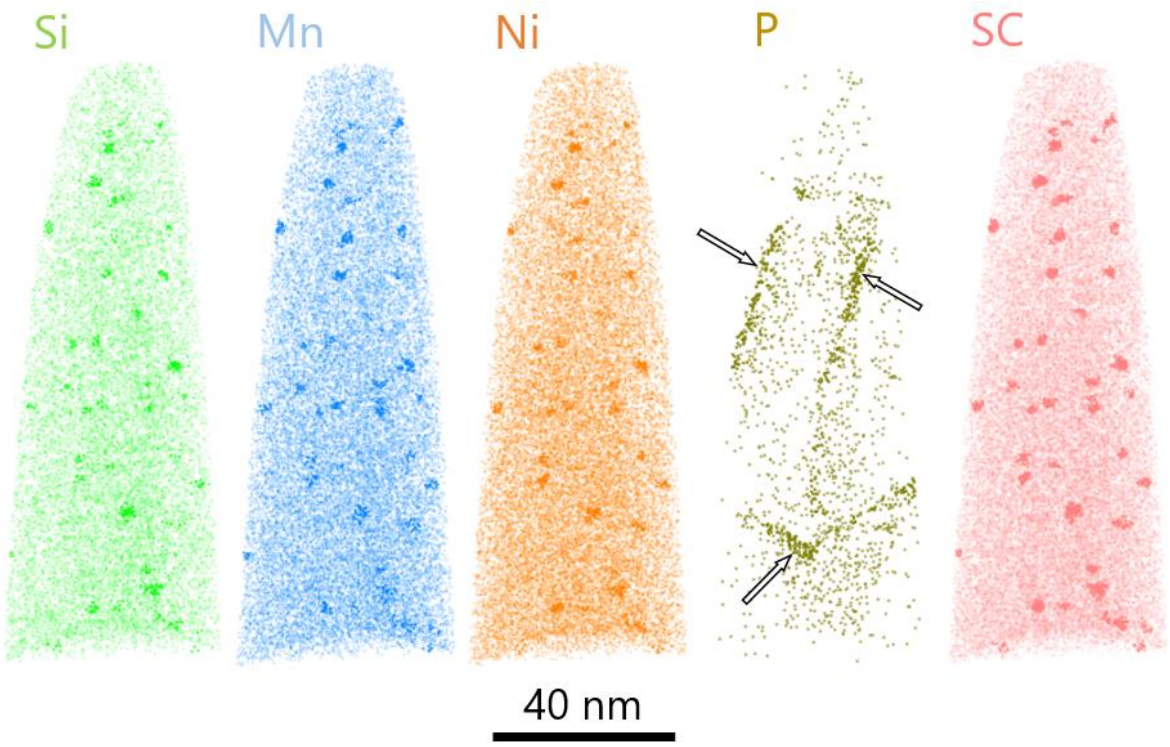

Figure 37. *Atom maps of steel F irradiated up to 0.13 dpa. Solute clusters enriched in Si, Mn, Ni and P are observed. Arrows indicate solute clusters on dislocation lines.*

In one APT experiment on the high dose condition, Mn concentration is three times higher than the average one (4.4 instead of 1.3 at. %), Ni concentration is two times higher (1.5 instead of 0.7 at. %) and Cu concentration is also around two times higher (0.1 instead of 0.05 at. %). In this APT experiment high number density of solute clusters of around (16 ± 2) x 10^{23} m^{-3} with an average radius of (1.8 ± 0.4) nm is identified (Fig. 36). Fe level inside these clusters (59 at. %) is lower than in other volumes at the given condition (~78 at. %). Contrary to other cases, P atoms are not found inside the solute clusters, but these clusters are enriched in Cu (0.85 at. %) and Al (0.48 at. %). Due to a significant difference in global composition, this volume is excluded from comparison with other experiments.

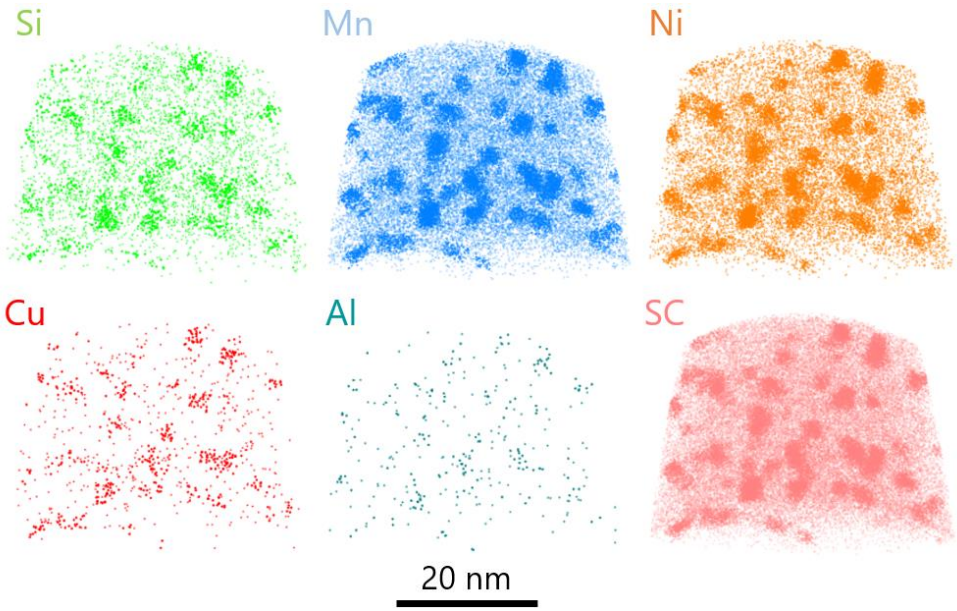

Figure 38. *Atom maps of enriched in solutes volume of steel F irradiated up to 0.13 dpa. Solute clusters enriched in Si, Mn, Ni, Cu and Al are observed.*

The results about solute cluster properties observed in steel F are reported in figures 39, 40 and 41. Figure 39 shows the number density as a function of dose, measured in each volume and averaged on all ones.

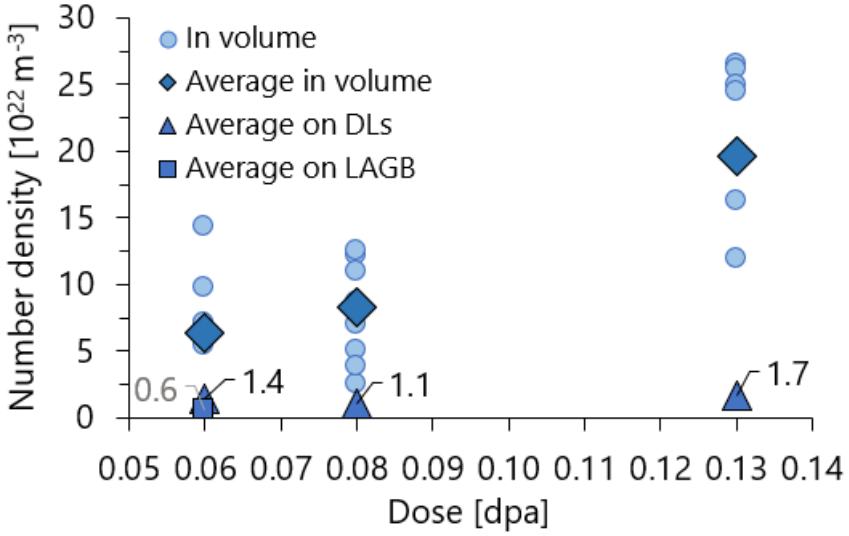

Figure 39. *Number density of solute clusters in steel F as a function of irradiation dose. Pale circles represent the number density of clusters inside ferrite matrix for each APT experiment. Diamonds represent the average number density of clusters inside ferrite matrix. Triangles (with black data labels) represent the average number density of clusters formed on dislocation lines. Square (with grey data label) represents the average number density of clusters formed on low-angle GB.*

The number density of clusters formed on dislocation lines doesn't evolve with accumulated dose. The number density of clusters inside the ferritic matrix at the medium dose of 0.08 dpa is

slightly higher than at the low dose of 0.06 dpa (8 vs 6 x 10^{22} m^{-3}). With further increase of irradiation dose up to 0.13 dpa, the number density significantly grows (20 x 10^{22} m^{-3}).

Size distribution of solute clusters located in the ferritic matrix, and along dislocation lines and LAGB are reported in figures 40 and 41 respectively. In both cases, the size is the equivalent spherical radius. Number density for each class size is also presented.

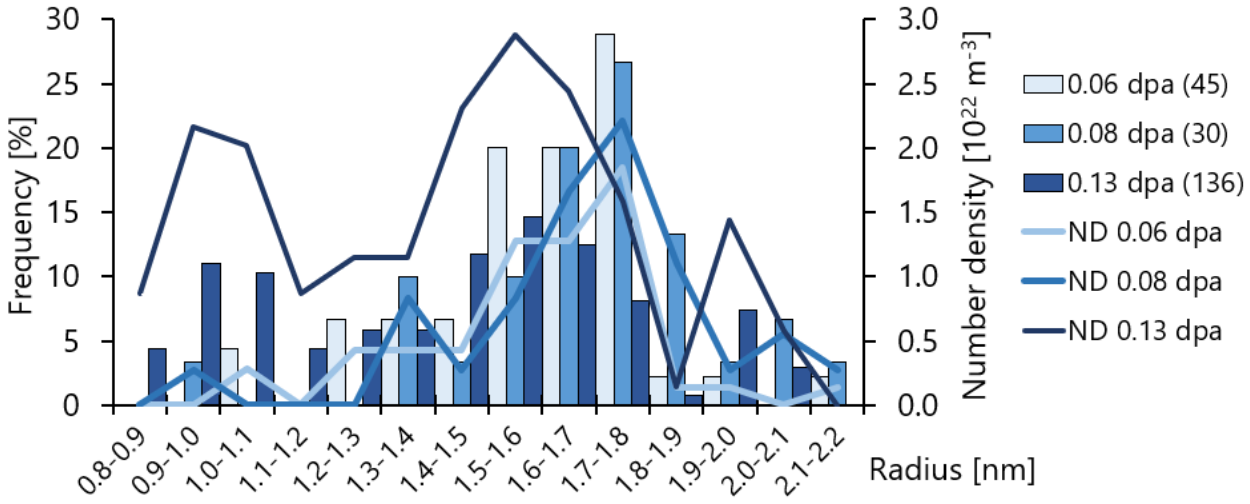

Figure 40. *Size distribution for clusters formed inside ferritic matrix.*

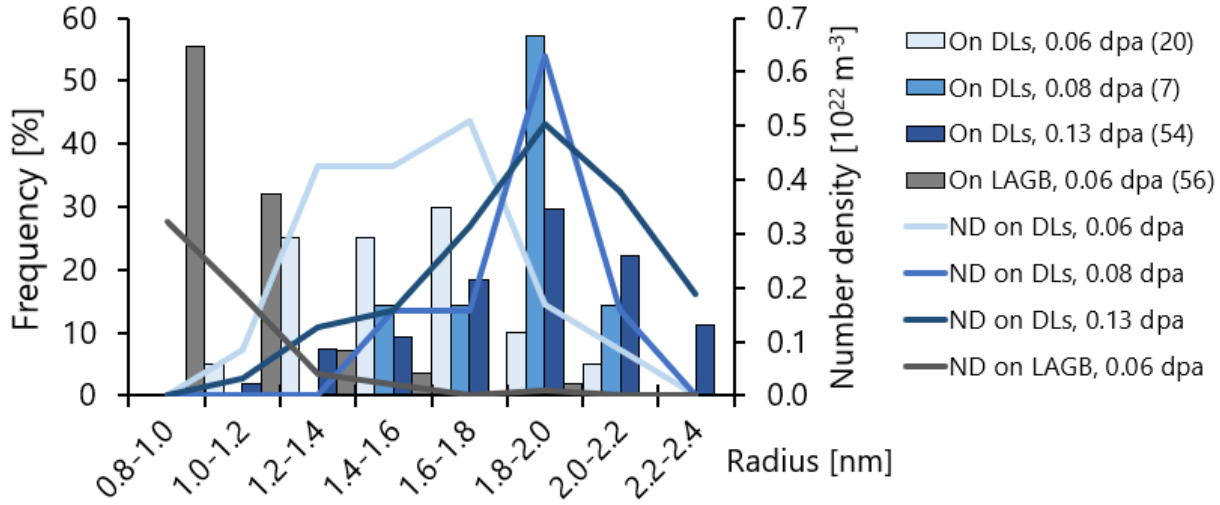

Figure 41. *Size distribution for clusters formed on dislocation lines and LAGB.*

The size of solute clusters formed inside ferritic matrix does not notably evolve from low to medium doses (1.6 vs 1.7 nm). At the highest dose, a bimodal cluster size distribution is observed, resulting in a lower mean size than for lower doses (1.4 vs ~1.6 nm). The detailed discussion about bimodal cluster size distribution observed here and in the case of steel E will be delivered in chapter IV. The size of clusters formed on dislocation lines slightly grows during irradiation from 0.06 to 0.08 dpa (1.6 to 1.8 nm). At 0.13 dpa radius of clusters formed on dislocation lines remains the same as at 0.08 dpa (1.8 nm), but a higher dispersion of sizes is observed (1 to 2.4 nm). Same as the case

of steel E, the average size of cluster formed on dislocation lines of LAGB is the smallest from all families (~1 nm).

The core composition of solute clusters is reported in Table 14. With the increase of irradiation dose, clusters inside ferritic matrix become more enriched in Si (2.9 to 5.4 at. %). No clear trend is observed for Mn (6.2 to 6.7 at. %) and Ni (7.0 to 8.1 at. %) considering error bars. Yet, the P concentration decreases with irradiation dose (3.3 to 1.4 at. %). Generally, higher levels of C (0.2 at. %), P (2.5 to 4.9 at. %) and Mo (~0.8 at. %) are found into the clusters formed along dislocation lines. Since clusters on LAGB were identified in the APT experiment in the laser mode, the results of composition measurements should be compared with care. These clusters are more enriched in C (1.3 at. %) and Mo (3.1 at. %), yet surprisingly low P content is measured (0.9 at. %).

Table 14. *Composition of solute clusters in steel F. Values are given in at. %. "nd" means not detected. The uncertainty margins are given by two standard deviations from APT data on a given condition. *Composition of clusters formed on LAGB is measured from the experiment in the laser mode.*

Type	Dose		Si	Mn	Ni	P	Cu	C	Mo	Fe
In volume	0.06		2.9	6.2	7.0	3.3	0.1	nd	0.4	80.1
	dpa	±	0.5	0.7	0.7	0.5	0.1		0.2	1.2
	0.08		3.8	5.8	7.2	1.7	0.1	nd	0.5	80.8
	dpa	±	0.6	0.7	0.8	0.4	0.1		0.2	1.2
	0.13		5.4	6.7	8.1	1.4	0.2	0.2	0.2	77.7
	dpa	±	0.4	0.4	0.5	0.2	0.1	0.1	0.1	0.7
On dislocations	0.06		1.8	5.6	4.7	4.9	nd	0.6	1.2	80.8
	dpa	±	0.5	0.9	0.9	0.9		0.3	0.5	1.6
	0.08		3.5	3.1	5.7	2.5	nd	0.1	0.7	84.4
	dpa	±	1.3	1.2	1.6	1.1		0.1	0.6	2.5
	0.13		3.5	4.0	5.0	2.6	nd	0.2	0.4	84.2
	dpa	±	0.4	0.5	0.5	0.4		0.1	0.1	0.8
On LAGB*	0.06		2.9	6.4	4.5	0.9	0.1	1.3	3.1	80.6
	dpa	±	0.8	1.1	1.0	0.4	0.1	0.5	0.8	1.8

Same as in the previous section, the evolution of relative cluster as a function of relative global solute contents is plotted (Fig. 42). Similar to steel E, higher Ni and lower Mn cluster over global ratios are observed. With increase of irradiation dose in materials with the same global Si concentration, the higher cluster Si content is measured. Mainly, with increase of global solute content, the cluster solute concentration also increases. This tendency is especially evident in the high dose (0.13 dpa) condition.

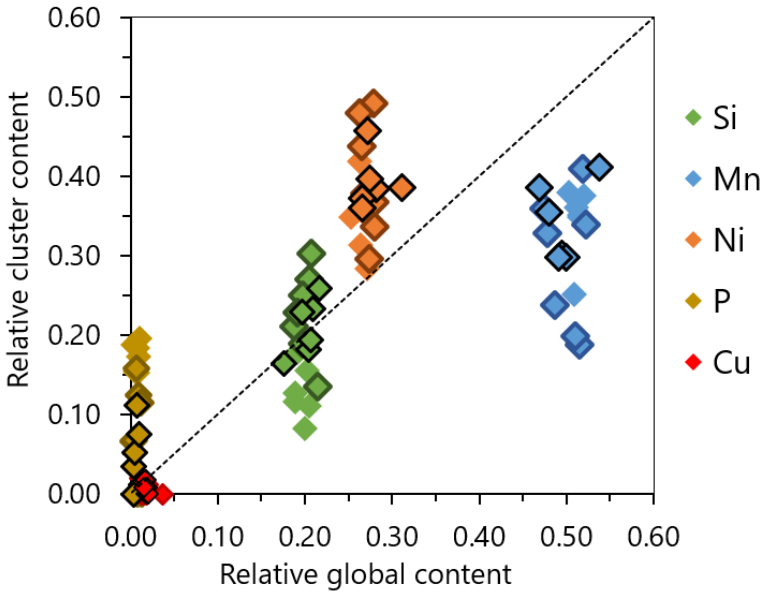

Figure 42. *Evolution of relative cluster solute content as a function of relative global solute content in steel F (both values are given excluding all chemical species except Si, Mn, Ni, P and Cu and normalised to 1). Each diamond represents the results obtained in one APT experiment. Low dose represented by symbols without border, medium dose by symbols with darker border and high dose by symbols with black border. 1:1 trend line is also plotted.*

In summary, solute clusters formed inside ferritic matrix and on dislocation lines are observed in steel F. Number density of clusters formed inside ferrite matrix increases with accumulation of irradiation dose. Same as in steel E, the average cluster radius grows from low to medium doses and decreases at high dose condition, due to the additional formation of smaller clusters. With increase of accumulated dose clusters become slightly more enriched in Si and less enriched in P. Mn and Ni cluster content insignificantly (~1 at. %) vary between irradiation conditions.

2.4 Steel I: 0.04 at.% Cu, 0.019 at.% P, 1.62 at.% Ni, 1.84 at.% Mn

Low-Cu (0.04 at. %), low-P (0.019 at. %), high-Ni (1.62 at. %), high-Mn (1.84 at. %) steel I[4] is selected to evaluate the effect of Ni and Mn/Ni synergy by comparing it with steel F. RPV steel I was irradiated up to medium (0.08 dpa) and high (0.13 dpa) doses.

Global and matrix concentrations of main elements are presented in Table 15. As in steels E and F, a high dispersion of the P global (0.009 to 0.057 at. %) and a deletion of P matrix

[4] It is important to keep in mind that these values are the bulk ones, including Mn into carbides. The Mn remaining in matrix in reference state, measured by APT is 1.11 at. %.

concentrations (~0.01 at. %) are observed at both irradiation doses. At the highest dose, the matrix is slightly depleted in Ni in comparison with the global concentration (decrease of 0.13 at. %).

Table 15. *Concentration of Si, Mn, Ni, P and Cu measured by APT (at. %). Uncertainty margins are represented by two standard deviations between APT experiments on a given condition.*

Dose	Volume		Si	Mn	Ni	P	Cu
Reference	Global/Matrix		0.53	1.11	1.61	0.019	0.046
		±	0.03	0.05	0.12	0.002	0.004
0.08 dpa	Global		0.58	1.11	1.47	0.012	0.038
		±	0.06	0.13	0.21	0.030	0.009
	Matrix		0.56	1.09	1.42	0.008	0.037
		±	0.05	0.13	0.22	0.012	0.009
0.13 dpa	Global		0.48	1.11	1.52	0.028	0.040
		±	0.10	0.19	0.17	0.037	0.006
	Matrix		0.43	1.05	1.39	0.016	0.035
		±	0.07	0.19	0.10	0.015	0.010

In the steel I, solute clusters enriched in Si, Mn, Ni, P are observed at all irradiation doses (Fig. 43 and 44). Here again, these clusters are located either in the ferritic matrix or along dislocation lines located in volume or being a part of low-angle GB.

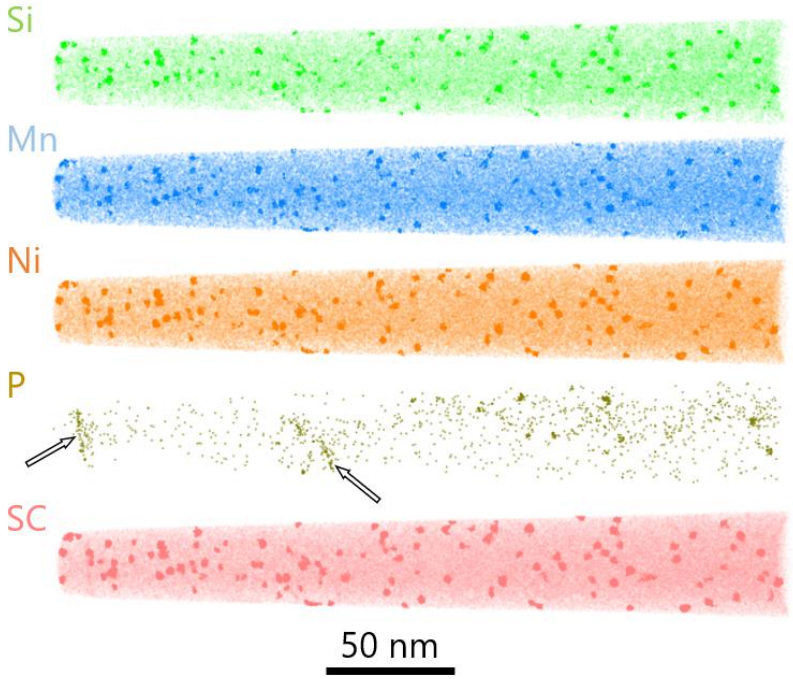

Figure 43. *Atom maps of steel I irradiated up to 0.08 dpa. Solute clusters enriched in Si, Mn, Ni and P are observed. Arrows indicate solute clusters on dislocation lines.*

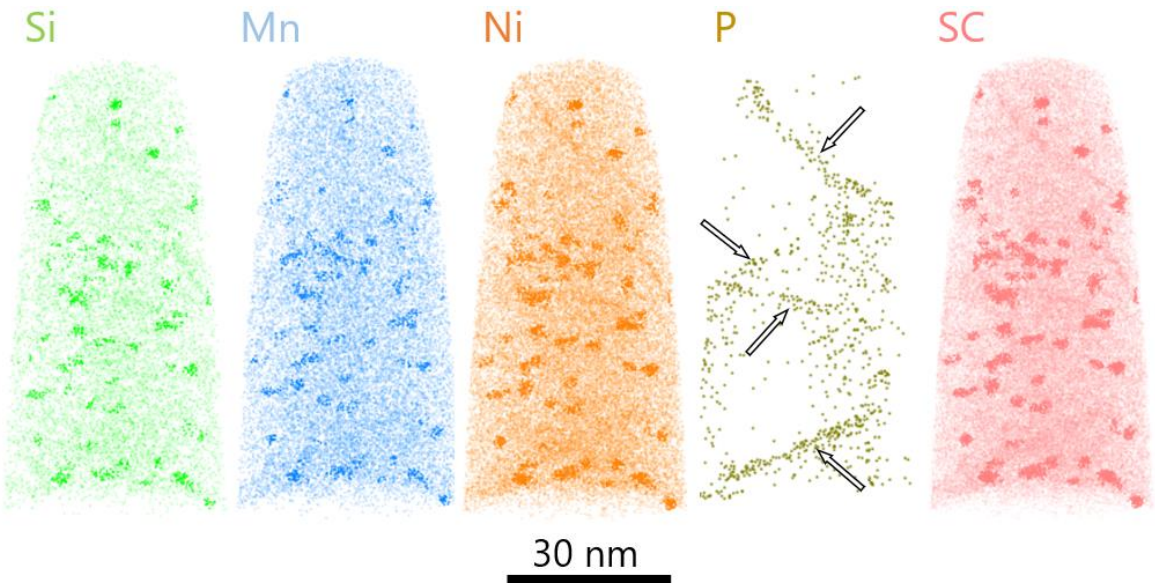

Figure 44. *Atom maps of steel I irradiated up to 0.13 dpa. Solute clusters enriched in Si, Mn, Ni and P are observed. Arrows indicate solute clusters on dislocation lines.*

After irradiation at 0.08 dpa, the number density of clusters inside ferritic matrix is around (4 ± 0.7) x 10^{23} m^{-3} with an average radius of (1.2 ± 0.2) nm. Number density of clusters formed on dislocation lines is significantly lower and equals to (1.9 ± 0.7) x 10^{22} m^{-3} with the average radius of around (1.4 ± 0.2) nm. The solute clusters found on the dislocation lines of the low-angle GB in one of the APT experiments are treated separately (atom maps and concentration profile are available in appendix B.1). Their number density equals to (0.9 ± 0.2) x 10^{22} m^{-3} and the average radius is (1.1 ± 0.2) nm. The number density of clusters on LAGB in steel I is 4 and 1.6 times larger than in steels E and F respectively (0.9 vs 0.24 and 0.58 x 10^{22} m^{-3}). The distance between dislocations in steel I in smaller than in steels E and F (6 vs 17 and 9 nm), and the calculated surface density in higher.

At the high dose (0.13 dpa), same as for medium dose, the majority of clusters are observed inside ferritic matrix. Their number density is (8 ± 1) x 10^{23} m^{-3} with an average radius of (1.1 ± 0.2) nm. The number density of clusters formed on dislocation lines is around (2.4 ± 0.7) x 10^{22} m^{-3} and the average radius is (1.4 ± 0.2) nm.

Figure 45 shows the average and per-volume number density of clusters as a function of irradiation dose. The number density of clusters inside the ferritic matrix is twice higher at 0.13 dpa than at 0.08 dpa (8 vs 4 x 10^{23} m^{-3}). With the increase of irradiation dose from 0.08 to 0.13 dpa average number density of clusters formed on dislocation lines increases too, but to a lesser extent (from 1.9 to 2.4 x 10^{22} m^{-3}).

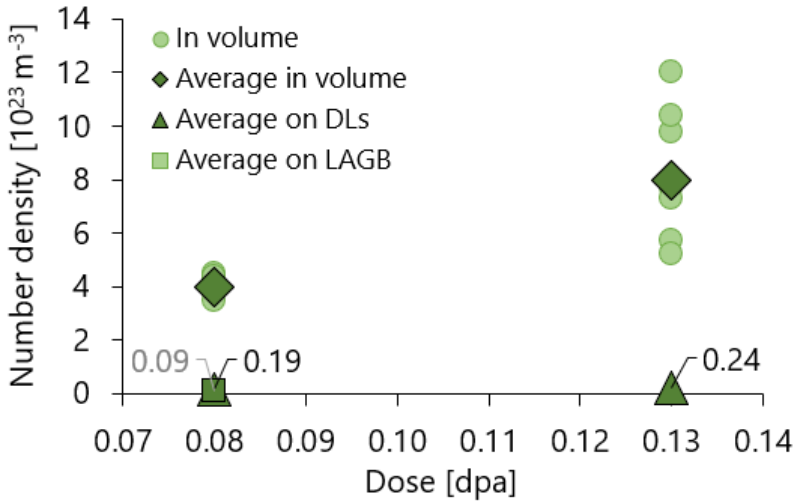

Figure 45. *Number density of* clusters *in steel I as a function of irradiation dose. Pale circles represent the number density of clusters inside ferrite matrix for each APT experiment. Diamonds represent the average number density of clusters inside ferrite matrix. Triangles (with black data labels) represent the average number density of clusters formed on dislocation lines. Square (with grey data label) represents the average number density of clusters formed on low-angle GB.*

Information about the cluster size distribution is reported in figures 46 and 47. Contrary to steels E and F, a monomodal size distribution for clusters formed inside ferritic matrix in the high dose condition is observed. A slight decrease in the average radius with accumulation of irradiation dose is visible.

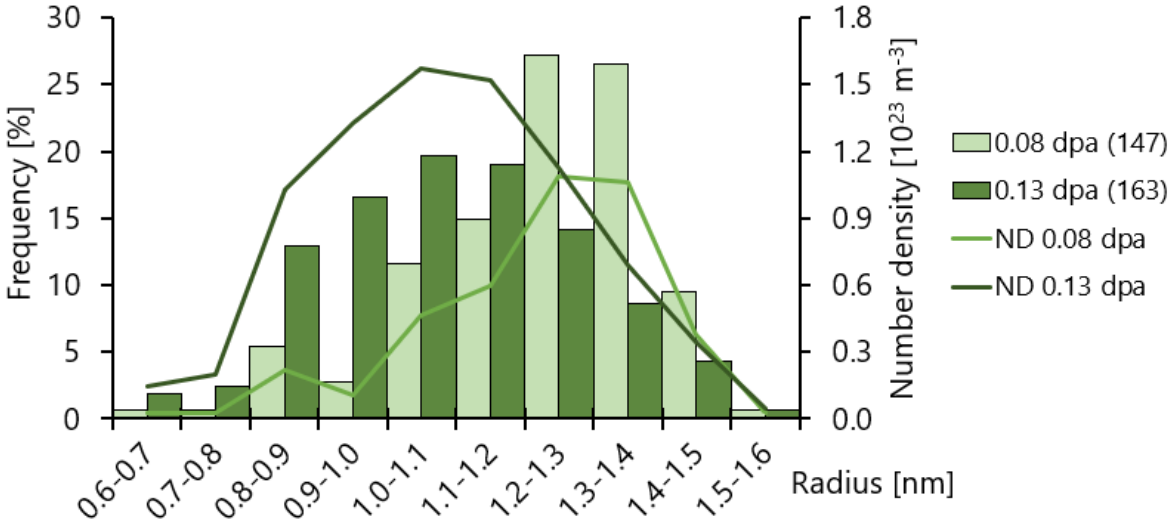

Figure 46. *Size distribution for clusters formed inside ferritic matrix.*

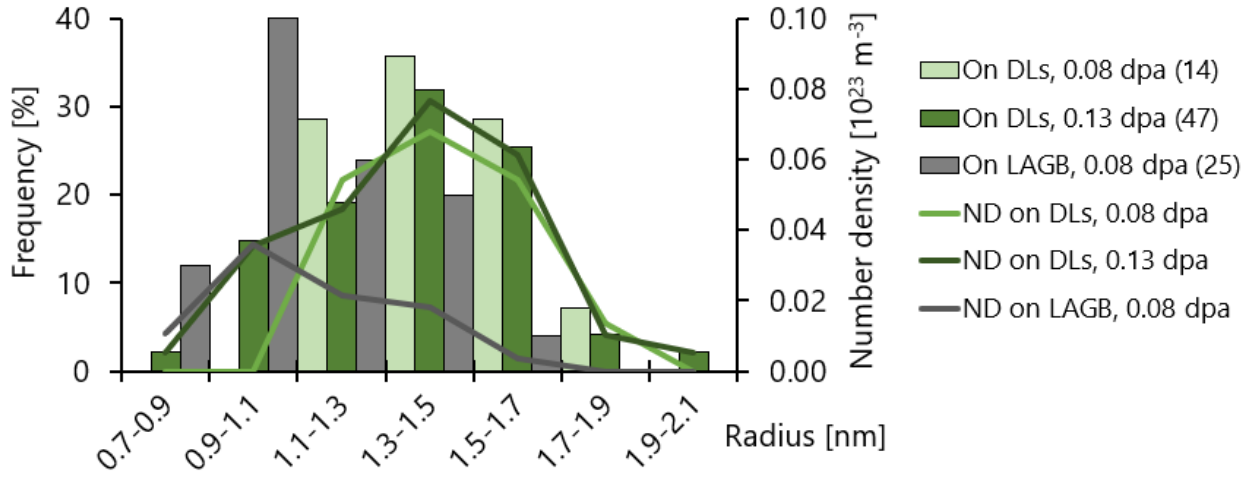

Figure 47. *Size distribution for clusters formed on dislocation lines and low-angle grain boundary.*

Detailed information about cluster composition evaluated after the plateau erosion is delivered in Table 16. Contrary to every material studied before, solute clusters inside ferritic matrix are slightly enriched in Al (~0.3 at. %). This tendency is not observed for clusters along dislocation lines. These former ones are more enriched in P (~2 vs ~0.6 at. %) and C (~0.3 vs 0 at. %) and less in Si (~4 vs ~6 at. %), Mn (~5 vs ~7 at. %) and Ni (~9 vs ~13 at. %). With the increase of irradiation dose clusters inside ferritic matrix became more enriched in Si, Mn and Ni. Contrary, P cluster content decreases with dose.

Table 16. *Composition of solute clusters in steel I (at. %). "nd" means not detected. The uncertainty margins are given by two standard deviations from APT data on a given condition.*

Type	Dose		Si	Mn	Ni	P	Cu	C	Mo	Al	Fe
In volume	0.08 dpa		6.0	5.3	12.7	0.9	0.2	nd	0.2	0.4	74.3
		±	0.6	0.5	0.8	0.2	0.1		0.1	0.1	1.0
	0.13 dpa		6.2	7.7	13.8	0.3	0.2	nd	0.3	0.3	70.4
		±	0.7	0.7	0.9	0.2	0.1		0.2	0.1	1.2
On dislocations	0.08 dpa		3.6	4.9	8.8	2.5	nd	0.2	0.4	0.1	79.6
		±	0.9	1.0	1.4	0.7		0.2	0.3	<0.1	1.9
	0.13 dpa		3.2	4.3	9.0	2.1	nd	0.3	1.0	0.2	79.9
		±	0.5	0.6	0.9	0.4		0.2	0.3	0.1	1.2
On LAGB	0.08 dpa		3.6	4.9	7.9	2.0	0.2	0.8	1.0	0.2	79.6
		±	0.7	1.1	0.9	0.6	0.2	0.3	0.4	0.2	1.6

Comparison between cluster and global relative solute contents (both values are given excluding all chemical species except Si, Mn, Ni, P and Cu and normalised to 1) is reported in figure 48.

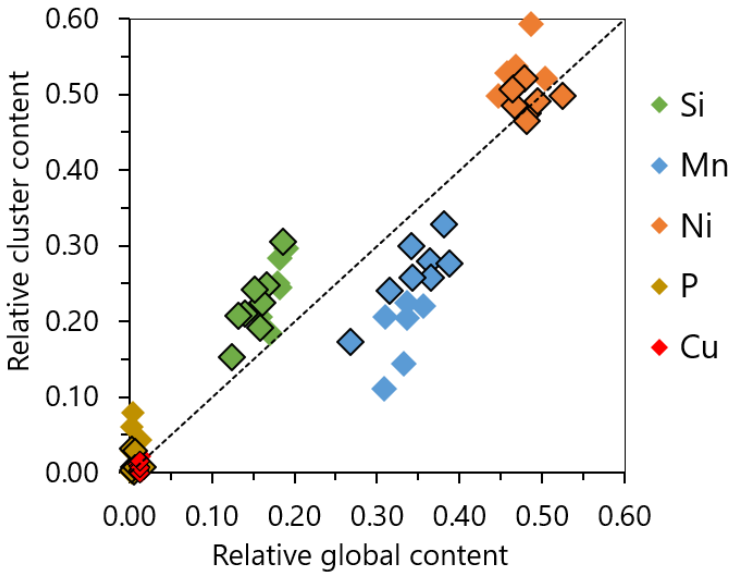

Figure 48. *Evolution of relative cluster solute content as a function of relative global solute content in steel I irradiated at 0.08 and 0.13 dpa. Each diamond represents the results obtained in one APT experiment. Medium dose is represented by symbols without border and high dose by symbols with black border. 1:1 trend line is also plotted.*

Same as in other steels, Mn cluster over global ratio is below 1:1 line. Yet, with increase of irradiation dose from 0.08 to 0.13 dpa, Mn symbols are located closer to 1:1 line and a higher Mn cluster enrichment is measured. The other difference in comparison with steels E and F, is the higher Si cluster content (above 1:1 line). At the same time symbols representing Ni are located lower and closer to 1:1 line. P relative cluster content is lower than in steels E and F. Generally, the tendency where higher cluster solute content is measured in volumes with the higher global solute concentration is evident.

Results described previously are obtained from ferritic phase (composition similar to the nominal one). In several APT experiments, solute enriched or depleted ferritic and austenitic phases, carbides and interfaces are observed. These results are described further.

In one of APT experiments (R5209), two enriched in solutes regions are intercepted (Fig. 49). The first one is a ferritic phase enriched in Ni (2 at. %) and C (0.5 at. %). The second grain is enriched in Mn (3.8 at. %), Ni (3 at. %), C (2.2 at. %) and Cu (0.084 at. %). The second region has a composition similar to the austenitic phase studied in the non-irradiated state. Also, no pole figures were identified of APT detector map. Hence, a conclusion is made that the second grain is austenite. No solute cluster in the austenitic phase were found, which is coherent with literature data in which clusters in austenitic steels were only observed at higher irradiation doses of several dpa [23,24]. The number density of clusters in ferritic area is (10 ± 3) x 10^{23} m^{-3}, which is by a factor of 2.5 larger than the average measured at medium dose (4 x 10^{23} m^{-3}). The average cluster radius is (1.1

± 0.1) nm and is similar to the average radius in other APT experiments (1.2 nm). Due to the high Ni global content and atypical number density, the results obtained on this volume are not included in the average calculation.

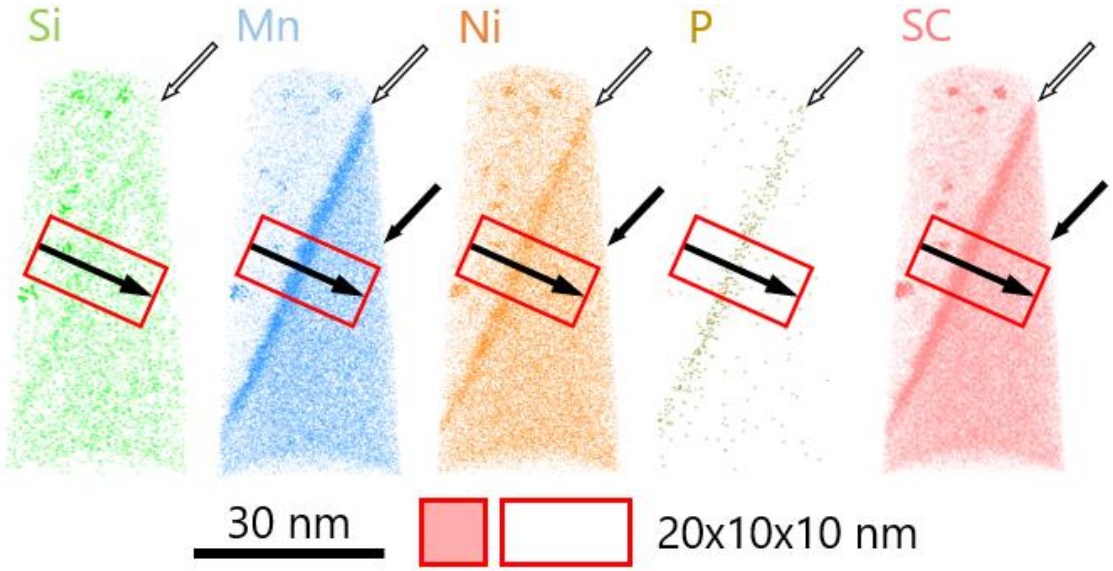

Figure 49. *Atom maps of steel I irradiated up to 0.08 dpa. White arrows indicate GB with solute segregation. Black arrows indicate austenitic phase enriched in Mn, Ni, C and Cu.*

The concentration profile through ferrite / austenite interface is plotted and presented in figure 50. Enrichments in C, P, Mn, Mo and Ni at the interface region are observed (Table 17). Additional profile where only P and Mo (low concentration) are presented is available in appendix B.1.

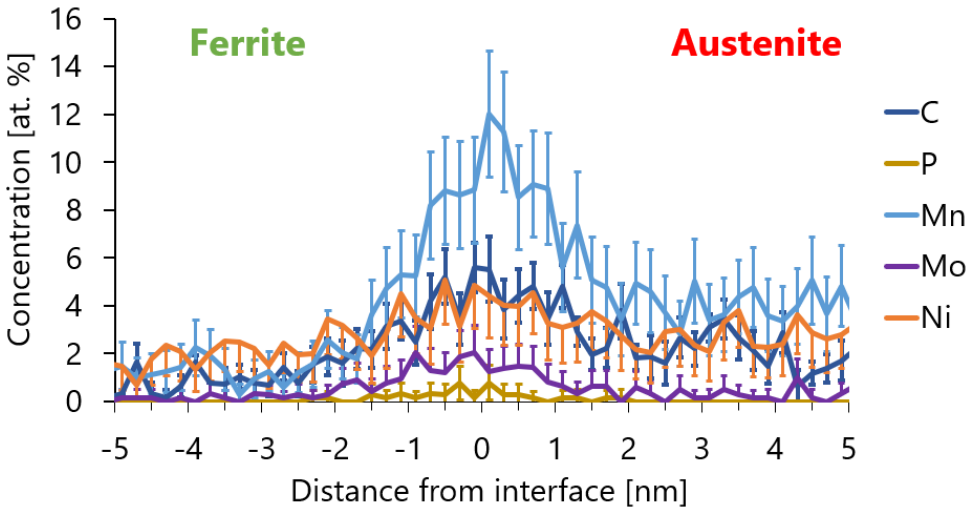

Figure 50. *Concentration profile plotted through ferrite / austenite interface. Enrichments in C, P, Mn, Mo and Ni atoms are visible. Error margins are represented by two standard deviations. For visual simplicity, for some of the solutes the error margins only in one direction are presented.*

Table 17. *Solute concentrations at ferrite / austenite interface. Uncertainty margins are represented by two standard deviations.*

Element	Average concentration at interface region [at. %]	Nominal concentration [at. %]	Enrichment factor
C	4.3 ± 0.5	0.1 ± 0.1	44.8
P	0.5 ± 0.2	0.019 ± 0.004	24.2
Mn	8.9 ± 0.7	1.1 ± 0.1	8.0
Mo	1.6 ± 0.3	0.2 ± 0.1	7.4
Ni	4.1 ± 0.5	1.6 ± 0.2	2.6

Another volume with M_3C carbide (Fe-25C-12Mn-1Mo) and austenite phase enriched in Mn (4.3 at. %), Ni (3.4 at. %), C (2.1 at. %) and Cu (0.105 at. %) is studied (Fig. 51). No solute clusters are observed in both carbide and austenite grain. The concentration profile through the interface is plotted and showed in figure 52.

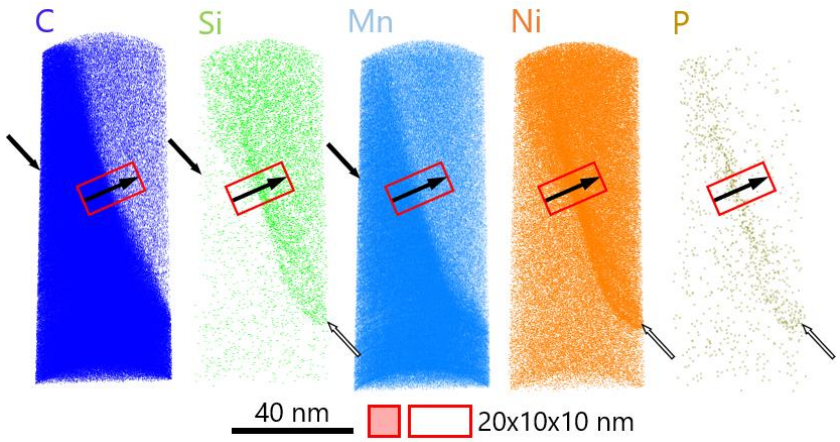

Figure 51. *Atom maps of steel I irradiated up to 0.08 dpa. Black arrows indicate M_3C carbide enriched in C and Mn and depleted in Si. White arrows indicate carbide / austenite interface.*

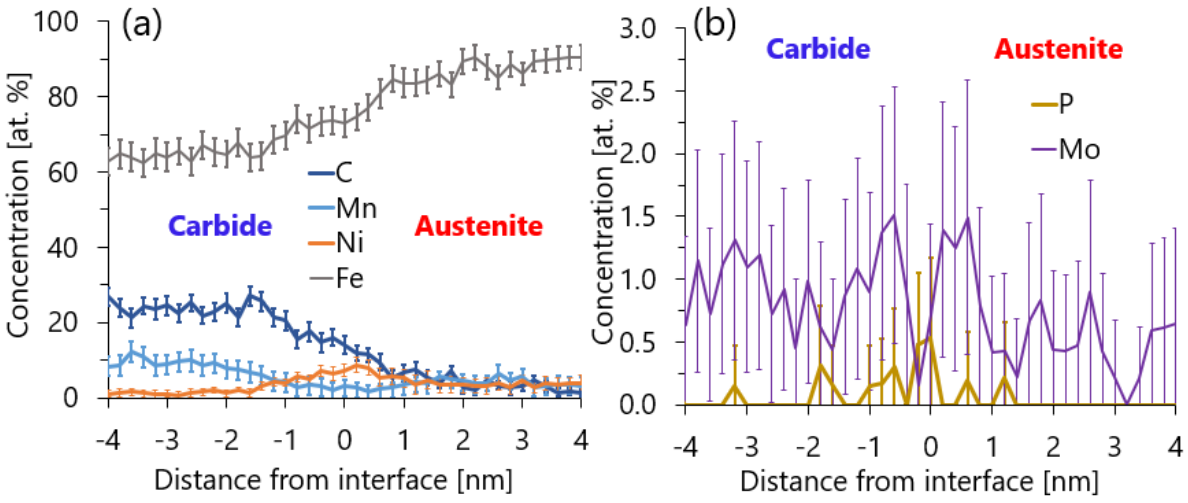

Figure 52. *Concentration profiles of carbide / austenite interface. (a) For C, Mn, Ni and Fe atoms. (b) For P and Mo atoms. Error margins are represented by two standard deviations.*

Higher concentrations of C, P, Mn, Mo and Ni atoms are measured at the interface. Yet, in the case of C, Mn and Mo atoms, no interface enrichment is evaluated. The enrichment factors equal to around 24 for P atoms (0.5 ± 0.2 vs 0.019 ± 0.004 at. %) and to ~2.6 for Ni (4.1 ± 0.5 vs 1.6 ± 0.1 at. %).

In material irradiated up to the high dose the enriched in solutes phases are also observed. The first examples (R5224) are the ferritic phase depleted in Mn (0.76 vs 1.11 at. %) and M_3C carbide (Fe-25C-15Mn-2Mo). The atoms maps are represented in figure 53. Like in other cases, no solute cluster in carbide was found. The number density of cluster formed inside the volume of ferritic matrix is (5 ± 0.5) x 10^{23} m^{-3} with an average radius of (1.1 ± 0.1) nm. Number density of clusters formed on dislocation lines is (2 ± 0.5) x 10^{22} m^{-3} with an average radius of (1.4 ± 0.1) nm.

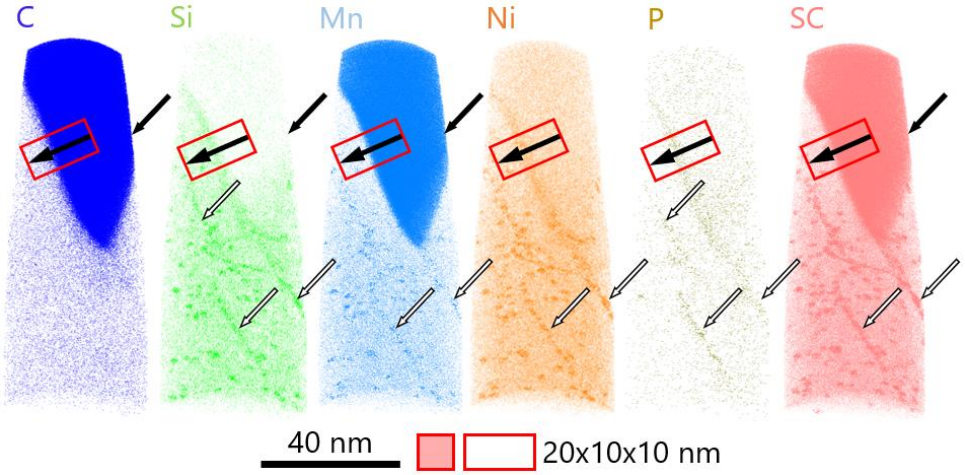

Figure 53. *Atom maps of steel I irradiated up to 0.13 dpa. Black arrows indicate M_3C carbide enriched in C and Mn and depleted in Si. White arrows indicate clusters formed on dislocation lines.*

Evolution of solute concentration through the carbide / ferrite interface is shown in figure 54. The interface is enriched in P atoms (0.3 ± 0.2 vs 0.019 nominal at. %) by a factor of 14.2.

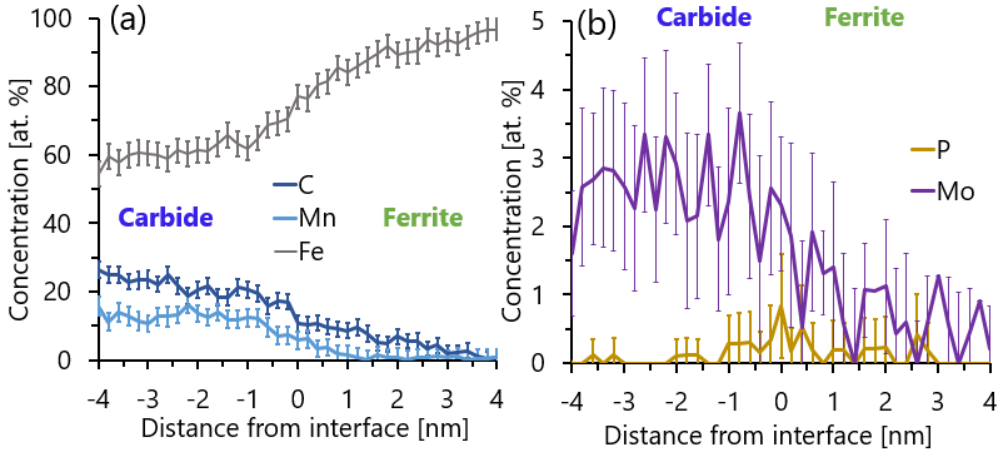

Figure 54. *Concentration profiles of carbide / ferrite interface. (a) For C, Mn and Fe atoms. (b) For P, Si, Ni and Mo atoms. Error margins are represented by two standard deviations.*

Another volume (R5222) with an atypical solute enrichment is observed in steel I irradiated up to 0.13 dpa (Fig. 55). It is enriched in Mn (3.9 at. %), Ni (2.7 at. %), C (0.9 at. %) and Cu (0.067 at. %). In this volume, a large number density of solute clusters (23 ± 1) x 10^{23} m^{-3} with the average radius of (1.3 ± 0.2) nm is observed. The cluster number density and the average radius are comparable to the results obtained in high-Ni (~3 at. %) model RPV materials irradiated up to ~0.2 dpa [25,26].

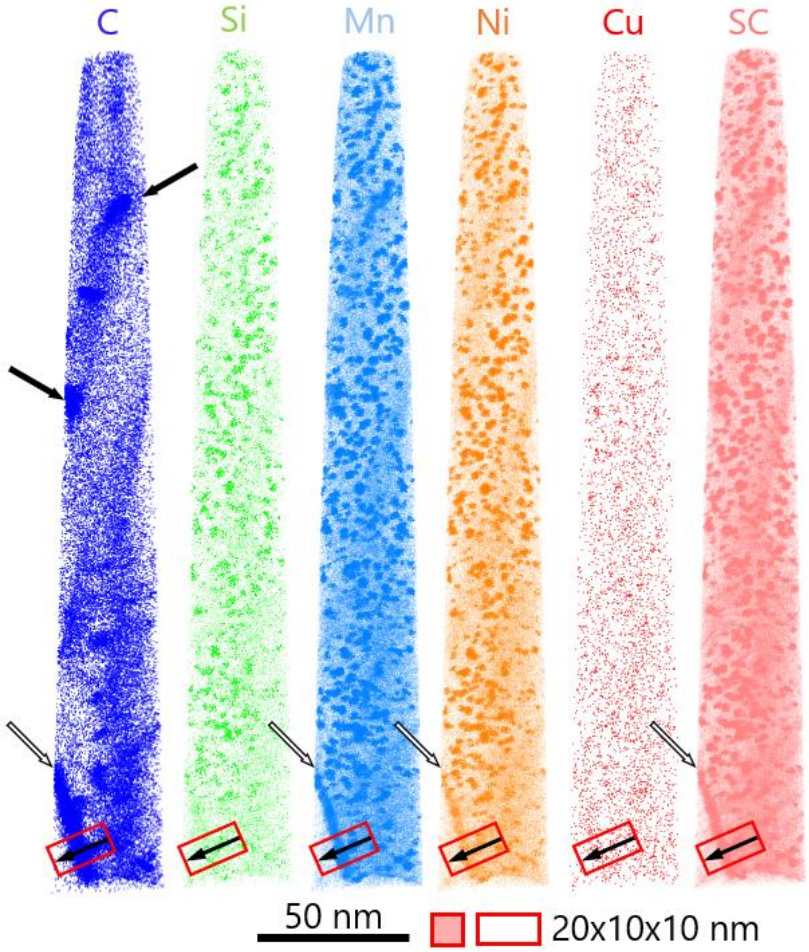

Figure 55. *Atom maps of steel I irradiated up to 0.13 dpa. White arrow indicates the interface between enriched and regular ferritic phases. Black arrows indicate C segregations.*

The composition of the enriched phase is equivalent to the composition of austenitic phases studied in steel I at non-irradiated and irradiated states. But, contrary to all other cases, solute clusters were identified. Yet, clustering is not expected in austenitic steels at the dose of 0.13 dpa [23,24].

As it was noted before, no crystallographic orientations are visible on the APT detector maps of austenitic volumes. The APT detector desorption maps of multiple events are reported in figure 54. In the case of enriched phase (Fig. 56.a) detector map is more disturbed and blurrier than in

ferrite (Fig. 56.c), albeit it doesn't look like a typical map obtained from the austenitic volume (Fig. 56.b). The [011] pole is identified, and the correct interplanar distances for bcc lattice (~0.2 nm) are obtained. The conclusion is made that enriched in solutes phase is, in fact, ferrite.

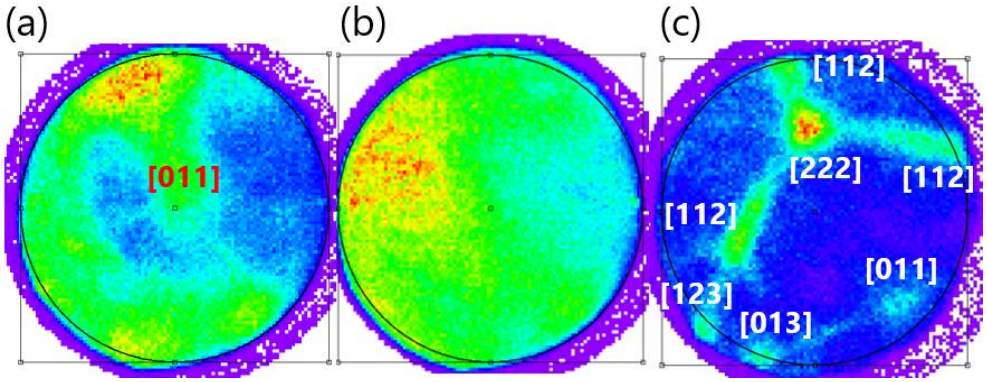

Figure 56. *APT detector desorption maps of multiple events. (a) Enriched in solutes grain. (b) Austenite grain. (c) Ferrite grain.*

As it is evident from the concentration prolife presented in figure 57, the GB region is enriched in C, P, Mn, Mo and Ni. A separate graph for elements with low nominal solute content (P and Mo) is given in appendix B.1. Enrichment at GB region measured at half-maximum of solute concentration is reported in Table 18.

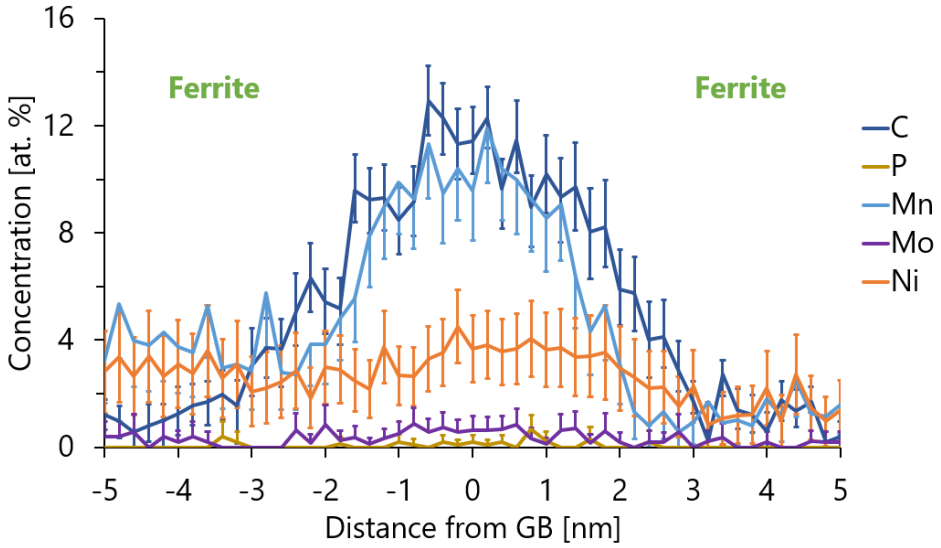

Figure 57. *Concentration profile through GB. Enrichment in C, P, Mn, Mo and Ni atoms is observed. Error margins are represented by two standard deviations.*

Table 18. *Solute concentrations at GB. Uncertainty margins are represented by two standard deviations.*

Element	Average concentration at GB region [at. %]	Nominal concentration [at. %]	Enrichment factor
C	10.5 ± 0.5	0.1 ± 0.1	109.1
P	0.5 ± 0.2	0.019 ± 0.004	23.8
Mn	8.9 ± 0.5	1.1 ± 0.1	8.6
Mo	0.7 ± 0.1	0.2 ± 0.1	3.1
Ni	3.6 ± 0.3	1.6 ± 0.1	2.2

Most of the studied interfaces have high P (factor of 20) and Mo (factor of 8) enrichments. Both P and Mo are known to segregate to GBs and interfaces during thermomechanical treatment. Also, promoted by irradiation, P GB/interface segregation is well documented. Significant enrichments in C (factor of 40), Mn (factor of 8) and Ni (factor of 3) at the interfaces between ferritic and austenitic phase are observed.

Finally, since several regions with atypical solute concentrations were studied, the evolution of the relative cluster as a function of relative global solute contents is reported in figure 58. In these experiments P and Cu cluster contents are significantly lower than of Si, Mn and Ni, and for visual simplicity are not presented.

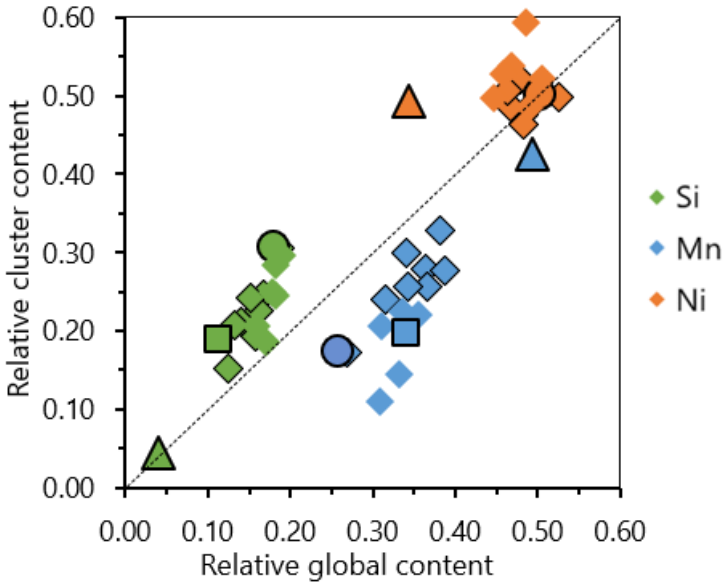

Figure 58. *Evolution of relative cluster solute content as a function of relative global solute content in steel I (both values are given excluding all chemical species except Si, Mn, Ni, P and Cu and normalised to 1). Diamond symbols represent the clusters formed in "normal" ferritic matrix (with no borders for 0.08 dpa and with black borders for 0.13 dpa). Square symbols represent experiment R5209. Triangles represent clusters from R5222. Circle symbols represent the clusters from experiment R5224. 1:1 trend line is also plotted.*

The Mn and Si cluster over global ratios in R5209 and R 5224 volumes follow almost the same tendency as clusters in "normal" steel I (Mn below and Si above 1:1 lime). In the case of experiment R5222, even though global Mn and Ni contents are by a factor of ~3 higher than the nominal value, Mn and Si cluster solute relative content still distributed around 1:1 line. Albeit, higher Ni relative cluster over relative global ratio is observed.

In conclusion, a high density of solute clusters formed inside ferrite volume and on dislocation lines and low-angle GB was measured. Number density of clusters located into ferritic matrix increases with irradiation dose. Average cluster radius remains almost the same. Clusters are more enriched in Si, Mn and Ni, and less in P, than steels E and F. Different types of enriched/depleted in solute ferritic and austenitic phases and carbides were observed.

2.5 Steel N: 0.05 at.% Cu, 0.037 at.% P, 0.67 at.% Ni, 1.51 at.% Mn

Low-Cu (0.05 at. %), medium-P (0.037 at. %), medium-Ni (0.67 at. %), high-Mn (1.51 at. %) steel N[5] is selected to study the effect of P on microstructure evolution under neutron irradiation. APT is utilised to evaluate the global and matrix solute concentrations in reference state and after irradiation up to 0.075 dpa. The results reported in Table 19.

Table 19. *Concentration of Si, Mn, Ni, P and Cu measured by APT (at. %). Uncertainty margins are represented by two standard deviations between APT experiments on a given condition.*

Dose	Volume		Si	Mn	Ni	P	Cu
Reference	Global/Matrix		0.48	1.05	0.62	0.030	0.040
		±	0.05	0.07	0.03	0.004	0.014
0.08 dpa	Global		0.48	1.07	0.69	0.026	0.043
		±	0.04	0.15	0.08	0.026	0.005
	Matrix		0.47	1.06	0.68	0.021	0.043
		±	0.04	0.14	0.08	0.026	0.005

After irradiation ferritic matrix is only slightly depleted in P. Even though global P content is 1.5 times higher than in steels E, F and I (0.03 vs ~0.02 at. %), the matrix depletion is on a similar level (~0.01 at. %).

Solute clusters formed in the ferritic matrix and on dislocation lines are visible (Fig. 59). Same as in other steels, they are enriched in Si, Mn, Ni and P. The number density of clusters inside ferritic matrix is around $(5 \pm 2) \times 10^{22}$ m^{-3} with the average radius of around (1.4 ± 0.3) nm. The

[5] It is important to keep in mind that these values are the bulk ones, including Mn into carbides. The Mn remaining in matrix in reference state, measured by APT is 1.05 at. %.

number density of clusters formed along dislocation lines is lower by a factor 3: (1.8 ± 0.6) x 10^{22} m^{-3}. The average radius of latter is about (1.6 ± 0.3) nm.

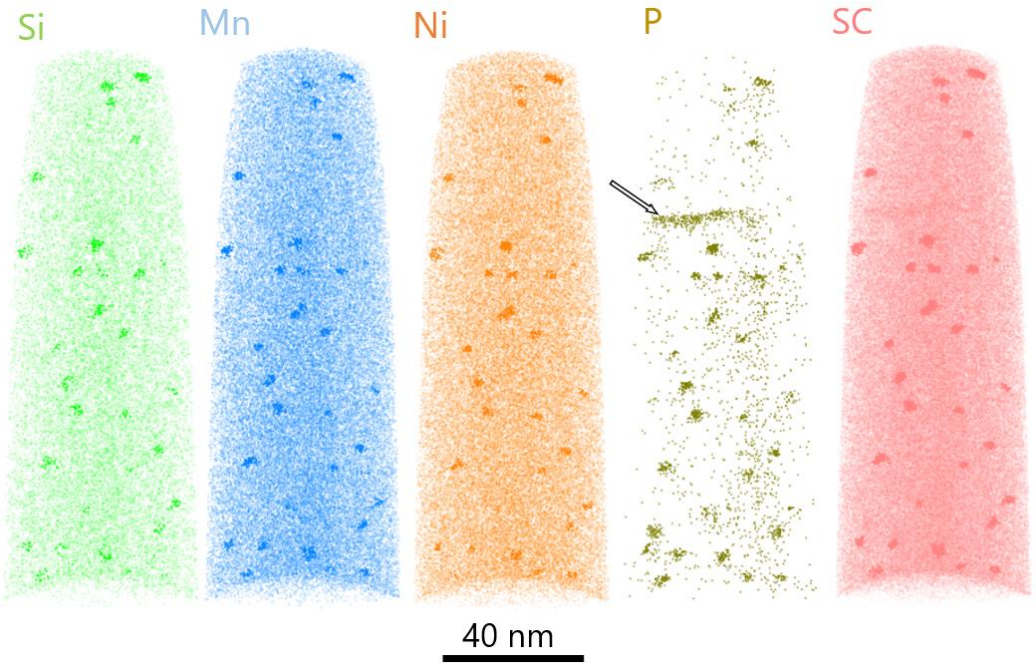

Figure 59. *Atom maps of steel N irradiated up to 0.075 dpa. Solute clusters enriched in Si, Mn, Ni and P are observed. Arrow indicates solute clusters on dislocation line.*

Steel N is one of the cases where the APT experiment in the laser-assisted mode is performed. In this volume, a low-angle grain boundary composed of edge dislocations is intercepted (Fig. 60). Alongside these dislocation lines, solute clusters were identified (concentration profile is available in appendix B.1). Their number density is (0.3 ± 0.05) x 10^{22} m^{-3}, and the average radius is (1.4 ± 0.1) nm. The misorientation angle of LAGB is 1.2° and the distance between dislocations is 12 nm.

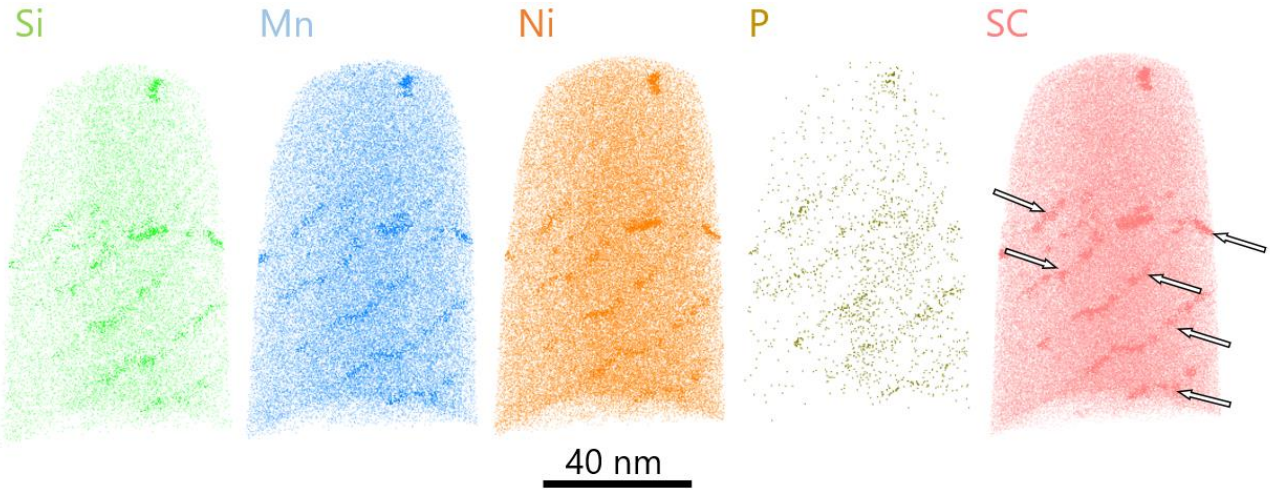

Figure 60. *Atom maps of steel N irradiated up to 0.075 dpa. Arrows indicate solute clusters formed on low-angle GB. This volume was obtained in laser mode.*

Cluster size distribution is reported in figure 61. Same as in other steels, clusters formed on dislocation lines (1.6 nm) are bigger than the ones formed in volume (1.4 nm) and on LAGB (1.4 nm). The size distribution clusters located in the ferritic matrix is rather large (0.7 to 2 nm).

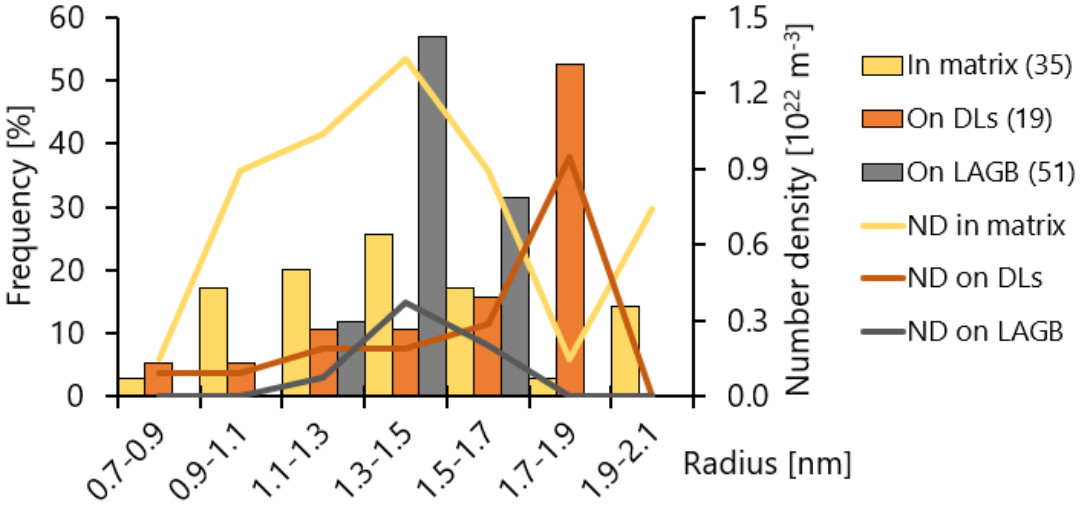

Figure 61. *Cluster size distribution in steel N irradiated up to 0.075 dpa.*

Clusters identified inside the ferritic matrix are more enriched in Mn (5.2 vs 3.5 at. %) and Ni (5.4 vs 4.2 at. %), and less in C (0 vs 0.2 at. %) and Mo (0.1 vs 0.7 at. %) than the ones formed on dislocation lines. In-volume clusters have lower total solute content than in other steels (16.7 vs >20 at. %). Clusters formed on low-angle GB (the experiment in the laser mode) are less enriched in Si (1.5 vs ~ 2.7 at. %) and P (1.5 vs ~3.4 at. %) than the other two families. Results of composition measurements are reported in Table 20.

Table 20. *Composition of solute clusters in steel N. Values are given in at. %. "nd" means not detected. The uncertainty margins are given by two standard deviations. *Composition of clusters formed on LAGB is measured from the experiment in the laser mode.*

Type	Dose		Si	Mn	Ni	P	Cu	C	Mo	Fe
In volume	0.075 dpa		2.8	5.2	5.4	3.1	0.2	nd	0.1	83.3
		±	0.6	0.8	0.8	0.6	0.1		0.1	1.4
On dislocations	0.075 dpa		2.6	3.5	4.2	3.7	nd	0.2	0.7	85.0
		±	0.5	0.6	0.6	0.6		0.2	0.3	1.1
On LAGB*	0.075 dpa		1.5	6.2	5.3	1.5	nd	0.2	0.5	84.8
		±	0.3	0.5	0.5	0.3		0.1	0.2	1.5

Solute clusters formed inside the ferritic matrix were identified in only four APT experiments. Their relative solute concentrations as a function of global solute contents for each APT experiment are presented in figure 62.

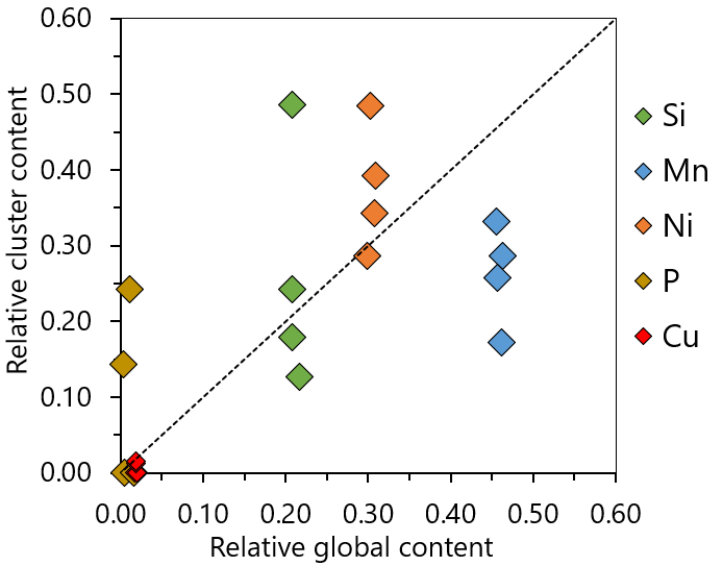

Figure 62. *Evolution of relative cluster solute content as a function of relative global solute content in steel N irradiated up to 0.075 dpa (both values are given excluding all chemical species except Si, Mn, Ni, P and Cu and normalised to 1). Each diamond represents the results obtained in one APT experiment. 1:1 trend line is also plotted.*

The high dispersion of relative cluster contents between APT experiments is observed. Also, similar to the other steels, Mn symbols are located below 1:1 line which corresponds to lower Mn cluster over global ratio. Same as in steels E and F symbols representing Ni and Si are distributed above and around 1:1 line correspondingly.

To summarise, in steel N irradiated up to 0.075 dpa, solute clusters formed inside ferritic matrix, on dislocation lines and on low-angle GB were observed. These clusters are more enriched in P but have a lower total solute content than other studied steels.

2.6 Steel O: 0.05 at.% Cu, 0.054 at.% P, 0.66 at.% Ni, 1.50 at.% Mn

Low-Cu (0.05 at. %), high-P (0.054 at. %), medium-Ni (0.66 at. %), high-Mn (1.50 at. %) steel O[6] is the second material selected to study the effect of P on microstructure evolution under neutron irradiation. Material irradiated up to the dose of 0.063 dpa is available for APT research.

Global and matrix concentrations of solutes of interest are reported in Table 21. Only a very slight depletion in P is observed in the irradiated matrix.

[6] It is important to keep in mind that these values are the bulk ones, including Mn into carbides. The Mn remaining in matrix in reference state, measured by APT is 0.99 at. %.

Table 21. *Concentration of Si, Mn, Ni, P and Cu measured by APT (at. %). Uncertainty margins are represented by two standard deviations between APT experiments on a given condition.*

Dose	Volume		Si	Mn	Ni	P	Cu
Reference	Global/Matrix		0.52	0.99	0.63	0.048	0.043
		±	0.04	0.10	0.05	0.009	0.006
0.063 dpa	Global		0.60	1.07	0.75	0.055	0.057
		±	0.09	0.12	0.05	0.021	0.007
	Matrix		0.60	1.07	0.75	0.048	0.056
		±	0.09	0.12	0.05	0.022	0.006

Solute clusters were observed in every APT experiment. Atom maps of Si, Mn, Ni and P are shown in figure 63. The number density of clusters formed inside ferritic matrix is around $(12 \pm 4) \times 10^{22}$ m^{-3} with the average radius of (1.2 ± 0.2) nm. The number density of clusters formed on dislocation lines is smaller by a factor of 6 and is about $(2 \pm 2) \times 10^{22}$ m^{-3} with the average radius of (1.2 ± 0.2) nm.

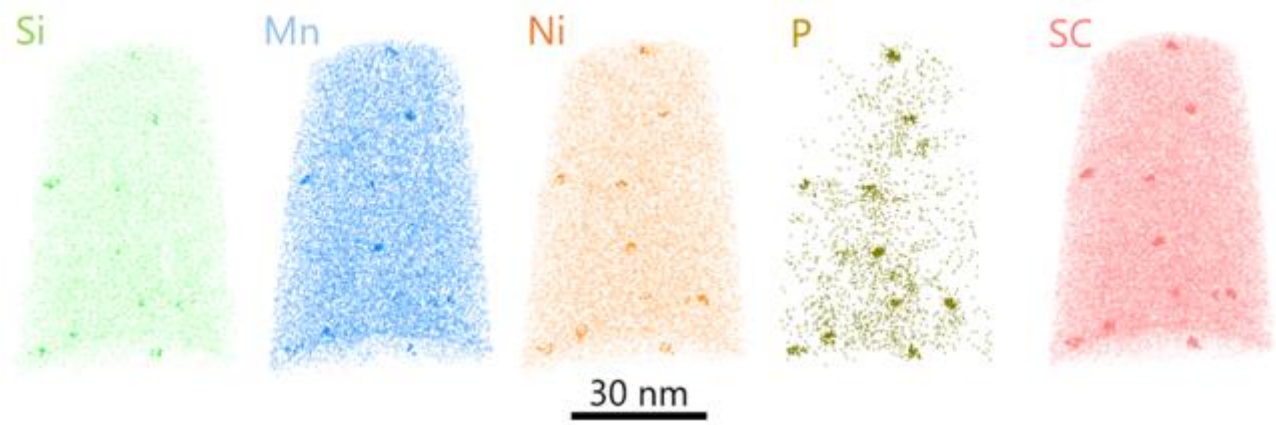

Figure 63. *Atom maps of steel O irradiated up to 0.063 dpa. Solute clusters enriched in Si, Mn, Ni and P are observed.*

The cluster size distribution is shown in figure 64. Clusters formed inside ferritic matrix have a monomodal size distribution and their size ranges from 0.7 to 1.7 nm. Only 5 clusters formed on dislocation lines are studied. The latter have a thinner size distribution, ranging from 0.9 to 1.5 nm.

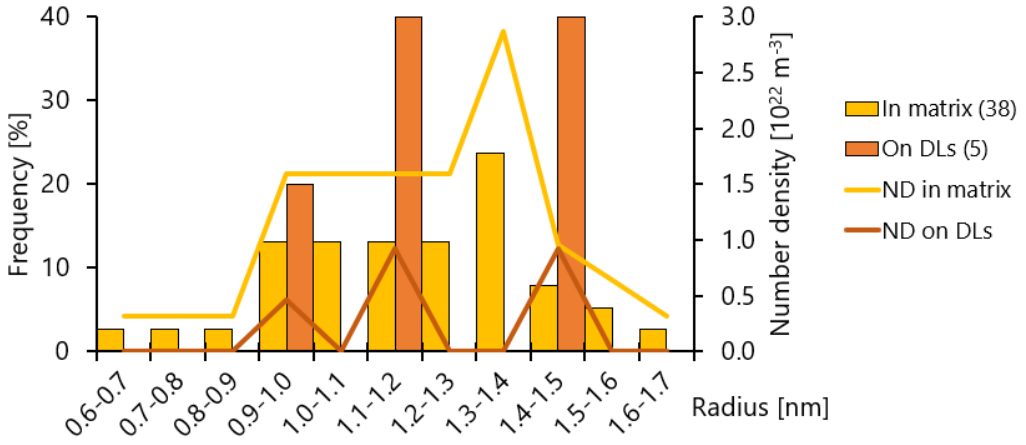

Figure 64. *Cluster size distribution in steel O irradiated up to 0.063 dpa.*

Solute clusters formed inside ferritic matrix are enriched in Si, Mi, Ni, P and to a lower extent in Mo (Table 22). Similar to steel N, the total solute cluster enrichment (17.9 at. %) is lower than in most of the other conditions (>20 at. %). Clusters formed on dislocation lines are highly enriched in P (7.8 at. %), but do not contain C or Mo atoms, contrary to what is observed in other steels.

Table 22. *Solute cluster composition measured in steel O. Values are given in at. %. "nd" means not detected. The uncertainty margins are given by two standard deviations.*

Type	Dose		Si	Mn	Ni	P	Cu	C	Mo	Fe
In volume	0.063 dpa		1.8	5.8	4.5	4.5	0.2	nd	1.0	82.1
		±	0.4	0.8	0.7	0.7	<0.1		0.3	1.3
On dislocations	0.063 dpa		1.3	2.6	3.9	7.8	nd	nd	nd	84.5
		±	1.1	1.6	2.0	2.7				3.7

In the present case, the dependence of Mn cluster as a function of global relative content is evident (Fig. 65). Symbols representing Mn are located higher and closer to 1:1 line than in other steels. Contrary, Ni is slightly below 1:1 line. The interesting observation is significantly lower than in other materials Si cluster over global ratio. At the same time clusters are highly enriched in P.

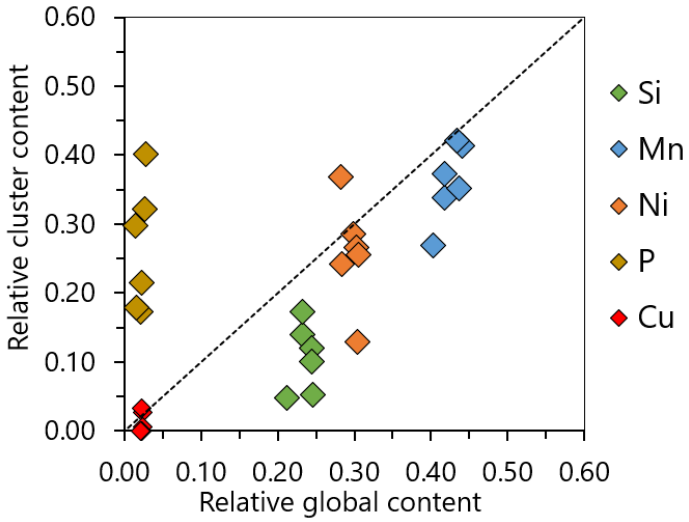

Figure 65. *Relative cluster solute content as a function of relative global solute content in steel O irradiated up to 0.063 dpa (both values are given excluding all chemical species except Si, Mn, Ni, P and Cu and normalised to 1). Each diamond represents the results obtained in one APT experiment. 1:1 trend line is also plotted.*

Additionally, to ferritic matrix, a M_3C carbide is observed. Two ferrite / carbide interfaces were studied (Fig. 66).

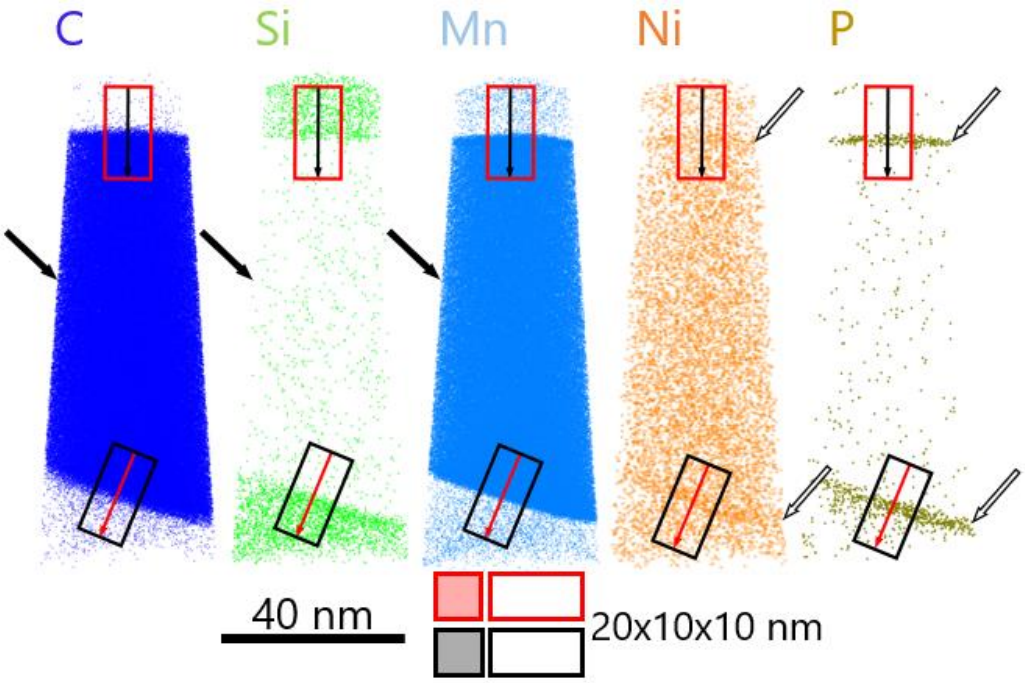

Figure 66. *Atom maps of steel O irradiated up to 0.063 dpa. Black arrows indicate M_3C carbide enriched in C and Mn and depleted in Si. White arrows indicate ferrite / carbide interfaces.*

The carbide is enriched in C (~25 at. %), Mn (15at.%) and Mo (~2at. %) as visible on figure 67. The interfaces are enriched in P, Ni and also in Mo (Fig. 68).

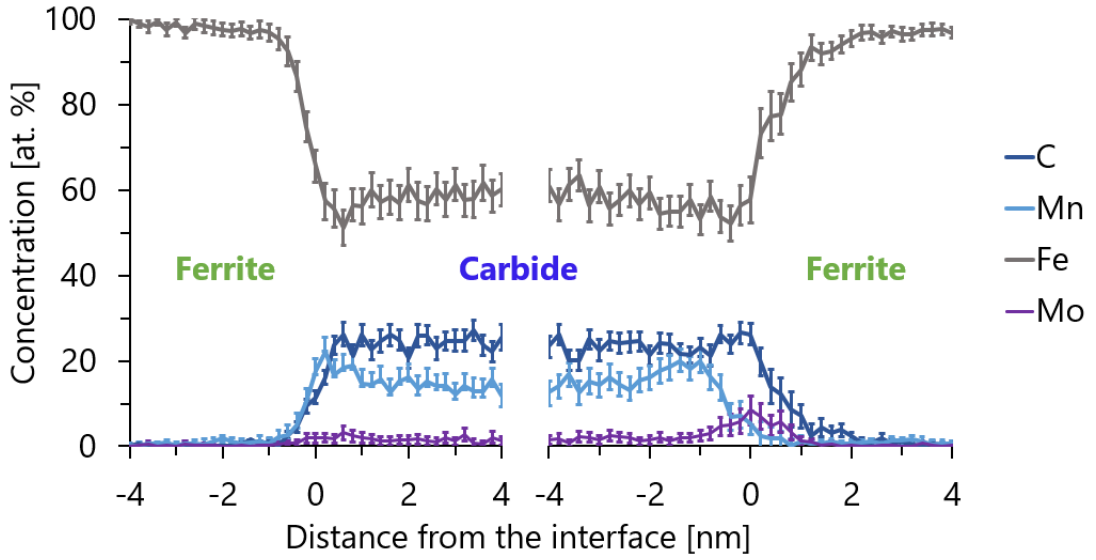

Figure 67. *Concentration profile of ferrite / carbide interfaces for C, Mn, Fe and Mo atoms. Error margins are represented by two standard deviations.*

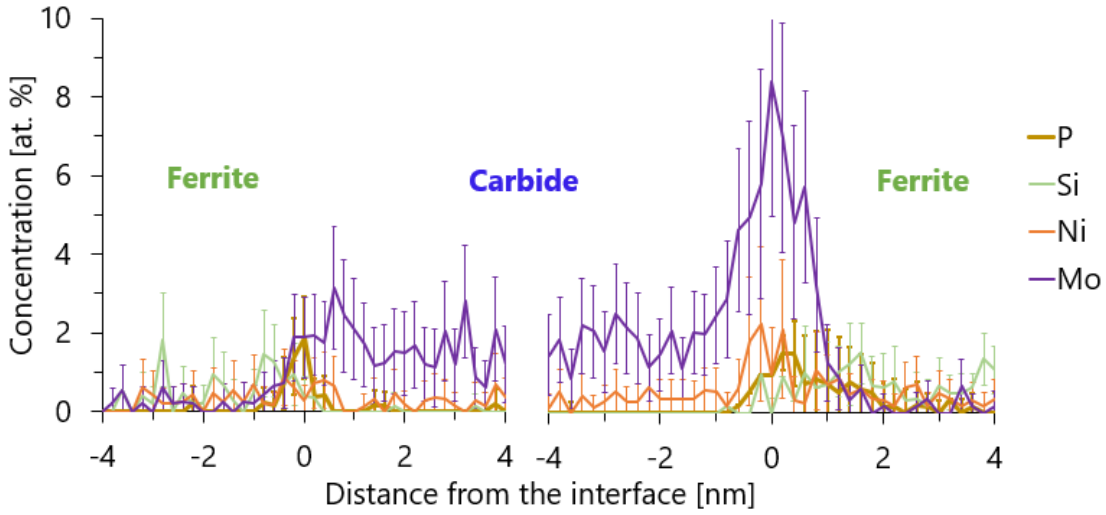

Figure 68. *Concentration profile of ferrite / carbide interfaces for P, Ni and Mo atoms. Error margins are represented by two standard deviations.*

The high Mo enrichment is observed only on the bottom interface (Table 23). Additional concentration profiles with only P and Ni atoms are available in appendix B.1.

Table 23. *Solute concentrations at ferrite / carbide interfaces. Uncertainty margins are represented by two standard deviations.*

Element	Average concentration [at. %]		Nominal concentration [at. %]	Enrichment factor	
	Top interface	Bottom interface		Top interface	Bottom interface
P	0.9 ± 0.3	1.0 ± 0.4	0.047 ± 0.004	18.5	21.5
Mo	-	7.0 ± 1.1	0.21 ± 0.01	-	34.8
Ni	1.4 ± 0.4	1.3 ± 0.4	0.63 ± 0.02	2.2	2.0

Similar to the case observed in other steels the ferrite / carbide interfaces are enriched in P (factor of 20) and Ni (factor of 2).

In conclusion, in steel O irradiated up to 0.063 dpa, solute clusters enriched in Si, Mn, Ni, P and Mo were observed. These clusters had formed inside the ferritic matrix and along dislocation lines. A significant P enrichment is measured in both cluster families.

2.7 Steel W: 0.28 at.% Cu, 0.053 at.% P, 1.61 at.% Ni, 1.86 at.% Mn

High-Cu (0.28 at. %), high-P (0.053 at. %), high-Ni (1.61 at. %) and high-Mn (1.86 at. %) steel W[7] is selected to study the combined effect of high concentration of named solutes on the microstructure evolution under neutron irradiation and was irradiated at 0.06 dpa.

After irradiation, the ferritic matrix is depleted in Si, Mn, Ni, P, Cu and also Al (Table 24). The steel W is the only material where noteworthy solute depletion is observed.

Table 24. *Concentration of Si, Mn, Ni, P and Cu measured by APT (at. %). Uncertainty margins are represented by two standard deviations between APT experiments on a given material.*

Dose	Volume		Si	Mn	Ni	P	Cu	Al
Reference	Global/Matrix		0.49	1.18	1.57	0.043	0.27	0.056
		±	0.08	0.13	0.21	0.022	0.04	0.028
0.06 dpa	Global		0.55	1.09	1.65	0.033	0.289	0.056
		±	0.16	0.23	0.22	0.036	0.044	0.013
	Matrix		0.46	0.90	1.27	0.023	0.107	0.033
		±	0.19	0.16	0.07	0.025	0.022	0.013

The depletion of solutes in the matrix is coherent with the presence of a high number density - $(16.5 \pm 0.9) \times 10^{23}$ m^{-3} - of clusters enriched in Si, Mn, Ni, P, Cu and also Al. The average radius of solute clusters is about (1.4 ± 0.3) nm. An example of APT volume is shown in figure 69. The number density of clusters formed on dislocation lines is around $(2.2 \pm 0.9) \times 10^{22}$ m^{-3}. It remains insignificant in comparison with density of clusters located into the matrix. The average radius of clusters along dislocation line equals to (1.5 ± 0.1) nm.

[7] It is important to keep in mind that these values are the bulk ones, including Mn into carbides. The Mn remaining in matrix in reference state, measured by APT is 1.18 at. %.

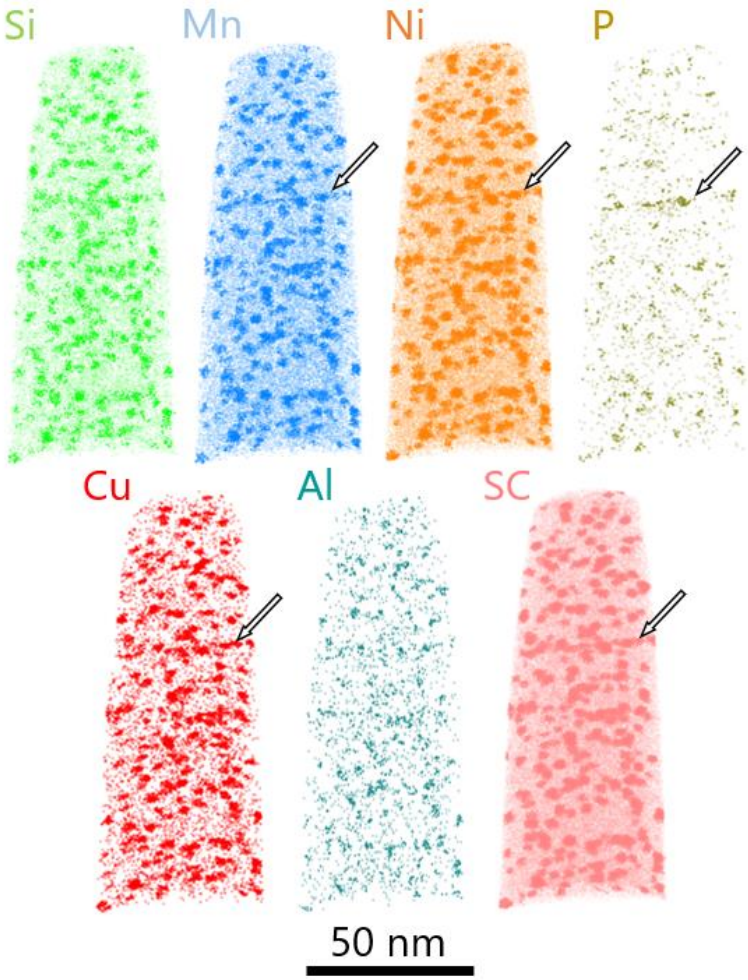

Figure 69. *Atom maps of steel W irradiated at 0.06 dpa. Solute clusters enriched in Si, Mn, Ni, P, Cu and Al are identified. Arrows indicate solute clusters on dislocation line.*

A monomodal cluster size distribution is observed (Fig. 70). The cluster size has a wide range from 0.6 to 2.2 nm. The average size of clusters formed on dislocation lines is on the same level as the size of the volume ones (1.5 vs 1.4 nm).

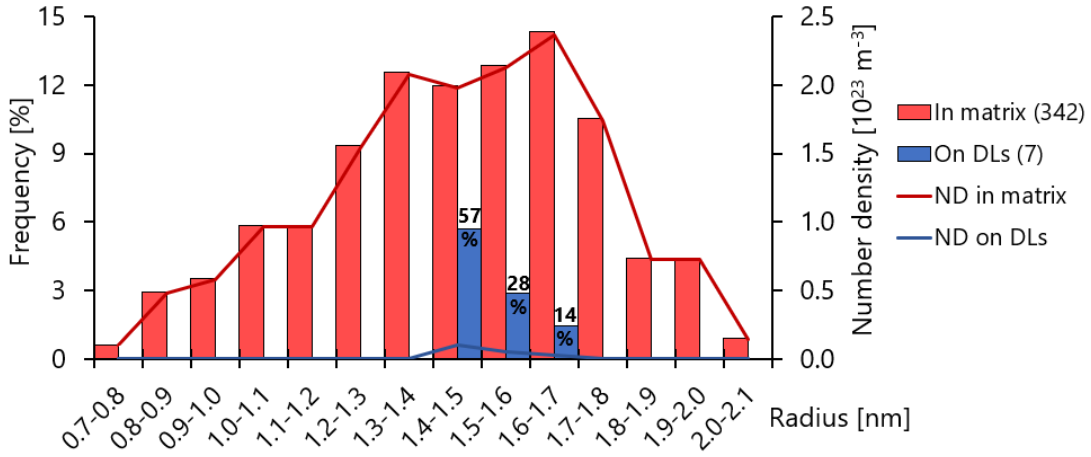

Figure 70. *Cluster size distribution in steel W irradiated up to 0.06 dpa. For visual simplicity the represented observation frequency of formed on DLs clusters in divided by a factor of 10.*

The results of cluster composition measurements are reported in Table 25. A high enrichment of solutes (~33 at. %) is observed in steel W. Solute clusters formed inside ferritic matrix are more enriched in Si (4.2 vs 3.3 at. %), Mn (8.0 vs 5.7 at. %), Ni (13.6 vs 11.9 at. %), Cu (5.8 v 3.4 at. %) and Al (1.3 vs 0.8 at. %) than the clusters formed on dislocation lines. On the contrary, clusters formed on dislocation lines are more enriched in P (2.2 vs 0.5 at. %) and C (0.4 vs 0 at. %).

Table 25. *Solute cluster composition measured after plateau erosion in steel W. Values are given in at. %. "nd" means not detected. The uncertainty margins are given by two standard deviations.*

Type	Dose		Si	Mn	Ni	P	Cu	C	Mo	Al	Fe
In volume	0.06 dpa		4.2	8.0	13.6	0.5	5.8	nd	0.4	1.3	66.2
		±	0.1	1.1	0.2	<0.1	0.1		<0.1	0.1	0.2
On dislocations	0.06 dpa		3.3	5.7	11.9	2.2	3.4	0.4	0.4	0.8	72.1
		±	0.8	1.0	1.5	0.7	0.8	0.3	0.3	0.4	2.0

The relationship between cluster and global solute contents (both values are given excluding other elements apart Si, Mn, Ni, P and Cu and normalised to 1) for each APT experiment is presented in figure 71. Number density of solute clusters in steel W is the highest from all studied materials (16.5 x 10^{23} m^{-3}), and the distinct dependence of the cluster solute concentration from the global solute content is evident for Si, Mn, Ni, Cu and, to the less extent, for P atoms.

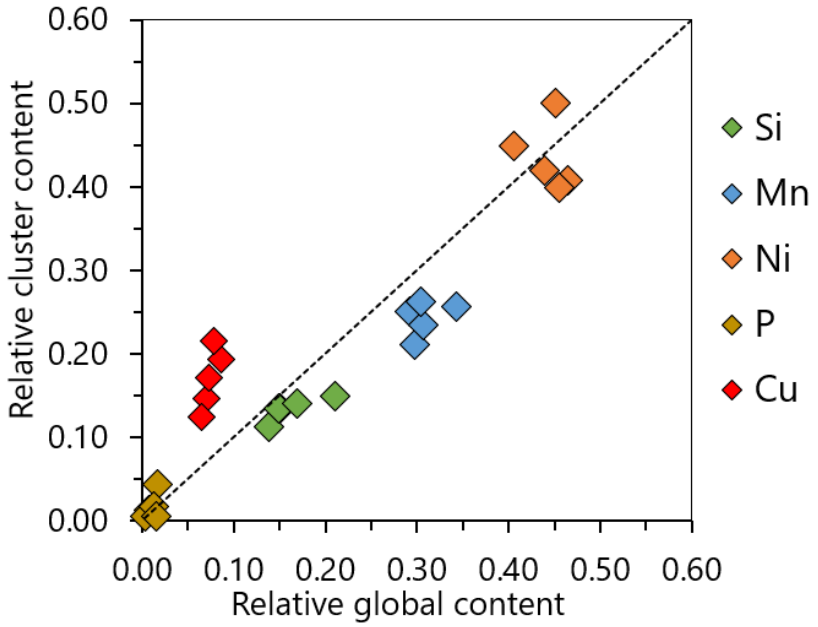

Figure 71. *Relative cluster solute content as a function of relative global solute content measured by APT in steel W irradiated up to 0.06 dpa. Each diamond represents the results obtained in one APT experiment. 1:1 trend line is also plotted.*

Mostly ferritic phase with composition matching to the nominal is observed in APT volumes. Yet, in one of the APT experiments, a region enriched in Mn (4.7 at. %), Ni (3.5 at. %), C (1.8 at. %) and Cu (0.69 at. %) is intercepted. Atoms maps of the latter volume are shown in figure 72.

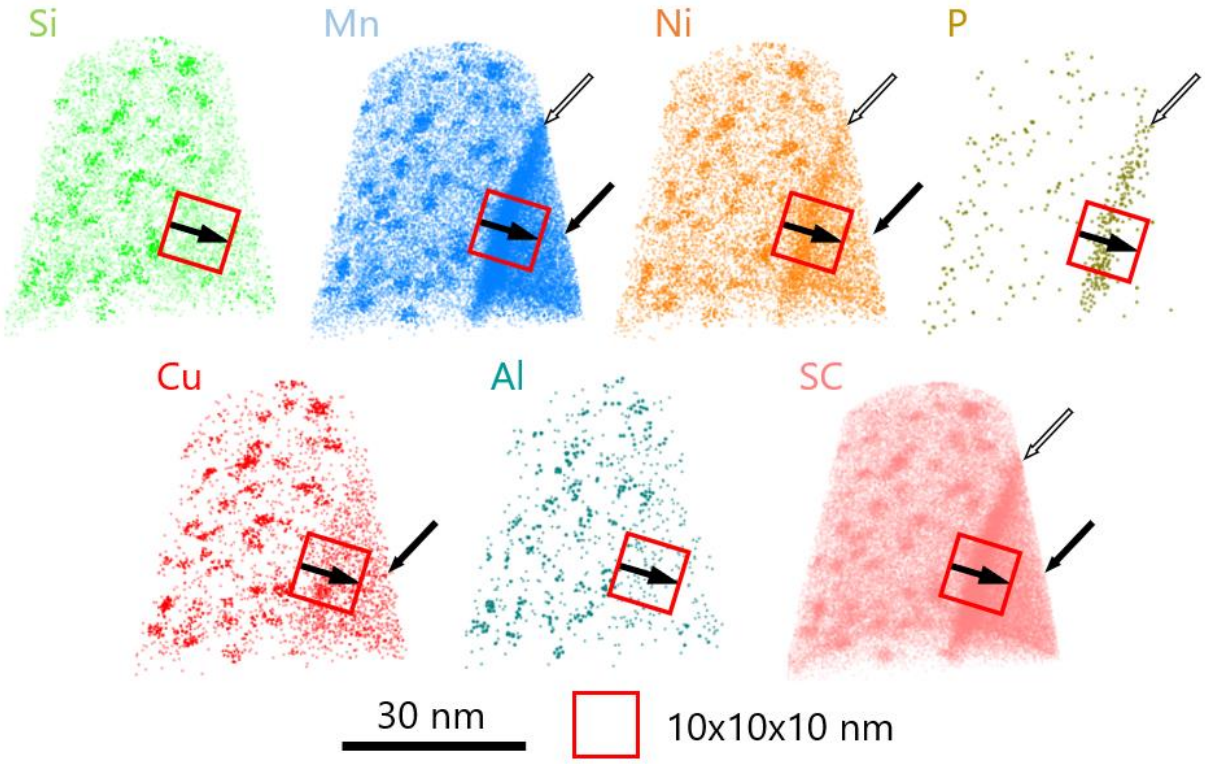

Figure 72. *Atom maps of steel W irradiated at 0.06 dpa. White arrows indicate the interface with solute segregation. Black arrows indicate enriched (probably austenitic) phase.*

No solute clusters are found in this enriched phase. Composition of the enriched phase is comparable with the composition of austenitic phase studied during experiments on the non-irradiated steel I. Presence of austenitic phase in steel W was also confirmed by EBSD on the non-irradiated materials. Taking these facts into account, a conclusion was made this enriched phase is austenite. A concentration profile through the ferrite / austenite interface is represented in figure 73. Additional profile with only P, Mo and Cu concentrations is available in appendix B.1.

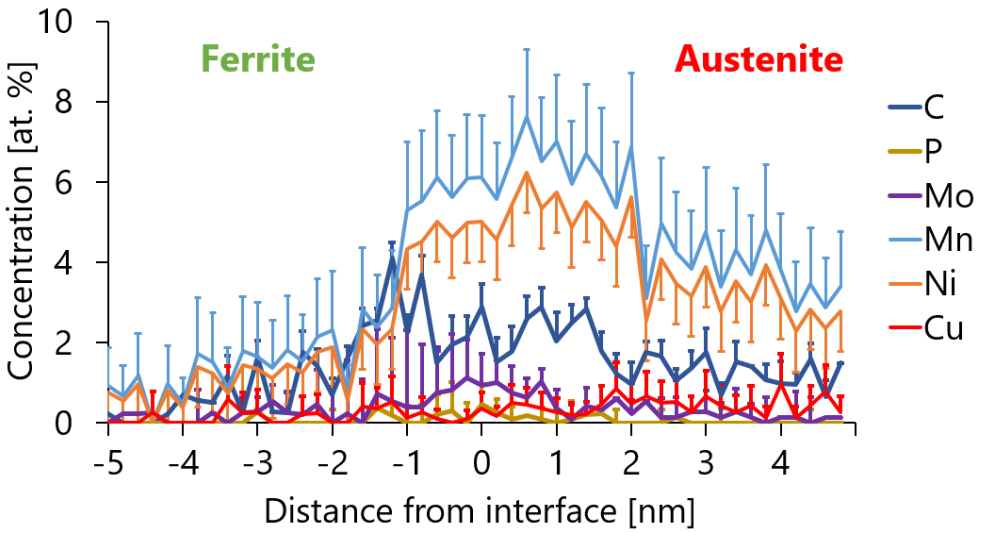

Figure 73. *Concentration profile plotted through ferrite / austenite interface. Enrichment in C, P, Mo, Mn, Ni and P atoms is observed. Error margins are represented by two standard deviations. For visual simplicity, for some of the solutes the error margins only in one direction are presented.*

Enrichment in C, P, Mo, Mn and Ni on the interface is evident. No statistically significant enrichment in over elements is evaluated. From the concentration profile, the enrichment at the interface (at the half-maximum of concentration) is calculated. Results are reported in Table 26.

Table 26. *Concentration of enriched solutes at ferrite / austenite interface. Uncertainty margins are represented by two standard deviations.*

Element	Average concentration at interface region [at. %]	Nominal concentration [at. %]	Enrichment factor
C	4.3 ± 0.5	0.16 ± 0.07	26.9
P	0.5 ± 0.2	0.04 ± 0.01	11.5
Mn	9.1 ± 0.7	1.18 ± 0.07	7.7
Mo	1.6 ± 0.3	0.2 ± 0.02	8.0
Ni	4.0 ± 0.5	1.5 ± 0.1	2.7

Similar to the observations of interface segregations is steel I, a significant enrichment in C, P and Mo, known to segregate during thermomechanical treatment, and in Mn and Ni highly enriched in austenitic phase is observed.

In steel W, the highest cluster number density from all studied materials is measured. As in other steels, solute clusters are enriched in Si, Mn, Ni and P. Additionally, a significant enrichment in Cu and enrichment in Al are measured. In the present case, a larger range of cluster sizes than in other steels is found

Summary

Microscale ESBD and atomic scale APT techniques were used to study the microstructure of chemically-tailored RPV steels in the reference and irradiated states.

With EBSD, it was shown that medium-Ni RPV steels (D, E, F, N, O) have a bainitic structure. In the two high-Mn/high-Ni RPV steels (I and W), a partially degenerated bainitic structure is observed. In all RPV steels, the microstructure is mostly composed from upper bainite with intergranular carbides.

The chemical composition of ferritic matrix in the non-irradiated state was measured with APT. The results have shown a good correlation with the values provided by the steel manufacturer. A depletion of the matrix in C, Mn and Mo due to carbides formation is observed. A depletion of the matrix in P is mostly related to the segregation onto GBs during thermomechanical treatments. Apart from carbides, CEFs were observed in the unirradiated RPV steel W (super-saturated in Cu). The number density of these precipitates is around 6×10^{21} m^{-3}. In all other steels, no solute cluster is observed before irradiation.

APT investigation on neutron irradiated materials was performed. Chemical composition measurements showed depletion of ferritic matrix in P after irradiation. Al the same time, in the most of studied conditions no statistically meaningful depletion in Mn, Ni and Si were observed. The exception is high-solute steel W where matrix was depleted in Mn, Ni, Si, Cu and Al. Solute clusters formed inside the ferritic matrix, along dislocation lines and on dislocation network of low-angle GBs were observed. In general, the number density of solute clusters located in the ferrite increases with increase of global solute concentration and irradiation dose. High amount of Fe atoms associated with "in volume" (~75-80 at. % Fe) and "on dislocation lines" (~85 at. % Fe) solute clusters was observed. Owing to CCC model described in chapter II 3.3.5, it was confirmed what Fe is indeed present inside solute clusters and is not APT artefact. High dispersion of tip-to-tip results shows the strong correlation between local chemical composition and characteristics of solute clusters. This is particularly visible in material with cluster number density is high enough (> 10^{23} m^{-3}) to have a statistically relevant number of cluster in each volume.

In the present chapter results of APT study on irradiated chemically-tailored steels were presented and described separately for each material. Dispersion of volume-to-volume results for a single alloy was demonstrated. In the following chapter, the discussion on APT results will be performed. Cross-comparison between chemically-tailored RPV steels to understand the effect of global solute concentration of Cu, P, Mn and Ni will be given.

References

1. R. Chaouadi, R. Gerard, E. Stergar, W. Van Renterghem. Journal of Nuclear Materials 519 (2019): 188-204. https://doi.org/10.1016/j.jnucmat.2019.03.030

2. S.I. Wright, M.M. Nowell. Microscopy and Microanalysis 12 (2006): 72–84. https://doi.org/10.1017/S1431927606060090

3. S. Zajac, V. Schwinn, K. H. Tacke. Materials Science Forum Vols. 500-501 (2005): 387–394. https://doi:10.4028/www.scientific.net/msf.500-501.387

4. M. Müller, D. Britz, L. Ulrich, T. Staudt, F. Mücklich. Metals 10 (2020): 630. https://doi:10.3390/met10050630

5. H.K.D.H. Bhadeshia. Bainite is Steels: Theory and Practice, Third Edition. CRC Press (2019). ISBN 1351574817

6. A. Navarro-Lopez, J. Hidalgo, J. Sietsma, M.J. Santofimia. Materials Characterization 128 (2017): 248–256. http://dx.doi.org/10.1016/j.matchar.2017.04.007

7. W. Van Renterghem, E. Stergar, R. Chaouadi. Effect of Nickel–Manganese Concentration on the Microstructure of Chemically-Tailored RPV Steels, SCK CEN restricted report 26724015, R-6490

8. A. Akhatova, F. Christien, V. Barnier, B. Radiguet, E. Cadel, F. Cuvilly, P. Pareige. Applied Surface Science 463 (2019): 203–210. https://doi.org/10.1016/j.apsusc.2018.08.085

9. L. Zhang, B. Radiguet, P. Todeschini, C. Domain, Y. Shen, P. Pareige. Journal of Nuclear Materials 523 (2019): 434-443. https://doi.org/10.1016/j.jnucmat.2019.06.002

10. P. Wells. PhD Thesis 'The Character, Stability and Consequences of Mn-Ni-Si Precipitates in Irradiated Reactor Pressure Vessel Steels', (2016): 221. https://escholarship.org/uc/item/3vh4k9tf

11. B. Gomez-Ferrer, C. Heintze, C. Pareige. Journal of Nuclear Materials 517 (2019): 35-44. https://doi.org/10.1016/j.jnucmat.2019.01.040

12. P. Auger, P. Pareige, S. Welzel, J-C. Van Duysen. Journal of Nuclear Materials 280 (2000): 331–44. https://doi.org/10.1016/S0022-3115(00)00056-8

13. P.D. Edmondson, C.P. Massey, M.A. Sokolov, T.M. Rosseel. Journal of Nuclear Materials 545 (2021): 152740. https://doi.org/10.1016/j.jnucmat.2020.152740

14. P.D. Styman, J.M. Hyde, K. Wilford, A. Morley, G.D.W. Smith. Progress in Nuclear Energy 57 (2012): 86-92. https://doi.org/10.1016/j.pnucene.2011.10.010

15. E.D. Eason, G.R. Odette, R.K. Nanstad, T. Yamamoto. Journal of Nuclear Materials 433 (2013): 240-254. https://doi.org/10.1016/j.jnucmat.2012.09.012

16 L. Messina, T. Schuler, M. Nastar, M. Marinica, P. Olsson. Acta Materialia 191 (2020): 166–85. https://doi.org/10.1016/j.actamat.2020.03.038

17. E. Meslin et al. Journal of Nuclear Materials 406 (2010): 73–83. https://doi.org/10.1016/j.jnucmat.2009.12.021

18. M.G. Burke, R.J. Stofanak, J.M. Hyde, C.A. English, W.L. Server. Effects of Radiation on Materials, ASTM STP 1447 (2002). https://www.osti.gov/servlets/purl/835565

19. M.G. Burke, R.J. Stofanak, J.M. Hyde, C.A. English, W.L. Server. Conference paper 'Characterization of Irradiation Damage in A508 Gr 2 and Gr 4N Forging Steels'

20. G. Monet. Journal of Nuclear Materials 508 (2018): 609-627. https://doi.org/10.1016/j.jnucmat.2018.06.020

21. B. Gault, M. Moody, J. Cairney, S. Ringer. Atom Probe Microscopy, Springer Series in Materials Science, Springer New York (2012). https://doi.org/10.1007/978-1-4614-3436-8

22. V. Kuksenko. PhD thesis. Université de Rouen (2011)

23. A. Etienne, B. Radiguet, N.J. Cunningham, G.R. Odette, P. Pareige. Journal of Nuclear Materials 406 (2010): 244–250. http://dx.doi.org/10.1016/j.jnucmat.2010.08.043

24. L. Tan, R.E. Stoller, K.G. Field, Y. Yang, H. Nam, D. Morgan, B.D. Wirth, M.N. Gussev, J.T. Busby. JOM 68 (2016). https://www.osti.gov/pages/servlets/purl/1236587

25. B. Jenkins, J. Douglas, N. Almirall, N. Riddle, P. Bagot, J.M. Hyde, G.R. Odette, M. Moody. Materialia 11 (2020): 100717. https://doi.org/10.1016/j.mtla.2020.100717

26. N. Almirall, P. Wells, T. Yamamoto, K. Wilford, T. Williams, N. Riddle, G.R. Odette. Acta Materialia 179 (2019): 119–28. https://doi.org/10.1016/j.actamat.2019.08.027

Chapter IV: Influence of the bulk chemical composition on the microstructure evolution under neutron irradiation

In the present chapter, APT results presented in chapter III on the materials with different bulk chemical compositions are compared and a discussion about observed tendencies on solute cluster formation is given.

One of the most important questions in the scientific community studying the embrittlement and the microstructure evolution of RPV steels concerns the mechanism at the origin of the formation of solute-enriched features (clusters / precipitates). It would be impossible to answer that question in one PhD research. Yet, the goal here is to provide additional information on this subject.

The following chapter is divided into three parts. In the first part, the possible mechanisms of cluster formation are reminded, supported by experimental data and information from atomistic modelling. In the second part, the effect of Mn, Ni, P and Cu bulk ($\propto$ global) concentrations on the solute cluster formation and associated cluster formation mechanism are discussed. In the third part, a comparison of the results obtained in the current work with results reported in literature are performed.

Since Mn takes part in carbide formation, bulk Mn concentration is not representative of the amount of Mn in the initial ferritic solid solution. Hence, same as in the chapter III, the nominal solute concentration will be represented by the matrix values measured by APT in the non-irradiated state.

The number density of clusters formed on dislocation lines does not vary significantly (from 0.1 to 0.2 x 10^{23} m^{-3}) whatever is the global chemical composition and has a minor contribution in the total number density of solute clusters in most studied materials. The only exception is medium Ni/Mn CT RPV steel E, where a low number density of clusters was observed. Further, the main focus and comparison will be performed on clusters formed inside the ferritic matrix. And the term "clusters" will be used instead of "clusters formed inside the ferritic matrix".

For the sake of simplicity, the comparison between materials will be performed using the average values of measured cluster properties (number density, size, solute content). The detailed results of APT measurements are presented in chapter III and appendix B.3.

When a comparison between materials studied in the current PhD project is performed, the term “CT RPV” won’t be written. When comparison with materials studied in other studies (commercial RPV, model RPV), the term “CT RPV” will be utilised.

1 Mechanism for cluster formation

In the last 40 years, many scientists focused on the studies of the possible mechanisms of solute clusters and precipitates formation. The two most developed mechanisms are the radiation enhanced diffusion due to vacancy supersaturation and the radiation-induced segregation due to solute and PDs flux coupling. Both mechanisms were explained in detail in chapter I, and further, a concise summary will be given.

1.1 Radiation enhanced diffusion

In the present research, both low-Cu and high-Cu CT RPV steels are studied, and possible radiation enhanced mechanisms of CEFs and MNSFs formation will be investigated separately.

(i) *Irradiation enhanced Cu clustering*. In Cu bearing steels, where Cu bulk concentration is above 0.1 at. %, CEFs formation will be accelerated by radiation enhanced diffusion [1-4]. Indeed, in most RPV materials, Cu is supersaturated in the matrix due to its low solubility limit in Fe, estimated to be around 0.007 at. % at 300 °C [5]. Homogeneous [6-8] and heterogenous [5,9-12] CEFs are formed at low doses, as low as 0.01 dpa. They further act as favourable sites for segregation of solutes, such as Mn, Ni and Si by radiation-induced or enhanced mechanism which will be described in the following paragraph [13,14].

(ii) *Irradiation enhanced Mn-Ni-Si clustering*. The nominal concentrations of Mn, Ni and Si in the RPV steels are usually below their solubility limits in the ferritic matrix at operation temperatures of PWR [5]. However, Monte Carlo modelling proposes the formation of the so-called “late-blooming” phases in RPV steels irradiated at doses above 0.1 dpa. This phenomenon seems to occur after long time irradiation, when Cu becomes undersaturated in the matrix, and formation of CEFs is over [15,16]. The compositions of equilibrium Mn-Ni-Si phases were predicted by CALPHAD modelling [17]. A high number density of Mn, Ni and Si enriched-features was observed in “model” RPV steels irradiated up to the doses above 0.2 dpa (detailed information is given in chapter I and in appendix A.2) [18-20]. In APT experiments on high-Cu steels, MNSFs heterogeneously formed on CEFs with shell-like and co-precipitated appendage structures were observed [18]. MNSFs are predicted to form heterogeneously on GBs, dislocation network and small self-interstitial atom loops [16,18-20]. These SIA loops are formed via radiation-induced

segregation. Therefore, RIS has an essential role in the nucleation of MNSFs. It should be noted that it is not possible to distinguish homogeneous nucleation from heterogeneous formation on small PD loops using APT [16]. For typical commercial RPV steel (with nominal compositions ~0.7 Ni at. %; > 1.0 Mn at. %, ~0.5 Si at. %) the average composition of MNSFs is expected to be similar to the predicted G or Γ_2 phases (excluding Fe) [20].

The open question is the high amount of Fe (up to 50 at. %) measured by APT inside MNS features, although modelling predicts formation of Fe-free phases [17-18]. Correlative APT/STEM-EDS study in which the experimental EDS spectrum had been compared with modelled ones (with MNSFs Fe concentrations ranging from 0 to 57 at. %) was performed. Results suggest that MNSFs are expected to be almost Fe free (less than 6 at. %) [21]. However, the study focused on the ability of APT to precisely measure the composition of nanosized features was performed on FeCr model alloy. To do so, the CCC model, which is in detail described in chapter II, was utilised. The conclusion was made that Fe atoms are indeed the part of Cr-rich precipitates and not the APT artefact [22]. To evaluate if the composition measurements on CT RPV steels are affected by APT artefacts the CCC model was utilised. Results confirmed that Fe atoms are actually part of solute clusters and should be kept for composition measurements.

1.2 Radiation-induced segregation

Radiation-induced formation of solute clusters is based on the interaction of point defects such as vacancies and self-interstitial atoms with solute elements. Solutes can be dragged with PDs towards sinks and generate a local enrichment, taking thus part in point defect-solutes clusters (PDSCs) formation. These processes are extensively studied by atomistic modelling. The following description is based on the *ab initio* DFT calculations of PD-solute interactions (jump frequency, migration barrier). Result of which were further used as input data for (Self-Consistent Mean Field) SCMF method in order to obtain the PD-solute transport coefficients, and to predict the possible RIS tendencies at nanoscale [23-27]. The data obtained from DFT and SCMF calculations can be subsequently used to predict the irradiation-induced microstructure evolution at microscale (formation of PDSCs, solute clusters, precipitates…) with OKMC modelling [28-30].

(i) *SIA mechanism.* Modelling predicts that solute atoms can form a stable dumbbell with SIA and pin PDs, creating a sink for further PD and solute segregation [23,27,31-33]. The ability of Si atoms to migrate by SIA mechanism is debatable. Results of Messina and co-workers showed neither positive nor negative interaction of Si with SIA [27,34]. However, positive interaction was observed in several other studies [35-37]. Mn is expected to have a strong positive interaction with

SIA atoms resulting in significant enrichment at PD sinks [38]. P-SIA is the most diffusive mixed dumbbell, and most SIA can be associated with P atoms even though it has a much lower global concentration than Mn [23,27]. A significant effect of P on the solute cluster formation was observed by APT experiments in FeCr system. Yet, the effect of P saturates below the dose of 0.1 dpa, due to low global concentration [39,40]. Even though solute-SIA mixed dumbbells with Ni atoms are less stable than for Mn and P atoms, Messina stated that Ni diffusion by SIA is still possible at operating temperatures of RPV steel [27]. DFT calculations predict that Mn and Ni atoms decorating <111> SIA loop will create a stronger strain in vicinity of the loop. And the latter field will enhance the strength of interactions of the decorated loop with other solutes. Contrary, repulsive chemical interaction between Si and P was observed. If SIA loop is already decorated by P atoms, Si segregation towards these loops decreases [41].

(ii) *Vacancy mechanism*. Ni, Cu, Si, Mn and P have high binding energy with vacancies and can be dragged by them towards the sinks [27]. Yet, a stronger effect was observed for Cu and Ni. Cu-vacancy clusters were observed in research on low-Cu materials, where Cu concentration was not sufficient enough to result in precipitation [31,42-49]. Ni has a strong interaction with vacancies, and Ni atoms were usually found in Cu-Ni-V clusters [44,50-53]. An increase in Ni global concentration results in the increase of the number density of solute-V clusters, which could act as the nuclei for heterogeneous Cu precipitation [53-54]. Si atoms associated with V clusters were observed in several studies [41,44,51,55]. Mn is also expected to be transported by V-drag, and Mn-vacancy clusters were observed in the literature [44,54,55]. P has a high attraction with V and can be transported by both V and SIA, yet SIA-P diffusion is expected to be dominant [23,27].

So, under irradiation, solutes are transported owing to coupling to the flux of PDs towards sinks. The common sinks are dislocation lines and grain boundaries. Point defect clusters also act as sinks, since distortion of the strain field around them is an energetically favourable site for PDs segregation. In the absence of GBs and dislocation lines nearby, these PDCs are the preferable target for PDs migration [56,57]. V clusters can migrate in three dimensions, and small SIA loops can migrate in one dimension before being pinned by solute atoms [23,28,46,58]. The continuous flux of solutes towards PDCs results in the enrichment and formation of solute clusters. For example, the predicted number density of Mn-Ni clusters in Fe-Mn-Ni model alloy was estimated to be on the same level as the number density of SIA loops in pure Fe [59]. In the case of pure Fe, the ratio between V clusters and SIA loops was estimated to be 6 to 4, which can be attributed to a dominant clustering of V over SIA [60].

To evaluate the possibility of RIS, the steady state PD concentrations are calculated and represented in appendix C.1. The results of calculations showed that sufficient for radiation-induced segregation point defect concentrations were achieved during RADAMO-13 irradiation.

1.3 Time parameters

The precise description of the time evolution for PDCs, solute clusters and precipitates formation is rather complicated. The atomistic kinetic Monte Carlo (AKMC) modelling predicts Mn-Ni-SIA clusters to be formed before Cu-V clusters, further CEFs are formed accelerated by radiation enhanced diffusion, and formation of Mn-Ni-Si RIS clusters occurs later [61]. These results are coherent with experimental observations where CEFs were already observed at 0.025 dpa and Mn-Ni clusters only at the dose above 0.1 dpa [62]. MNSFs are expected to form later, at the doses above 0.2 dpa. A tentative schematic view of the irradiation production of nanoscale features as a function of dose (proportional to time) is given in figure 1.

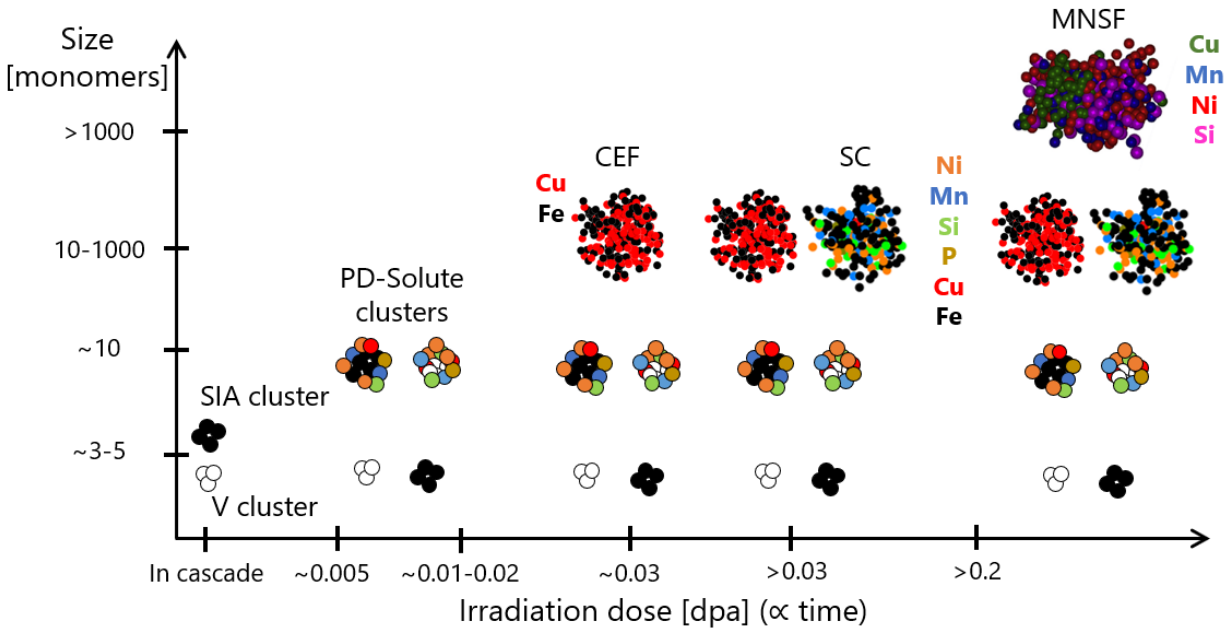

Figure 1. *Evolution of the different populations of the nanosized microstructure features as a function of irradiation dose (proportional to time).*

From the presented above features only solutes clusters, Cu- and Mn-Ni-Si-enriched features can be identified with APT. Small PD cluster and PD-solute clusters have a size below resolution limit and could not be studied directly. Therefore, a comparison between experimental results and atomistic modelling is essential.

2 Effect of bulk chemical composition on solute cluster formation

2.1 Effect of Mn and Ni concentrations and their synergy

In commercial RPV materials, both Mn and Ni atoms are usually found inside solute clusters also enriched in Si, Cu and P [63-66]. Synergetic segregation of Mn and Ni was both predicted by modelling [33,59,61] and observed experimentally [57,67]. It was experimentally confirmed that Mn-enriched clusters could form under irradiation without Ni in the binary undersaturated FeMn alloy. Yet, the number density of these clusters is lower than the typical ND observed in more solute enriched commercial RPV materials [57]. The sub-chapter 2.1 is divided into four sections focusing on the dose, Mn and Ni effects on solute cluster formation, and on the synergy between Mn and Ni.

2.1.1 Dose effect

The effect of Mn and Ni on solute cluster formation is studied on four CT RPV steels with various Mn and Ni contents. Nominal concentrations of irradiation sensitive solutes measured with APT in the non-irradiated state and available irradiation doses are reported in Table 1.

Table 1. *Nominal concentration of irradiation sensitive solutes measured with APT at the non-irradiated state and irradiation doses of studied specimens.*

ID	Type	Nominal concentration [at. %]					Dose [dpa]		
		Si	Mn	Ni	P	Cu	Low	Medium	High
D	Med-Ni/Low-Mn	0.51	0.02	0.70	0.013	0.051	-	0.091	-
E	Med-Ni/Mn	0.56	0.59	0.66	0.024	0.048	0.069	0.092	0.138
F	Med-Ni/High-Mn	0.49	1.26	0.69	0.017	0.046	0.059	0.078	0.134
I	High-Ni/Mn	0.53	1.10	1.60	0.019	0.046	-	0.082	0.132

Three irradiation does are available for steels E and F. Steel I was irradiated up to two doses. Only one irradiation condition was studied in the case of steel D. Therefore, the effect of irradiation dose on the microstructure evolution will be investigated on steels E, F and I.

The main cluster properties are number density, size (results will be presented in the form of equivalent radius calculated from the number of atoms and assuming that clusters are spherical) and chemical composition. From the former two, degradation of mechanical properties (irradiation hardening) can be predicted. From the latter, information about nature/formation mechanism can be evaluated.

(i) ***Effect on cluster number density***. Detailed information about cluster number density measured in each studied steel is presented in chapter III and in appendix B.3. In Table 2 information about average cluster number density for a given steel and irradiation dose is presented.

Table 2. *Average number density of solute clusters measured with APT.*

ID	Type	Number density [10^{22} m^{-3}]				
				High dose		
		Low dose	Medium dose	Total	Small (R<1.5nm in E) (R<1.3nm in F)	Big (R>1.5nm in E) (R>1.3nm in F)
D	Med-Ni/Low-Mn	-	below 0.4	-	-	-
E	Med-Ni/Mn	2.6±1.5	3.4±1.6	8.6±2.6	4.3±2.1	4.3±2.1
F	Med-Ni/High-Mn	6.4±1.7	8.3±2.7	19.6±3.1	7.1±2.0	12.5±2.7
I	High-Ni/Mn	-	40.2±6.6	80.3±11.3	-	-

With the increase of irradiation dose, number density of solute clusters progressively increases. More precisely, from low to medium dose (by ~0.02 dpa), number density of clusters increases by a factor of 1.3 for steels E (from 2.6 to 3.4 x 10^{22} m^{-3}) and F (from 6.4 to 8.3 x 10^{22} m^{-3}). With further increase of irradiation dose from medium to high values (by ~0.05 dpa), cluster number density more than doubles in E (from 3.4 to 8.6 x 10^{22} m^{-3}), F (from 8.3 to 19.6 x 10^{22} m^{-3}), and I (from 40.2 to 80.3 x 10^{22} m^{-3}).

In E and F, irradiated up to the high dose, two cluster families with different sizes are observed. Number density of small (R < 1.5 nm for E and R < 1.3 nm for F) clusters is 4.3 x 10^{22} m^{-3} in the case of E and is 7.1 x 10^{22} m^{-3} in the case of F. Number density of big (R > 1.5 nm for E and R > 1.3 nm for F) clusters is 4.3 x 10^{22} m^{-3} in E and 12.5 x 10^{22} m^{-3} in F (Table 2). Detailed discussion on the evolution of the cluster size will be performed in the section ii.

Based on the data obtained in low and medium dose conditions a linear trend of number density increment is plotted (Fig. 2). This "*linear predicted*" number density in the high dose condition is almost the same as the measured with APT number density of big clusters (*13.1* vs 12.5 x 10^{22} m^{-3} in F and *5.4* vs 4.3 x 10^{22} m^{-3} in E). The additional increase in the number density is attributed to the formation of small clusters, which were not formed or had a size below resolution limit of APT at medium and low doses.

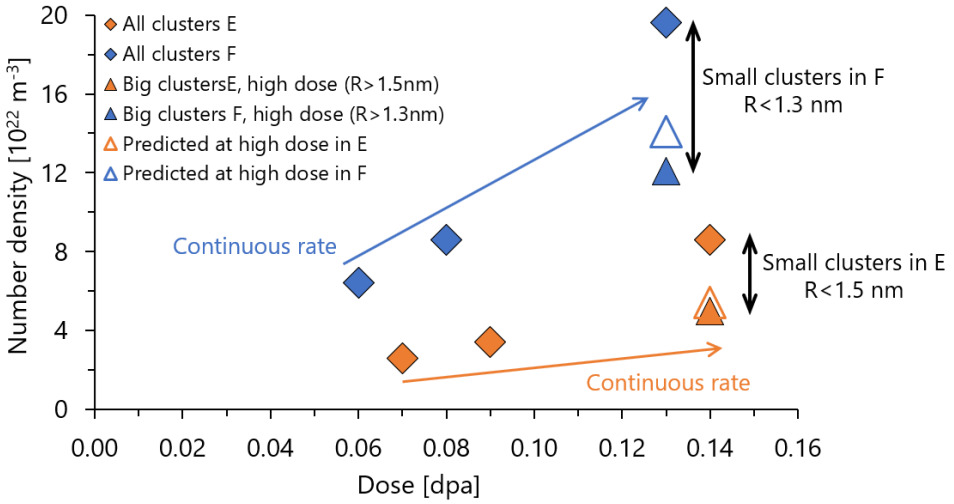

Figure 2. *Evolution of cluster number density as a function of irradiation dose. Diamonds represent the average number density for each condition. Filled triangles represent the number density of big clusters (R >1.5 / 1.3 nm) for two conditions where bimodal cluster size distribution is observed. Empty triangles represent the predicted from linear trend number density.*

To conclude, with the increase of irradiation dose, the number density of clusters increases in all studied materials, which is coherent with theoretical expectations and literature observations [5,63,64,68,69]. In the next section, an evaluation of dose effect on cluster size will be performed.

(ii) ***Effect on cluster size***. Cluster size is represented by the equivalent radius, calculated from the number of atoms after half-maximum erosion. Additional information is available in chapter III and in appendix B.3. In Table 3 information about the average cluster size for a given material and irradiation dose is presented.

Table 3. *Average solute cluster radius measured with APT.*

ID	Type	Average radius [nm]				
		Low dose	Medium dose	High dose		
				All	Small	Big
F	Med-Ni/Mn	1.3 ± 0.3	1.5 ± 0.3	1.4 ± 0.3	1.1 ± 0.2	1.6 ± 0.2
F	Med-Ni/High-Mn	1.6 ± 0.2	1.7 ± 0.3	1.4 ± 0.3	1.0 ± 0.1	1.6 ± 0.2
I	High-Ni/Mn	-	1.2 ± 0.2	1.1 ± 0.2	-	-

With increase of irradiation dose from low to medium value, the average cluster radius increases in the case of E (from 1.3 to 1.5 nm) and F (from 1.6 to 1.7 nm). With further increase of irradiation dose (from medium to high), a bimodal cluster size distribution is observed in E and F (Fig. 3). The average radius of all clusters decreases from 1.5 to 1.4 nm in the case of E and from 1.7 to 1.4 nm in the case of F. In steel I, with increase of irradiation dose from medium to high value

the average cluster radius also decreases from 1.2 to 1.1 nm. However, contrary to E and F a monomodal cluster radius distribution is observed.

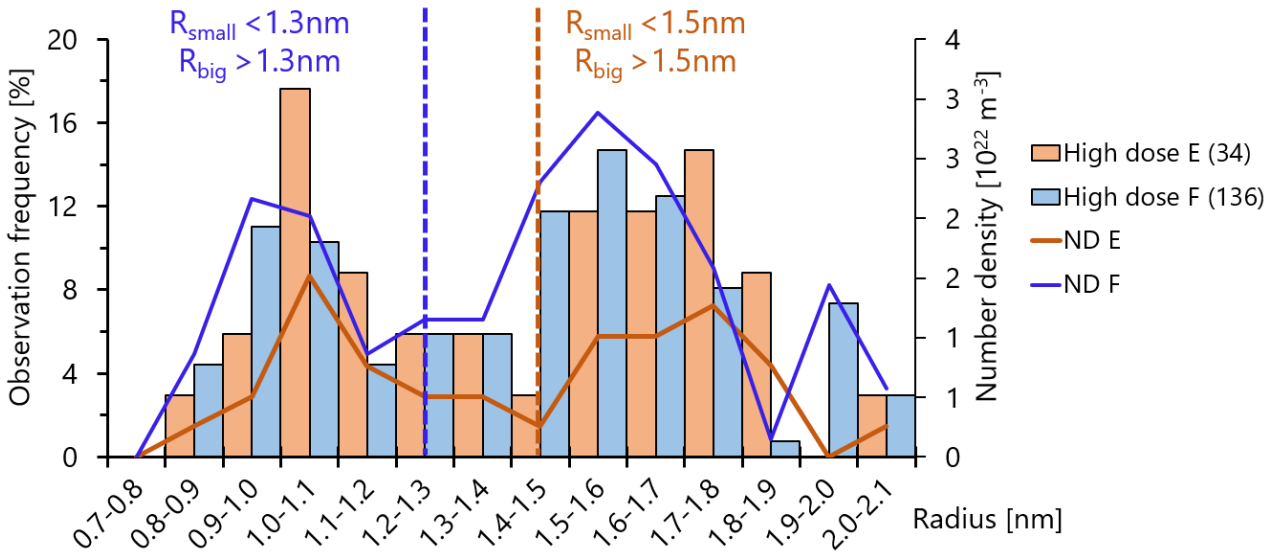

Figure 3. *Cluster radius distribution in steels E and F irradiated up to high dose. Bimodal cluster size distribution is observed.*

From the cluster radius distribution chart, clusters are divided into "small" and "big" families. In steel E clusters with radius below 1.5 nm are defined as small and with radius above 1.5 nm are defined as big, whereas the threshold is 1.3 nm in the case of steel F (Table 3). Average radius of small clusters is 1.1 nm in E and 1.0 nm in F. Average radius of big clusters is 1.6 nm in E and F. In both steels the average radius of big clusters is similar to the average cluster radius measured at the medium dose (1.5-1.7 nm). Cluster growth saturates around 1.6 nm and in agreement with literature data, where average cluster radius is usually evaluated to be below 1.6 nm [18,20,63,68]. Bigger clusters (up to 1.8 nm) were only observed in the study of Dohi and co-workers [64]. In addition, large clusters (average radius above 2 nm) were found in model RPV steels subjected to high dose (4 dpa) ion irradiation [70]. Dose effect of the cluster composition will be studied next.

(iii) ***Effect on cluster composition***. Under neutron irradiation solutes such as Si, Mn, Ni, P and Cu are expected to be transported towards sinks resulting in a decrease in their matrix concentrations. The matrix solute depletion calculated as the difference between global (excluding carbides and GBs) and matrix (excluding clusters and decorated in solutes dislocation lines) concentrations is presented in Table 4.

Table 4. *Matrix solute depletion after irradiation.*

ID	Solute	Matrix solute depletion [at. %]		
		Low dose	Medium dose	High dose
E	Mn	0.01	0.01	0.01
	Ni	0.01	0.01	0.02
	Si	0.01	0.01	0.02
	P	0.010	0.014	0.012
	Cu	0.004	0.003	0.001
F	Mn	0.01	0.01	0.02
	Ni	0.01	0.02	0.03
	Si	0.01	0.01	0.02
	P	0.003	0.007	0.009
	Cu	below 0.001	0.001	0.001
I	Mn	-	0.02	0.06
	Ni	-	0.05	0.13
	Si	-	0.02	0.05
	P	-	0.011	0.012
	Cu	-	0.001	0.005

In the majority of cases, the matrix depletion in Mn, Ni and Si is around 0.01-0.02 at. % and is below the variation of the global concentration (up to 0.1 at. %) between APT experiments on the given condition. Therefore, such a low matrix depletion is not statically meaningful. Steel I is the only material where noteworthy matrix depletion is observed. Matrix is depleted in Ni by 0.05 at. % in the medium dose and by 0.13 at. % in the high dose condition. In the high dose condition of I, the depletion in Mn (0.06 at. %) and Si (0.05 at. %) are also detected. In all cases, matrix is depleted in P by ~0.01 at. % which contributes to around half of its nominal concentration of ~0.02 at.%.

Concentrations of Si, Mn, Ni, and P inside solute clusters are presented in figure 4. The total concentration of other species such as Cu, Mo, Al and C is below 1 at. % and is not presented. Balance is in Fe.

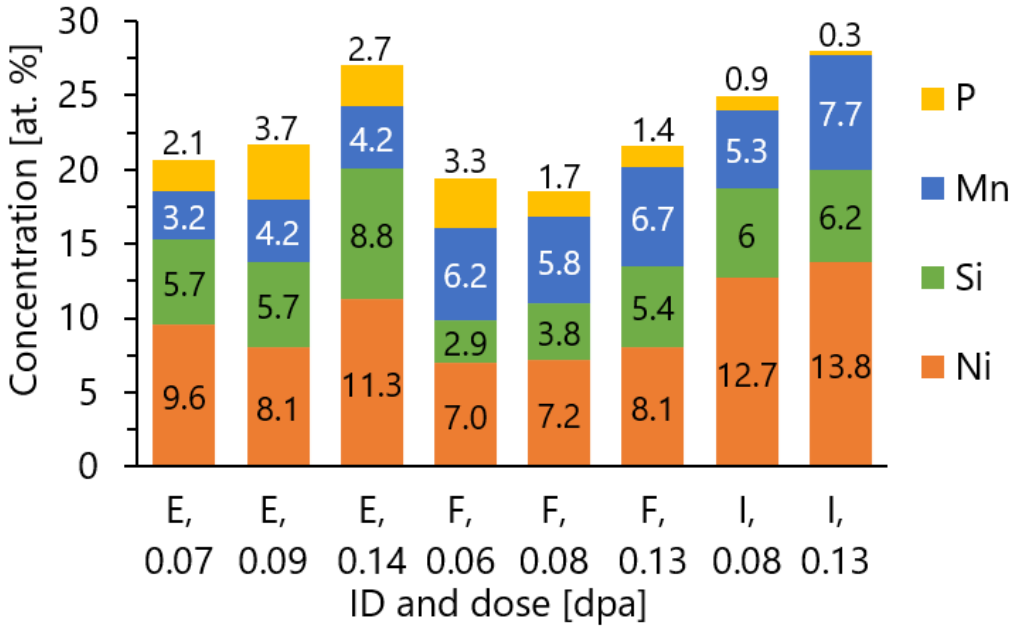

Figure 4. *Concentration of main solutes measured inside clusters in steels E, F and I irradiated to the doses ranging from 0.06 to 0.14 dpa.*

In the case of E, cluster solute concentrations almost do not evolve between low and medium irradiation doses, apart from 1.3 times higher Mn content (4.2 vs 3.2 at. %) and 1.5 times higher P content (3.7 vs 2.1 at. %). With further increase of irradiation dose, P content slightly decreases (from 3.7 to 2.8 at. %), but Ni (8.1 vs 11.3 at. %) and Si (5.7 vs 8.8 at. %) concentrations increase. Mn content remains the same (4.2 vs 4.2 at. %).

In steel F, Ni (from 7.0 to 7.2, and finally to 8.1 at. %) and Si (from 2.9 to 3.8, and further to 5.4 at. %) concentrations continuously increase from low to medium and from medium to high doses. Contrary, P content decreases with the increase of irradiation dose (from 3.3 to 1.7, and to 1.4 at. %). Mn concentration slightly decreases from low to medium dose (from 6.2 to 5.8 at. %) but further increases at the high dose (up to 6.7 at. %).

In the case of I, cluster concentrations of Mn (5.3 to 7.7 at. %), Ni (12.7 to 13.8 at. %) and Si (6.0 to 6.2 at. %) increase and only P content decreases (0.9 to 0.3 at. %) with the increase of irradiation dose.

As it was shown in the literature, P-SIA dumbbell is highly mobile, and P atoms are the first ones to segregate on small PDCs [39,40]. In each material, the decrease of P cluster concentration is observed between medium and high irradiation doses, which correlates well with the significant P matrix depletion observed at medium dose (~50 % of P atoms have segregated).

The proposition is made that with the increase of irradiation dose, the magnitude of P segregation decreases due to depletion of P inside the ferritic matrix. To confirm or deny this hypothesis, we will measure the P concentration inside small and big clusters observed in high dose conditions (above 0.1 dpa) of E and F. The idea being that bigger clusters had nucleated at the lower irradiation dose when a high amount of P was present in solid solution. With the increase of irradiation dose P atoms had segregated towards solutes clusters, dislocation lines and GBs, and newly formed clusters, observed at the dose above 0.1 dpa are mostly P-free.

Figure 5 illustrates solute contents measured inside clusters in steels E (from 30 clusters) and F (from 120 clusters).

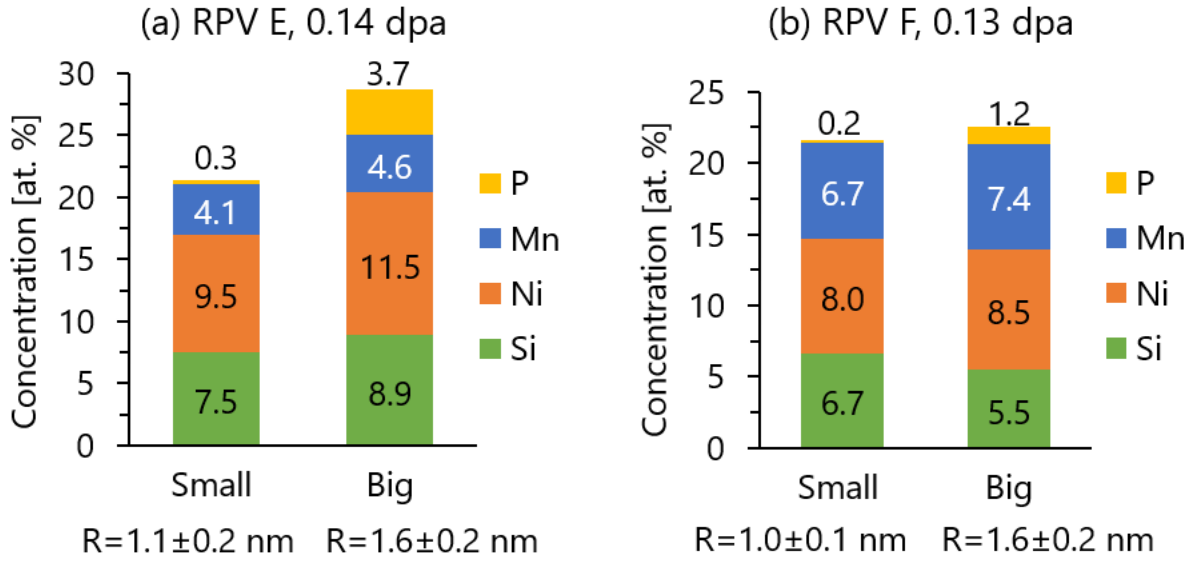

Figure 5. *Concentration of main solutes measured inside small and big clusters. (a) E irradiated up to 0.14 dpa. (b) F irradiated up to 0.13 dpa.*

In both cases (steels E and F), the only significant difference between small and big cluster solute concentrations is the lower P content in the former (0.3 in comparison with 3.7 at. % in the case of E and 0.2 in comparison with 1.2 at. % in the case of F). Additionally, evolution of solute content as a function of distance from the cluster core (represented by APT erosion profile) of steel F is plotted (Fig. 6). Figure 6.a represents the erosion profile in F, irradiated up to the low dose, plotted from 12 clusters. Figure 6.b represent the erosion profile plotted on 18 small clusters (R<1.3 nm) in F irradiated up to high dose.

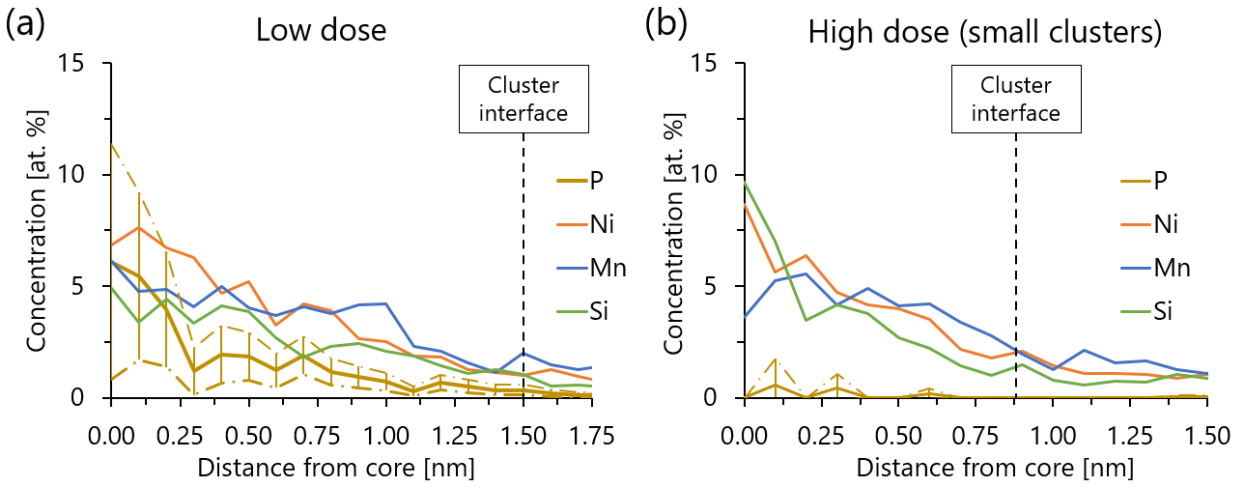

Figure 6. *Erosion profiles for clusters in F. Concentration of main solutes measured inside clusters is plotted. For visual simplicity, statistical uncertainty only for P atoms is plotted. (a) All clusters in the low dose condition. (b) Small clusters (R< 1.2 nm) in the high dose condition. The step size of the erosion profiles is 0.1 nm, and only radial volumes containing more than 80 atoms were selected.*

As we can see from the erosion profiles of the low dose condition (Fig. 6.a) the high P concentration is observed in the core region (below 0.25 nm). Even though P global content (~0.02 at %) is significantly lower than of Mn (1.3 at. %), Ni (0.7 at. %) and Si (0.5 at. %), their core concentrations are on a similar level (~5-7 at. %). Hence, P plays an important role in solute clustering in RPV steels. In the case of small clusters in steel F, irradiated up to the high dose (Fig. 6.b), low P cluster core content is observed. Indeed, with the increase of irradiation dose, the magnitude of P segregation decreases due to depletion of P inside the ferrite matrix. The same tendency is observed in steel E.

The main conclusions from the study on the dose effect are:

- With an increase of irradiation dose, solute cluster number density increases in all materials (E, F, I);
- In steels E and F, average cluster radius increases with irradiation dose before saturating at around 1.6 nm and new smaller clusters start to grow;
- With an increase of irradiation dose clusters become more enriched in Mn, Ni and Si;
- High dose condition of steel I is the only case where notable matrix depletion in Ni (0.13 at. %), Mn (0.06 at. %) and Si (0.05 at. %) is observed;
- Significant matrix depletion in P (~50 %) is observed in 7 from 8 cases;
- High P cluster content is measured in materials irradiated below 0.1 dpa, above 0.1 dpa new family of P-free clusters is found.

2.1.2 Effect of Mn

Effect of Mn bulk (∝ global) concentration on the solute cluster formation will be the first one to be tackled. It is studied on three medium-Ni steels D, E and F with various Mn content. The nominal concentrations of irradiation sensitive solutes and irradiation doses are presented in Table 1. Same as the previous section, the comparison will begin with an evaluation of the Mn effect on the cluster number density.

(i) ***Effect on cluster number density.*** The evolution of the number density of solute clusters as a function of nominal Mn concentration in non-irradiated state measured by APT is presented in figure 7. Information about average and measured in each APT experiment cluster number density is represented.

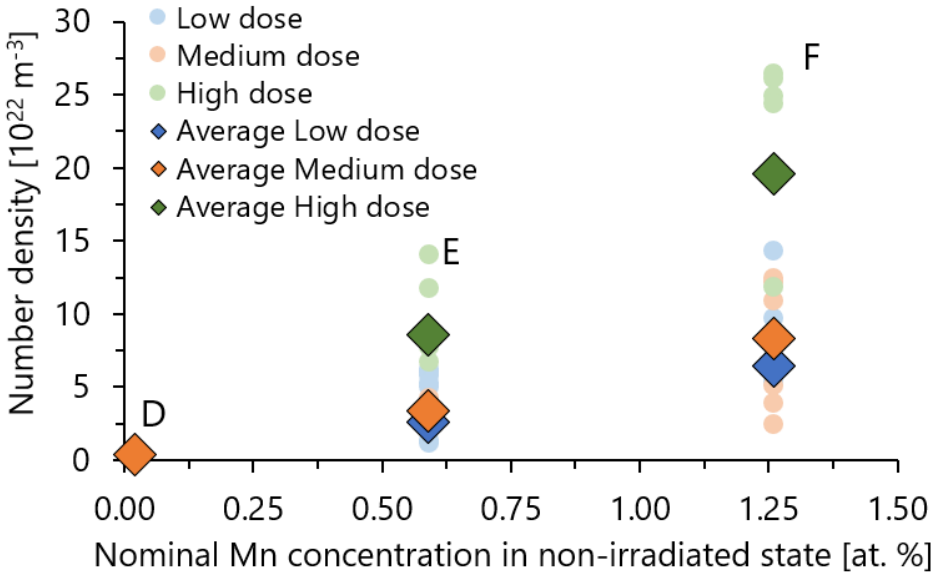

Figure 7. *Evolution of cluster number density as a function of nominal Mn concentration in non-irradiated state is presented. Pale circles represent the number density of clusters for each APT experiment. Diamonds represent the average values (pale circles can be hidden behind diamonds symbols).*

During APT experiments on the low-Mn (0.02 at. %) steel D irradiated up to 0.09 dpa, no solute clusters were found. There are two possible reasons why solute clusters were not detected by APT. Either cluster size is below resolution limit of APT, or their number density is below 4 x 10^{21} m^{-3}, which is lower than typical values (10^{22} to 10^{23} m^{-3}) presented in the literature [5,62-64].

As it was described in section 1.2, solute clusters can form by RIS onto V-clusters and SIA loops. Number density of SIA loops is usually identified with TEM. The minimum size (radius) possibly resolved by TEM is around 1 nm which equals to around 100 SIAs [71,72]. Number density of TEM-visible SIA loop at the irradiation dose of ~0.1 dpa is around (1 to 5) x 10^{21} m^{-3} [73-75]. Yet, in most of these observations were performed on Fe model alloys. In commercial RPV steel

irradiated up to 0.2 dpa, dislocation loops were not identified [72]. Which correlates well with the present PhD project, where no TEM-visible dislocation loops were observed in all CT RPV steels [76]. Positron annihilation spectroscopy (PAS) is usually utilised to evaluate number density of V-type defects, yet is it not as widespread as TEM and less information is available. In the PAS study on the commercial RPV steel, V-clusters with number density of around 10^{24} m^{-3} and size of around 0.2 nm (below 10 V) were observed [62].

To evaluate the possibility of solute cluster formation in steel D an analytical calculation was performed. APT data is used to evaluate the ratio in which solute atoms are segregating on sinks. Number of PD sinks for each CT RPV steel is evaluated from the number density of solute clusters (1 cluster equals 1 sink). Number of solute atoms segregated towards a single sink is taken from the average cluster size (number of solute atoms). Simultaneously the average number of atoms in vicinity of one sink (Nb_{at}^{S}) is calculated by dividing the total number of atoms in volume of 1 m^3 ($Nb_{at}^{m^3}$) by the ND of clusters: $Nb_{at}^{S} = Nb_{at}^{m^3}/N_D$. The calculation on CT RPV steels E, F, I, N and O irradiated up to the doses below 0.1 dpa showed that in average, from surrounding 1 sink volume, only 1 solute over 10300 solute atoms had segregated (segregation rate per one solute atom is 9.7 x 10^{-5}). With the average solute segregation rate will be utilised to estimate the size of solute clusters in steel D.

Now we should evaluate the number of sinks in steel D. Results of Gokhman and co-workers predict that SIA clusters with sizes above 3 monomers are stable [60]. Therefore, the proposition is made that SIA clusters are sinks for PD segregation. Number density of TEM-visible SIA loops in Fe model alloys is on the same level as the highest possible ND obtained from APT experiments (~4 x 10^{21} m^{-3}) [73-74]. With the constant segregation rate of 9.7 x 10^{-5} and sink number density of 4 x 10^{21} m^{-3} the average radius of solute clusters is estimated to be about 2.7 nm, which is obviously above resolution limit of APT. Yet, if these clusters exist, it would take too many experiments to observe them due to the low number density.

Results of KMC modelling performed by Soneda and co-workers predict no stable V-clusters in pure Fe at an irradiation dose rate of 10^{-8} dpa/s and irradiation temperature of 327 °C. These conditions are similar to parameters of current irradiation (3.75 x 10^{-8} dpa/s and 290 °C) [71]. Yet, it is known from atomistic modelling that solute atoms can stabilise V-clusters [28,31,44,45]. Hence, in the case of steel D, if we assume that V-clusters are the possible sinks for PD segregation (ND ~10^{24} m^{-3}) and use the constant segregation rate (9.7 x 10^{-5}), we evaluate that in average, 10 solutes will segregate on one sink. Considering detection limit of APT of 36 % (described in chapter

II), number of solutes in one cluster on APT reconstruction will be equal to 4. Average solute cluster content in studied materials is around 20 at. %, hence the total number of atoms of the cluster containing 4 solute atoms is 20 (radius ~0.5 nm). The resolution limit of APT identification procedure is 8 solute atoms, which approximately equals to the cluster of 40 atoms corresponding to a radius of ~0.7 nm.

Hence, in the case of steel D, if solute clusters were formed on V-clusters, their average radius (~0.5 nm) is below resolution limit of APT (~0.7 nm), and if clusters were formed on SIA-loops, they will be visible on APT (radius 2.7 nm) but were not detected due to low number density (~10^{21} m^{-3}). The slight shift of 1NN distribution of Si atoms (*V* parameter) was measured, which could be the indication of the first steps of solute clustering.

With an initial concentration of 0.6 at. % Mn (steel E) solute clusters start to be visible in the APT volumes irradiated up to the low dose with a number density of around 2.6 x 10^{22} m^{-3}. Increase of Mn concentration by 0.7 at. % (steel F) results in the increase of the cluster number density by a factor of 2.5, up to 6.4 x 10^{22} m^{-3}. At the medium irradiation dose similar tendency is observed and number density in steel F is around 2.5 times higher than in steel E (8.3 vs 3.4 x 10^{22} m^{-3}). At the high irradiation dose number density in steel F is 2.3 times higher than in steel E (19.6 vs 8.6 x 10^{22} m^{-3}). In average, in all irradiation doses with increase of global Mn concentration by the factor 2.1 (1.3 vs 0.6 at. %) number density of solute clusters multiplies by more than two times (2.4). The effect of Mn on solute cluster size will be investigate next.

(ii) ***Effect on cluster size.*** The information about average cluster size measured in steels E and F is presented in Table 3. At the low (1.6 vs 1.4 nm) and medium (1.7 vs 1.5) irradiation doses cluster size is bigger in more solute enriched steel F. In both materials, clusters exhibit a similar cluster growth from low to medium doses. In both E and F clusters growth saturated at radius of ~1.6 nm, and new smaller clusters (radius 1.0-1.1 nm) are observed in the high irradiation dose condition. The average cluster radius in high dose condition (1.4 nm) is closer to the presented in literature data [18,20,63,68]. Probably the most direct way to evaluate the effect of Mn bulk content on solute clusters is by comparison of cluster solute concentration, which will be done further.

(iii) ***Effect on cluster composition.*** Solute concentrations measured inside clusters are presented in figure 4. For all irradiation doses, a higher Mn concentration inside clusters is observed with increase in Mn global content. Mn concentration inside clusters in steel F in comparison with steel E is 1.9 times higher (6.2 vs 3.2 at. %) at the low dose, only 1.4 times higher (5.8 vs 4.2 at. %) at the medium dose and 1.6 times higher (6.7 vs 4.2 at. %) at the high dose. The average factor of

Mn cluster enrichment between F and E is around 1.6, which is close to the ratio (2.1) between global Mn concentration in the steel F in comparison to the steel E.

With the increase of the global Mn concentration, a higher number of Mn atoms are in solid solution, reason why they took the place of Ni and Si atoms inside the clusters. This is observed at every irradiation dose by the average decrease (E in comparison with F) of Ni (from 9.7 to 7.4 at. %) and Si (from 6.7 to 4.0 at. %) cluster contents.

Addition of 0.7 at. % Mn results in the decrease of P cluster content in medium (1.7 vs 3.7 at. %) and high (1.4 vs 2.7 at. %) dose conditions. This could be explained by the competition between Mn and P atoms for SIA transportation. Only in the low dose condition, P cluster concentration in F is higher than in E (3.3 vs 2.1 at. %). Low dose condition of steel E in the only case where number density of clusters formed on dislocation lines is on the level of number density of clusters formed in ferritic matrix (2.3 vs 2.6 x 10^{22} m^{-3}). High P cluster content is measured on the clusters formed alongside dislocation lines (5.5 at. %) could be the reason of lower P enrichment of volume clusters.

In general, the dependence of the nominal solute concentration of the cluster solute content is observed, which is coherent with RIS formation mechanism.

To conclude, at every irradiation dose from 0.06 to 0.14 dpa the notable effect of Mn on solute cluster formation is observed. Number density of solute clusters in high-Mn steel F is 2 to 3 times higher than in medium-Mn steel E. No matter of the Mn global content, radius of solute clusters increases with dose until it reaches the saturation at around 1.6 nm and the new, smaller clusters grow above APT resolution limit at irradiation doses above 0.1 dpa. With an increasing global Mn concentration, Mn cluster concentration increases in expense of Ni and Si concentrations, which agrees with RIS formation mechanism and the competition between solutes to interact with PDs.

In the next section effect of Ni bulk ($\propto$ global) concentration on the microstructure evolution under neutron irradiation will be studied.

2.1.3 Effect of Ni

Evaluation of Ni effect on solute cluster formation is performed on high-Mn steels F and I with medium and high Ni concentrations. The nominal contents of irradiation sensitive solutes and irradiation doses are presented in Table 1. Similar to the previous section, the effect of Ni content on number density will be evaluated first.

(i) ***Effect on cluster number density***. Number density of solute clusters observed in F and I is given in Table 2. To clearly see the effect of Ni content, the evolution of cluster ND as a function of Ni nominal concentration measured by the APT is presented (Fig. 8.a).

Number density of solute clusters is bigger at both medium and high doses in steel I. With two times increase of Ni nominal content (1.6 vs 0.7 at. %), the number density of solute clusters increases almost by a factor of five (4.8) at the medium dose (8.3 to 40.2 x 10^{22} m^{-3}) and by a factor of four (4.1) at high dose (19.6 to 80.3 x 10^{22} m^{-3}). The strong effect (4 to 5 times increase) of Ni content on solute cluster number density is evident. A similar high number density of clusters in high-Ni (1.5 at.%) materials was observed in the literature [18-20,63]. Effect on Ni of solute cluster size will be studied next.

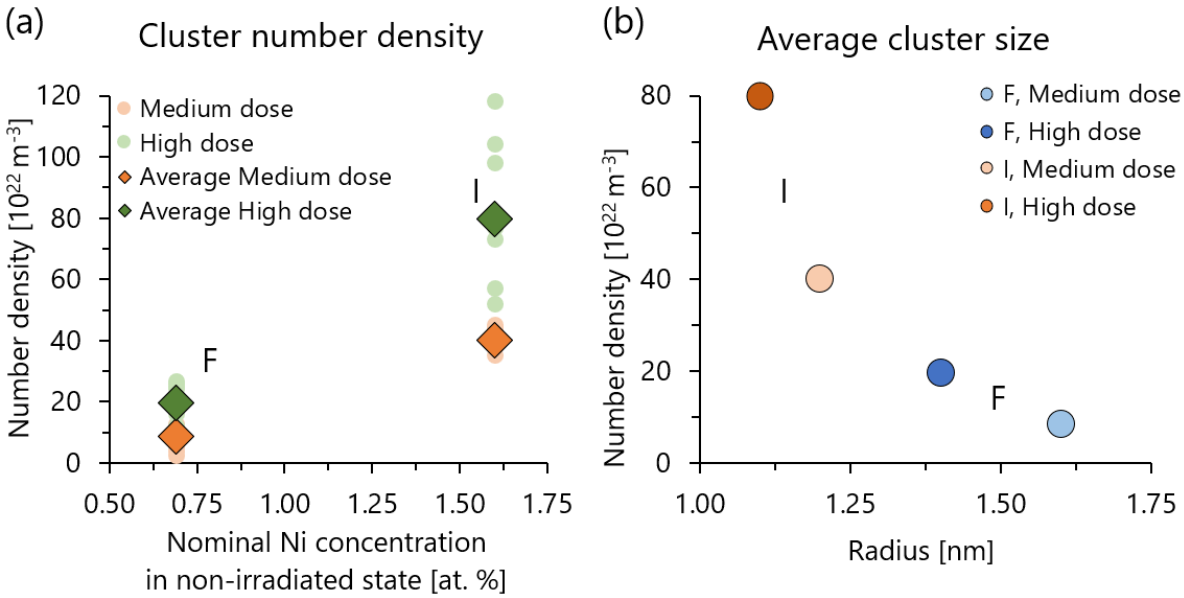

Figure 8. *Cluster properties in steels F and I. (a) Evolution of cluster number density as a function of nominal Ni concentration in non-irradiated state is presented. Pale circles represent number density of clusters for each APT experiment. Diamonds represent the average values (pale circles can be hidden by diamonds symbols). (b) Average cluster radius for a given number density.*

(ii) ***Effect on cluster size***. Average cluster size measured in steels F and I is reported in Table 3 and in figure 8.b. At both irradiation doses cluster radius is smaller in I than in F (1.2 vs 1.7 nm at the medium dose and 1.1 vs 1.4 nm at the high dose). The cluster size distribution in F was described earlier. In the case of I, a monomodal cluster size distribution is observed. The calculations on APT data showed that the segregation rate in I in the medium dose condition is by a factor of two bigger than in F (3.03 vs 1.46 x 10^{-4}). Even with a stronger segregation rate in the case of I, due to an increase of the cluster number density (effectively sinks for segregation), fewer solute atoms end up on a single cluster and hence the average cluster size is smaller.

(iii) ***Effect on cluster composition***. Solute contents measured inside clusters are presented in figure 4. The nominal Ni concentration is two times (2.3) higher in I than in F. Ni cluster concentration in I is higher than if F by a factor of 1.8 (7.2 to 12.7 at. %) at medium dose and by a factor of 1.7 (8.1 to 13.8 at. %) at the high dose. Here a direct correlation between nominal and cluster Ni concentrations is observed.

P cluster content in I is lower than if F at medium (0.9 vs 1.7 at. %) and high (0.3 vs 1.4 at. %) doses. And it seems like P has a less prominent effect on solute clusters in high-Ni material. As it was shown in the literature, the magnitude of Ni-V diffusion is high, and in the case of steel I, the PDCs can be pinned (effectively creating a sink) by V-Ni pairs rather than by P-SIA [27,53,59]. To evaluate the latter proposition, the erosion profile on 20 clusters from steel I irradiated up to the medium dose is plotted (Fig.9). On the erosion profile the high Ni concentration (~10 at. %) is observed in the core region (below 0.25 nm). Mn and Si core concentrations are on a similar level (~5 at. %), and P core concentration is below 1 at. %. In steel I, insignificant effect of P on solute cluster formation is observed. Although, considering statistical error and lateral resolution of APT (~0.5 nm) the firm conclusion that clusters were indeed formed on the small PDC pinned by Ni atoms cannot be made.

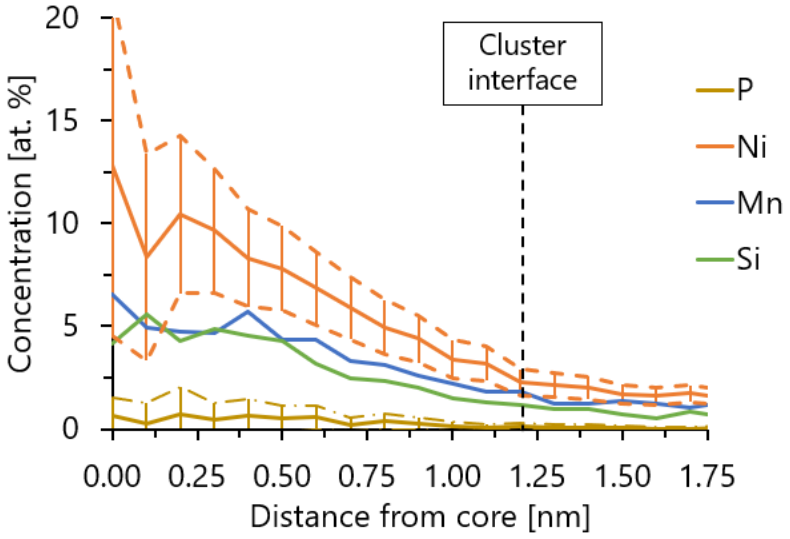

Figure 9. *Erosion profile of clusters in I irradiated up to medium dose. Concentration of main solutes measured inside clusters is plotted. For visual simplicity, statistical uncertainty only for Ni and P atoms are plotted. The step size of the erosion profile is 0.1 nm, and only radial volumes containing more than 80 atoms were selected.*

Mn cluster content is almost the same in both materials at medium dose (~5.5 at.%) and slightly higher in I (7.7 vs 6.7 at. %) at the high dose condition. Si cluster concentration is higher in I than in F at medium (6.0 vs 3.8 at. %) and high (6.2 vs 5.4 at. %) doses. The total increase of solute

enrichment in I can be attributed to the synergy between Mn, Ni and Si, since with the increase of Ni segregation magnitude, the segregation of Mn and Si also increased. Or maybe in the case of steel I a mechanism of cluster formation different from RIS, such as REP, is activated?

Even though a high Fe content (~75 at. %) is measured inside the clusters studied in the present project (confirmed by CCC model) the probability of predicted by modelling Mn-Ni-Si precipitation is studied. To do so, the cluster concentration of other solutes and Fe are excluded, and sum of Mn, Ni and Si contents is normalised to 100%. The average relative cluster Mn-Ni-Si concentrations in steel I are 22Mn-53Ni-25Si at the medium dose and 28Mn-53Ni-22Si at the high dose. At both doses, relative Mn-Ni-Si concentrations are similar to the predicted by modelling Fe-free G-phase (21Mn-55Ni-24Si). Ternary plot with relative Mn, Ni and Si cluster concentrations is reported in figure 10.

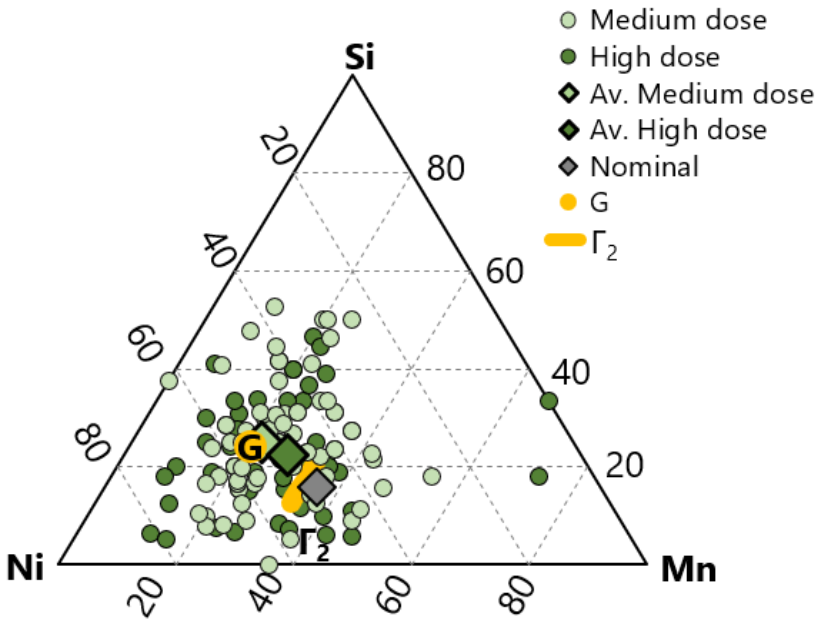

Figure 10. *Ternary plot with relative Mn, Ni and Si cluster concentrations excluding Fe, other species and normalised to 100%. Light green and deep green symbols represent clusters observed in steel I at medium and high doses respectively. Only clusters containing at least 10 solute atoms are represented.*

On the ternary plot a high dispersion of Mn-Ni-Si relative cluster concentrations is observed. After irradiation at both medium (0.08 dpa) and high (0.13 dpa) doses, only a few clusters correspond to Γ_2 and G stoichiometries. At both irradiation doses a high dispersion of cluster relative concentrations is observed. Considering the following observations:

- Only a few clusters have relative concentrations close to predicted phases (Γ_2 and G);
- High Fe concentration inside the clusters (~75 % at.).

The conclusion is made that the observed tendencies are in agreement with an irradiation-induced segregation formation mechanism rather than radiation enhanced precipitation.

The same procedure is performed for steel F (Fig. 11). The same tendency as in steel I is observed.

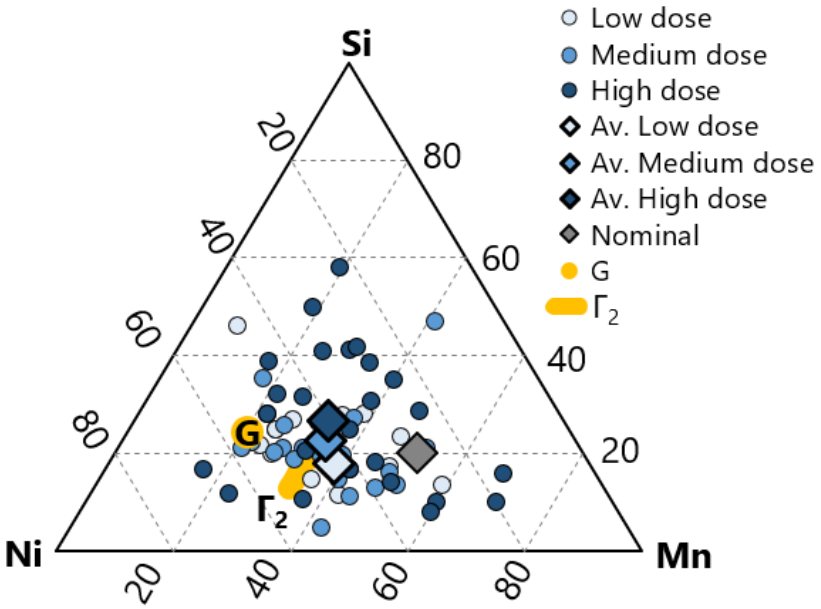

Figure 11. *Ternary plot with relative Mn, Ni and Si cluster concentration excluding Fe, other species and normalised to 100%. Light blue, blue and deep blue symbols represent clusters observed in steel F at low, medium and high doses respectively. Only clusters containing at least 10 solute atoms are represented.*

2.1.3 Synergy between Mn and Ni

To fully understand the synergy between Mn and Ni on the microstructure evolution in ferritic steels, an additional study on high-Ni (~1.5 at. %) and medium-Mn (~0.7 at. %) steel is necessary to evaluate the separate effect of increase of Ni content in the medium Ni/Mn material. Unfortunately, the material with the latter composition was not studied in the framework of the PhD project.

However, during APT experiments on steel I irradiated up to the high dose, a Mn depleted (0.76 instead of 1.10 at. %) volume is intercepted (R5224). Ni (1.5 at. %) and Si (0.5 at. %) contents are unchanged. The total size of the volume is 6.3 million atoms, and the total number of identified clusters is 114. Number density equals (50.5 ± 4.8) x 10^{22} $m^{-3,}$ and the average cluster radius is (1.1 ± 0.1) nm. Results obtained in this experiment are named I* and will represent the high-Ni/med-Mn steel. Further, a comparison between I* and steels E, F and I in the high dose condition will be performed (Table 5).

Table 5. *Solute concentrations and cluster number densities in steels with variable Mn and Ni contents.*

ID	Mn [at. %]	Ni [at. %]	Number density [10^{22} m^{-3}]	Effect	Increase of ND vs E [10^{22} m^{-3}]
E	0.6	0.7	8.6	Med Ni/Mn	-
F	1.3	0.7	19.6	+ Mn	11.0
I*	0.8	1.5	50.5	+ Ni	41.9
I	1.1	1.5	80.3	+ Ni and Mn	71.7

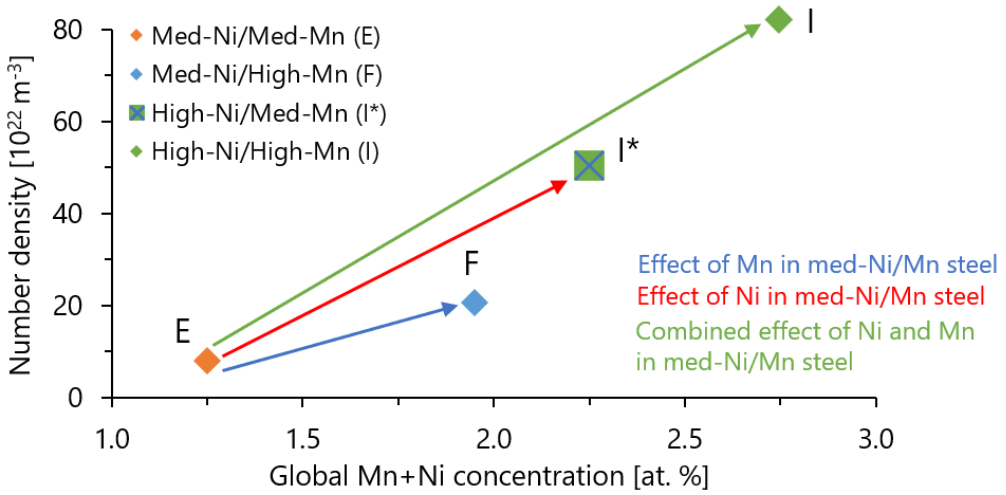

Figure 12. *Evolution of cluster number density as a function of combined Mn+Ni concentrations in materials irradiated up to the high dose. Diamonds represent the average values for material where several APT experiments are performed. Crossed square symbol is the number density evaluated from one APT experiment on I* where lower than expected global Mn concentration is measured.*

The addition of Mn to the steel E results in the increase of ND by 11 x 10^{22} m^{-3}. At the same time, addition of Ni to steel E rises the ND by 41.9 x 10^{22} m^{-3}. Hence, it is obvious that Ni has a stronger effect on the solute cluster number density than Mn. Yet, the question concerning the Mn/Ni synergy remains.

The estimated total increase of cluster number density when Mn and Ni are added separately (F + I*) equals to 52.9 x 10^{22} m^{-3} [(11 + 41.9) x 10^{22} m^{-3}]. When these solutes are added simultaneously, the number density of solute clusters increases by 71.7 x 10^{22} m^{-3} (from 8.6 to 80.3 x 10^{22} m^{-3}). The synergistic effect of Mn and Ni of number density is larger (71.7 vs 52.9 x 10^{22} m^{-3}) in comparison with the separate effect of these solutes.

As it was described in chapter III, austenitic phase was observed in the high-Ni/Mn steel I with electronic microscopy (EBDS, TEM) [76]. The composition of austenitic phase was evaluated by means of TEM-EDS. The latter is enriched in Ni (2.5 at. %) and Mn (3.5 at. %) [76]. During

APT experiments in non-irradiated state a dedicated study on the austenite phase was performed. The APT results confirmed that the austenitic phase is enriched in Ni (2.9 at. %) and Mn (3.9 at. %), and additionally, in Cu (0.082 at. %) and C (1.7 at. %).

During APT experiments in the irradiated state no site-specific lift-outs were performed. Yet, in several APT experiments an enriched in Mn, Ni, Cu and C phase was randomly. There are no direct confirmations (EBSD, TEM) that indeed austenitic phases were intercepted during APT experiments on irradiated materials. Yet, since the global composition of enriched phases is similar to the austenite phase observed in the reference steel, a proposition that they are in reality the austenitic phases is made. Information about irradiation conditions and global concentrations of irradiation sensitive solutes and C of these phases is given in Table 6.

Table 6. *Global concentration of irradiation sensitive solutes and C measured with APT. Information about irradiation doses is also given.*

ID	Dose [dpa]	Concentration [at. %]						Solute clusters
		Mn	Ni	Si	P	Cu	C	
I ref. (F)	-	1.1	1.6	0.5	0.019	0.046	0.1	No
I ref. (A)	-	3.9	2.9	0.4	0.007	0.082	1.7	No
R 5209	0.082	3.8	3	0.4	0.006	0.084	2.2	No
R 5218	0.082	4.3	3.4	0.4	0.013	0.105	2.1	No
R 5222	0.132	3.9	2.7	0.3	0.005	0.067	0.9	Yes

In non-irradiated state and in two APT experiments (R5209 and R5218) on the medium dose condition no solute clusters are observed. Formation of clusters in austenitic steels is only expected at the higher doses of several dpa [77,78]. Absence of clusters at the irradiation dose of around 0.1 dpa is coherent with the results available in the literature. Also, no pole figures are observed in the detector maps of these two experiments. Taking the two latter facts into account a conclusion is made that indeed austenitic phase is intercepted.

However, in one APT experiment (R5222) on steel I irradiated up to the high dose of 0.13 dpa, 624 clusters are identified. The volume consists of 7.3 million atoms, and the cluster number density is $(23 \pm 1) \times 10^{23}$ m^{-3}, with the average cluster radius of (1.3 ± 0.2) nm. Measured number density and size are on the same level as in high-Ni (~3 at. %) model RPV materials irradiated up to ~0.2 dpa [19,20]. Clusters are enriched in Mn (19.2 at. %), Ni (22.2 at. %) and to a less extent in Si (2 at. %), C (1.1 at. %) and Cu (0.6 at. %), and the balance is Fe. Besides, pole figures on the APT detector map are identified. Therefore, a conclusion is made that the enriched in solutes phase is ferrite, not austenite.

Although additional information about enriched in solutes phases should be collected, it is a supplemental highlight of the synergy between Mn and Ni, starting from microscale (formation of austenitic phase) and continuing during irradiation (synergetic effect on cluster number density).

The main conclusions from the studies on Mn and Ni effect are:

- Mn has an enhancing effect on the solute cluster formation in CT RPV steels. With increasing Mn nominal concentration, the solute cluster number density increases;
- Ni has a strong promoting effect on solute cluster formation. With increasing Ni nominal concentration, number density of clusters strongly increases;
- In medium-Ni materials, P has an important role in solute clustering at doses below 0.1 dpa;
- Synergetic effect of Mn and Ni of solute cluster formation is observed;
- Cluster composition is linked to the global composition of material;
- The Mn, Ni and Si enrichments in clusters are in agreement with a radiation-induced segregation process rather than radiation enhanced precipitation;
- In the low-Mn CT RPV steel D, the non-detection of clusters indicates that clusters with the radius of around 2.7 nm have a number density lower than 4×10^{21} m^{-3} and/or clusters have small sizes of below 8 solute atoms or 0.7 nm in radius, below resolution limit of APT.

2.2 Effect of bulk P concentration

The effect of P on the solute cluster formation is not extensively studied. A bigger focus is on its effect on grain boundaries (segregation) and non-hardening embrittlement, yet P-rich clusters were observed in Fe-P (~0.045 at. %) model alloy and in high-P (~0.06 at. %) VVER weld [8,79,80]. Effect of P on microstructure evolution under irradiation is studied on the medium-P steel N and high-P steel O. Nominal concentrations Si, Mn, Ni, P and Cu measured in non-irradiated state and irradiation doses are presented in Table 7.

Table 7. *Irradiation doses and nominal concentration of irradiation sensitive solutes measured with APT at the non-irradiated state.*

ID	Type	Nominal concentration [at. %]					Dose [dpa]
		Si	Mn	Ni	P	Cu	
N	Medium-P	0.49	1.05	0.62	0.030	0.039	0.075
O	High-P	0.52	0.99	0.63	0.047	0.043	0.063

Steel O was irradiated up to a lower dose than steel N. However, the difference (0.012 dpa) is reasonably insignificant to make a direct comparison. The comparison will begin with evaluation of the P effect on number density.

(i) ***Effect on cluster number density.*** Solute clusters are observed in both N and O. Number density of solute clusters as a function of nominal P concentration in the non-irradiated state measured by the means of APT is presented in figure 13.a. In steel N with nominal P content of 0.030 at. % number density of observed solute clusters equals 5.2 x 10^{22} m^{-3}. In steel O with 1.6 times higher P nominal concentration (0.047 vs 0.030 at. %) number density of solute clusters is higher by a factor of 2.3 (12.1 x 10^{22} m^{-3}). Albeit O was irradiated up to a slightly lower dose (0.063 vs 0.075 dpa) than N, number density of solute clusters is two times higher. The mechanism resulting in the increase in cluster number density in steel O will be discussed in sub-section iii. Overall, a significant effect of high-P concentration of solute cluster number density is observed. In the next section effect of P on cluster size will be investigated.

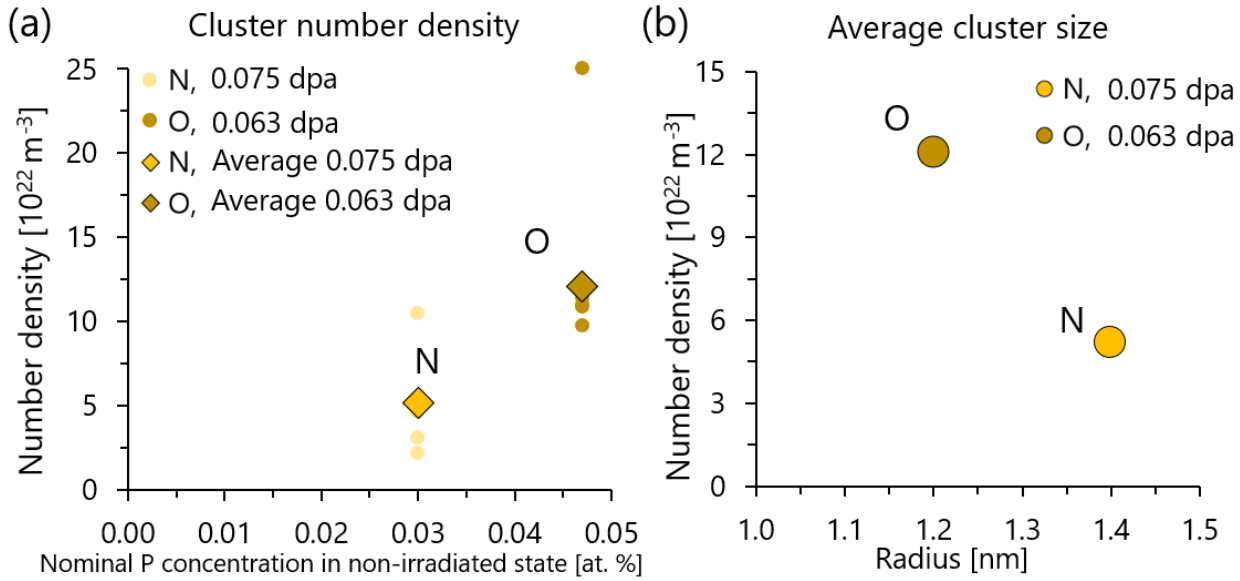

Figure 13. *Cluster properties in steels N and O. (a) Evolution of cluster number density as a function of nominal P concentration in non-irradiated state is presented. Pale circles represent number density of clusters for each APT experiment. Diamonds represent the average values (pale circles can be hidden by diamonds symbols). (b) Average cluster radius for a given number density.*

(ii) ***Effect on cluster size.*** On the right chart, the evolution of number density as a function cluster size is presented (Fig. 13.b). Steels O and N have relatively the same combined Si, Mn, Ni, Cu and P concentration (around 2.2 at. %). However, the cluster radius is smaller (1.2 in comparison with 1.4 nm) in the case of steel O, where a higher number density of clusters is observed (12.1 in comparison with 5.2 x 10^{22} m^{-3}).

The solute segregation rate in steels N and O is calculated. The segregation rate in O (7.80 x 10^{-5}) is by a factor of 1.5 higher than in N (5.24 x 10^{-5}). A slightly lower irradiation dose (0.063 vs 0.075) in the case of O could be the reason of the smaller cluster radius. If the solute segregation rate in steel O will remain constant, the average cluster radius at the dose of 0.075 dpa is expected to be 1.3 nm, which is close to the value of 1.4nm measured in N. P effect of solute cluster composition will be the next one to tackle.

(iii) ***Effect on cluster composition***. To deeper understand the effect of P on solute clustering a comparison between cluster compositions should be performed. Solute contents measured inside the cluster are reported in figure 14. Combined concentration of impurities (Cu, Mo, Al, C) is below 1 at. % and is not presented. Balance is in Fe.

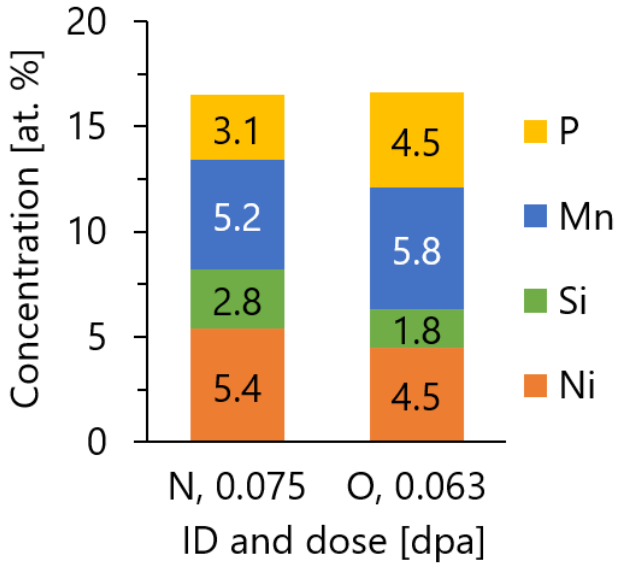

Figure 14. *Concentration of main solutes measured inside clusters in steels N and O irradiated to the doses ranging from 0.063 to 0.075 dpa.*

With a factor 1.6 increase in P nominal concentration (0.030 to 0.047 at. %), the P cluster content increases by a factor of 1.5 (3.1 to 4.5 at. %). Steels N and O have a similar nominal Mn, Ni and Si concentrations and with addition of phosphorus Mn and Ni cluster concentrations insignificantly vary (<1 at. %). Yet, 1.6 time decrease in Si cluster content is observed (from 2.8 to 1.8 at. %), which correlates well with repulsive interaction between Si and P predicted by DFT modelling [41].

The high mobility of P atoms by SIA diffusion is predicted by SCMF modelling [27]. To evaluate if P atoms are indeed the most diffusive and first one to segregate, the erosion profile could be utilised. Erosion profiles for steels N (from 9 clusters) and O (from 11 clusters) are presented in figure 15.

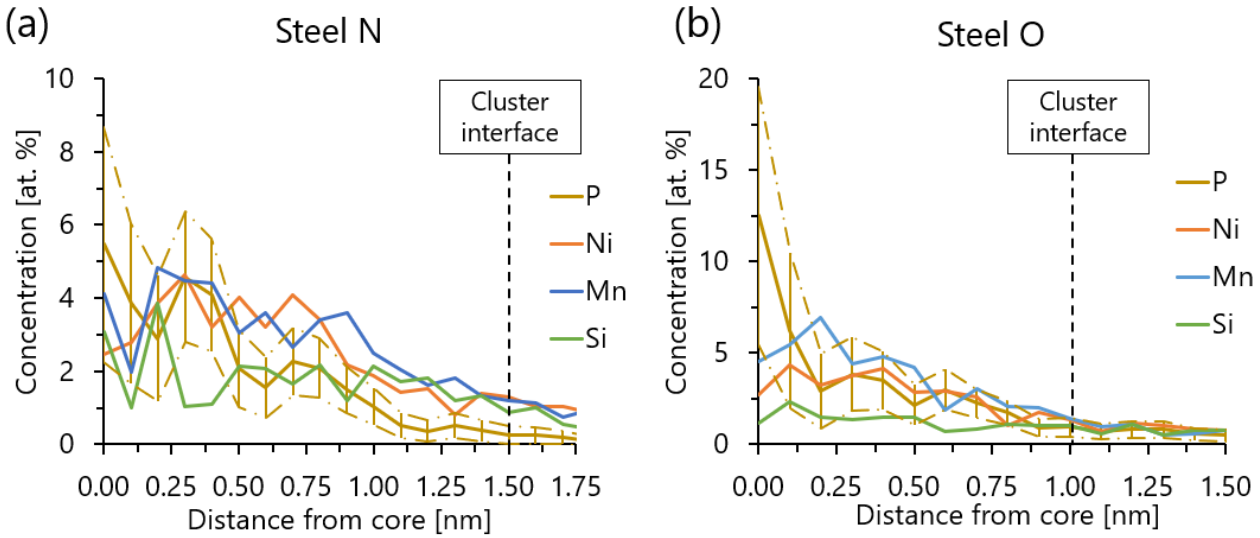

Figure 15. *Erosion profiles for clusters in N and O. Concentration of main solutes measured inside clusters is plotted. For visual simplicity, statistical uncertainty only for P atoms is plotted. (a) Medium-P steel N (0.075 dpa) (b) High-P steel O (0.063 dpa). The step size of the erosion profiles is 0.1 nm, and only radial volumes containing more than 80 atoms were selected.*

In steel N (Fig. 15.a), alike to the case of low-P (~0.02 at. %) steel F irradiated up to 0.059 dpa tendency is observed (Fig. 6). Cluster core is enriched in Mn, Ni, Si and P (~4 at. %). However, in the case of O (Fig. 15.b), the high P concentration (~10 at. %) is observed closer to the cluster core. Considering statistical error and lateral resolution of APT (~0.5 nm) the firm conclusion that clusters were indeed formed on the small PDC pinned by mobile P-SIA dumbbell cannot be made. Yet, this data confirms the important role of P in solute cluster formation.

In addition, we can compare steels N and O with low-P (~0.02 at. %) steel F, which has 0.2 at. % higher Mn content and was irradiated up to 0.059 dpa. In the case of steel N, similar to the low-P steel F number density (5.2 vs 6.4 x 10^{22} m^{-3}), P cluster content (3.1 vs 3.3 at. %) and P core concentration on erosion profile (~5 at. %) are observed. At the same time in steel O higher than in steel F number density (12.1 vs 6.4 x 10^{22} m^{-3}), P cluster content (4.5 vs 3.3 at. %) and P core concentration on erosion profile (10 vs 5 at. %) are measured.

Because of high P (above 3 at. %) and high Fe (above 80 at. %) concentrations inside the clusters, the mechanism of cluster formation in steels N and O is concluded to be rather radiation-induced segregation than radiation enhanced precipitation.

The main conclusions from the study on P effect are:

- No significant evolution of microstructure in medium-P steel is observed;
- High-P concentration results in increase of cluster number density;

- The important role of P on the solute cluster formation was confirmed by the high P concentration inside the cluster core;
- In medium-P and high-P steels N and O solute cluster compositions are in agreement with radiation-induced segregation formation.

2.3 Effect of the high Cu, P, Ni, Mn concentrations and the synergy between solutes

Steel W is heavily concentrated in solute elements (~3.6 at. %) and is the only high-Cu material studied in the current project (Table 8).

Table 8. *Irradiation dose and nominal concentration of irradiation sensitive solutes measured with APT at non-irradiated state.*

ID	Type	Nominal concentration [at. %]					Dose [dpa]
		Si	Mn	Ni	P	Cu	
W	High solutes	0.49	1.18	1.57	0.043	0.266	0.06

Steel W has almost the same Mn (~1.2 at. %) and Ni (~1.5 at. %) concentrations as steel I. The main difference concerns P (0.043 in comparison with 0.019 at. %) and Cu (0.27 in comparison with 0.04 at. %) contents. As it was shown in the previous section, the difference of P concentration by 0.017 at. % between steels N and O irradiated up to 0.075 and 0.063 dpa results in the increase of cluster number density by ~7 x 10^{22} m^{-3}. Cluster number density in steel I irradiated up to 0.08 dpa is around 40 x 10^{22} m^{-3}. With such a high number density, the effect of P (~7 x 10^{22} m^{-3}) is expected to be insignificant. Hence, the only noteworthy difference between steels W and I is the Cu content.

Results presented in the literature on high-Cu materials predict the accelerated formation of CEFs [1-4,69]. In addition, formation of Mn-Ni-Si enriched structures on the CEFs interfaces was observed [18,70]. They can have a complex morphology such as Cu-rich core with Mn-Ni-Si-shell and Mn-Ni-Si-appendage. Therefore, the term solute-enriched features (SEFs) will be used. Number density of clusters and solute-enriched features in steels I and W as a function of irradiation dose is presented in figure 16.

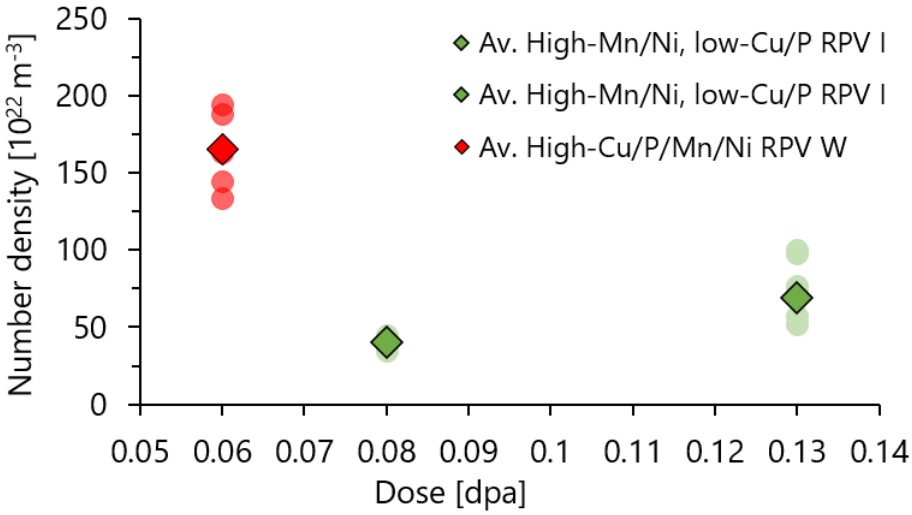

Figure 16. *Evolution of cluster (I) and solute-enriched feature (W) number densities as a function of irradiation dose. Pale circles represent number density of clusters for each APT experiment. Diamonds represent the average values (pale circles can be hidden by diamonds symbols).*

The strong effect of Cu bulk content on SEF formation is observed. Even at the dose of 0.06 dpa, which is two times lower than the high dose condition of steel I (0.13 dpa), the number density of solute-enriched features in steel W is more than two times higher than of clusters in I [(165 ± 9) in comparison to 80.3] x 10^{22} m^{-3}. Average solute enriched features radius is (1.4 ± 0.3) nm.

The ferritic matrix is depleted in Cu (by 0.16 at. %), Ni (0.38 at. %), Mn (0.29 at. %), Si (0.09 at. %), P (0.010 at. %) and Al (by 0.023 from nominal concentration of 0.056 at. %). Which is significantly more than in the case of steel I irradiated up to 0.08 dpa (Ni - 0.05, Mn - 0.02 and Si - 0.02 at. %). Here a strong synergy between Cu and other solutes is observed, since with addition of Cu, the magnitude of matrix depletion (i.e. high segregation on sinks) of other solutes increases by a factor of 8 for Ni, of 15 for Mn and of 5 for Si. The evaluated segregation rate in steel W is 1.95 x 10^{-3}, which is by a factor of ~20 higher than the average segregation rate of CT RPV steels of 9.7 x 10^{-5}.

To give indication on the possible mechanism involved in solute-enriched features formation in steel W, a graph with the evolution of feature solute content as a function of nominal solute concentration is presented (Fig. 17). A high Al concentration (1.3 at %) is found inside solute-enriched features in steel W. Al is not known to have a strong clustering or precipitation tendency at the operation conditions of RPV steels, and the exact mechanism of its segregation in the present case is not known. Cu (0.27 at. %) is in supersaturation in the ferritic matrix and diffuses potently by radiation enhanced diffusion with an enrichment factor of ~20 (5.8 vs 0.27 at. %). Lower enrichment tendency is observed for Mn (factor of 6.8), Ni (factor of 8.6), Si (factor of 8.6) and P

atoms (factor of 12.5). Could the difference in enrichment factors be due to different formation mechanisms: driven by RED in the case of Cu, and RIS in the case of Mn, Ni, Si and P?

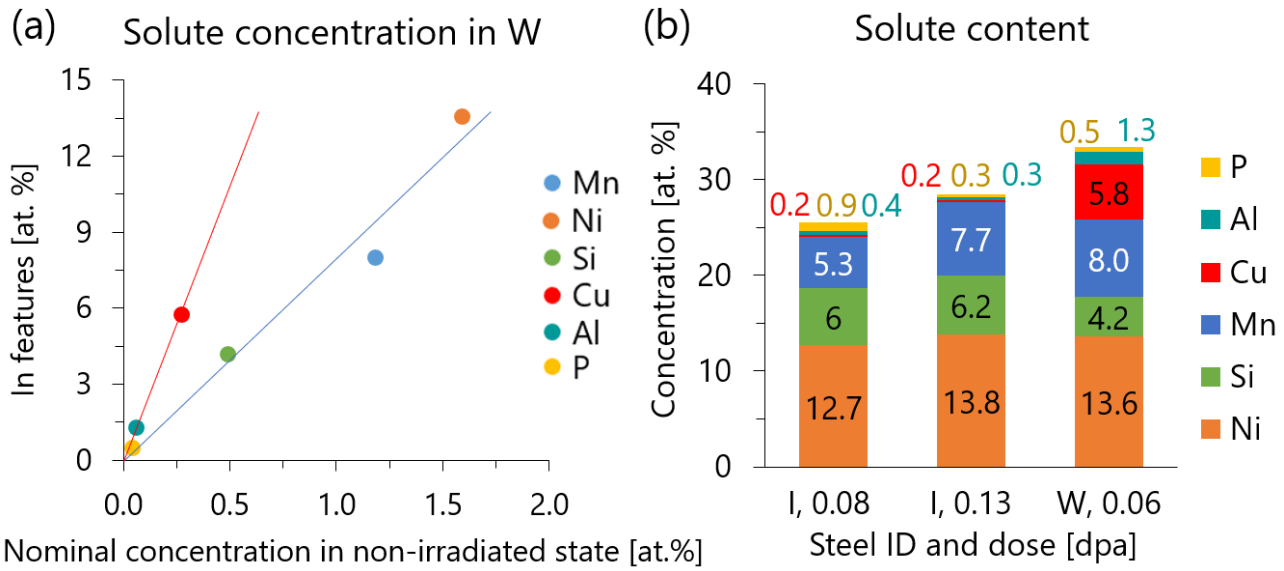

Figure 17. *(a) Evolution of enriched feature solute concentrations as a function of nominal concentration in steel W. Red line is the trend for Cu atoms. Blue line is the trend for Mn, Ni and Si. (b) Solute concentrations of clusters and solute-enriched features observed in steels I and W irradiated from 0.06 to 0.13 dpa.*

In the present study, several distinct morphologies of solute-enriched features are observed. Big (radius above ~1.7 nm) solute-enriched features usually contain a Cu-enriched core with Mn-Ni-Si appendage structure (Fig. 18) [18,20,81].

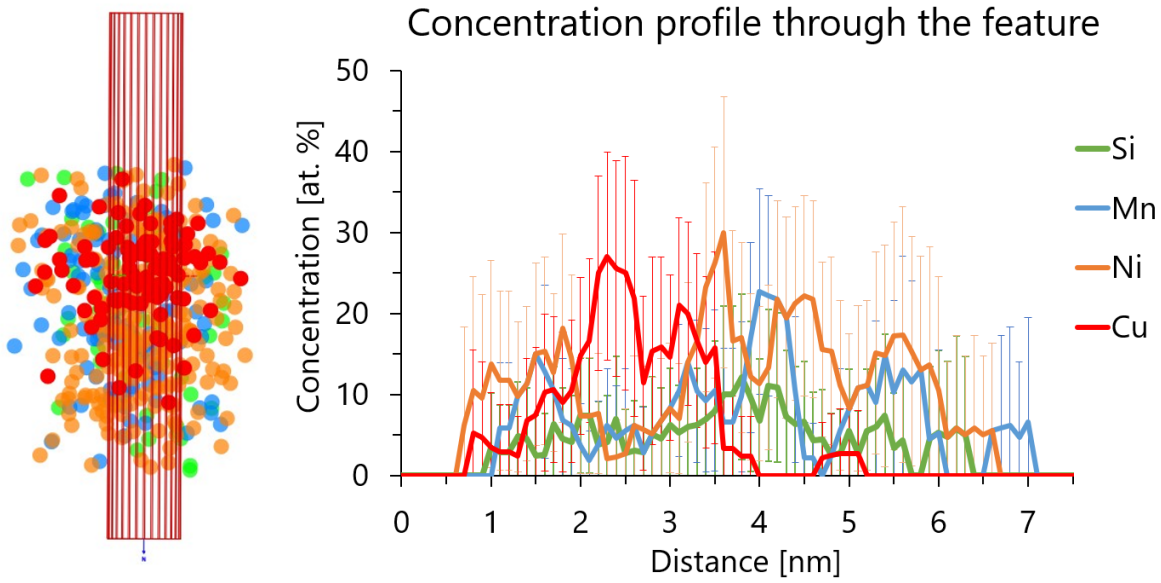

Figure 18. *Concentration profile through solute-enriched feature. Radius of section is 0.7 nm, section height is 0.5 nm, step size is 0.1 nm. Cu-enriched feature with Mn-Ni-Si appendage is observed. Statistical error of measurements is also presented.*

Solute-enriched features with a radius ranging from 1.2 to 1.7 nm usually contain Cu atoms in the core area with Mn-Ni-Si shell-like structure around it (Fig. 19).

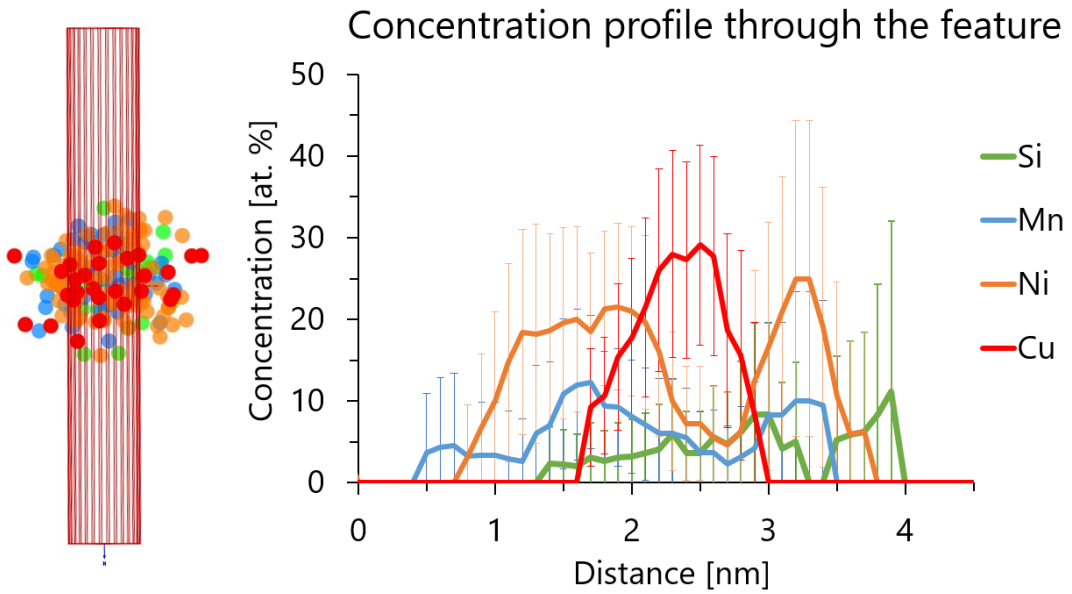

Figure 19. *Concentration profile through solute-enriched feature. Radius of section is 0.7 nm, section height is 0.5 nm, step size is 0.1 nm. Cu-enriched core with Mn-Ni-Si shell is observed. Statistical error of measurements is also presented.*

Both Cu-core with MNS-appendage or with MNS-shell morphologies of solute-enriched features were observed in the literature [18,70,81].

Besides, within the SEFs population, especially for small size (radius below 1.2 nm), a different morphology is observed. Some of them do not have a distinct Cu-rich core but rather exhibit a random distribution of Cu, Si, Mn, Ni and P atoms (Fig. 20.a). Also, Cu-free SEFs with radius around 1 nm are observed (Fig. 17.b).

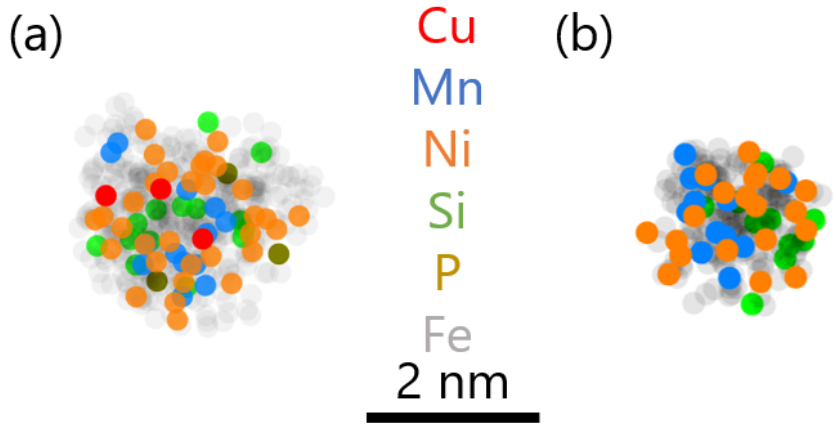

Figure 20. *Atom maps of solute-enriched features. (a) Cu, Si, Mn, Ni and P enriched feature. (b) Mn, Ni, Si enriched feature.*

The of evolution of SEF Cu content as a function of radius is presented in figure 21 (from APT experiment containing 24 features).

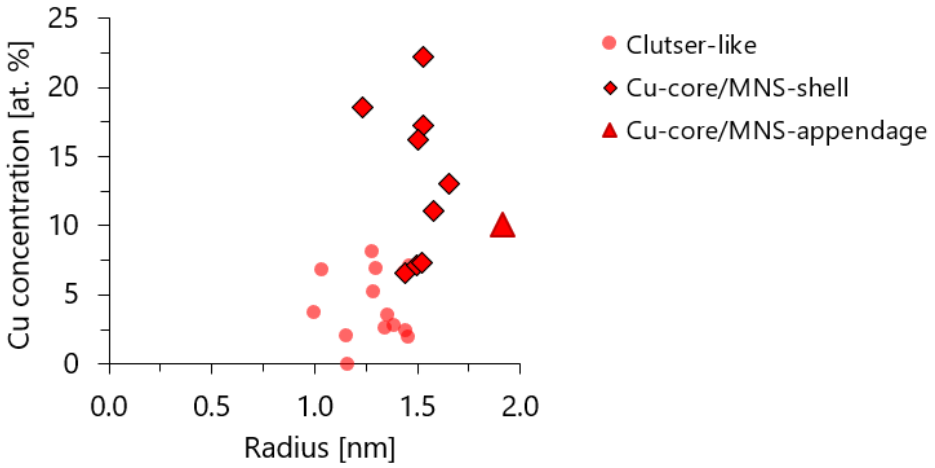

Figure 21. *Evolution of Cu concentration as a function of solute-enriched feature radius. Radius is calculated from number of atoms after half-maximum erosion. Cu concentration measured in the core erosion after plateau erosion.*

Most of features don't have a distinct Cu-core but rather a diluted distribution of solute atoms. Their radius is ranging from ~0.9 to 1.5 nm and they contain around ~5 at. % of Cu. They are identified as solute clusters formed by RIS. The second group is the features with Cu-rich core and Mn-Ni-Si shell. Their size is bigger than of clusters (1.2 to 1.7 nm) and Cu content varies from ~7 to 22 at. %. (10 ± 2 at. % Cu in average). But, if the erosion procedure is performed only for Cu atoms, the core composition is (~18 ± 3) at. %, which is similar to the Cu-content measured in the reference steel W (~15 at. %). Due to the similar Cu concentration as inside the features found in the non-irradiated material, a conclusion that Cu-enriched core is formed by radiation enhanced mechanism is made. Finally, one feature with Cu-core and Mn-Ni-Si appendage is identified. With the biggest radius of 1.9 nm and core Cu content of ~10 at. %.

In the case of high-Cu RPV steels, Cu diffusion is also driven by chemical potential due to its supersaturation in ferrite matrix, contrary to the other solutes of interest. That's why at the early irradiation doses and high supersaturation, Cu diffusion is fast and vast number of CEFs is formed. Further, with the increase of irradiation dose, Cu supersaturation lowers (observed by matrix depletion) and effect of thermodynamically driven Cu diffusion mitigates. From this moment, a formation of low-Cu and Cu-free clusters is governed by radiation-induced segregation. This conclusion is coherent with the lower Cu content measured inside the cluster-like features. Also, P atoms, known to be transported by SIAs, are found inside these clusters.

CEFs are predicted to act as sites for Mn-Ni-Si segregation [16,18,70]. In the present research, a similar morphology of CEF with Mn-Ni-Si shell and appendage structures, as in the materials irradiated up to 1.5 dpa is observed [18]. To evaluate the nature of MNS segregation, a ternary plot with relative Mn, Ni and Si concentrations inside features (excluding Fe, other solutes and normalised to 100%) is plotted (Fig. 22). The average solute ratio of 31Mn-53Ni-16Si is similar to the composition of predicted Fe-free Γ_2 phase (33Mn-48Ni-19Si). However, a high dispersion of the relative Mn-Ni-Si concentrations for an individual clusters is observed. This dispersion could be due to the local heterogeneity of solutes, which are dragged by the flux of PDs in the same ratio as they are randomly present inside the matrix. Taking latter and high Fe concentration (around 66 at. %) into account, we can conclude that in high-solutes steel W Mn-Ni-Si shell and appendage structures are more probably formed by radiation-induced segregation than by radiation enhanced diffusion.

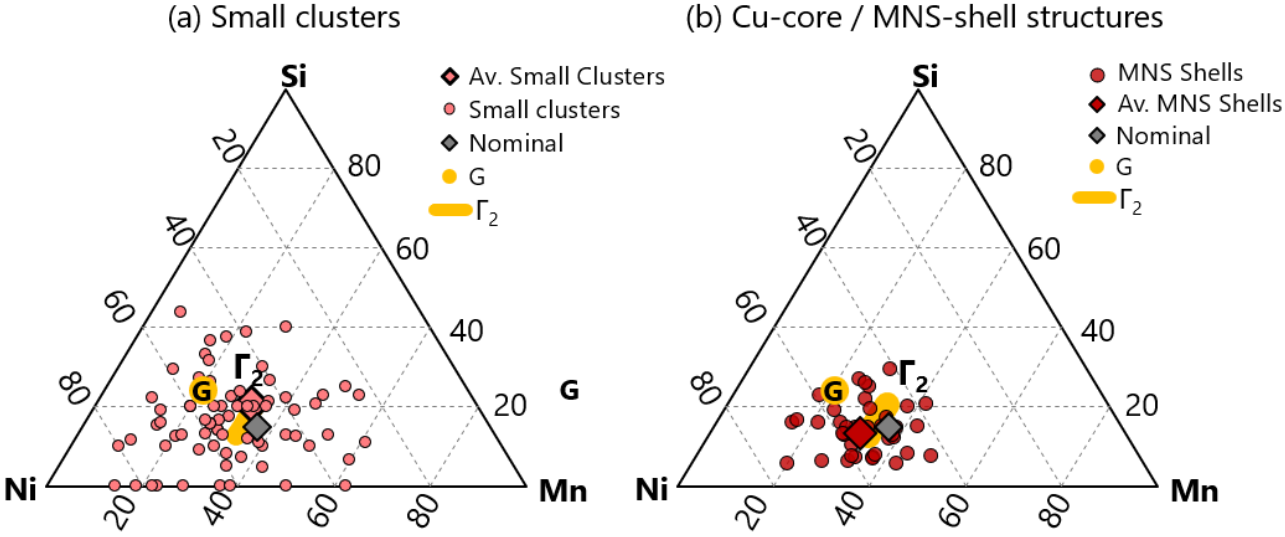

Figure 22. *Ternary plot with relative Mn, Ni and Si solute-enriched features concentration excluding Fe, other species and normalised to 100%. Pink symbols represent cluster-like features. Dark red symbols represent the features which have a distinct Cu-enriched core and MNS shell structure.*

The main conclusions from the study on high solute content effect are:

- High Cu nominal concentration results in the formation of a high number density of CEFs;
- Cu has a synergetic effect with Mn, Ni and Si, enhancing the magnitude of their segregation which is observed by significant matrix depletion of latter;
- At low irradiation dose, CEFs formation is enhanced by the radiation defects supersaturation;

- With longer irradiation and local depletion of Cu inside the matrix (toward solubility limit), Cu-free solute clusters, also enriched in Mn, Ni, Si and P, are formed due to solute-PD flux coupling resulting in radiation-induced segregation;
- CEF-core/MNS-shell and CEF/MNS-appendage and structures were observed at the dose of 0.06 dpa;
- For most of the clusters, shell structures and appendages, the relative Mn-Ni-Si concentrations do not correspond to thermodynamically predicted G or Γ_2 phases, suggesting the Mn-Ni-Si feature formation mechanism is governed by radiation-induced segregation.

3 Benchmark of these results with those from the literature

Comparison of the results obtained in the present research with literature is presented further. Compositions of steels F, N and O are relatively close to compositions of A508B, A533B and 16MND5 RPV base metals extensively studied in the literature. Yet, the composition of steel E is rather peculiar due to its lower Mn concentration. Mn is an important carbide former in western commercial RPV materials and usually present in a global concentration of around 1 at. % [85]. The effect of P on the solute cluster formation is not extensively studied, a bigger focus is on its effect on grain boundary (segregation) and non-hardening embrittlement, yet P-rich clusters were observed in Fe-P (~0.045 at. %) model alloy and in high-P (~0.06 at. %) VVER weld and [8,79,80]. High-Ni steel I has a composition similar to the composition of RPV weld metals and will be compared separately from base metal-like RPV materials. In modern RPV materials, Cu content is limited to ~0.05 at. %. Therefore, comparison of the results obtained on high-Cu (0.27 at. %) steel W will be performed with FeCu model alloys.

In Table 9 information about base metal-like RPV materials studied by APT either from this PhD project or literature are presented.

Table 9. *Irradiation conditions and global solute concentrations of main elements taking part in clustering are presented. *Only information about bulk solute concentrations was given.*

Author	ID	Dose [dpa]	T_{irrad} [°C]	Si [at.%]	Mn [at.%]	Ni [at.%]	P [at.%]	Cu [at.%]
Present work	E	0.07-0.14	290	0.56	0.59	0.66	0.024	0.05
Present work	F	0.06-0.13	290	0.54	1.26	0.69	0.017	0.05
Present work	N	0.08	290	0.47	1.05	0.62	0.030	0.04
Present work	O	0.06	290	0.52	0.99	0.63	0.047	0.04
P. Auger [5]	Chooz A	0.1-0.18	270	0.63	1.26	0.53	0.021	0.06
E. Meslin [49]	16MND5	0.2	300	0.48	1.07	0.60	0.008	0.05
K. Dohi* [64]	SA533B	0.05-0.18	290	0.53	1.43	0.61	0.013	0.08
P. Wells [18]	LG	0.2	300	0.49	1.09	0.59	-	0.01
P. Wells [18]	LH	0.2	300	0.45	0.97	0.72	-	0.08
N. Almirall [20]	R39	0.21	290	0.41	1.47	0.66	0.007	0.06

RPV steels were irradiated at temperatures around 290 °C in commercial and material test reactors. The only exception is Chooz A steel irradiated at a lower temperature of 270 °C. From the

database of mechanical tests performed on the low-Cu RPV materials, it was evaluated that irradiation hardening is proportional to the square root of irradiation dose. In the low-Cu steels solute clusters are the main source of hardening, and their number density is expected to be proportional to hardening. To correlate the microstructural and hardening data, results are often presented as a function of the square root of irradiation dose [69]. The evolution of solute cluster number density as a function of the square root of irradiation dose is presented in figure 23.

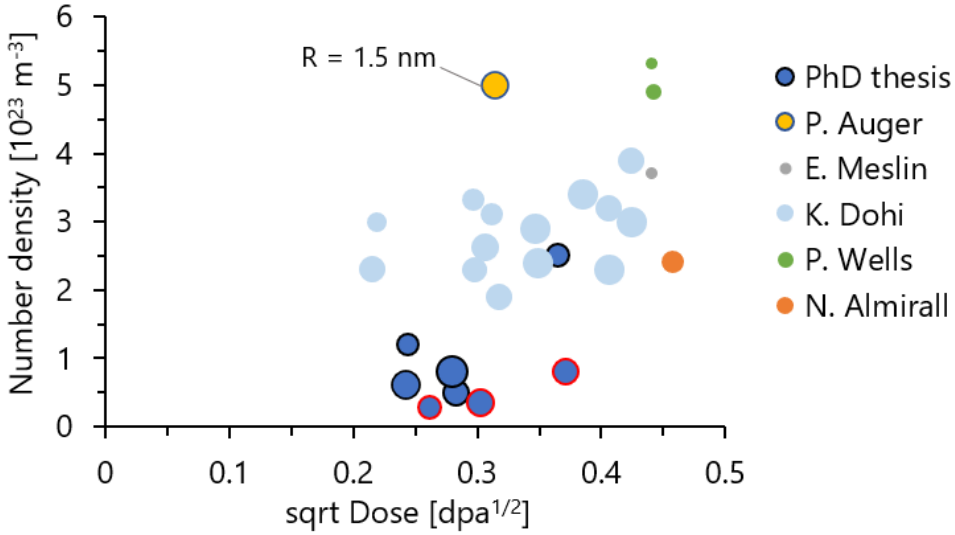

Figure 23. *Evolution of cluster number density as a function of the square root of irradiation dose for steels with close compositions. Marker size represents the average cluster radius (value for P. Auger is presented). Results on CT RPV steel E are highlighted by red border.*

On the overall, results obtained in this work are coherent with literature data. Number density of clusters in materials studied in the current project is slightly lower, and the average cluster radius is bigger than in other studies apart from the results of Dohi and co-workers. A higher number density of solute clusters in RPV steel irradiated at the lower temperature of 270 °C is also observed. The number density of clusters in steel E with low Mn (~0.6 at. %) and global solute concentration is the lowest from all cases.

Due to the non-identical cluster composition measurement procedures (erosion, excluding or including Fe) used by different laboratories, the comparison of composition measurements is complicated. Thus a comparison of the relative cluster concentrations of Si, Mn, Ni, Cu, P (excluding Fe and other solutes) normalised to 100 % is performed. Relative solute cluster concentrations are presented in Table 10.

Table 10. *Irradiation conditions and relative cluster solute concentrations of Si, Mn, Ni, Cu and P (excluding Fe and impurities) normalised to 100% is presented. Initial Fe concentration before normalisation is also presented for comparison.*

Author	ID	Dose [dpa]	T_{irrad} [°C]	Relative concentration [at. %]					Initial Fe [at.%]
				Si [at.%]	Mn [at.%]	Ni [at.%]	Cu [at.%]	P [at.%]	
Present work	E	0.07	290	27.2	15.3	45.9	1.4	10.0	79.1
Present work	E	0.09	290	25.1	19.3	37.2	0.5	17.0	77.7
Present work	E	0.14	290	31.4	15.4	41.5	0.7	9.9	72.8
Present work	F	0.06	290	14.9	31.8	35.9	0.5	16.9	80.1
Present work	F	0.08	290	20.4	31.2	38.7	0.5	9.1	80.8
Present work	F	0.13	290	24.8	30.7	37.2	0.9	6.4	77.7
Present work	N	0.08	290	16.8	31.1	32.3	1.2	18.6	83.3
Present work	O	0.06	290	10.7	34.5	26.8	1.2	26.8	82.1
P. Auger	Chooz A	0.10	270	36.6	27.5	29.0	6.9	-	86.9
E. Meslin	16MND5	0.20	300	-	100.0	-	-	-	91.6
K. Dohi	SA533B	0.05	290	17.0	29.4	39.8	13.5	-	61.8
K. Dohi	SA533B	0.05	290	23.2	21.6	33.9	10.3	-	60.4
K. Dohi	SA533B	0.09	290	24.8	24.8	39.3	11.1	-	60.6
K. Dohi	SA533B	0.10	290	25.2	25.5	38.4	11.3	-	59.7
K. Dohi	SA533B	0.10	290	23.8	25.1	39.9	11.3	-	54.7
K. Dohi	SA533B	0.09	290	28.6	21.9	39.4	10.1	-	58
K. Dohi	SA533B	0.09	290	23.8	27.9	40.6	11.4	-	60.6
K. Dohi	SA533B	0.12	290	25.6	24.6	40.6	9.2	-	61.5
K. Dohi	SA533B	0.18	290	29.7	22.6	39.1	8.6	-	57.3
K. Dohi	SA533B	0.12	290	23.9	26.9	40.1	9.1	-	60.2
K. Dohi	SA533B	0.15	290	24.7	25.3	40.4	9.9	-	60.9
K. Dohi	SA533B	0.17	290	26.7	25.4	39.0	9.2	-	58.8
K. Dohi	A533B	0.18	290	28.0	23.6	39.9	8.8	-	59.9
K. Dohi	SA533B	0.17	290	26.8	27.1	40.5	8.8	-	57.4
P. Wells	LG	0.20	300	27.2	25.5	46.9	0.4	-	53.3
P. Wells	LH	0.20	300	20.3	25.2	39.7	14.8	-	58.7
N. Almirall	R39	0.21	290	32.8	19.7	46.7	0.9	-	65.5

To simplify the discussion, in the following text, the results obtained from the literature will be presented in italic font when compared to values obtained in the present project on CT RPV materials (*literature* vs present project). Regarding composition measurements, the first big difference is the lower amount of Fe associated with solute clusters in other studies (*~60* vs ~80 at.

%). The other big difference is the absence of P inside the solute clusters in literature data. In most cases, P cluster concentration is not presented and P is attributed to "other" solutes. Also, a higher amount of Cu inside the clusters (*5 to 10* vs ~1 at. %) was observed in the results of Dohi and Wells and could be attributed to higher global Cu concentration (*0.08* vs 0.05 at. %). Relative concentrations of Mn (*~25* vs ~26 at. %), Ni (*~40* vs 37 at. %) and Si (*~26* vs ~20 at. %) observed in present PhD research are in good agreement with literature data.

Due to its high-Ni (1.5 at. %) global concentration, the composition of steel I is closer to the RPV weld metals. In the Table 11 information about weld metal-like materials studied by APT from current PhD project and literature are presented.

Table 11. *Irradiation conditions and global solute concentrations of main elements taking part in clustering is presented.*

Author	ID	Dose [dpa]	T_{irrad} [°C]	Si [at.%]	Mn [at.%]	Ni [at.%]	P [at.%]	Cu [at.%]
Present work	I	0.08-0.13	290	0.54	1.25	1.50	0.019	0.04
P.D. Styman [86]	R3U	0.10	284	0.42	1.48	1.50	0.02	0.07
K. Lindgren [63]	H, S	0.07-0.1	284-295	0.28	1.10	1.49	0.02	0.05
M.K. Miller [87]	E	0.10	284	0.42	1.48	1.50	0.016	0.07
M.K. Miller [87]	N	0.09	284	0.28	1.37	1.58	0.027	0.05
B. Jenkins [19]	G	0.17	290	0.35	1.15	1.44	0.001	0.03
P. Wells [18]	CM6	0.20	300	0.33	1.09	1.34	-	0.01
N. Almirall [20]	R22	0.21	290	0.41	1.51	1.59	0.011	0.05

Most of RPV steels have relatively the same solute concentrations, apart from Si global concentration, which is slightly higher in the case of steel I (*0.3-04* vs 0.5 at. %). RPV steels were irradiated at temperatures of around 290 °C at commercial and test reactors. Number density of solute clusters linearly grows with the square root of irradiation dose (Fig. 24).

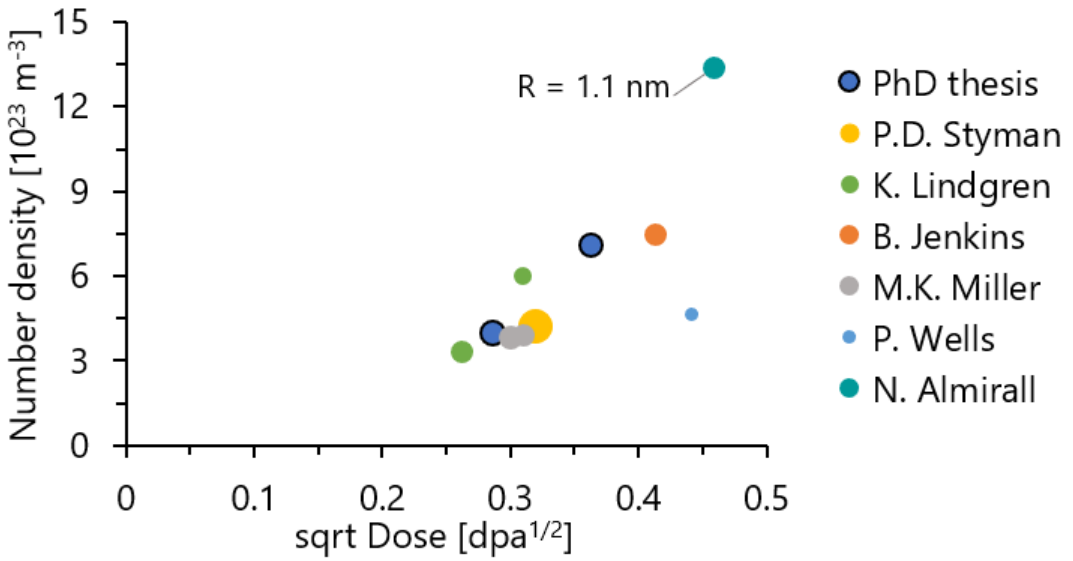

Figure 24. *Evolution of cluster number density as a function of the square root of irradiation dose for steels with close to RPV weld material compositions (high-Ni). Marker size represents the average cluster radius (value of N. Almirall is presented).*

Number density and cluster radius obtained on high-Ni steel I are in good agreement with results from the literature. Same as for the base metal-like materials, the relative solute cluster concentrations are presented in Table 12.

Table 12. *Irradiation conditions and relative cluster solute concentrations of Si, Mn, Ni, Cu and P (excluding Fe and impurities) normalised to 100% is presented. Initial Fe concentration before normalisation is also presented for comparison.*

Author	ID	Dose [dpa]	T_{irrad} [°C]	Relative concentration [at. %]					Initial Fe [at.%]
				Si [at.%]	Mn [at.%]	Ni [at.%]	Cu [at.%]	P [at.%]	
Present work	I	0.08	290	23.9	21.4	50.6	0.8	3.6	74.3
Present work	I	0.13	290	22.0	27.3	48.9	0.7	1.1	71.2
P.D. Styman	R3U	0.10	284	13.2	32.4	48.8	3.4	0.7	59.0
K. Lindgren	H	0.10	290	12.0	30.1	54.2	3.6	-	58.5
K. Lindgren	S	0.07	284	11.6	29.1	58.1	1.2	-	57.0
M.K. Miller	E	0.10	284	13.7	49.3	35.6	1.4	-	63.5
M.K. Miller	N	0.09	284	12.1	48.5	37.9	1.5	-	67.0
B. Jenkins	G	0.17	290	19.6	23.3	54.0	1.7	0.7	46.3
P. Wells	CM6	0.20	300	15.5	25.6	58.9	0.2	0.0	49.6
N. Almirall	R22	0.21	290	18.6	26.5	54.1	0.8	0.0	63.4

As in the previous comparison, a difference in Fe associated with solute clusters between current research and literature data is observed (*~60* vs 71 to 75 at. %). Once again, P relative cluster concentration is slightly higher in the present research (*0.0 to 0.7* vs 1.4 to 3.2 at. %). This could be

attributed to the fact that in other studies, P was attributed to "other" solutes. Cu relative cluster concentration is in agreement with literature in the case of steel I (*0.2 to 3.6* vs ~ 1.0 at. %). Relative cluster concentration of Ni (*~49* vs 50 at. %), Si (*12 to 20* vs 20 at. %) and Mn (*23 to 32* vs 21 to 27 at. %) correlate well with results presented in the literature, apart from results of Miller and co-workers where higher Mn content (*~50* vs ~25 at. %) was measured in materials with the higher global Mn concertation (*1.4 to 1.5* in comparison with ~1.2 at %).

Results obtained on the high-solutes (high-Cu) steel W are compared with results obtained on decommissioned RPV materials from previous NPP generations and Fe model alloys. In Table 13, information about high-Cu RPV steels and model alloys studied by APT from the current PhD project and literature are presented.

Table 13. *Irradiation conditions and global solute concentrations of main elements taking part in clustering is presented.*

Author	ID	Dose [dpa]	T_{irrad} [°C]	Si [at.%]	Mn [at.%]	Ni [at.%]	P [at.%]	Cu [at.%]
Present work	W	0.06	290	0.49	1.18	1.59	0.040	0.27
P. Wells [18]	LD	0.20	300	0.53	1.08	1.00	-	0.21
M.K. Miller [1]	Palisades	0.02	288	0.36	1.29	1.14	0.014	0.18
S. Connolly [88]	SL 092	0.03	290	1.01	1.33	0.57	-	0.25
P. Pareige [89]	VVER 440	0.15	270	0.75	0.98	0.23	0.052	0.14
P.D. Edmondson [90]	Zion	0.01	320	1.23	1.16	0.68	0.034	0.21
S. Shu [91]	H6	0.02	290	-	1.05	-	-	0.78
L. Liu [92]	FeCu0.6Ni	0.01	290	-	-	0.58	-	0.44
L. Liu [92]	FeCu0.6NiMn	0.01	290	-	1.44	0.58	-	0.45
L. Liu [92]	FeCu0.8NiMn	0.01	290	-	1.44	0.77	-	0.45

Here, higher dispersion of global solute concentrations is observed. Cu concentration varies from ~0.2 to 0.3 at. % for RPV steels and could be as high as 0.8 at. % in the case of model alloys. Two materials have a very high Si concentration (above 1 at. %), and in most of the cases global Ni concentration presented in literature is lower than in steel W (*~0.6* vs 1.5 at. %). The evolution of solute cluster number density as a function of the square root of irradiation dose is reported in figure 25.

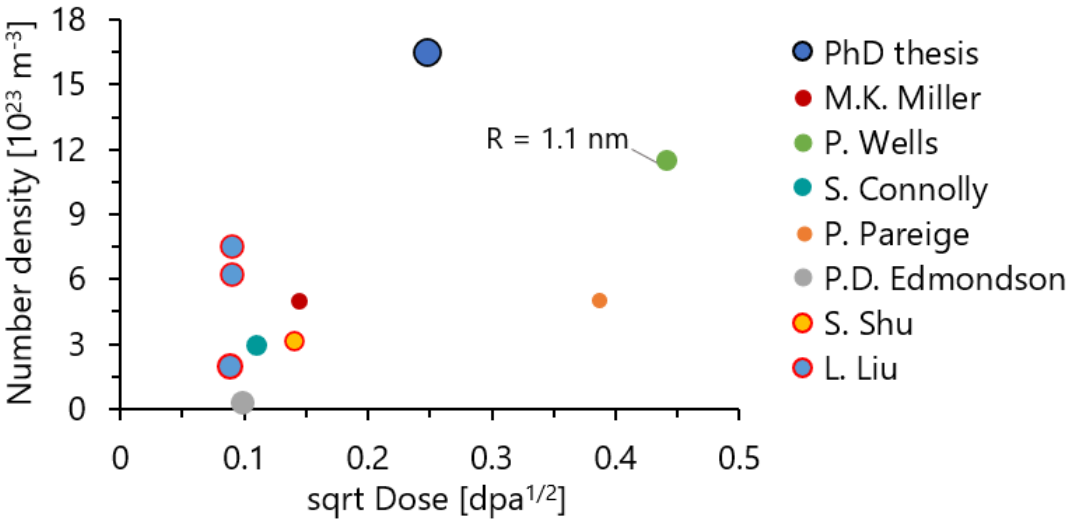

Figure 25. *Evolution of cluster number density as a function of the square root of irradiation dose for high-Cu RPV steel and model alloys is presented. Marker size represents the average cluster radius (value for P. Wells presented). Results obtained on model alloys are highlighted by red border.*

Most of the materials were irradiated up to about 0.02 dpa, a dose where a high number density of CEFs should have been formed. The effect of the global composition on the solute cluster formation in high-Cu materials can be clearly seen in the results obtained by Liu and co-workers. Indeed, the addition of 1.4 at. % Mn to Fe-0.45Cu-0.58Ni increases the number density of clusters from 1.9 to 6.2 x 10^{23} m^{-3}, and with further addition of 0.2 at. % Ni, number density further increased to 7.5 x 10^{23} m^{-3}. Number density of clusters in high-solute steel W is almost two times higher than the average values obtained in the literature and could be due to the higher global combined solute concentration of Mn, Ni, Si, P and Cu (3.6 at. %) in comparison with materials presented in the literature (~*2.5* at. %).

Comparison of cluster solute concentrations will be performed with the relative solute contents (excluding Fe, other species and normalised to 100%) Relative solute cluster concentrations are reported in Table 14.

Table 14. *Irradiation conditions and relative cluster solute concentrations of Si, Mn, Ni, Cu and P (excluding Fe and impurities) normalised to 100% is presented. Initial Fe concentration before normalisation is also presented for comparison.*

Author	ID	Dose [dpa]	T_{irrad} [°C]	Relative concentration [at. %]					Initial Fe [at.%]
				Si [at.%]	Mn [at.%]	Ni [at.%]	Cu [at.%]	P [at.%]	
Present work	W	0.06	290	13.1	24.9	42.4	18.1	1.6	66.2
P. Wells	LD	0.20	300	15.5	24.6	37.7	22.2	-	58.6
M.K. Miller	Palisades	0.02	288	0.3	0.5	0.9	98.2	0.2	11.4
S. Connolly	SL 092	0.03	290	12.0	31.3	12.5	44.4	-	48.2
P. Pareige	VVER 440	0.15	270	10.1	11.5	9.0	55.5	-	63.4
P.D. Edmondson	Zion	0.01	320	5.0	12.5	12.5	57.5	-	60.0
S. Shu	H6	0.02	290	-	12.0	-	88.0	-	50.0
L. Liu	FeCu0.6Ni	0.01	290	-	-	14.3	91.4	-	47.5
L. Liu	FeCu0.6NiMn	0.01	290	-	20.3	22.8	57.0	-	52.6
L. Liu	FeCu0.8NiMn	0.01	290	-	23.3	26.7	50.0	-	52.0

A high amount of Fe associated with clusters is found both in the present research and in literature (*~50 to 60* vs 66 at. %). The only exception is the results obtained by Miller and co-workers where only 11 at. % of Fe inside clusters was found. Also, in the same study clusters are significantly enriched only in Cu (98.2 at. %), which varies from all other results obtained in high-Cu RPV materials. Results of the present research correlate well with data obtained by Wells and co-workers. Close results on the relative Si cluster concentration are obtained (*~5-15* vs 13 at. %). Lower Cu (*~50* vs 18 at. %) and higher Ni (*~10* vs 42 at. %) enrichments in comparison with the results of Connolly, Pareige and Edmondson are owing to the higher Ni global solute content (1.6 vs *~0.6* at. %). In the ternary and quaternary model alloys, more significant Cu enrichment is observed than in the case of present research (*~50 to 90* vs 17 at. %).

A high dispersion between observed cluster compositions in the high-Cu materials could be attributed to the more complex mechanism of clusters/precipitate formation. In the case of low-Cu RPV materials, cluster formation is governed by RIS, and cluster composition is directly related to the global concentrations of Mn, Ni, Si, Cu and P. In the case of high-Cu materials, a competition between radiation enhanced CEFs formation and radiation-induced Mn, Ni, Si, P, Cu segregation with the unknown magnitude could bring ambiguity to results.

To confirm the RIS nature of clusters observed in the present project, the evolution of relative cluster Mn, Ni, Si, Cu, P contents (excluding all chemical species except Si, Mn, Ni, P and Cu and normalised to 1) as a function of their relative nominal contents (—//—) is presented in figure 26.

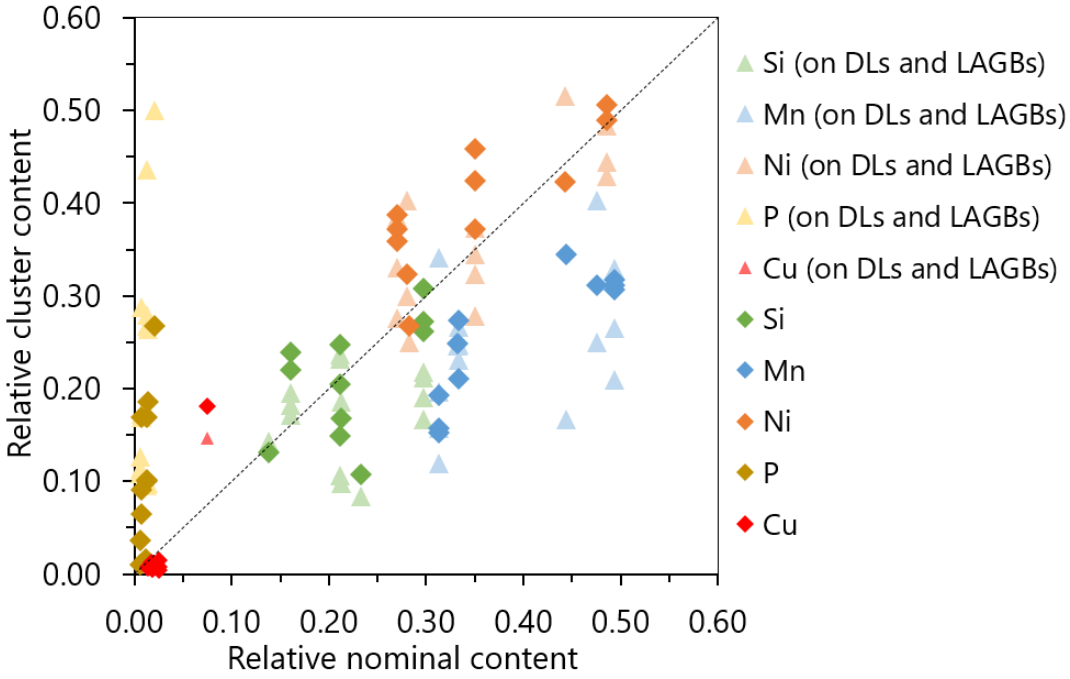

Figure 26. *Evolution of relative cluster solute content as a function of relative nominal solute content (both values given excluding Fe, impurities and normalised to 1). Pale triangles represent clusters observed on dislocation lines and low-angle GBs. Diamonds represent cluster formed in ferrite matrix. 1:1 trend line is also plotted.*

In the present PhD project, relative cluster compositions are in good agreement with the nominal compositions of solutes. Most of the cases are dispersed around a 1:1 trend line and therefore correspond to cluster formation by RIS. But why not directly on the 1:1 line? First of all, the 1:1 line represents the unbiased solute with PD flux coupling, where random distribution of solutes in ferritic matrix is the only important variable. From the atomistic modelling, we know it is not the case, and different solutes have weaker and stronger PD interaction magnitude [27]. Further, the case of every solute is described:

- P is strongly above 1:1 due to its high mobility by SIA mechanism, which results in significant cluster enrichment with a “cluster over nominal” (CoN) ratio of 10.3. Also, even higher enrichment is observed on dislocation lines (CoN of 24) known to be the sinks for SIA annihilation;
- Due to its low nominal content (~0.05 at. %) most of the clusters have a low Cu enrichment (CoN 0.5), apart from the high Cu (0.27 at. %) steel W (CoN of 2.4). In that

case, Cu is supersaturated, and its diffusion magnitude is amplified by thermodynamic driving force in addition to PD flux coupling, which results in above 1:1 line enrichment;

- Si is the closest to 1:1 solute for volume (CoN of 1.0) and also for formed on dislocations lines (CoN of 0.8) clusters, owing to its ability to diffuse by both V and Si mechanisms. In addition, Si content was always the same (~0.5 at. %), without atypically low or high concentrations, which could have resulted in unexpected enrichment tendencies;
- Ni has a higher than 1 CoN ratio of 1.2 for in volume and 1.0 for formed dislocation lines clusters. A significant effect of Ni on solute cluster number density was observed in the present PhD and literature [19,20,70,87]. From the obtained result, it is concluded that Ni is the dominant alloying element (from Mn, Si, Mo, Al), resulting in solute cluster formation in the western RPV steels.;
- Mn has a lower CoN ratio of 0.7 for in volume and 0.6 for formed on dislocation lines clusters. In the present PhD, it was observed that the separate effect of Mn on solute cluster number density is by order of 4 times lower than of Ni. It is also confirmed by lower enrichment in clusters (~6 at. % vs ~10 at. %). In general, Mn can diffuse by SIA mixed dumbbell and by V-drag, but it seems that its migration magnitude is lower than of P for SIA diffusion and of Ni in the case of V-drag.

Results of present research both on number density and cluster composition measurements are in agreement with solute cluster formation by RIS. But what is observed in literature? Cluster compositions observed in literature are presented in a form of evolution of relative cluster content as a function of relative nominal content excluding Fe and other solutes and normalised to 1 on figure 27 [5,18-20,63,64,68,70,86,87,93,94].

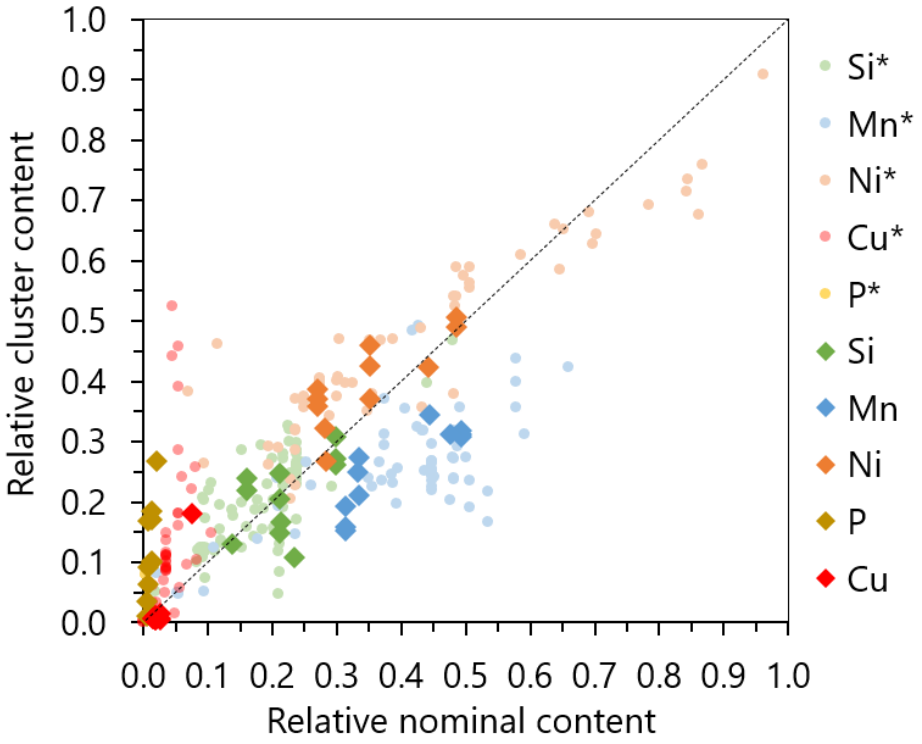

Figure 27. *Evolution of relative cluster solute content as a function of relative nominal solute content (both values given excluding Fe, impurities and normalised to 1). Pale circles are results from the literature. Diamonds are the results of the present PhD research. 1 : 1 trend line is also plotted.*

CoN values available in literature correlate well with the results obtained in the current PhD research for Si (*1.2* vs 1), Ni (*1.3* vs 1.2), Mn (*0.7* vs 0.7) and P (*14.2* vs 10.3), yet it should be noted that information for P was given only in 3 cases. The slightly higher effect of Si in literature could be attributed to repulsive P-Si interaction, and since in present PhD high P cluster content was measured, the lower Si content hence could be expected [41]. The other difference is higher Cu CoN ration from literature data (*2.4* vs 0.5). The reason is that a wide range of Cu nominal compositions is presented in the literature, and in the present research 10 out of 11 studied conditions are in low-Cu (~0.05 at. %) steels.

Using Thermo-Calc with TCFE8: Steels/Fe-Alloys v 8.1 database, the equilibrium state of the system at 290 °C was evaluated. Results had not predicted the formation of G and Γ_2 phases for a wide range of compositions studied in the present research. Hence, Mn-Ni-Si radiation enhanced precipitation is not expected. Taking into account the following observations:

- High amount of Fe inside clusters (66 to 83 at. %);
- High dispersion of solute cluster relative concentrations (Fig. 10,11,22);
- High P cluster concentration (up to 5 at. %);
- G or Γ_2 phases are not predicted at 290 °C by Thermo-calc.

We could argue that the mechanism of Mn-Ni-Si cluster formation is still in favour of a radiation-induced segregation process.

Conclusions on the benchmark with literature:

- Good correlation between this PhD research and data from literature on Mn, Ni and Si cluster concentrations is observed;
- Number density of clusters in the present PhD research is slightly lower than those presented in literature;
- Average cluster size observed in the PhD research is bigger than in literature data;
- The radiation-induced segregation process for cluster formation cannot be ruled out. Flux coupling between point defects and solutes can explain most of the observed results.

Summary

The goal of the present chapter was to evaluate the effect of bulk composition on the microstructure evolution under irradiation. If possible additional information about the nature of these nanosized features should have been identified. The effect of Mn, Ni, their synergy, P, and synergy between Cu, Mn, Ni and P were studied. In addition, study on the dose effect was performed. The summary of the results is given further.

The main conclusions are the following:

- In low-alloyed steel (~1.3 at. % in comparison with 2.2 at. %) for commercial materials), no solute clusters at the irradiation dose of 0.09 dpa were observed. The calculations predict that if solute clusters were formed, their number density is below 4 x 10^{21} m^{-3} (with an estimated radius of 2.7 nm), or below the resolution of APT (below 0.7 nm in radius). Slight shift in 1NN distribution of Si atoms was evaluated after irradiation (first steps of solute clustering).
- With an increase of irradiation dose from 0.06 to 0.14 dpa number density of solute clusters progressively increases. Average cluster size grows with the increase of irradiation dose until saturating around 0.1 dpa, and in the high dose condition average cluster size decreases. With an increase of irradiation dose clusters become more enriched in alloying elements (medium to high nominal concentrations ~0.5-1.5 at. %) such as Mn, Ni and Si, and depleted in P (impurity with low nominal concentration ~0.02 at. %);
- The addition of Mn promotes formation of solute clusters under neutron irradiation. With the increase of the nominal Mn content by the factor of ~2, number density of solute clusters multiplies 2-3 times;
- Ni has a strong enhancing effect on solute cluster formation. With the increase of Ni nominal content by a factor of 2, the number density of solute clusters increases by a factor of 4-5. In addition, high Ni cluster concentration (~9 at. %) was observed in most of materials (for comparison Mn ~6 at. %, Si ~5 at. %). Additional confirmation of the important role of Ni was observed with erosion profile, where high Ni core concentration was detected (~12 at. %);
- A synergetic effect between Mn and Ni on solute cluster formation was observed. With simultaneous addition of these solutes, number density increase is larger than in the case where Mn and Ni were added separately. In general, with higher Ni nominal content, higher cluster Mn, Ni and Si enrichment was observed;

- P has an important role in solute cluster properties in medium-Ni materials. No matter low (~0.02 at. %) or medium (~0.03 at. %) P nominal concentration, high P core concentration (~5 at. %), and high P matrix depletion (~50 % of P atoms) were observed. P effect became even more notable in high (~0.05 at. %) P material. Due to the high mobility of P-SIA dumbbell, P is expected to be the first solute to pin the PDCs and segregate, which is observed by high P core concentration on erosion profile (~10 at.%);
- High Cu nominal content, as expected, results in formation of high number density of CEFs due to PD oversaturation under irradiation. Also, a synergy of Cu with other solutes was observed by the high matrix depletion in Mn, Ni and Si in high-Cu steel;
- For all low-Cu materials cluster solute concentrations vary with the nominal solute concentrations. The observed enrichment tendencies are in agreement with the flux coupling between PD and solutes, resulting in solute segregation on PD sinks and solute cluster formation;
- In high-Cu material, CEFs formation was accelerated by irradiation. Most of compositions of Mn-Ni-Si-shell and Mn-Ni-Si-appendage structures, formed on the CEFs interfaces do not correspond to the predicted G and Γ_2 phases, and hence more probably formed by RIS;

On the point of view of microstructural characterisation, the results obtained are in good agreement with those described in the literature with comparable initial parameters (chemistry and irradiation conditions).

In the next chapter, obtained microstructural data will be compared with the results of tensile tests to evaluate the effect of bulk chemical composition on the irradiation hardening in CT RPV steels. These observations could be used to improve the long-term prediction of irradiation effects and prolong the lifetime of the current fleet of nuclear power plants.

References

1. M.K. Miller, M.A. Sokolov, R.K. Nanstad, K.F. Russell. Journal of Nuclear Materials 351 (2006): 187–96. https://doi.org/10.1016/j.jnucmat.2006.02.013

2. M.K. Miller, K.F. Russell. Journal of Nuclear Materials 371 (2007): 145–60. https://doi.org/10.1016/j.jnucmat.2007.05.003

3. P.D. Edmondson, M.K. Miller, K.A. Powers, R.K. Nanstad. Journal of Nuclear Materials 470 (2016): 147–54. https://doi.org/10.1016/j.jnucmat.2015.12.038

4. A. Wagner, A. Ulbricht, F. Bergner, E. Altstadt. Nuclear Instruments and Methods in Physics Research Section B: Beam Interactions with Materials and Atoms 280 (2012): 98–102. https://doi.org/10.1016/j.nimb.2012.03.008

5. P. Auger, P. Pareige, S. Welzel, J-C. Van Duysen. Journal of Nuclear Materials 280 (2000): 331–44. https://doi.org/10.1016/S0022-3115(00)00056-8

6. G.R. Odette, G.E. Lucas. JOM 53 (2001): 18–22. https://doi.org/10.1007/s11837-001-0081-0

7. G.R. Odette, Radiation Effects and Defects in Solids 144 (1998): 189–231. https://doi.org/10.1080/10420159808229676

8. E.D. Eason, G.R. Odette, R.K. Nanstad, T. Yamamoto (Eds). A Physically Based Correlation of Irradiation-Induced Transition Temperature Shifts for RPV Steels. Report ORNL/TM-2006/530 (2007): 250. https://info.ornl.gov/sites/publications/files/Pub2592.pdf

9. P. Auger, P. Pareige, M. Akamatsu, D. Blavette. Journal of Nuclear Materials 225 (1995): 225–30. https://doi.org/10.1016/0022-3115(94)00522-2

10. B. Radiguet, P. Pareige, A. Barbu. Nuclear Instruments and Methods in Physics Research Section B: Beam Interactions with Materials and Atoms 267 (2009): 1496–99. https://doi.org/10.1016/j.nimb.2009.01.146

11. B. Radiguet, A. Barbu, P. Pareige. Journal of Nuclear Materials 360 (2007): 104–17. https://doi.org/10.1016/j.jnucmat.2006.09.007

12. P. Pareige, B. Radiguet, A. Barbu. Journal of Nuclear Materials 352 (2006): 75–79. https://doi.org/10.1016/j.jnucmat.2006.02.073

13. H. Ke, P. Wells, P. D. Edmondson, N. Almirall, L. Barnard, G.R. Odette, D. Morgan. Acta Materialia 138 (2017): 10–26. https://doi.org/10.1016/j.actamat.2017.07.021

14. J. Ke, H. Ke, G.R. Odette, D. Morgan. Journal of Nuclear Materials 498 (2018): 83–88. https://doi.org/10.1016/j.jnucmat.2017.10.008

15. G.R. Odette, MRS Proceedings 373 (1994): 137. https://doi.org/10.1557/PROC-373-137

16. G.R. Odette , T. Yamamoto, T.J. Williams, R.K. Nanstad, C.A. English. Journal of Nuclear Materials 526 (2019): 151863. https://doi.org/10.1016/j.jnucmat.2019.151863

17. W. Xiong, H. Ke, R. Krishnamurthy, P. Wells, L. Barnard, G.R. Odette, D. Morgan. MRS Communications 4 (2014): 101–5. https://doi.org/10.1557/mrc.2014.21

18. P. Wells, T. Yamamoto, B. Miller, T. Milot, J. Cole, Y. Wu, G.R. Odette. Acta Materialia 80 (2014): 205–19. https://doi.org/10.1016/j.actamat.2014.07.040

19. B. Jenkins, J. Douglas, N. Almirall, N. Riddle, P. Bagot, J.M. Hyde, G.R. Odette, M. Moody. Materialia 11 (2020): 100717. https://doi.org/10.1016/j.mtla.2020.100717

20. N. Almirall, P. Wells, T. Yamamoto, K. Wilford, T. Williams, N. Riddle, G.R. Odette. Acta Materialia 179 (2019): 119–28. https://doi.org/10.1016/j.actamat.2019.08.027

21. P.D. Edmondson, C.M. Parish, R.K. Nanstad. Acta Materialia 134 (2017): 31–39. https://doi.org/10.1016/j.actamat.2017.05.043

22. C. Hatzoglou, B. Radiguet, G. Da Costa, P. Pareige, M. Roussel, M. Hernandez-Mayoral, C. Pareige. Journal of Nuclear Materials 522 (2019): 64–73. https://doi.org/10.1016/j.jnucmat.2019.05.022

23. L. Messina, M. Nastar, T. Garnier, C. Domain, Pär Olsson. Physical Review B 90, (2014): 104203. https://doi.org/10.1103/PhysRevB.90.104203

24. L. Messina, Z. Chang, P. Olsson. Nuclear Instruments and Methods in Physics Research Section B: Beam Interactions with Materials and Atoms 303 (2013): 28–32. https://doi.org/10.1016/j.nimb.2013.01.049

25. L. Messina, P. Olsson, M. Nastar, W. Gudowski. Proceedings of ICAPP 2015, Paper 15572. https://www.researchgate.net/publication/301232158

26. L. Messina. PhD thesis. KTH Royal Institute of Technology (2015)

27. L. Messina, T. Schuler, M. Nastar, M. Marinica, P. Olsson. Acta Materialia 191 (2020): 166–85. https://doi.org/10.1016/j.actamat.2020.03.038

28. N. Castin, G. Bonny, A. Bakaev, F. Bergner, C. Domain, J.M. Hyde, L. Messina, B. Radiguet, L. Malerba. Materials Today Energy 17 (2020): 100472. https://doi.org/10.1016/j.mtener.2020.100472

29. N. Castin, G. Bonny, A. Bakaev, F. Bergner, C. Domain, J.M. Hyde, L. Messina, B. Radiguet, L. Malerba. SSRN Electronic Journal (2019). https://doi.org/10.2139/ssrn.3427540

30. N. Castin, L. Messina, C. Domain, R. Pasianot, P. Olsson. Physical review B 96 (2017): 214117. https://doi.org/10.1103/PhysRevB.95.214117

31. E. Vincent, C.S. Becquart, C. Domain. Nuclear Instruments and Methods in Physics Research B 255 (2007) 78–84. https://doi.org/10.1016/j.nimb.2006.11.033

32. P. Olsson, T. Klaver, C. Domain. Physical Review B 82 (2010): 044102 https://doi.org /10.1103/PhysRevB.81.054102

33. D. Terentyev, A. Zinovev, G. Bonny. Journal of Nuclear Materials 475 (2016): 132-139. http://dx.doi.org/10.1016/j.jnucmat.2016.04.005

34. L. Huang, M. Nastar, T. Schuler, L. Messina. Physical Review Materials 5 (2021): 033605. https://doi.org/10.1103/PhysRevMaterials.5.033605

35. H. Abe, E. Kuramoto. Journal of Nuclear Materials 271&272 (1999): 209-213. https://doi.org/10.1016/S0022-3115(98)00741-7

36. F. Maury, A. Lucasson, P. Lucasson, P. Moser, Y. Loreaux. Journal of Physics. F: Metal Physics 15 (1985): 1465. https://doi.org/10.1088/0305-4608/15/7/007

37. L. Tan, R.E. Stoller, K.G. Field, Y. Yang, H. Nam, D. Morgan, B.D. Wirth, M.N. Gussev, J.T. Busby. The Journal of The Minerals, Metals & Materials Society 65 (2016). https://doi.org/10.1007/s11837-015-1753-5

38. H. Watanabe, S. Masaki, S. Masubuchi, N. Yoshida, K. Dohi. Journal of Nuclear Materials 439 (2013) 268–275. http://dx.doi.org/10.1016/j.jnucmat.2012.08.029

39. C. Pareige, V. Kuksenko, P. Pareige. Journal of Nuclear Materials 456 (2015): 471–476. http://dx.doi.org/10.1016/j.jnucmat.2014.10.024

40. B. Gomez-Ferrer, C. Heintze, C. Pareige. Journal of Nuclear Materials 517 (2019): 35-44. https://doi.org/10.1016/j.jnucmat.2019.01.040

41. C. Domain, C.S. Becquart. Journal of Nucler Materials 499 (2018): 582–594. https://doi.org/10.1016/j.jnucmat.2017.10.070

42. T. Whiting, P. Burr, D. King, M. Wenman. Journal of Applied Physics 126 (2019): 115901. https://doi.org/10.1063/1.5109483

43. E. Vincent, C.S. Becquart, C. Domain. Journal of Nuclear materials 359 (2006): 227-273. https://doi.org/10.1016/j.jnucmat.2006.08.022

44. E. Vincent, C.S. Becquart, C. Domain. Journal of Nuclear Materials 382 (2008): 154–159. https://doi.org/10.1016/j.jnucmat.2008.08.019

45. M.I. Pascuet, N. Castin, C.S. Becquart, L. Malerba. Journal of Nuclear Materials 412 (2011): 106–115. https://doi.org/10.1016/j.jnucmat.2011.02.038

46. N. Castin, M.I. Pascuet, L. Malerba. Journal of Nuclear Materials 429 (2012): 315–324. http://dx.doi.org/10.1016/j.jnucmat.2012.06.020

47. A.T. Al-Motasem, M. Posselt, F. Bergner, U. Birkenheuer. Journal of Nuclear Materials 414 (2011): 161–168. https://doi.org/10.1016/j.jnucmat.2011.02.051

48. Y. Nagai, Z. Tang, M. Hassegawe, T. Kanai, M. Saneyasu. Physical Review B (63): 134110. https://doi.org/10.1103/PhysRevB.63.134110

49. E. Meslin, B. Radiguet, P. Pareige, A. Barbu. Journal of Nuclear Materials 399 (2010): 137–145. https://doi.org/10.1016/j.jnucmat.2009.11.012

50. M.J. Konstantinovic, I. Uytdenhouwen, G. Bonny, N. Castin, L. Malerba, P. Efsing. Acta Materialia 179 (2019): 183-189. https://doi.org/10.1016/j.actamat.2019.08.028

51. M.J. Konstantinovic, A. Ulbricht, T. Brodziansky, N. Castin, L. Malerba. Journal of Nuclear Materials 540 (2020): 152341. https://doi.org/10.1016/j.jnucmat.2020.152341

52. S. Glade, B. Wirth, G.R. Odette, P. Asoka-Kumar. Journal of Nuclear Materials 351 (2006): 197–208. https://doi.org/10.1016/j.jnucmat.2006.02.012

53. O. Gorbatov, N. Gornostyrev, P. Korzhavyia, A. Rubana. Scripta Materialia 102 (2015): 11–14. http://dx.doi.org/10.1016/j.scriptamat.2015.01.016

54. A.T. Al-Motasem, M. Posselt, F. Bergner. Journal of Nuclear Materials 418 (2011): 215–222. https://doi.org/10.1016/j.jnucmat.2011.07.002

55. R. Ngayam-Happy, C.S. Becquart, C. Domain. Journal of Nuclear Materials 440 (2013): 143–152. http://dx.doi.org/10.1016/j.jnucmat.2013.04.081

56. A. Cerezo, S. Hirosawa, I. Rozdilsky, G.D.W. Smith. Philosophical Transitions of the Royal Society A 361 (2003): 463-477. https://doi.org/10.1098/rsta.2002.1139

57. E. Meslin, B. Radiguet, M. Loyer-Prost. Acta Materialia 61 (2013): 6246–6254. http://dx.doi.org/10.1016/j.actamat.2013.07.008

58. C. Fu, J. Torre, F. Willaime, J. Bocquet, A. Barbu. Nature Materials 4 (2005). https://doi.org/10.1038/nmat1286

59. L. Messina, M. Chiapetto, P. Olsson, C. Becquart, L. Malerba. Physica Status Solidi A 213, (2016): 2974–80. https://doi.org/10.1002/pssa.201600038

60. A. Gokhman. F. Bergner. Radiation Effects and Defects in Solids: Incorporating Plasma Science and Plasma Technology, 165 (2010): 216-226, https://doi.org/10.1080/10420151003631928

61. R. Ngayam-Happy, C.S. Becquart, C. Domain, L. Malerba. Journal of Nuclear Materials 426 (2012): 198–207. http://dx.doi.org/10.1016/j.jnucmat.2012.03.033

62. E. Meslin et al. Journal of Nuclear Materials 406 (2010): 73–83. https://doi.org/10.1016/j.jnucmat.2009.12.021

63. K. Lindgren, M. Boåsen, K. Stiller, P. Efsing, M. Thuvander. Journal of Nuclear Materials 488 (2017): 222–30. https://doi.org/10.1016/j.jnucmat.2017.03.019

64. K. Dohi. ASME Pressure Vessels and Piping Conference (2010): 95–102. https://doi.org/10.1115/PVP2010-25514

65. F. Bergner, M. Lambrecht, A. Ulbricht, A. Almazouzi. Journal of Nuclear Materials 399 (2010): 129–136. https://doi.org/10.1016/j.jnucmat.2009.11.011

66. P. Pareige, J.C. Van Duysen, P. Auger. Applied Surface Science 67 (1993): 342-347. https://doi.org/10.1016/0169-4332(93)90336-A

67. E. Meslin, B. Radiguet, P. Pareige, C. Toffolon, A. Barbu. Experimental Mechanics 51 (2011): 1453–1458. https://doi.org/10.1007/s11340-011-9476-1

68. K. Fukuya, K. Ohno, H. Nakata, S. Dumbill, J.M. Hyde. Journal of Nuclear Materials 312 (2003): 163–73. https://doi.org/10.1016/S0022-3115(02)01675-6

69. C.A. English, J.M. Hyde. 'Radiation Damage of Reactor Pressure Vessel Steels' In Comprehensive Nuclear Materials. Elsevier (2012): 151–80. https://doi.org/10.1016/B978-0-08-056033-5.00087-2.

70. N. Almirall, P. Wells, T. Yamamoto, K. Yabuuchi, A. Kimura, and G.R. Odette. Journal of Nuclear Materials 536 (2020): 152173. https://doi.org/10.1016/j.jnucmat.2020.152173

71. N. Soneda, S. Ishino, A. Takahashi, K. Dohi. Journal of Nuclear Materials 323 (2003): 169-180. https://doi.org/10.1016/j.jnucmat.2003.08.021

72. M. Hernandez-Mayoral, D. Gomez-Briceno. Journal of Nuclear Materials 399 (2010): 146-153. https://doi:10.1016/j.jnucmat.2009.11.013

73. F. Bergner, F. Gillemot, M. Hernández-Mayoral, M. Serrano, G. Török, A. Ulbricht, E. Altstadt. Journal of Nuclear Materials 461 (2015): 37–44. https://doi.org/10.1016/j.jnucmat.2015.02.031

74. D. T Hoelzer, F. Ebrahimi. MRS Online Proceedings Library 373 (1994): 57–62. https://doi.org/10.1557/PROC-373-57

75. L.L. Horton, J.Bentley, K.Farrell. Journal of Nuclear Materials 108-109 (1982): 222-223. https://doi.org/10.1016/0022-3115(82)90490-1

76. W Van Renterghem, E. Stergar, R. Chaouadi. Effect of Nickel–Manganese Concentration on the Microstructure of Chemically-Tailored RPV Steels, SCK CEN restricted report 26724015, R-6490

77. A. Etienne, B. Radiguet, N.J. Cunningham, G.R. Odette, P. Pareige. Journal of Nuclear Materials 406 (2010): 244–250. http://dx.doi.org/10.1016/j.jnucmat.2010.08.043

78. L. Tan, R.E. Stoller, K.G. Field, Y. Yang, H. Nam, D. Morgan, B.D. Wirth, M.N. Gussev, J.T. Busby. JOM 68 (2016). https://www.osti.gov/pages/servlets/purl/1236587

79. M.K. Miller, R. Jayaram, K.F. Russell. Journal of Nuclear Materials 225 (1995): 215-224. https://doi.org/10.1016/0022-3115(94)00667-9

80. M.K. Miller, K.F. Russell. Applied Surface Science 94/95 (1996): 378-383. https://doi.org/10.1016/0169-4332(95)00400-9

81. S. Shu, P. Wells, N. Almirall, G. R. Odette, D. Morgan. Acta Materialia 157 (2018): 298-306. https://doi.org/10.1016/j.actamat.2018.07.037

82. E. Vincent, C.S. Becquart, C. Domain. Nuclear Instruments and Methods in Physics Research Section B 228 (2005): 137-141. https://doi.org/10.1016/j.nimb.2004.10.035

83. J. Marian, B.D. Wirth, G.R. Odette, J.M. Perlado. Computational Materials Science 31 (2004): 347–367. https://doi.org/10.1016/j.commatsci.2004.03.023

84. A. Barashev, A. Arokiam. Philosophical Magazine Letters 85 (2006): 321-332. https://doi.org/10.1080/09500830600788927

85. N. Soneda (Ed.). Irradiation Embrittlement of Reactor Pressure Vessels (RPVs) in Nuclear Power Plants. Elsevier (2015). https://doi.org/10.1016/C2013-0-17428-4

86. P.D. Styman, J.M. Hyde, D. Parfitt, K. Wilford, M.G. Burke, C.A. English, P. Efsing. Journal of Nuclear Materials 459 (2015): 127–134. http://dx.doi.org/10.1016/j.jnucmat.2015.01.027

87. M.K. Miller, K.A. Powers, R.K. Nanstad, P. Efsing. Journal of Nuclear Materials 437 (2013): 107–115. http://dx.doi.org/10.1016/j.jnucmat.2013.01.312

88. S. Connolly, J.M. Hyde, P. Pareige, P.D. Styman, K. Wilford. Transactions, SMiRT-23 (2015). https://www.researchgate.net/publication/304247587

89. P. Pareige, B. Radiguet, A. Suvorov, M. Kozodaev, E. Krasikov, O. Zabusov, J. P. Massoud. Surface and Interface Analysis 36 (2004): 581–584. https://doi.org/10.1002/sia.1705

90. P.D. Edmondson, C.P. Massey, M.A. Sokolov, T.M. Rosseel. Journal of Nuclear Materials 545 (2021): 152740. https://doi.org/10.1016/j.jnucmat.2020.152740

91. S. Shu, B. Wirth, P. Wells, D. Morgan, G.R. Odette. Acta Materialia 146 (2018): 237–52. https://doi.org/10.1016/j.actamat.2017.12.006.

92. L. Liu, K. Nishida, K. Dohi, A. Nomoto, N. Soneda, K. Murakami, Z. Li, D. Chen, N. Sekimura. Journal of Nuclear Science and Technology 53 (2016): 1546–53. https://doi.org/10.1080/00223131.2015.1136902

93. T. Takeuchi, A. Kuramoto, J. Kameda, T. Toyama, Y. Nagai, M. Hasegawa, T. Ohkubo, T. Yoshiie, Y. Nishiyama, and K. Onizawa. Journal of Nuclear Materials 402 (2010): 93–101. https://doi.org/10.1016/j.jnucmat.2010.04.008

94. H. Huang, B. Radiguet, P. Todeschini, G. Chas, P. Pareige. MRS Proceedings 1264 (2010): 1264-BB05-18. https://doi.org/10.1557/PROC-1264-BB05-1

Chapter V: Correlation with irradiation hardening and embrittlement

Information about irradiation promoted evolution of microstructure, such as the formation of solute clusters, was delivered in chapters III and IV. These solute clusters are likely the main source of irradiation hardening and consequently embrittlement, that limit the lifetime of NPPs. To confirm this statement, a correlation between solute cluster properties and irradiation hardening should be demonstrated. Understanding of the source of mechanical properties degradation under neutron irradiation is a key to ensure safe operation conditions and to extend the lifetime of the PWR fleet.

In this chapter, the cluster characteristics measured by APT (mainly number density and cluster size) will be related to the tensile test data collected at SCK CEN on the chemically-tailored RPV steels irradiated to different dose levels. In order to make these comparisons, several hardening models linking the cluster properties with the yield stress will be utilised. The obstacle strength of the solute clusters will also be estimated.

1 Comparison of microstructure and mechanical properties evolution under irradiation

Two main irradiation hardening tendencies were distinguished from experiments on surveillance samples of commercial RPV steels [1-7]. For low-Cu (< 0.1 at. %) RPV steels a linear hardening as a function of square root of irradiation dose was observed. For high-Cu (>0.1 at. %) RPV steels, a different tendency was reported. At low irradiation dose, a high number density of CEFs had formed. Their number density saturates with depletion of Cu from the matrix at the irradiation dose below about 0.03 dpa [8,9]. Further, a linear-like dependence between irradiation hardening and square root of dose, same as in low-Cu materials, was observed. Irradiation hardening of commercial low-Cu RPV steels is expected to be lower than in the case of their high-Cu counterparts [6]. The irradiation hardening as a function of sqrt of irradiation dose for low-Cu (base) and high-Cu (weld) RPV materials is presented in figure 1.a.

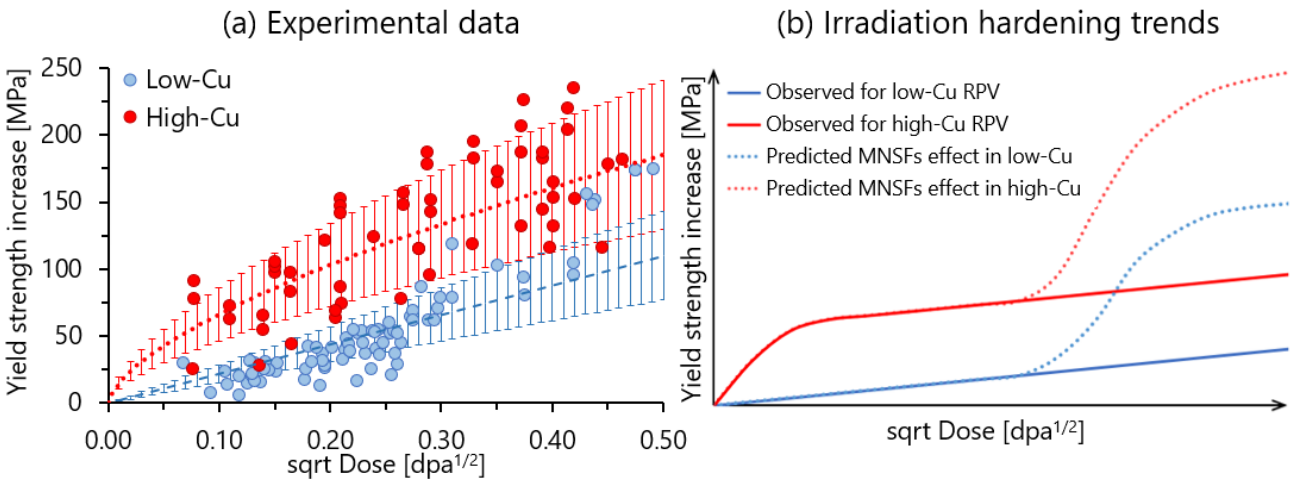

Figure 1. *(a) Yield strength increase as a function of square root of irradiation dose for RPV base (low-Cu) and weld (high-Cu) materials. Results are reproduced from the data available in the references 1-3. A 30% uncertainty margin is also added. (b) Irradiation hardening tendencies in RPV steels. Red line represents hardening tendency for high-Cu steels. Blue line represents hardening tendency for low-Cu materials. Dashed lines are the predicted by modelling irradiation hardening in due to formation of MNSFs [10].*

A theory of severe irradiation hardening in RPV steels at high irradiation doses (around 0.2 dpa) due to the formation of a large volume fraction of MNSFs (also defined MNSPs) was proposed by Odette and co-workers [10] (Fig. 1.b). Experimental research on model RPV materials with a wide range of Cu (~0.00-0.25 at. %), Mn (0.1-1.5 at. %), Ni (0.2-3.5 at. %) and Si (0.1-1.3 at. %) concentrations were performed. These model steels were irradiated in the high-flux MTRs. The results showcased the existence of severe irradiation hardening (up to 400 MPa) at the higher doses around 0.2 dpa for enriched in solutes materials (Mn+Ni+Si ~4 at. %) [10-14]. Detailed information is available in appendix A.2. In these studies, information about high dose (~0.2 dpa) and very high dose (~1.8 dpa) conditions were collected. Yet, due to a limited data on irradiation hardening of these materials at the low (below 0.05 dpa) and moderate (around 0.1 dpa) doses, the exact irradiation hardening trends are hard to evaluate. Results of irradiation hardening on a set of materials from the IVAR database exhibit the linear-like hardening tendency as a function of square root of irradiation dose [15]. Also, close to linear hardening tendency (as function of sqrt of accumulated dose) is observed on surveillance samples of WWER-440 steel [16].

The yield strength increase/irradiation hardening ($\Delta\sigma_y$) measured with tensile tests at SCK CEN as a function of square root of irradiation dose for CT RPV steels is presented in figure 2.

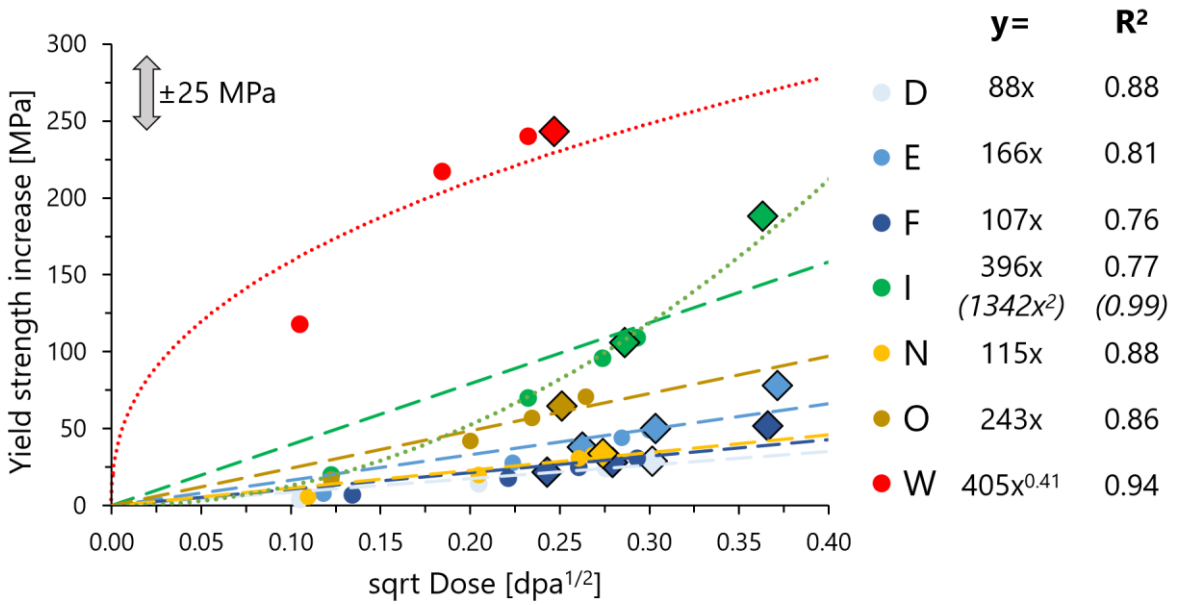

Figure 2. *Yield strength increase as a function of the square root of irradiation dose for seven chemically-tailored RPV steels. Circle symbols represent the values of the tensile tests. From these values trend lines were plotted. Large diamond symbols represent the specimens studied in the current PhD project. Equations and coefficients of determination for trend lines are indicated. Default uncertainty margin of 25 MPa is also shown [17].*

Low-Cu (~0.05 at. %), medium-Ni (~0.7 at. %) and low-P (~0.02 at. %) steels D, E and F, with different Mn bulk concentrations (0.04 to 1.8 at. %), exhibit a linear hardening tendency, evolving slowly with the square root of dose. This hardening tendency is typical for low-Cu RPV steels. Similar linear hardening tendency is observed in the low-Cu, medium-Ni, high-Mn (~1.5 at. %) and medium-P (~0.03 at. %) and high P (~0.05 at. %) steels N and O. In the low-Cu, high-Ni (~1.5 at. %), high-Mn (~1.8 at. %) and low-P steel I a liner trend with a higher slope is identified. Also, it should be noted that in the latter case an exponential-like irradiation hardening trend fits the experimental data well. Finally, the high-solutes (0.28Cu-1.6Ni-1.2Mn-0.05P at. %) steel W has a completely different hardening tendency. As expected for high-Cu materials, a severe hardening effect is observed at the lower irradiation doses, which becomes linear-like as a function of sqrt of dose upon depletion of Cu inside the ferrite matrix.

The initial microstructure of chemically tailored RPV steels (carbides, grain size, dislocation density), is not expected to evolve during irradiation. So, it is generally considered to have no influence on irradiation hardening in RPV steels. However, it should be recalled that owing to EBSD, retained austenite phase was observed in the steels I and W. Even though the firm experimental data confirming the effect of retained austenite was not collected, its presence might affect their post-irradiation behaviour.

Linear hardening tendencies with low slope as a function of sqrt of dose of steels D, E, F and N correlate well with the results of APT experiments. Indeed, for the most of irradiation conditions, a relatively low number density (below 0.9 x 10^{23} m^{-3}) of solute clusters was observed in these materials. Linear hardening trend as a function of sqrt of dose for high-P (0.047 at. %) steel O is stronger than of low-P (~0.02 at. %) D, E, F and medium-P (0.03 at. %) N. This is in good agreement with APT results, where higher number density of 1.2 x 10^{23} m^{-3} was measured in O. Exponential-like hardening tendency of steel I looks similar with the proposed effect of MNSFs formation (Fig. 1.a and Fig. 2). Yet, results of APT experiments are contradicting this theory. The composition of the solute clusters differs from the predicted G or Γ_2 phases (high dispersion of compositions for single clusters, ~70 at. % Fe) and these clusters were probably formed by RIS and not REP. Finally, the steel W with the high-Cu-content exhibits a significant irradiation hardening at a rather low irradiation dose of 0.06 dpa. It exhibits also the highest number density of solute-enriched clusters (16.5 x 10^{23} m^{-3}) from all studied steels as evaluated by APT.

Overall, irradiation hardening of chemically-tailored RPV steels measured with tensile tests correlates well, at least qualitatively, with the microstructure evolution (solute cluster formation) observed by APT. In the following section, in order to go deeper in the correlation, the hardening calculated from the microstructure characteristics will be compared to the measured one.

2 Comparison between measured and predicted irradiation hardening

The formation of nanosized solute clusters or precipitates is the main source of irradiation hardening in RPV steels. The main properties of solute clusters impacting irradiation hardening are their number density (N_D), their size (d) and their obstacle strength (α_{obs}). The number density and size are the variables obtained experimentally. The obstacle strength is a fitting parameter. The known post-irradiation hardening tendency for RPV materials is that yield stress increases linearly with $\sqrt{N_D d}$ or $\sqrt{f_V}$ [18,19]. The variation of the yield stress increase of CT RPV steels (measured with tensile tests) as a function of the square root of the product of solute cluster number density and size (measured with APT) is presented in Figure 3 which shows a linear trend. This observation confirms that the formation of solute clusters is the main cause of irradiation hardening in the chemically-tailored RPV steels.

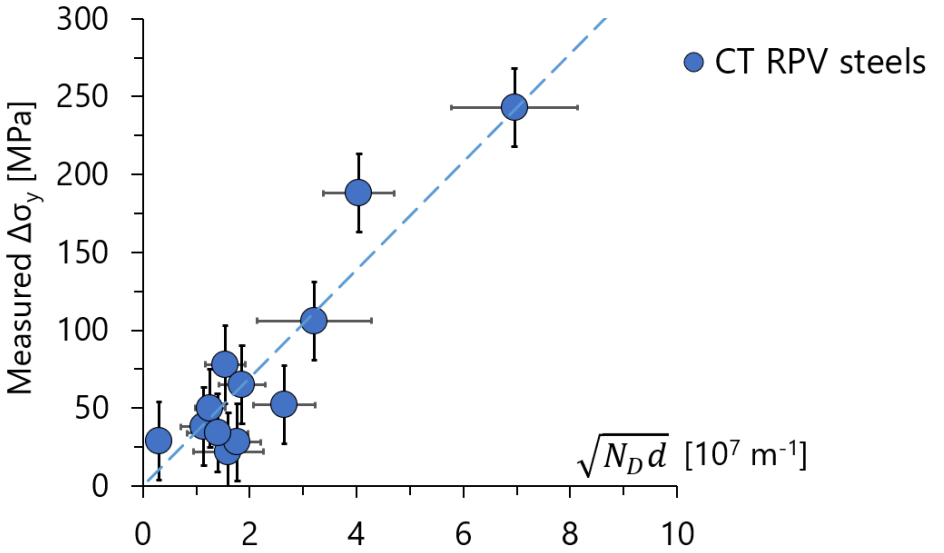

Figure 3. *Evolution of the measured tensile yield strength increase as a function of the square root of the product of cluster number density and size measured with APT. Uncertainty for the tensile test measurements is 25 MPa [17]. Uncertainly for cluster variables is given by the standard deviation between the results obtained for each APT experiment at the given condition.*

Further, the irradiation hardening was calculated with the Dispersed Barrier Hardening [DBH] (Eq. 5.1), Fridel-Kroupa-Hirsh [FKH] (Eq. 5.2), Bacon-Kocks-Scattergood [BKS] (Eq. 5.3) and Russel-Brown [RB] (Eq. 5.4, Eq. 5.5) models. The four models were described in detail in Chapter I.4. The obstacle strength (α) is adjusted by fitting the calculated yield stress with the measured one. The obstacle strength for DBH model is a coefficient which ranges between 0.1 and 1. In the case of the BKS model, the obstacle resistance term is utilised (4.5 GPa for an impenetrable object). For the RB model, a value of the shear modulus of the obstacle is selected. The obstacle strength in the case of FKH model is taken equal to about 0.25 and cannot be adjusted.

$$\tau_{sc} = \alpha_{sc}\mu b\sqrt{N_D d} \tag{5.1}$$

$$\tau_{sc} = \frac{1}{8}\mu b d N_D^{2/3} \tag{5.2}$$

$$\tau_{sc} = \left(\frac{\Omega_{sc}}{\Omega_\infty}\frac{ln(2\,D/b)}{ln(l/b)}\right)^{3/2}\frac{ln(l/b)}{2\pi}\mu b\sqrt{N_D d} \tag{5.3}$$

$$\tau_{sc} = \frac{\mu b}{L}\left[1-\frac{E_1^2}{E_2^2}\right]^{3/4} \qquad \frac{E_1}{E_2} = \frac{E_1^\infty log\frac{r}{r_0}}{E_2^\infty log\frac{R}{r_0}} + \frac{log\frac{R}{r}}{log\frac{R}{r_0}} \tag{5.4,5.5}$$

To account for the superposition of solute clusters with other obstacles, such as dislocation lines and carbides, equation 5.6 is utilised. The contribution of dislocation forest is the same for every studied steel (dislocation density around 10^{14} m^{-2}) and equals to 62 MPa. Since precise

information about carbide number density and size was not available, the value of 36 MPa utilised by Monet and Queyreau was selected [20, 21].

$$\Delta\sigma_{ir} = M\left(\sqrt{\tau_{df}^2 + \tau_c^2 + \tau_{sc}^2} - \sqrt{\tau_{df}^2 + \tau_c^2}\right) \quad (5.6)$$

Overall, a good correlation between the calculated yield strength increase owing to APT data and the measured irradiation hardening values is obtained with every selected model (Fig. 4).

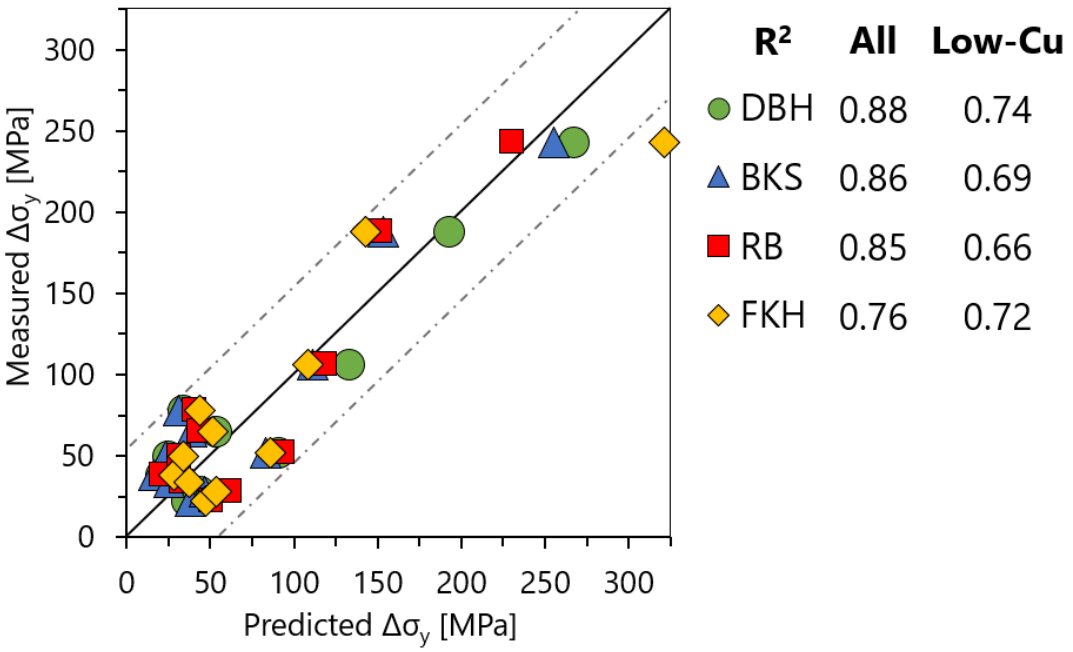

Figure 4. *Experimentally measured irradiation hardening in comparison to the calculated hardening from APT data using DBH, BKS, RB and FKH models.*

The calculated irradiation hardening of steel W is not following the same trends as other materials. Therefore, two different obstacle strength coefficients, one for all low-Cu steels and one for high-Cu W, were selected for DBH, BKS and RB models. The selected obstacle strength values are reported in Table 1.

Table 1. *Obstacle strength estimated with various models.*

Type	DBH	BKS [GPa] (~α)	RB [GPa]	FKH
Low-Cu steels	0.14	2.3 (~0.2)	62	~0.25
High-Cu steel	0.10	1.8 (~0.16)	73	~0.25
Pure Cu	-	-	48.5 [22]	-

The best fitted obstacle strength value for the whole set low-Cu steels is 0.14. However, if obstacle strength is fitted for each material separately, the lowest value is 0.11 in the case of steel F, 0.13 for I, 0.17 for N and O, and the highest one is 0.22 in the case of steel E. The obstacle strength in steel E deviates the most from the mean value. The probable explanation is that steel E

is the only medium-Mn (0.8 at. %) steel then all the others are high-Mn (above 1.5 at. %). This difference in bulk Mn content could have an effect on the carbide distribution, hence, modifying the irradiation hardening response of steel E.

Also, as it was described in chapter IV, two cluster families (enriched in P and P-free) were identified in the high dose conditions of steels E and F. When contribution of these cluster families is calculated separately, the similar obstacle strength values (difference of 0.01) for the P-enriched and P-free families are observed.

The obstacle strength selected for low-Cu steels with the DBH model equals to 0.14. The solute cluster resistance for low-Cu steels obtained from the BKS model equals to 2.3 GPa. The obstacle strength $\alpha_{sc} = \left(\frac{\Omega_{sc}}{\Omega_{\infty}} \frac{ln(2D/b)}{ln(l/b)}\right)^{3/2}$ could also be derived from the BKS model. The calculated value of the obstacle strength equals to 0.2 and is higher than the one of the DBH model. The solute cluster shear modulus in low-Cu steels equals to 62 GPa according to the RB model.

The obstacle strength for W evaluated with the DBH model equals to 0.1, which is lower than that of low-Cu materials (0.14). The obstacle resistance in the high-solutes steel W evaluated with the BKS model equals to 1.8 GPa (α ~ 0.16), which is lower than in the case of low-Cu steels (2.3 GPa and α ~ 0.2). The fitted obstacle shear modulus value in steel W equals to 73 GPa, which is larger than that of the low-Cu steels (62 GPa), and significantly larger than the value originally used by Russel and Brown for the CRPs (48.5 GPa) [22].

To evaluate the accuracy of the various models, the R-squared values were calculated. All three models (DBH, BKS and RB) where the obstacle strength can be adjusted show a better accuracy than the FKH model on the whole set of materials. Yet, in the case of low-Cu steels, the DBH and FKH models are the most satisfactory ones. In conclusion, the DBH model (considering a superposition with other obstacles) is preferable to predict irradiation hardening of RPV steels. The advantage of the DBH model over the FKH model is the possibility to tune the values for a wider range of materials with different bulk compositions and mechanical properties by adjusting the obstacle strength coefficient. The advantage over the BKS and RB models is the simplicity and possibility to cross-compare results with the large number of studies where the DBH model was also utilised [23-25]. The obstacle strength of CT RPV steels (0.1-0.2) is in good agreement with the results (0.1 to 0.2) reported in literature [23-25].

3 Comparison with the codified embrittlement trend curves

As it was described previously, irradiation hardening is the most important contributor to irradiation embrittlement of RPV steels, which is the main issue limiting the operation time of PWRs. Embrittlement is usually quantified by the shift of ductile-to-brittle transition temperature ΔT_{41J}. To account for irradiation embrittlement, correlation methods to estimate the transition temperature shift considering material bulk chemical composition and irradiation fluence were developed.

The current state of the art and comparison between various models is well described in the work by Mark Kirk [26]. In United States the second revision of the Regulatory Guide 1.99 is adopted by the Nuclear Regulatory Commission (NRC) [27]. The other notable examples developed in US are WR-C(5)R1 transition temperature shift (TTS) equation of the ASTM E900-15 standard [28] and 10CFR50.61a model, also called EONY[1][7,8,29]. In the case of French and Belgian surveillance programs the FIS model is utilised [30,31]. In Japan, irradiation embrittlement is estimated with Japan Electric Association Code JEAC4201 model [32,33]. The latest version is JEAC4201-2007, coefficients of which were adjusted in 2013. However, in the latest version the additional microstructural data, such as number density of irradiation promoted features in utilised. The older version JEAC4201-2004 uses only the bulk chemical composition, similar to other described above models. All the presented above equations are described in detail in the appendix D.1.

In the present research, the DBTT shift was not directly measured. Yet, it is possible to roughly estimate the DBTT shift from the YS increase in materials where irradiation hardening is the main source of embrittlement. From the database of commercial RPV steels where both Charpy and tensile tests were performed, the average ratio between yield strength increase and ductile-to-brittle transition temperature shift was evaluated [34, 35]:

$$\Delta T_{41J} \approx 0.65 \times \Delta\sigma_y \tag{5.12}$$

Since this value was not directly measured, the term “converted DBTT shift” will be utilised. It should also be noted that the obtained ratio is simply derived from a linear fit between the DBTT-change (ΔT_{41J}) and yield strength change ($\Delta\sigma_y$) and does not precisely account for the embrittlement mechanisms such as intergranular fracture.

Calculation of the DBTT shift will all described above models was performed and available in the appendix D.1. The profound comparison between various models is out of scope of the project.

[1] Named after developers Eason, Odette, Nanstad and Yamamoto

Therefore, only three models, namely FIS, EONY and JEAC4201-2004 (further referred as JEAC), showed the better precision will be utilised. The DBTT shifts converted from the tensile tests as a function of the one predicted by the FIS, EONY and JEAC models based on the bulk composition and irradiation dose are reported in figure 5.

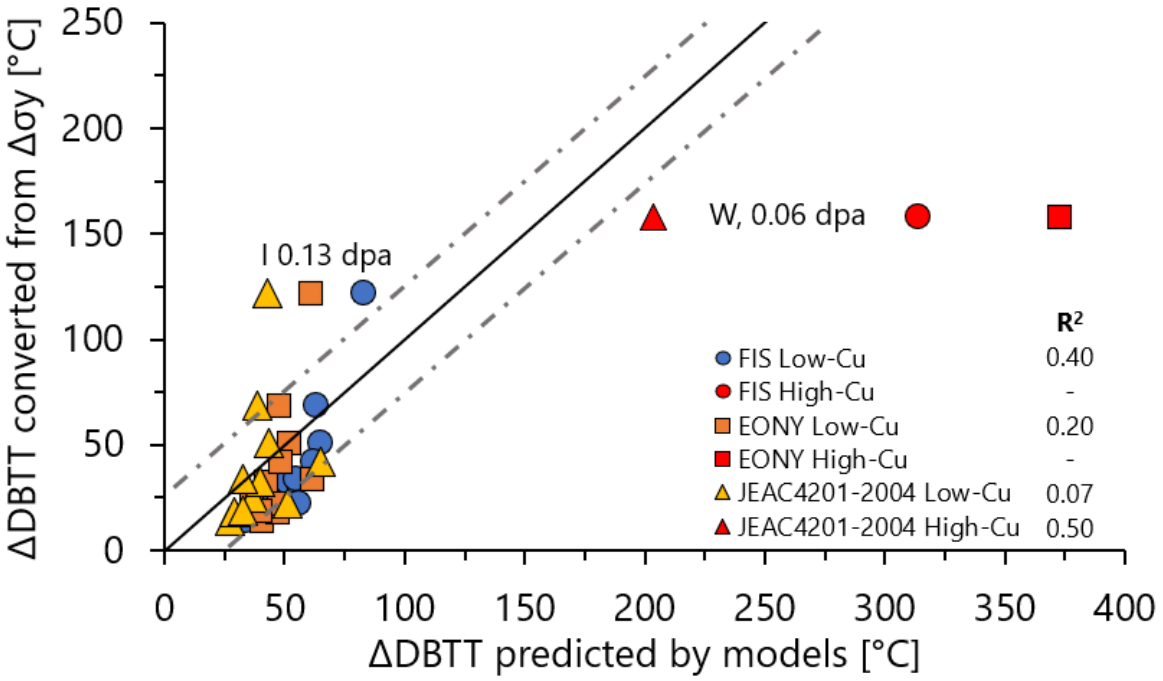

Figure 5. *Estimated embrittlement of the CT RPV steels. Converted values are obtained from the yield stress increase measured by tensile tests. Predicted values are calculated from the bulk chemical composition and accumulated dose. Uncertainty margin of around 25 °C was selected from the literature [36].*

The results for the high-solutes steel W irradiated up to 0.06 dpa are significantly overestimated by FIS and EONY models. The predicted values are 314°C by FIS and 373°C by EONY models, in comparison with the estimated value of 168 °C. The FIS model cannot precisely predict the DBTT shift in high-Cu materials, since Cu concentration in French and Belgium RPV materials is limited to 0.08 wt. %, which is significantly lower than the Cu concentration in steel W (0.28 wt. %). The EONY model also overestimates the DBTT shift, even though it has a CRP term devoted to account for the embrittlement of high-Cu materials. It can be concluded that due to its atypical composition, the embrittlement of high-solute steel W cannot be accurately predicted by codified models. It should be noted that the Japanese model (JEAC) works better than its US and European counterparts, and he DBTT shift of W is only slightly overestimated (203 vs 168 °C).

The embrittlement is underestimated by all three models for the high-Ni steel I irradiated up to 0.13 dpa. The Ni concentration (1.5 wt. %) in steel I is beyond the concentration range of French, Belgium and Japanese commercial RPV materials (up to around 0.8 wt. %) [7], and the FIS and

JEAC models are not designed to precisely evaluate the embrittlement for high-Ni materials. In the EONY model, Ni content doesn't affect the embrittlement contribution of the matrix features. It is only used to evaluate the CRP term, which equals to 0 in the steels with Cu content below 0.072 wt. %. Hence, the EONY model is not accurate enough to account for the Ni effect in the low-Cu materials. The other reason of the observed underestimation could be attributed to the austenitic phase found in this steel. The austenite volume fraction evaluated with EBSD is around 0.7 %. It is not clear if this rather low fraction of austenite can have an effect on the mechanical properties of this steel. Yet, this possibility should be pointed out.

In general, the predicted embrittlement using the FIS, EONY and JEAC4201-2004 models of low-Cu CT RPV steels correlates satisfactory with the values converted from the tensile tests data.

Summary

The correlation between the evolution of microstructure and the mechanical properties in chemically-tailored RPV steels subjected to neutron irradiation was investigated. In general, the solute cluster properties such as their number density and size obtained with APT correlate well with the irradiation hardening measured with tensile tests. The various materials follow the irradiation hardening trends observed in literature for low- and high-Cu materials.

The only exception is the low-Cu, high-Ni steel I, where both exponential-like and linear-like hardening tendency as a function of square root of dose are observed. A strong non-linear hardening behaviour was predicted by US researches due to the formation of MNSFs. This theory was questioned since MNSFs were not observed in our APT experiments. Therefore, to make a final conclusion about hardening tendency in RPV steel I, an additional research on material irradiated up to the higher dose, above 0.2 dpa, should be performed. Also, the presence of a second austenite phase should be accounted for.

A comparison between several hardening models was performed. The DBH model seems to give the best agreement with the measured irradiation hardening caused by solute clusters. The obstacle strength of the solute clusters in chemically-tailored RPV steels ranges from 0.1 to 0.2 and is in good agreement with values obtained in literature (0.1-0.2) [23-25]. Similarly to commercial RPV materials, a linear evolution of irradiation hardening as a function of the square root of the product of solute cluster number density and size was observed for CT RPV steels. Hence, chemically-tailored RPV steels are a good and reliable alternative to commercial materials for microstructure and mechanical properties research.

A comparison between embrittlement estimated from the tensile test data and models predictions was performed. It should be noted that the embrittlement values estimated from the tensile test data are only roughly estimates of the actual values. Overall, a satisfactory agreement between calculated and predicted values for low-Cu/low-P/medium-Ni CT RPV steels is observed.

References

1. M. Lambrecht, L. Malerba, A. Almazouzi. Journal of Nuclear Materials 378 (2008): 282–290. https://doi.org/10.1016/j.jnucmat.2008.06.030

2. R. Chaouadi, R. Gerard. Journal of Nuclear Materials 345 (2005): 65-74. https://doi.org/10.1016/j.jnucmat.2005.05.001

3. R. Chaouadi. RADAMO Database: Available Irradiated RPV Materials for Advanced Microstructural Investigations, SCK CEN restricted report 27710469, T-0093

4. K. Dohi, K. Nishida, A. Nomoto, N. Soneda, H. Matsuzawa, M. Tomimatsu. ASME Pressure Vessels and Piping Conference (2009): 403–9. https://doi.org/10.1115/PVP2009-77658

5. T. Takeuchi, A. Kuramoto, J. Kameda, T. Toyama, Y. Nagai, M. Hasegawa, T. Ohkubo, T. Yoshiie, Y. Nishiyama, and K. Onizawa. Journal of Nuclear Materials 402 (2010): 93–101. https://doi.org/10.1016/j.jnucmat.2010.04.008

6. C.A. English, J.M. Hyde. 'Radiation Damage of Reactor Pressure Vessel Steels' In Comprehensive Nuclear Materials. Elsevier (2012): 151–80. https://doi.org/10.1016/B978-0-08-056033-5.00087-2

7. N. Soneda (Ed.). Irradiation Embrittlement of Reactor Pressure Vessels (RPVs) in Nuclear Power Plants. Elsevier (2015). https://doi.org/10.1016/C2013-0-17428-4

8. E. Eason, G.R. Odette, R.K. Nanstad, T. Yamamoto (Eds). A Physically Based Correlation of Irradiation-Induced Transition Temperature Shifts for RPV Steels. Report ORNL/TM-2006/530 (2007): 250. https://info.ornl.gov/sites/publications/files/Pub2592.pdf

9. E. Meslin et al. Journal of Nuclear Materials 406 (2010): 73–83. https://doi.org/10.1016/j.jnucmat.2009.12.021

10. G.R. Odette, T. Yamamoto, T.J. Williams, R.K. Nanstad, C.A. English. Journal of Nuclear Materials 526 (2019): 151863. https://doi.org/10.1016/j.jnucmat.2019.151863

11. P. Wells, T. Yamamoto, B. Miller, T. Milot, J. Cole, Y. Wu, G.R. Odette. Acta Materialia 80 (2014): 205–19. https://doi.org/10.1016/j.actamat.2014.07.040

12. N. Almirall, P. Wells, T. Yamamoto, K. Wilford, T. Williams, N. Riddle, G.R. Odette. Acta Materialia 179 (2019): 119–28. https://doi.org/10.1016/j.actamat.2019.08.027

13. N. Almirall, P. Wells, T. Yamamoto, K. Yabuuchi, A. Kimura, and G.R. Odette. Journal of Nuclear Materials 536 (2020): 152173. https://doi.org/10.1016/j.jnucmat.2020.152173

14. B. Jenkins, J. Douglas, N. Almirall, N. Riddle, P. Bagot, J.M. Hyde, G.R. Odette, M. Moody. Materialia 11 (2020): 100717. https://doi.org/10.1016/j.mtla.2020.100717

15. R.K. Nanstad, G.R. Odette, N. Almirall, J. P. Robertson, W. L. Server, T. Yamamoto, P. Wells. Report: ORNL/TM-2017/172 (2016). http://www.osti.gov/scitech/

16. A. Kryukov, L. Debarberis, U. von Estorff, F. Gillemot, F. Oszvald. Journal of Nuclear materials 422 (2012: 173-177. https://doi.org/10.1016/j.jnucmat.2011.12.026

17. R. Chaouadi, R. Gérard, E. Stergar, W. Van Renterghem. Journal of Nuclear Materials 519 (2019): 188–204. https://doi.org/10.1016/j.jnucmat.2019.03.030

18. G. Monnet, L. Vincent. 'Multiscale Modeling of Radiation Hardening' In Handbook of Mechanics of Materials. Springer (2019). https://doi.org/10.1007/978-981-10-6884-3_8

19. K. Fukuya. Journal of Nuclear Science and Technology 50:3 (2013): 213-254. http://dx.doi.org/10.1080/00223131.2013.772448

20. G. Monnet. Journal of Nuclear Materials 508 (2018): 609-627. https://doi.org/10.1016/j.jnucmat.2018.06.020

21. S. Queyreau, G. Monnet, B. Devincre. Acta Materialia 58 (2010): 5586-5595. https://doi.org/10.1016/j.actamat.2010.06.028

22. K.C. Russell, L.M. Brown. Acta Metallurgica 20 (1972): 969-974. https://doi.org/10.1016/0001-6160(72)90091-0

23. F. Bergner, F. Gillemot, M. Hernández-Mayoral, M. Serrano, G. Török, A. Ulbricht, E. Altstadt. Journal of Nuclear Materials 461 (2015): 37–44. http://dx.doi.org/10.1016/j.jnucmat.2015.02.031

24. M. Lambrecht, E. Meslin, L. Malerba, M. Hernández-Mayoral, F. Bergner, P. Pareige, B. Radiguet, A. Almazouzi. Journal of Nuclear Materials 406 (2010): 84–89. https://doi.org/10.1016/j.jnucmat.2010.05.020

25. H. Huang. PhD thesis. Université de Rouen (2012)

26. M. Kirk. International Review of Nuclear Reactor Pressure Vessel Surveillance Programs, ASTM STP1603 (2018). https://doi.org/10.1520/STP160320170009

27. NRC Regulatory Guide 1.99 Revision 2, Task ME 305-4 (1988). https://www.nrc.gov/docs/ML0314/ML031430205.pdf

28. ASTM E900-15, Standard Guide for Predicting Radiation-Induced Transition Temperature Shift in Reactor Vessel Materials (2017). https://doi.org/10.1520/E0900-15

29. E.D. Eason, G.R. Odette, R.K. Nanstad, T. Yamamoto. Journal of Nuclear Materials 433 (2013): 240–254. http://dx.doi.org/10.1016/j.jnucmat.2012.09.012

30. C. Brillaud, F. Hedin, B. Houssin. ASTM International (1987): 420-447. https://doi.org/10.1520/STP25666S

31. P. Todeschini, Y. Lefebvre, H. Churier-Bossennec, N. Rupa, G. Chas, C. Benhamou. Revision of the irradiation embrittlement correlation used for the EDF RPV fleet. Paper A084-T01 (2010)

32. N. Soneda, A. Nomoto. Journal of Engineering for Gas Turbines and Power 132 (2010): 102918. https://doi.org/10.1115/1.4001056

33. N. Soneda, K. Nakashima, K. Nishida, K. Dohi. Proceedings of the ASME 2013 Pressure Vessels and Piping Conference, PVP2013-98076 (2013). https://doi.org/10.1115/PVP2013-98076

34. R.K. Nanstad, M.A. Sokolov, D.E. McCabe. Journal of ASTM International 5 (2008). https://doi.org/10.1520/JAI101346

35. Y. Nishiyama, K. Onizawa, M. Suzuki, J.W. Anderegg, Y. Nagai, T. Toyama, M. Hasegawa, J. Kameda. Acta Materialia 56 (2008): 4510-4521. https://doi.org/10.1016/j.actamat.2008.05.026

36. N. Castin, G. Bonny, M.J. Konstantinovic, A. Bakaev, F. Bergner, C. Courilleau, C. Domain, B. Gomez-Ferrer, J.M. Hyde, L. Messina, G. Monnet, M.I. Pascuet, B. Radiguet, M. Serrano, L. Malerba. Materials Science (2022). https://doi.org/10.48550/arXiv.2204.11441

General conclusions

Neutron irradiation of reactor pressure vessel steels results in the formation of nanosized features such as point defect clusters, solute clusters and precipitates. These objects can hinder dislocation motion and result in irradiation hardening. For most commercial PWRs, irradiation hardening is the main contributor to irradiation embrittlement which can limit the lifetime of nuclear power plants.

Different parameters influence the magnitude of irradiation hardening. The most noteworthy factors are: irradiation temperature and flux, accumulated dose and bulk chemical composition. In this study, the latter two parameters were investigated.

The main objective of this thesis was to study the influence of the bulk chemical composition and irradiation dose on the microstructure evolution and the consequent irradiation hardening of RPV steels. To do so, further steps were undertaken:

- To study the effect of the bulk chemical composition, seven chemically-tailored RPV steels were forged following the industrial recipes. Their bulk compositions were tuned to focus on the effect of two alloying (Mn and Ni) and two impurity (Cu and P) elements;
- To evaluate the dose effect, steels were irradiated at 290 °C in the BR2 MTR under high flux conditions (from 1 to 2.5 x 10^{17} n/m^{2}s, E > 1 MeV). Three irradiation doses of around 0.06, 0.08 and 0.13 dpa, which represent exposure equivalent to 25-50 years of operation of commercial NPPs were selected;
- To correlate the microstructure evolution and mechanical properties degradation through the irradiation hardening measured by tensile tests at SCK CEN.

Solute clusters and precipitates formed under neutron irradiation were characterised by Atom Probe Tomography. APT allows obtaining information about the number density, size and chemical composition of solute clusters. However, great care should be taken to account for the limitations of this technique. The question of the presence of Fe atoms inside solute clusters observed by APT is important to evaluate the nature and mechanism of clusters formation (radiation-induced or radiation enhanced), since Mn-Ni-Si precipitates are predicted to be Fe-free. An additional data mining procedure was performed to evaluate the effects of APT artefacts on the measured solute cluster composition. The results of the CCC model confirmed that the majority of Fe atoms observed inside the clusters are not an APT artefact.

The collected results are expected to be useful from both the practical and fundamental points of view. The observed microstructure evolution can be correlated with the results of tensile tests to improve the prediction of the post-irradiation behaviour and to extend the lifetime of the current PWR fleet up to 60 or even 80 years of operation. From the fundamental point of view, the presented results can provide additional information in support of radiation-induced or radiation enhanced solute cluster formation mechanisms.

Effect of the Mn and Ni on the microstructure evolution and their synergy

Mn has an accelerating effect on solute cluster formation. In the low-Mn (0.04 at. %) steel D, no solute clusters were observed at 0.09 dpa. If these clusters were present, their number density is below 4 x 10^{21} m^{-3}. Only a small shift in 1NN distribution of Si atoms was measured after irradiation, which could be a sign of early stages of solute clustering. Yet, it should be noted that steel D has the lowest bulk solute concentration in irradiation sensitives solutes[1] of the studied materials, which is also lower than the commercial RPV materials (~1.3 at. % vs ~2.2 at. %). the further increase of bulk Mn content up to 0.8 at. % (steel E), solute clusters were finally observed with a number density of about 3 x 10^{22} m^{-3}. With a further increase of bulk Mn content up to 1.8 at. % (steel F), the number density of clusters grew up almost to 10^{23} m^{-3}. Accordingly, clusters became more enriched in Mn, at the expense of Ni and Si atoms. The Mn-Ni-Si ratio inside the clusters followed the evolution of the bulk concentration ratios, which supports the RIS origin of these features.

Ni has a strong effect on irradiation-induced microstructure evolution. In the case of steel I, in which 1 at. % of Ni was added to steel F, the number density of clusters strongly increased by factors of 5 and 4 in the medium and high dose conditions. With the simultaneous addition of 0.8 at. % Ni and 0.7 at. % Mn to steel E, the cluster number density was stronger in comparison with the two cases where these solutes were added separately[2], confirming therefore the synergetic interaction between Ni and Mn. In general, with the addition of Ni, clusters became more enriched in Mn, Ni and Si. The synergetic interaction not only between Mn and Ni, but also with Si was observed.

To understand the nature of the observed solute clusters, a comparison with literature data was performed. Atomistic modelling suggests that P-SIA pair can pin a small PDC creating a sink for further solute segregation. The erosion profiles plotted on the clusters in medium-Ni steels E and

[1] Mn, Ni, Si, Cu and P
[2] 7 x 10^{23} m^{-3} in comparison with (4+1) x 10^{23} m^{-3}

F irradiated to doses below 0.1 dpa showed a high P concentration inside the cluster core. Therefore, it was proposed that P has an important role in solute cluster formation. However, in steels E and F irradiated up to a dose of about 0.13 dpa, a second family of smaller clusters was identified. These clusters were also enriched in Mn, Ni and Si, but to a less extent in P. Furthermore, from the erosion profiles, it was evaluated that P atoms are distributed through the whole cluster and not specifically at the core. Therefore, a hypothesis was proposed that these clusters were formed later, when there was not enough P in the matrix. The formation mechanism is then different from the P-SIA one. In the case of high-Ni steel I, the cluster core was not enriched in P. Upon comparison with atomistic modelling, it was proposed that in high Ni steel, PDCs were pinned not by P-SIA, but by Ni-V pairs. Both described above hypotheses suggest that the clusters were formed by RIS. The possibility of RED mechanism of Mn-Ni-Si features formation was also studied. To do so, the relative Mn-Ni-Si ratios inside the clusters were compared with those predicted by Thermocalc phases. Even though the average relative cluster ratios were in some cases similar to the predicted phases, high dispersion of Mn-Ni-Si ratios for single clusters were observed, with only a few cases corresponding to the predicted phases. Additionally, in all materials, the clusters had a high amount of Fe inside them (70-80 at. %). Also, as was noted before, in medium-Ni materials irradiated to doses below 0.1 dpa, the clusters were enriched in P, which is not expected in the case of MNSFs. Taking all these observations into account, a conclusion was made that the cluster formation mechanism is rather RIS than REP.

Effect of Cu and P on the microstructure evolution and their synergy

Cu is known to have a strong effect on the microstructure evolution under irradiation due to the accelerated formation of CEFs in materials with the bulk Cu content above ~0.10 at. %. For example, in high-solute steel W[3] at the rather low dose of 0.06 dpa, the number density of solute features was as high as 10^{24} m^{-3}. The morphology study on the solute-enriched features showed that CEFs interfaces acted as sinks for the segregation of other solutes. Hence, the synergetic effect of Cu on the segregation of other solutes, most notably, Mn, Ni and Si was observed. The ratio between Mn, Ni and Si inside clusters was almost the same as their ratio in the bulk. This observation is a strong supporter of the radiation-induced formation mechanism. No evident synergy between Cu and P in the high-Cu (~0.28 at. %) / high-P(~0.05 at. %) steel W was observed.

The effect of P was studied on low-Cu/medium-P (0.037 at. %) and low-Cu/high-P (0.054 at.%), N and O steels. With an increase of P bulk content, the number density of clusters increased

[3] 1.8Mn-1.6Ni-0.5Si-0.27Cu-0.05P at.%

by a factor of 2 (from 5 to 12) x10^{22} m^{-3}, most probably due to creation of the additional segregation sinks by a P-SIA mechanism. In both N and O steels, no synergy between Cu and P was observed. Yet, in high-P steel O, with the increase of P cluster content, clusters became less enriched in Si, and a negative P-Si synergy was noted.

Evolution of solute cluster number density with irradiation dose

The study on the dose effect was performed on steels E, F and I. In the case of steels E and F, the cluster number density grew by a factor of 1.3 between low and medium dose conditions, and more than doubled between medium and high dose cases. By contrast, the average radius of clusters grew up to around 1.6 nm at the medium dose condition, and with further irradiation decreased to about 1.4 nm. Moreover, in the high dose case, two families of clusters defined as "small" and "big" were distinguished[4]. In addition, it was evaluated that the big clusters were at least four times more enriched in P than the small ones. A proposition was made, that the surge of cluster number density in the high dose condition was due to the additional formation of smaller, low-P clusters.

In the case of steel I, only a comparison between medium and high doses was performed. At the high dose condition, the cluster number density is 1.7 times higher, yet, the radius remained almost the same (1.1-1.2 nm). Due to the high number density (above 4 x 10^{23} m^{-3}) and low P (~0.02 at. %) content, the latter has an insignificant effect on the solute cluster evolution between 0.08 and 0.13 dpa. Consequently, no bimodal cluster size distribution due to formation of P-free clusters was observed in high dose condition of steel I, contrary to E and F.

As expected, with an increase in irradiation dose, the number density of solute clusters increased in all materials. Concerning the cluster composition, in general, with the increase of irradiation dose, the clusters became more enriched in Mn, Ni and Si at the expenses of Fe, yet less enriched in P, probably due to depletion of the matrix in P.

Correlation between solute cluster formation and irradiation hardening

The correlation between the irradiation-induced microstructure and mechanical properties evolution in chemically-tailored RPV steels subjected to neutron irradiation was performed. In general, solute cluster properties, such as number density and size obtained with APT correlated well with irradiation hardening measured with tensile tests at SCK CEN. Same as in commercial

[4] Average radius of small clusters is ~1.1 nm and of big ones is ~1.6 nm

RPV databases, a linear evolution of irradiation hardening as a function of the square root of solute cluster number density and size was observed for CT RPV steels.

To estimate the obstacle strength of solute clusters, a comparison between several hardening models, namely DBH, BKS, RB and FKH was performed. DBH model seemed to be preferable to obtain reliable values for irradiation hardening caused by solute clusters. The obstacle strength of solute clusters of low-Cu steels, particularly E, F, I, N and O, was around 0.14 and is in good agreement with values presented in the literature (0.1-0.2). In steel E, a slightly higher obstacle strength value of 0.22 was measured. The divergent irradiation hardening tendency could be due to the different carbide distribution, since steel E is the only medium-Mn[5] steel studied. The other outlier, in which irradiation hardening had been initially overestimated was the high-solute steel W. In this material, contrary to other cases, two families of obstacles, namely CEFs and solute clusters, were observed. Therefore, it was fair to use a different obstacle strength value than 0.14, which was originally selected for steels where solute clusters are the only type of obstacles. It was not possible to precisely evaluate the hardening contribution of CEFs and SCs, yet the total obstacle strength, estimated with DBH for high-solutes steel W, was 0.10 and lower than of solute clusters in low-Cu materials.

Future work and perspectives

In the present study, information on seven CT RPV steels in a total of 12 conditions was collected. Yet, experiments on a few additional cases could be beneficial.

The first interest is APT experiments on the high dose condition (0.14-0.2 dpa) of the low-alloyed steel D, where no solute clusters were observed at 0.09 dpa. It is interesting to see whether the solute clusters will finally form or not at a higher dose, much later than in the other steels. If no solute clusters would be observed, the TEM study of this condition could be useful to see if the notable number density of dislocation loops has formed, and this low-alloyed steel follows the irradiation behaviour more typical to low-alloyed Fe model alloys than to commercial RPV materials. Additional statistical data mining to evaluate the presence of solute fluctuations should also be performed.

Another interesting point are APT experiments on the high-Mn/Ni steel I, at the dose of 0.2 dpa. This material has a bulk composition similar to the model RPV steels where MNSFs were found at the dose of 0.2 dpa by US researchers. Studying steel I at 0.2 dpa will allow to make a

[5] 0.8 at. % Mn in bulk

direct comparison with the latter study and contribute to the discussion about the nature of these solute clusters / precipitates (radiation-induced or enhanced mechanism). Furthermore, it could be beneficial to perform a STEM-EDX study of this material, to evaluate the Fe concentration in the solute features with other techniques than APT technique. This is a highly complex task which demands an operator skilled in both TEM and data mining.

The other way to provide an addition insight of the MNSFs formation mechanism is to perform the post-irradiation annealing on steel I. The ideal annealing parameters are hard to define. Taking into account the previous studies, the annealing at 400 °C for 50 hours can be sufficient to observe the partial dissolution of radiation-induced clusters, yet remaining the number density of latter high enough to be detected by APT.

The second idea is to perform a more direct comparison between microstructure evolution observed by APT and predicted by OKMC modelling. Unfortunately, it is impossible to study all the possible bulk compositions with experimental techniques such as APT, since it will take a huge amount of time and will have an enormous cost to forge, irradiate and characterise these materials. At the same time, the capabilities of the computational modelling are almost unlimited, concerning both various bulk compositions and irradiation doses up to several dpa. Yet, to make the results predicted by modelling reliable - it should be fed with experimental data. Since in this study a significant number of materials with various bulk compositions and irradiated up to several doses were studied, it could be useful to implement this data to improve the already developed OKMC models.

Appendices

Appendix A

A.1 Data on solute clusters observed in literature.

Table 1. *Irradiation conditions and bulk solute concentrations of the main elements taking part in clustering.*

Author	ID	Dose [dpa]	T_{irrad} [°C]	Si [at.%]	Mn [at.%]	Ni [at.%]	P [at.%]	Cu [at.%]
T. Takeuchi	Steel A	0.01	290	0.61	1.35	0.66	0.03	0.15
[1]	—//—	0.02	290	0.61	1.35	0.66	0.03	0.15
	—//—	0.06	290	0.61	1.35	0.66	0.03	0.15
	—//—	0.15	290	0.61	1.35	0.66	0.03	0.15
	Steel B	0.01	290	0.39	1.48	0.64	0.01	0.04
	—//—	0.02	290	0.39	1.48	0.64	0.01	0.04
	—//—	0.06	290	0.39	1.48	0.64	0.01	0.04
	—//—	0.15	290	0.39	1.48	0.64	0.01	0.04
H. Huang	16MND5	0.03	288	0.60	1.20	0.80	0.01	0.05
[2]	—//—	0.06	288	0.60	1.20	0.80	0.01	0.05
	—//—	0.08	288	0.60	1.20	0.80	0.01	0.05
	—//—	0.11	288	0.60	1.20	0.80	0.01	0.05
P. Auger	Chooz A	0.04	270	0.63	1.26	0.53	0.021	0.08
[3]	—//—	0.10	270	0.63	1.26	0.53	0.021	0.08
	—//—	0.18	270	0.63	1.26	0.53	0.021	0.08
	—//—	0.24	270	0.63	1.26	0.53	0.021	0.08
K. Lindgren	H	0.03	295	0.28	1.10	1.49	0.02	0.05
[4]	H	0.1	295	0.28	1.10	1.49	0.02	0.05
	S	0.07	284	0.28	1.10	1.49	0.02	0.05
K. Fukuya	A1	0.12	290	0.51	1.24	0.56	0.026	0.11
[5]	A2	0.08	290	0.51	1.24	0.56	0.026	0.11
	B1	0.03	290	0.59	1.49	0.54	0.021	0.15
	B2	0.08	290	0.59	1.49	0.54	0.021	0.15

Table 2. *Irradiation conditions, solute cluster properties and compositions. In some cases, information about solute concentration was demonstrated only with graphical representation and the approximate values (~) are estimated.*

Author	ID	Dose [dpa]	T_{irrad} [°C]	N_D x10^{23} [m^{-3}]	R [nm]	Si [at.%]	Mn [at.%]	Ni [at.%]	P [at.%]	Cu [at.%]	Fe [at.%]
T.	Steel A	0.01	290	1.0	1.1	~2.0	~2.5	~3.0	-	~3.0	~87
Takeuchi	—//—	0.02	290	5.2	1.1	~2.5	~3	~3.5	-	~2.0	~86
[1]	—//—	0.06	290	8.3	1.3	~3	~3.5	~2.5	-	~2.0	~87
	—//—	0.15	290	6.2	1.4	~3.5	~3.0	~4.0	-	~2.0	~85
	Steel B	0.01	290	-	-	-	-	-	-	-	-
	—//—	0.02	290	0.4	1.1	~2.0	~7.0	~6.0	-	~1.0	~84
	—//—	0.06	290	1.4	1.2	~3.0	~6.0	~5.5	-	~0.5	~85
	—//—	0.15	290	2.1	1.4	~4.0	~5.0	~5.0	-	~0.0	~85
H. Huang	16MND5	0.03	288	0.1	1.5	~8.0	~6.0	~10.0	~0.6	~0.3	~70
[2]	—//—	0.06	288	0.4	1.5	—//—	—//—	—//—	—//—	—//—	—//—
	—//—	0.08	288	0.6	1.5	—//—	—//—	—//—	—//—	—//—	—//—
	—//—	0.11	288	0.9	1.5	—//—	—//—	—//—	—//—	—//—	—//—
P. Auger	Chooz A	0.04	270	3.0	1.5	4.8	3.6	3.8	-	0.9	87
[3]	—//—	0.1	270	5.0	1.5	—//—	—//—	—//—	-	—//—	—//—
	—//—	0.18	270	9.0	2.0	—//—	—//—	—//—	-	—//—	—//—
	—//—	0.24	270	11.0	1.5	—//—	—//—	—//—	-	—//—	—//—
K.	H	0.03	295	4.0	0.7	~2.0	~10.0	~15.0	-	-	~73
Lindgren	H	0.1	295	6.0	0.9	~5.0	~12.0	~22.0	-	-	~60
[4]	S	0.07	284	3.3	1.2	~5.0	~12.0	~25.0	-	-	~57
K.	A1	0.12	290	3.1	1.30	4.0	8.0	7.0	-	15.0	66
Fukuya	A2	0.08	290	6.8	1.05	1.0	4.0	5.0	-	11.0	79
[5]	B1	0.03	290	3.3	1.05	2.0	4.0	7.0	-	11.0	74
	B2	0.08	290	5.8	1.05	3.0	5.0	6.0	-	9.0	78

A.2 Data on Mn-Ni-Si-enriched features observed in literature.

Table 1. *Irradiation conditions and bulk solute concentrations of main elements taking part MNSFs formation.*

Author	ID	Dose [dpa]	T_{irrad} [°C]	Si [at.%]	Mn [at.%]	Ni [at.%]	P [at.%]	Cu [at.%]	$\Delta\sigma_y$ [MPa]
P. Wells [6]	LC	0.2	300	0.53	0.97	0.91	-	0.21	-
	LD	—//—	300	0.52	1.08	1.00	-	0.21	-
	LG	—//—	300	0.49	1.09	0.86	-	0.01	-
	LH	—//—	300	0.45	0.97	0.72	-	0.08	-
	LI	—//—	300	0.43	1.2	0.72	-	0.15	-
	CM6	—//—	300	0.33	1.09	1.34	-	0.00	-
	LC	1.8	290	0.43	1.16	0.80	-	0.28	-
	LD	—//—	290	0.54	1.08	1.18	-	0.25	-
	LG	—//—	290	0.43	0.87	0.17	-	0.00	-
	LH	—//—	290	0.42	1.19	0.73	-	0.08	-
	LI	—//—	290	0.42	0.97	0.70	-	0.15	-
	CM6	—//—	290	0.39	1.42	1.69	-	0.00	-
N. Almirall [7]	R1	0.21	290	0.49	0.24	0.24	-	0.05	100
	R17	—//—	290	0.44	1.04	3.50	-	0.04	472
	R19	—//—	290	0.47	0.24	1.80	-	0.05	235
	R22	—//—	290	0.46	1.23	1.62	-	0.05	291
	R26	—//—	290	0.37	0.22	3.40	-	0.04	260
	R34	—//—	290	0.40	0.06	3.39	-	0.06	169
	R35	—//—	290	0.46	1.34	0.19	-	0.04	138
	R39	—//—	290	0.46	0.80	0.75	-	0.03	172
	R48	—//—	290	0.42	0.48	3.45	-	0.05	320
N. Almirall [8]	A13	4.0	290	1.26	0.98	3.23	-	0.05	-
	A16	$Fe3^+$	290	0.39	0.98	3.05	-	0.26	-
	A22	Ions	290	0.51	1.28	1.82	-	0.05	-
	A28	—//—	290	1.31	0.29	3.69	-	0.05	-
	A32	—//—	290	0.45	1.26	3.10	-	0.04	-
	A34	—//—	290	0.43	0.08	3.51	-	0.05	-
	A37	—//—	290	1.21	1.31	0.19	-	0.04	-
	A39	—//—	290	0.36	0.91	0.57	-	0.03	-
B. Jenkins [9]	C	0.21	290	0.45	1.24	3.17	0.01	0.04	~363
	G	—//—	290	0.35	1.15	1.44	0.00	0.03	~214
	K	—//—	290	0.38	0.21	3.39	0.00	0.04	~264
	RX12	—//—	290	0.07	0.05	3.54	0.00	0.02	~165

Table 2. *Irradiation conditions, MNSFs properties and relative solute concentrations excluding Fe and other solutes and normalised to 100%. Fe considered to be APT artefact but also presented.*

Author	ID	Dose [dpa]	T_{irrad} [°C]	N_D x10^{23} [m^{-3}]	R [nm]	Si [at.%]	Mn [at.%]	Ni [at.%]	P [at.%]	Cu [at.%]	-Fe [at. %]
P. Wells [6]	LC	0.2	300	9.2	1.2	15.7	23.6	35.1	-	25.7	60.8
	LD	—//—	300	11.5	1.1	15.5	24.6	37.8	-	22.2	58.6
	LG	—//—	300	5.3	0.7	27.2	25.5	46.8	-	0.5	53.3
	LH	—//—	300	4.9	0.9	20.3	251	39.8	-	14.8	58.7
	LI	—//—	300	6.9	1.1	14.2	27.4	34.2	-	24.2	57.2
	CM6	—//—	300	4.6	0.7	15.5	25.6	58.9	-	0.1	49.6
	LC	1.8	290	14.1	1.5	15.9	31.9	37.4	-	14.8	62.0
	LD	—//—	290	7.3	2	20.3	22.5	46.9	-	10.3	55.4
	LG	—//—	290	16.3	1.3	22.5	31.2	46.1	-	0.2	63.5
	LH	—//—	290	15.2	1.3	18.6	35.6	40.7	-	5.0	64.9
	LI	—//—	290	14.6	1.3	18.9	31.9	39.7	-	9.5	62.7
	CM6	—//—	290	19.5	1.5	11.9	35.5	52.5	-	0.1	58.9
N. Almirall [7]	R1	0.21	290	0.9	1.2	46.8	14.6	37.1	-	1.5	58.2
	R17	—//—	290	22.2	1.3	12.5	23.9	62.8	-	0.9	57.8
	R19	—//—	290	5.1	1.2	29.4	5.1	64.4	-	1.0	64.3
	R22	—//—	290	13.4	1.1	18.6	26.5	54.1	-	0.8	63.4
	R26	—//—	290	8.4	1.2	20.8	4.7	73.5	-	0.9	58.1
	R34	—//—	290	6.5	1.1	22.0	1.2	75.9	-	0.9	58.2
	R35	—//—	290	1.8	1.1	30.0	42.4	26.4	-	1.3	65.1
	R39	—//—	290	2.4	1.6	32.7	19.7	46.8	-	0.8	65.5
	R48	—//—	290	21.2	1.1	17.2	12.5	69.2	-	1.0	58.6
N. Almirall [8]	A13	4.0	290	6.6	2.7	24.7	13.9	60.9	-	0.5	Not
	A16	$Fe3^+$	290	2.2	2.9	9.9	19.3	65.1	-	5.7	given
	A22	Ions	290	4.9	2.5	17.7	23.9	57.5	-	0.9	—//—
	A28	—//—	290	5.9	2.4	26.5	5.0	68.0	-	0.6	—//—
	A32	—//—	290	4.7	2.9	10.8	22.7	65.9	-	0.6	—//—
	A34	—//—	290	1.1	2.6	23.1	8.2	67.7	-	0.9	—//—
	A37	—//—	290	0.6	2.0	39.8	20.4	38.4	-	1.4	—//—
	A39	—//—	290	3.3	2.0	22.9	29.3	47.0	-	0.8	—//—
B. Jenkins [9]	C	0.21	290	21.1	1.2	12.4	26.6	58.5	0.2	1.4	46.2
	G	—//—	290	7.5	1.1	19.5	23.2	54.0	0.8	1.6	46.3
	K	—//—	290	11.5	1.0	20.4	5.0	71.4	0.3	1.7	43.4
	RX12	—//—	290	7.0	0.8	5.2	1.3	90.9	0.2	0.7	42.0

A.3 Irradiation conditions and tensile test measurements

Table 1. *Irradiation conditions and hardening for tensile test specimens of CT RPV steels. Values of RADAMO-13 irradiation are in regular font. Values of RECALL-0 irradiation are in italic font. Combined values of two irradiations are in bold font [10].*

CT RPV steel ID	σ_y [MPa]	Sample ID	T_{irrad} [°C]	Fluence [10^{23} n/m^2]	Flux [10^{17} n/m^{2}s]	dpa/s [10^{-8}]	Dose [dpa]	$\Delta\sigma_y$ [MPa]
D	417	D-35	290	0.74	0.31	0.44	0.011	4
		D-10	290	2.90	1.20	1.73	0.042	14
		D-19	290	5.27	2.18	3.14	0.076	24
		D-26	290	6.34	2.62	3.77	0.091	29
E	483	E-35	290	1.00	0.41	0.60	0.014	8
		E-10	290	3.46	1.43	2.06	0.050	28
		E-19	290	5.60	2.31	3.33	0.081	44
		E-26	290	6.24	2.58	3.71	0.090	49
		E-R0	*290*	*3.20*	*1.32*	*1.90*	*0.046*	
				9.59			**0.138**	**78**
F	535	F-35	290	1.27	0.52	0.76	0.018	7
		F-10	290	3.38	1.40	2.01	0.049	18
		F-19	290	4.69	1.94	2.79	0.068	25
		F-26	290	5.99	2.48	3.57	0.086	31
		F-R0	*290*	*3.35*	*1.38*	*1.99*	*0.048*	
				9.34			**0.134**	**52**
I	492	I-35	290	1.05	0.43	0.63	0.015	20
		I-10	290	3.72	1.54	2.21	0.054	70
		I-19	290	5.21	2.15	3.10	0.075	96
		I-26	290	5.94	2.46	3.54	0.086	109
		I-R0	*290*	*3.20*	*1.32*	*1.90*	*0.046*	
				9.14			**0.132**	**188**
N	548	N-35	290	0.84	0.35	0.50	0.012	6
		N-10	290	2.95	1.22	1.76	0.042	20
		N-19	290	4.70	1.94	2.80	0.068	31
		N-26	290	5.00	2.07	2.98	0.072	33
O	544	O-35	290	1.05	0.43	0.63	0.015	17
		O-10	290	2.75	1.14	1.64	0.040	42
		O-19	290	3.81	1.57	2.27	0.055	57
		O-26	290	4.86	2.01	2.89	0.070	71
W	514	W-35	290	0.74	0.31	0.44	0.011	118
		W-10	290	2.37	0.98	1.41	0.034	217
		W-19	290	3.74	1.55	2.23	0.054	240
		W-26	290	4.18	1.73	2.49	0.060	243

Table 2. *Irradiation conditions and hardening values attributed to microstructure specimens of CT RPV steels [10].*

CT RPV steel ID	σ_y [MPa]	Sample ID	T_{irrad} [°C]	Fluence [10^{23} n/m^2]	Flux [10^{17} n/m^{2}s]	dpa/s [10^{-8}]	Dose [dpa]	$\Delta\sigma_y$ [MPa]
D	417	D12	290	1.28	0.53	0.76	0.018	6
		D21	290	4.12	1.70	2.45	0.059	19
		D28	290	6.29	2.60	3.74	0.091	29
E	483	E12	290	2.19	0.91	1.30	0.032	18
		E21	290	4.78	1.98	2.85	0.069	38
		E28	290	6.37	2.63	3.79	0.092	50
F	535	F12	290	2.79	1.15	1.66	0.040	15
		F21	290	4.09	1.69	2.43	0.059	22
		F28	290	5.40	2.23	3.21	0.078	28
I	492	I12	290	2.93	1.21	1.74	0.042	56
		I21	290	4.60	1.90	2.74	0.066	86
		I28	290	5.72	2.36	3.40	0.082	106
N	548	N12	290	1.86	0.77	1.11	0.027	12
		N21	290	4.05	1.67	2.41	0.058	27
		N28	290	5.21	2.15	3.10	0.075	34
O	544	O12	290	2.27	0.94	1.35	0.033	35
		O21	290	3.32	1.37	1.98	0.048	50
		O28	290	4.38	1.81	2.61	0.063	65
W	514	W12	290	1.55	0.64	0.92	0.022	184
		W21	290	3.22	1.33	1.92	0.046	234
		W28	290	4.25	1.76	2.53	0.061	243

References

1. T. Takeuchi, A. Kuramoto, J. Kameda, T. Toyama, Y. Nagai, M. Hasegawa, T. Ohkubo, T. Yoshiie, Y. Nishiyama, and K. Onizawa. Journal of Nuclear Materials 402 (2010): 93–101. https://doi.org/10.1016/j.jnucmat.2010.04.008

2. H. Huang, B. Radiguet, P. Todeschini, G. Chas, P. Pareige. MRS Proceedings 1264 (2010): 1264-BB05-18. https://doi.org/10.1557/PROC-1264-BB05-18

3. P. Auger, P. Pareige, S. Welzel, J-C. Van Duysen. Journal of Nuclear Materials 280 (2000): 331–44. https://doi.org/10.1016/S0022-3115(00)00056-8

4. K. Lindgren, M. Boåsen, K. Stiller, P. Efsing, M. Thuvander. Journal of Nuclear Materials 488 (2017): 222–30. https://doi.org/10.1016/j.jnucmat.2017.03.019

5. K. Fukuya, K. Ohno, H. Nakata, S. Dumbill, J.M. Hyde. Journal of Nuclear Materials 312 (2003): 163–73. https://doi.org/10.1016/S0022-3115(02)01675-6

6. P. Wells, T. Yamamoto, B. Miller, T. Milot, J. Cole, Y. Wu, G.R. Odette. Acta Materialia 80 (2014): 205–19. https://doi.org/10.1016/j.actamat.2014.07.040

7. N. Almirall, P. Wells, T. Yamamoto, K. Wilford, T. Williams, N. Riddle, G.R. Odette. Acta Materialia 179 (2019): 119–28. https://doi.org/10.1016/j.actamat.2019.08.027

8. N. Almirall, P. Wells, T. Yamamoto, K. Yabuuchi, A. Kimura, and G.R. Odette. Journal of Nuclear Materials 536 (2020): 152173. https://doi.org/10.1016/j.jnucmat.2020.152173

9. B. Jenkins, J. Douglas, N. Almirall, N. Riddle, P. Bagot, J.M. Hyde, G.R. Odette, M.. Moody. Materialia 11 (2020): 100717. https://doi.org/10.1016/j.mtla.2020.100717

10. R. Chaouadi. RADAMO Database: Available Irradiated RPV Materials for Advanced Microstructural Investigations, SCK CEN restricted report 27710469, T-0093

Appendix B

B.1 Additional figures for APT experiments

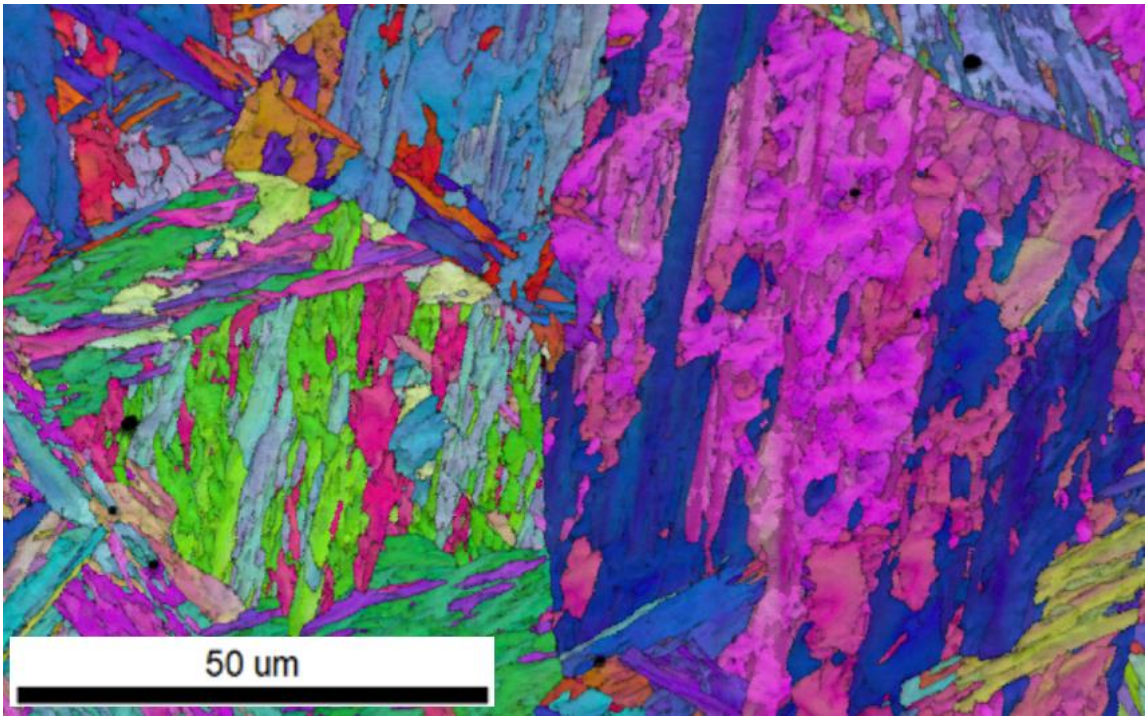

Figure 1. *CT RPV steel I. EBSD IPF map. Parent austenite grains are visible.*

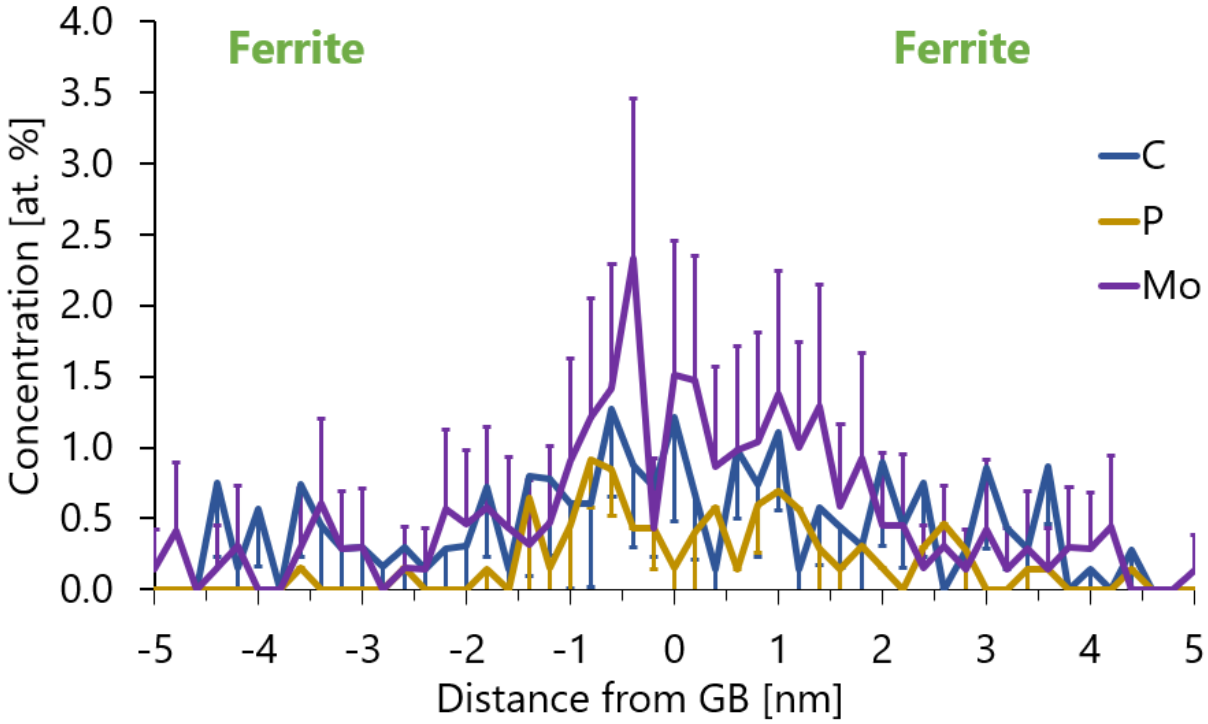

Figure 2. *CT RPV steel D irradiated up to 0.09 dpa (φt 6.29; E>1MeV). Concentration profile plotted through GB for C, P and Mo atoms.*

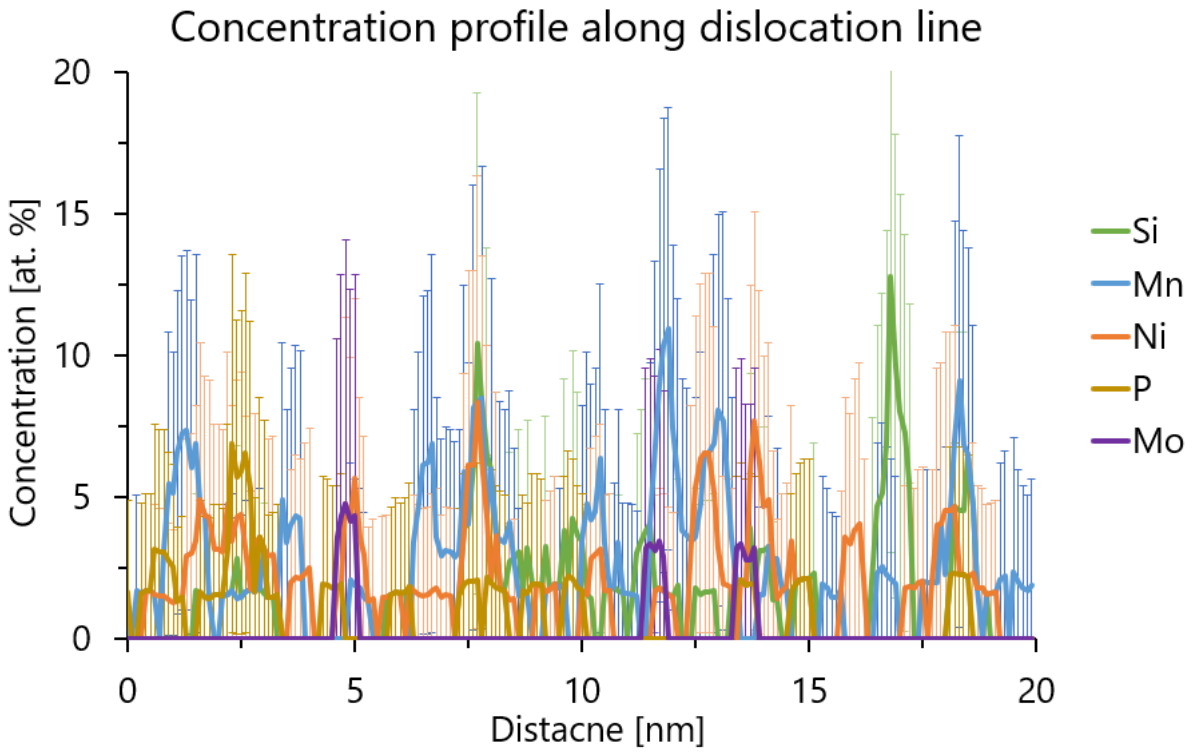

Figure 3. *CT RPV steel E irradiated up to 0.07 dpa (φt 4.78; E>1MeV). Concentration profile plotted alongside the dislocation line for Si, Mn, Ni, P and Mo atoms.*

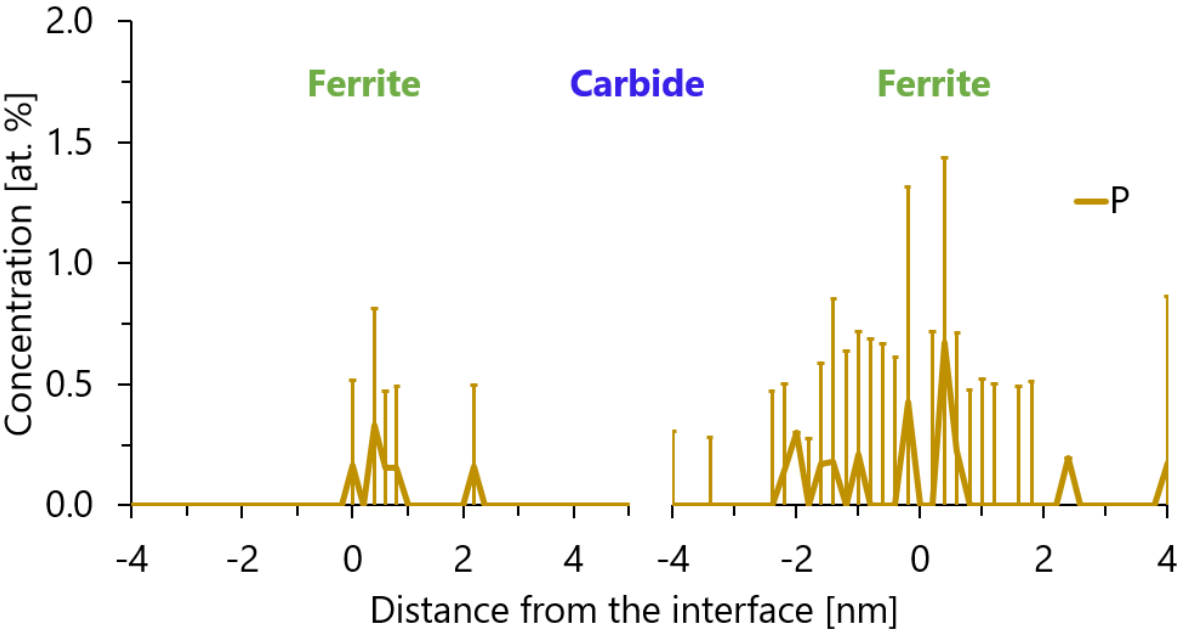

Figure 4. *CT RPV steel E irradiated up to 0.09 dpa (φt 6.37; E>1MeV). Concentration profile plotted through ferrite / carbide interfaces for P atoms.*

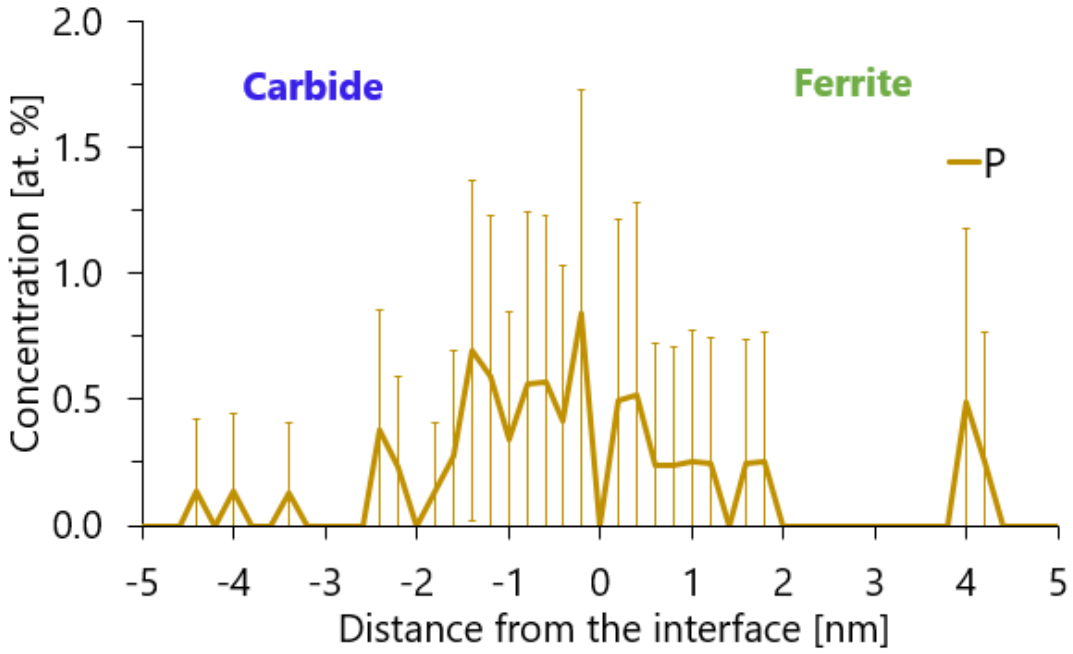

Figure 5. *CT RPV steel E irradiated up to 0.14 dpa (φt 9.59; E>1MeV). Concentration profile plotted through carbide / ferrite interface for P atoms.*

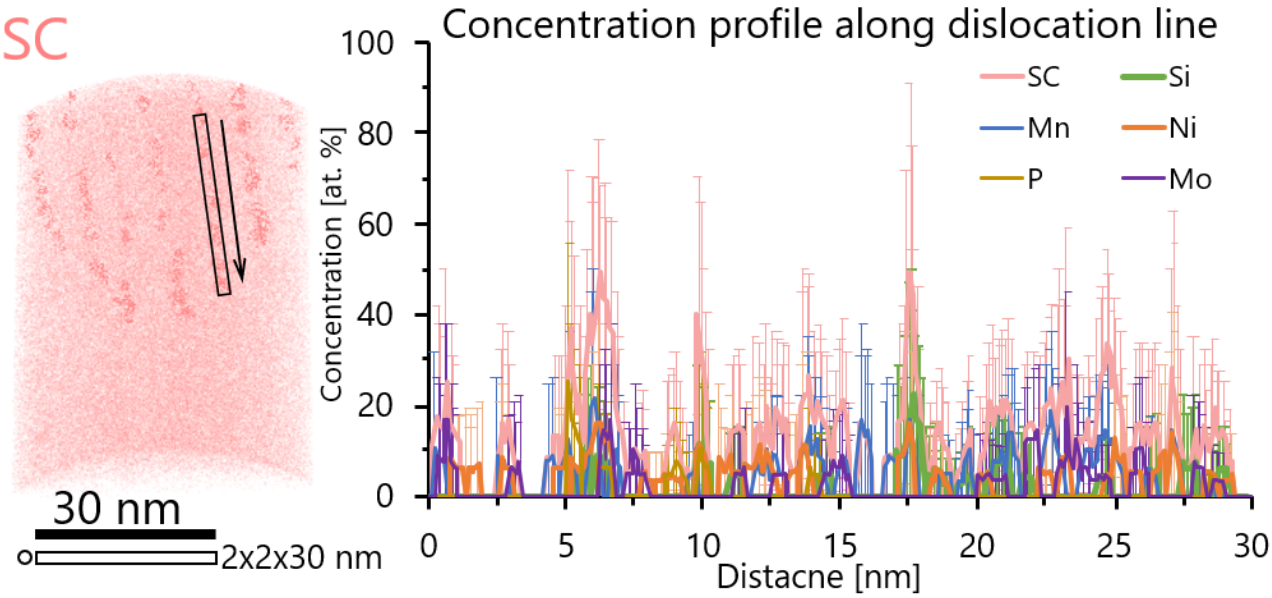

Figure 6. *CT RPV steel F irradiated up to 0.06 dpa (φt 4.09; E>1MeV). Concentration profile plotted along LAGB dislocation line for Si, Mn, Ni, P and Mo (and combined as SC) atoms.*

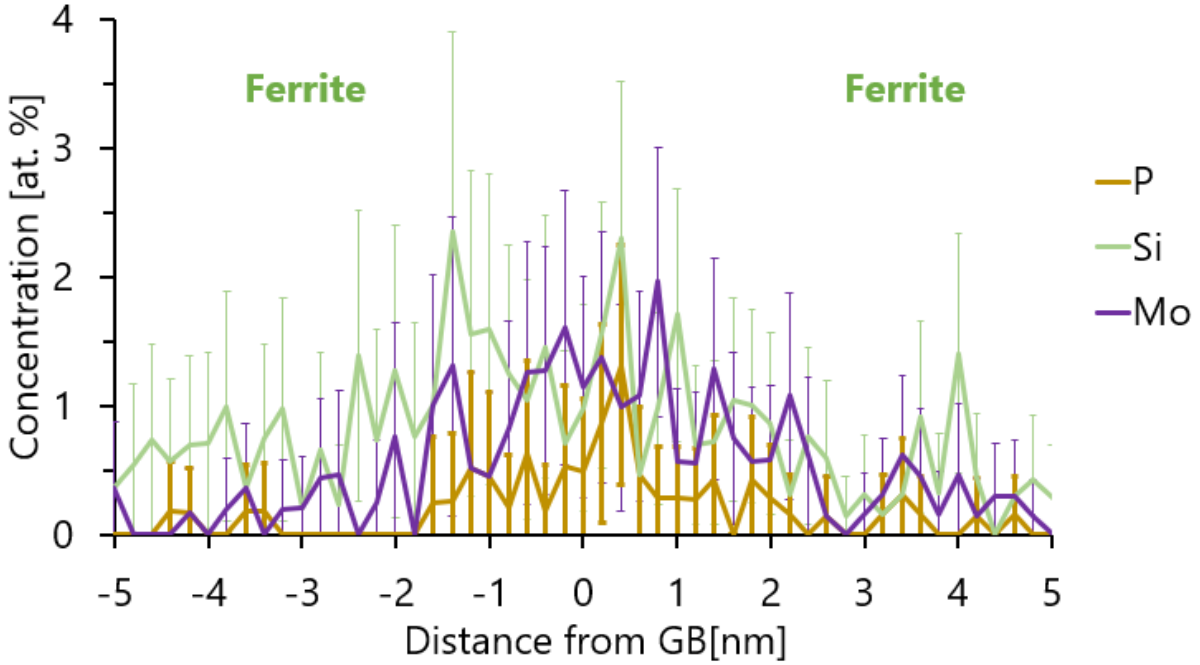

Figure 7. *CT RPV steel F irradiated up to 0.06 dpa (φt 4.09; E>1MeV). Concentration profile plotted through GB for P, Si and Mo atoms.*

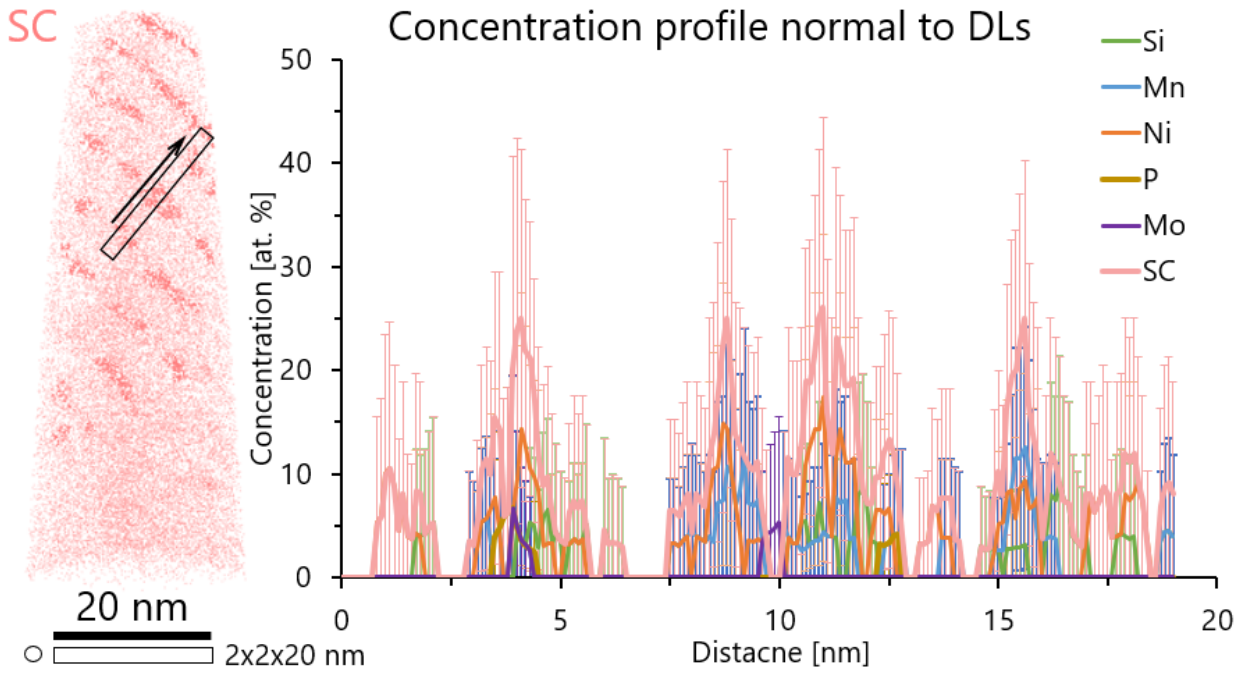

Figure 8. *CT RPV steel I irradiated up to 0.08 dpa (φt 5.72; E>1MeV). Concentration profile plotted normal to LAGB dislocation lines for Si, Mn, Ni, P and Mo (and combined as SC) atoms.*

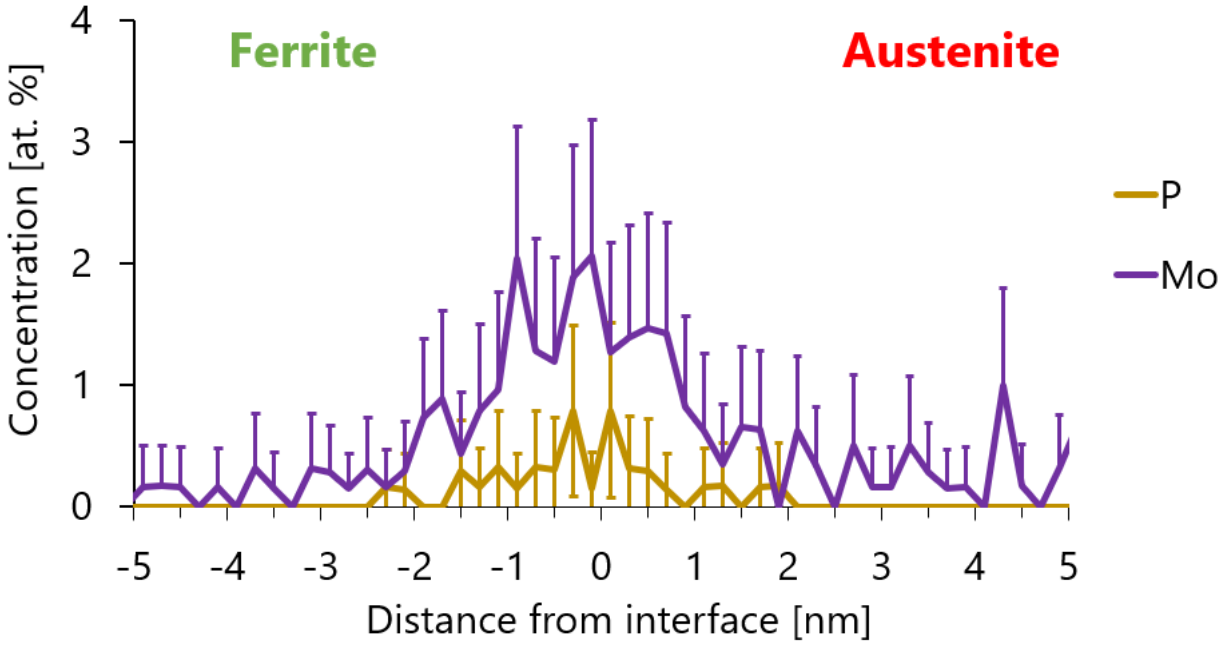

Figure 9. *CT RPV steel I irradiated up to 0.08 dpa (φt 5.72; E>1MeV). Concentration profile plotted through ferrite / austenite interface for P and Mo atoms.*

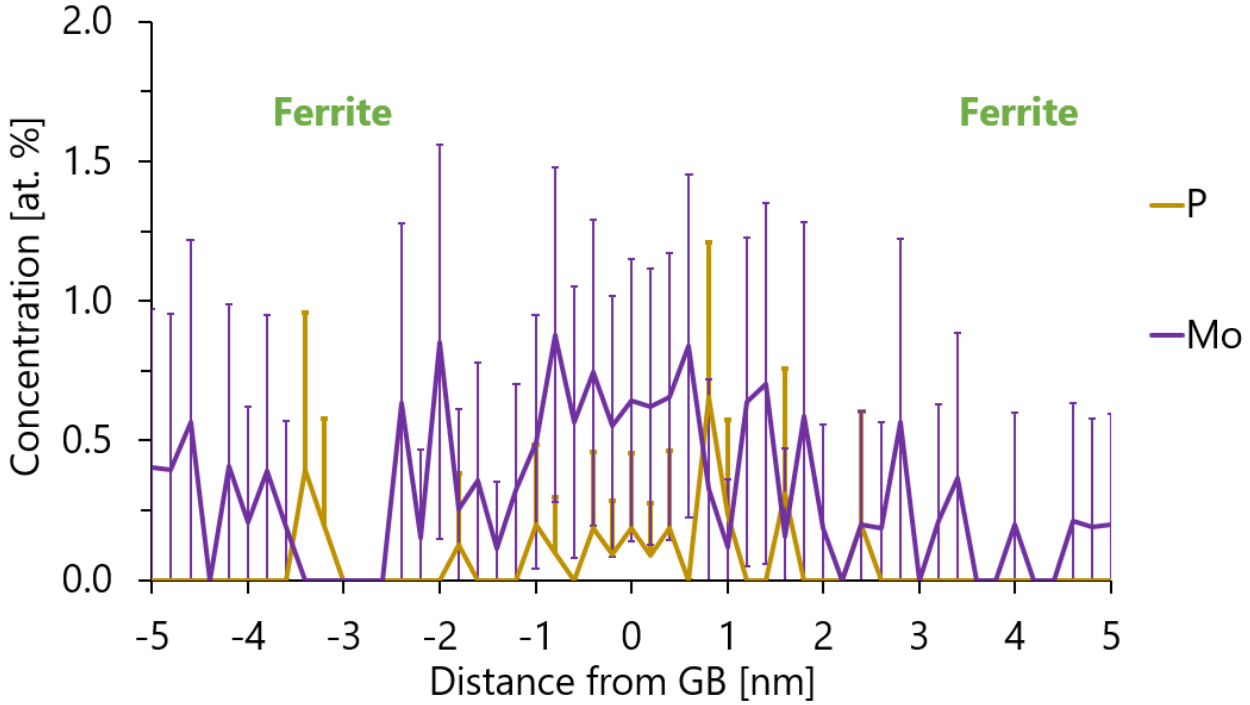

Figure 10. *CT RPV steel I irradiated up to 0.13 dpa (φt 9.14; E>1MeV). Concentration profile plotted through GB for P and Mo atoms.*

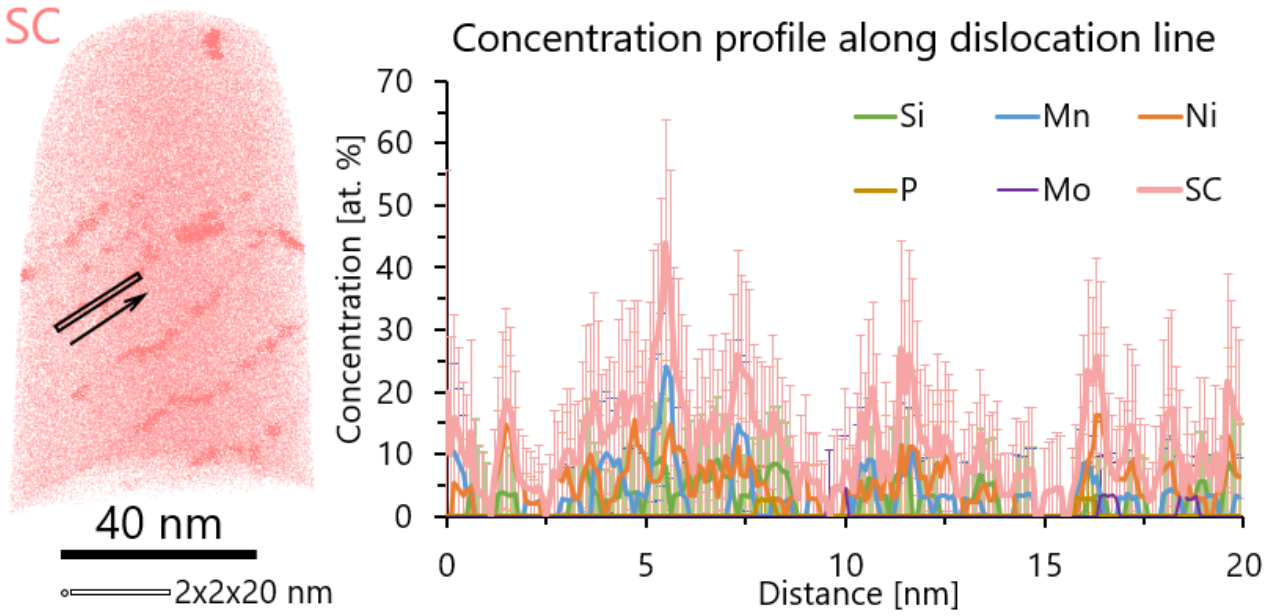

Figure 11. *CT RPV steel N irradiated up to 0.075 dpa (φt 5.21; E>1MeV). Concentration profile plotted alongside the LAGB dislocation line for Si, Mn, Ni, P and Mo (and combined as SC) atoms.*

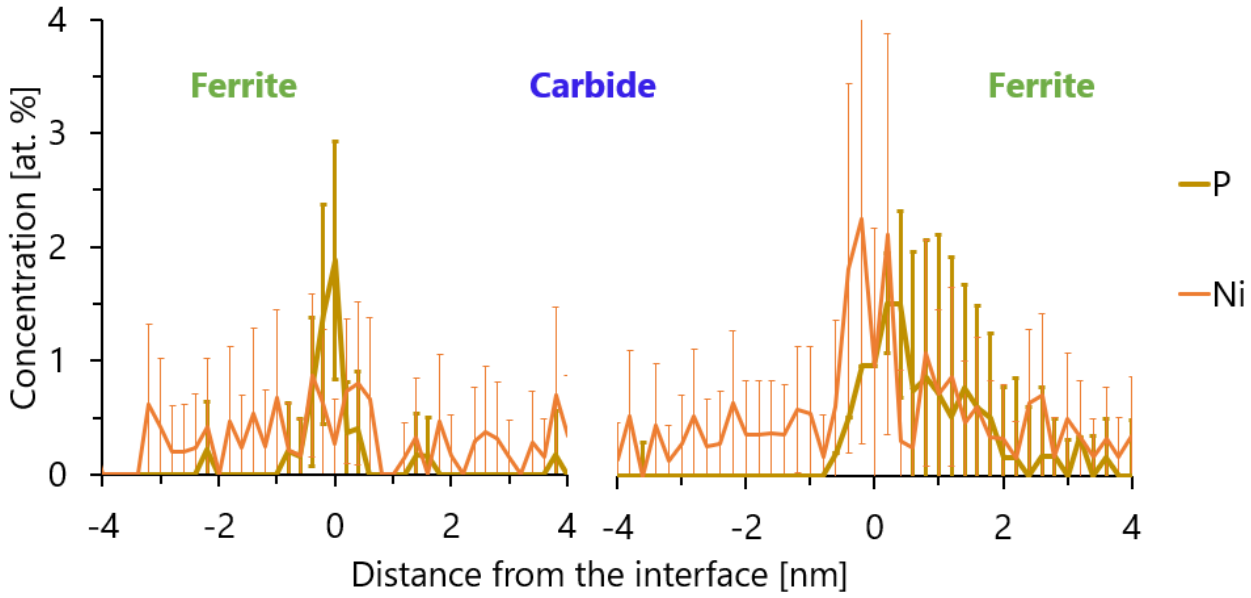

Figure 12. *CT RPV steel O irradiated up to 0.063 dpa (φt 4.38; E>1MeV). Concentration profile plotted through ferrite / carbide interfaces for P and Ni atoms.*

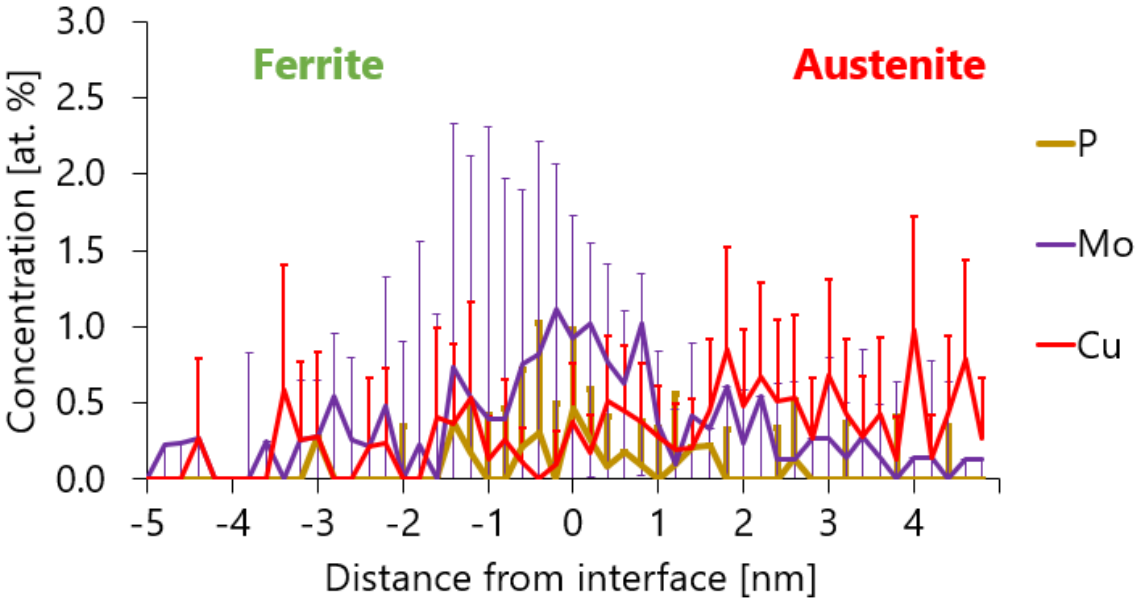

Figure 13. *CT RPV steel W irradiated up to 0.06 dpa (φt 4.25; E>1MeV). Concentration profile plotted through ferrite / austenite interface for P, Mo and Cu atoms*

B.2 X-Ray diffraction experiments

X-Ray diffraction is a non-destructive material analysis technique utilised to obtain information about crystallographic structure and phase data of materials. The scale of analysis is one the microscale and thousands of grains are studied result in significant statistical data collected.

Since the X-Ray wavelength (few angstrom) is similar to the interplanar distance on the lattice (2.87 Å), for the condition satisfying the Bragg's law the strong amplification of signal occurs which is observed as the intensive peaks at the diffractogram [1].

Experiments were performed on the Bruker D8 ADVANCE diffractometer with Co source and the X-Ray wavelength of 1.79 angstrom. The experiments were performed with Bragg-Brentano geometry where angle between sample surface in incident beam is θ and angle between detector and incident beam is 2θ. 2θ angles from 40° to 140° were utilised. The calibration for Rietveld refinement with Si etalon to account for the instrumental broadening was also performed.

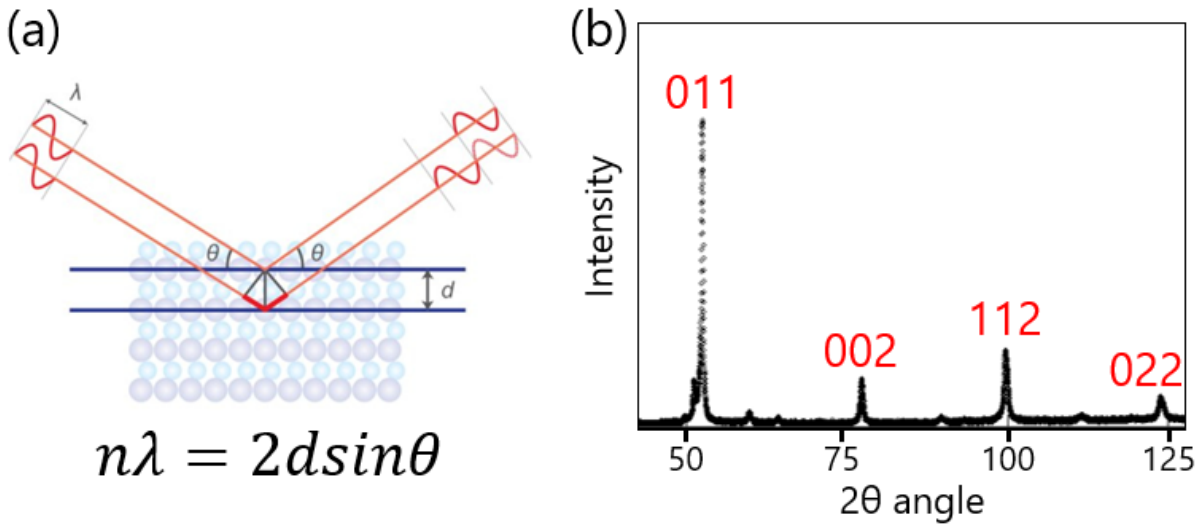

Figure 1. *(a) Planes satisfying the Bragg's condition [2]. (b) Diffractogram of CT RPV steel I in the non-irradiated state.*

The evolution of peak shape (broadening) could be caused by the decrease in the grain size on by the accumulation of microstrain in the lattice. The Material Analysis Using Diffraction (MAUD) software was utilised to extract the data about crystallographic properties of CT RPV steels [3]. The refinement procedure is based on fitting the experimental diffraction pattern with the calculated one by adjusting the lattice parameter, coherent domain size (CDS) and microstrain levels. These parameters are refined by least-squares procedure [4].

From the obtained CDS (D) and macrostrain ($\langle\varepsilon^2\rangle^{1/2}$) the equation from literature was utilised: $\rho = 3\sqrt{2\pi}\langle\varepsilon^2\rangle^{1/2}/Db$ [5]. The results are presented in Table 1.

Table 1. *Dislocation density in CT RPV steels measured with XRD.*

ID	D	E	F	I	N	O	W
Density [10^{14} m^{-2}]	0.89	1.05	1.90	2.67	1.41	1.26	1.56
Uncertainty [10^{14} m^{-2}]	0.02	0.02	0.02	0.07	0.04	0.02	0.07

The measured with XRD dislocation density of CT RPV steels is ranging from 0.9 to 2.7 x 10^{14} m^{-2}, this is in a good agreement with TEM measurements on steel I (10^{14} m^{-2}) and the data available in the literature [6,7].

References

1. C. Suryanarayana. M. Grant Norton. X-Ray Diffraction – A Practical Approach. https://doi.org/10.1007/978-1-4899-0148-4

2. X-Ray Diffraction. Rigaku web source. https://www.rigaku.com/fr/node/713

3. L. Lutterotti. MAUD version 2.96. http://maud.radiographema.eu/

4. P. Sahu, M. De, S. Kajiwara. Journal of Alloys and Compounds 346 (2002): 158–169. https://doi.org/10.1016/S0925-8388(02)00495-4

5. G. Dini, R. Ueji, A. Najafizadeh, S.M. Monir-Vaghefi. Materials Science and Engineering A 527 (2010): 2759–2763. https://doi.org/10.1016/j.msea.2010.01.033.

6. H. Liu, Q. Li. Materials Science and Engineering 490 (2019): 022019. https://doi:10.1088/1757-899x/490/2/022019

7. W. Van Renterghem, E. Stergar, R. Chaouadi. Effect of Nickel–Manganese Concentration on the Microstructure of Chemically-Tailored RPV Steels, SCK CEN restricted report 26724015, R-6490

B.3 APT experiments on irradiated materials

Table 1. *APT experiments on CT RPV steel D neutron irradiated in BR2 at 290 °C up to the dose of 0.091 dpa (φt 6.29; E>1MeV).*

Run	Number of atoms [10^6]	Number of clusters	ND x 10^{22} [m^{-3}]	R_{eq} [nm]	Number of cluster core atoms	Global concentration [at. %]					Cluster concentration [at. %]					
						Si	Mn	Ni	P	Cu	Si	Mn	Ni	P	Cu	Fe
3767	0.6	-	-	-	-	0.42	0.03	0.67	0.003	0.048	-	-	-	-	-	-
3773	1.1	-	-	-	-	0.52	0.02	0.71	0.003	0.053	-	-	-	-	-	-
3779	1.0	-	-	-	-	0.46	0.03	0.70	0.002	0.045	-	-	-	-	-	-
3850	0.7	-	-	-	-	0.44	0.03	0.64	0.002	0.051	-	-	-	-	-	-
3853	0.4	-	-	-	-	0.47	0.03	0.67	0.003	0.058	-	-	-	-	-	-
3855	0.8	-	-	-	-	0.45	0.02	0.65	0.001	0.046	-	-	-	-	-	-
4154	0.5	-	-	-	-	0.53	0.04	0.74	0.006	0.054	-	-	-	-	-	-
4167	0.9	-	-	-	-	0.54	0.01	0.73	0.013	0.050	-	-	-	-	-	-

Table 2. *APT experiments on CT RPV steel E neutron irradiated in BR2 at 290 °C up to the dose of 0.069 dpa (φt 4.78; E>1MeV).*

Run	Number of atoms [10^6]	Number of clusters	ND x 10^{22} [m^{-3}]	R_{eq} [nm]	Number of cluster core atoms	Global concentration [at. %]					Cluster concentration [at. %]					
						Si	Mn	Ni	P	Cu	Si	Mn	Ni	P	Cu	Fe
3948	0.8	2	5.0	1.5	216	0.60	0.47	0.81	0.006	0.042	8.3	3.7	7.9	0.0	0.5	79.6
3950	4.6	2	1.4	0.9	89	0.59	0.57	0.75	0.037	0.058	9.0	2.2	11.2	1.1	0.0	76.4
3957	1.0	2	6.2	1.1	75	0.54	0.55	0.75	0.021	0.058	5.3	2.7	14.7	0.0	0.0	77.3
3959	1.1	-	-	-	-	0.49	0.54	0.59	0.004	0.049	-	-	-	-	-	-
3961	1.3	1	1.2	-	-	0.51	0.59	0.63	0.041	0.043	-	-	-	-	-	-
3978	0.9	1	3.4	2.0	319	0.62	0.55	0.73	0.013	0.045	1.3	2.2	6.0	3.8	0.0	86.8
4270	2.9	1	0.5	-	-	0.61	0.57	0.75	0.053	0.055	-	-	-	-	-	-
4272	1.0	2	6.1	1.5	242	0.57	0.56	0.73	0.010	0.058	6.2	2.1	9.5	2.5	0.0	79.8
4273	1.1	2	5.8	1.4	158	0.64	0.60	0.78	0.009	0.060	7.0	4.4	10.8	0.0	0.6	77.2
4301	1.4	1	2.1	1.5	159	0.62	0.59	0.78	0.007	0.056	7.5	5.7	15.1	4.4	1.3	66.0

Table 3. *APT experiments on CT RPV steel E neutron irradiated in BR2 at 290 °C up to the dose of 0.092 dpa (φt 6.37; E>1MeV).*

Run	Number of atoms [10^6]	Number of clusters	ND x 10^{22} [m^{-3}]	R_{eq} [nm]	Number of cluster core atoms	Global concentration [at. %]					Cluster concentration [at. %]					
						Si	Mn	Ni	P	Cu	Si	Mn	Ni	P	Cu	Fe
4479	5.5	5	2.8	1.5	741	0.49	0.57	0.64	0.007	0.046	9.3	3.5	8.5	0.9	0.0	77.3
4487	2.3	4	4.0	1.7	677	0.50	0.58	0.62	0.005	0.048	4.7	3.5	8.1	3.8	0.1	79.3
4501	2.7	2	2.2	1.8	892	0.49	0.62	0.61	0.023	0.048	3.1	5.6	7.7	6.3	0.2	76.5
4504	0.5	1	3.2	-	-	0.57	0.61	0.66	0.013	0.050	-	-	-	-	-	-
4505	1.7	3	3.7	1.4	114	0.51	0.60	0.63	0.059	0.043	8.8	2.6	7.9	0.0	0.0	80.7
4827L	5.0	7	4.3	1.4	883	0.50	0.55	0.65	0.006	0.050	*7.6*	*3.7*	*11.7*	*2.8*	*0.2*	*73.7*

Table 4. *APT experiments on CT RPV steel E neutron irradiated in BR2 at 290 °C up to the dose of 0.138 dpa (φt 9.59; E>1MeV).*

Run	Number of atoms [10^6]	Number of clusters	ND x 10^{22} [m^{-3}]	R_{eq} [nm]	Number of cluster core atoms	Global concentration [at. %]					Cluster concentration [at. %]					
						Si	Mn	Ni	P	Cu	Si	Mn	Ni	P	Cu	Fe
5152	1.6	5	7.8	1.7	273	0.52	0.56	0.65	0.010	0.047	8.4	1.5	16.1	2.9	0.0	70.3
5155	0.5	-	-	-	-	0.46	0.56	0.66	0.070	0.051	-	-	-	-	-	-
5156	1.7	9	11.8	1.4	528	0.53	0.53	0.66	0.009	0.040	8.7	6.3	11.7	3.2	0.2	69.1
5171	1.3	7	14.1	1.2	383	0.50	0.54	0.58	0.011	0.047	5.7	2.6	7.8	0.0	0.5	83.3
5172	3.7	9	6.7	1.5	1253	0.52	0.52	0.57	0.009	0.040	7.5	3.0	11	3.9	0.2	74.0
5174	0.9	-	-	-	-	0.51	0.54	0.54	0.015	0.480	-	-	-	-	-	-
5208	1.4	4	7.7	1.8	772	0.50	0.57	0.6	0.013	0.045	8.8	5.2	15.7	3.5	0.1	65.5
5215	5.1	22	10.6	1.3	1759	0.50	0.55	0.59	0.008	0.041	9.0	4.9	10.8	2.2	0.3	72.3

Table 5. *APT experiments on CT RPV steel F neutron irradiated in BR2 at 290 °C up to the dose of 0.059 dpa (φt 4.09; E>1MeV).*

Run	Number of atoms [10^6]	Number of clusters	ND x 10^{22} [m^{-3}]	R_{eq} [nm]	Number of cluster core atoms	Global concentration [at. %]					Cluster concentration [at. %]					
						Si	Mn	Ni	P	Cu	Si	Mn	Ni	P	Cu	Fe
4581	3.0	8	6.6	1.5	490	0.50	1.35	0.71	0.007	0.052	3.7	7.3	5.9	3.9	0.0	78.6
4623	0.7	-	-	-	-	0.53	1.36	0.66	0.065	0.040	-	-	-	-	-	-
4625	0.8	4	14.3	1.6	679	0.48	1.30	0.70	0.019	0.042	3.4	9.7	9.3	4.1	0.4	72.9
4631	0.8	3	9.7	1.7	449	0.54	1.40	0.68	0.021	0.052	1.8	8.2	7.6	4.0	0.2	77.5
4633	11.5	26	5.9	1.5	1907	0.47	1.18	0.61	0.021	0.040	2.6	4.2	7.0	2.9	0.0	81.7
4890	2.2	6	7.0	1.7	603	0.48	1.18	0.62	0.024	0.043	1.7	5.8	4.8	3.0	0.0	84.4
4891	2.5	5	5.4	1.6	678	0.44	1.20	0.63	0.014	0.045	2.1	6.3	6.9	2.8	0.0	81.6
4895L	5.2	12	7.1	1.6	1532	0.45	1.25	0.69	0.008	0.041	*2.5*	*5.9*	*6.9*	*1.6*	*0.3*	*82.3*

Table 6. *APT experiments on CT RPV steel F neutron irradiated in BR2 at 290 °C up to the dose of 0.078 dpa (φt 5.40; E>1MeV).*

Run	Number of atoms [10^6]	Number of clusters	ND x 10^{22} [m^{-3}]	R_{eq} [nm]	Number of cluster core atoms	Global concentration [at. %]					Cluster concentration [at. %]					
						Si	Mn	Ni	P	Cu	Si	Mn	Ni	P	Cu	Fe
4017	2.0	3	3.9	1.5	318	0.50	1.19	0.68	0.031	0.044	5.0	4.4	9.1	0.0	0.0	81.4
4019	0.6	1	5.1	1.9	308	0.49	1.28	0.66	0.022	0.036	5.2	3.9	9.1	2.6	0.0	79.2
4082	3.8	11	8.7	1.7	1352	0.48	1.34	0.69	0.008	0.048	3.8	6.1	6.8	1.2	0.1	81.7
4084	1.0	5	12.2	1.6	225	0.49	1.33	0.70	0.012	0.030	4.4	7.9	5.7	1.3	0	78.9
4087	1.7	3	7.0	1.6	280	0.53	1.30	0.67	0.020	0.029	6.1	4.0	9.7	0.0	0.4	79.8
4133	1.3	7	12.5	1.4	440	0.51	1.22	0.72	0.031	0.094	4.1	7.8	7.3	2.5	0.0	78.3
4134	1.2	1	2.5	-	-	0.50	1.29	0.67	0.013	0.040	-	-	-	-	-	-
4143	3.1	13	10.9	1.7	1270	0.52	1.16	0.68	0.017	0.048	2.4	5.8	6.5	2.8	0.2	82.2

Table 7. *APT experiments on CT RPV steel F neutron irradiated in BR2 at 290 °C up to the dose of 0.134 dpa (φt 9.34; E>1MeV).*

Run	Number of atoms [10^6]	Number of clusters	ND x 10^{22} [m^{-3}]	R_{eq} [nm]	Number of cluster core atoms	Global concentration [at. %]					Cluster concentration [at. %]					
						Si	Mn	Ni	P	Cu	Si	Mn	Ni	P	Cu	Fe
4960	4.4	44	26.5	1.2	3172	0.54	1.24	0.73	0.032	0.045	4.0	6.1	6.6	0.2	0.3	82.2
4991L	2.2	24	26.1	1.5	2047	0.49	1.50	0.74	0.010	0.047	*3.8*	*9.5*	*8.6*	*0.8*	*0.4*	*75.4*
4996	1.2	12	24.9	1.6	1783	0.53	1.28	0.71	0.020	0.048	4.4	7.3	9.6	2.7	0.2	75
4997	1.0	*71*	*164.0*	*1.8*	*9139*	*0.41*	*4.37*	*1.52*	*0.008*	*0.101*	*2.5*	*19.7*	*16.6*	*0.1*	*0.9*	*59.1*
5026	0.6	3	11.9	1.4	331	0.57	1.38	0.75	0.012	0.049	4.5	6.9	10.6	1.2	0.0	76.4
5033	1.1	9	24.4	1.2	459	0.50	1.19	0.79	0.009	0.050	5.7	9.6	9.6	0.0	0.0	74.6
5216	15.0	87	16.2	1.5	7845	0.53	1.20	0.65	0.025	0.039	5.9	6.8	8.2	1.7	0.2	76.9

Table 8. *APT experiments on CT RPV steel I neutron irradiated in BR2 at 290 °C up to the dose of 0.082 dpa (φt 5.72; E>1MeV).*

Run	Number of atoms [10^6]	Number of clusters	ND x 10^{22} [m^{-3}]	R_{eq} [nm]	Number of cluster core atoms	Global concentration [at. %]					Cluster concentration [at. %]					
						Si	Mn	Ni	P	Cu	Si	Mn	Ni	P	Cu	Fe
4952	8.2	122	39.5	1.3	4401	0.58	1.13	1.42	0.010	0.036	6.0	5.4	12.2	0.7	0.2	74.9
4953	0.7	14	44.5	1.1	614	0.60	1.13	1.57	0.010	0.044	6.0	4.9	12.9	0.0	0.2	75.6
4955	0.5	8	38.4	1.3	214	0.60	0.97	1.53	0.008	0.039	7.5	2.8	15	0.0	0.0	73.8
4958	0.5	7	34.5	1.1	281	0.61	1.11	1.53	0.047	0.048	7.1	3.6	13.2	1.1	0.0	74.7
5034	0.9	15	44.9	1.1	991	0.58	1.05	1.71	0.013	0.040	4.4	4.9	12.4	1.9	0.2	75.7
5209	*0.2*	*10*	*108.0*	*1.1*	*794*	*0.42*	*1.27*	*1.98*	*0.026*	*0.043*	*4.5*	*4.7*	*14.4*	*0.1*	*0.1*	*74.9*
5209A	8.8	-	-	-	-	0.41	3.79	3.01	0.006	0.084	-	-	-	-	-	-
5214	0.6	10	43.8	1.1	750	0.53	1.13	1.64	0.010	0.048	6.5	7.1	15.3	1.9	0.7	68
5218A	1.0	-	-	-	-	0.41	4.31	3.36	0.013	0.105	-	-	-	-	-	-

Table 9. *APT experiments on CT RPV steel I neutron irradiated in BR2 at 290 °C up to the dose of 0.132 dpa (φt 9.14; E>1MeV).*

Run	Number of atoms [10^6]	Number of clusters	ND x 10^{22} [m^{-3}]	R_{eq} [nm]	Number of cluster core atoms	Global concentration [at. %]					Cluster concentration [at. %]					
						Si	Mn	Ni	P	Cu	Si	Mn	Ni	P	Cu	Fe
4999	0.6	19	76.5	1.1	802	0.40	1.22	1.49	0.057	0.038	4.0	8.6	13.3	0.2	0.1	73.2
5000	0.5	24	98.1	1.2	722	0.48	1.25	1.66	0.009	0.040	7.3	9.7	16.5	1.1	0.1	64.1
5003	2.4	67	73.1	1.2	1829	0.53	1.00	1.57	0.032	0.043	6.7	6.5	13.3	0.2	0.4	72.4
5022	0.6	24	104	1.0	901	0.54	1.14	1.61	0.019	0.034	6.3	8.4	13.0	0.0	0.3	71.4
5024	0.6	14	57.3	1.1	539	0.47	1.13	1.44	0.014	0.035	6.5	6.9	13.0	0.2	0.2	72.5
5036	1.6	33	51.7	1.0	619	0.48	1.04	1.45	0.023	0.038	5.3	7.1	14.4	0.8	0.0	72.2
5220	1.4	65	120	1.0	2012	0.42	1.23	1.47	0.009	0.040	6.4	8.5	15.6	0.1	0.2	68.3
5222	*7.3*	*624*	*234.0*	*1.3*	*25151*	*0.32*	*3.90*	*2.71*	*0.005*	*0.067*	*2.0*	*19.2*	*22.2*	*0.1*	*0.6*	*54*
5224	*6.3*	*114*	*50.5*	*1.1*	*2496*	*0.53*	*0.76*	*1.49*	*0.021*	*0.037*	*7.8*	*4.4*	*12.7*	*0.2*	*0.4*	*74*

Table 10. *APT experiments on CT RPV steel N neutron irradiated in BR2 at 290 °C up to the dose of 0.075 dpa (φt 5.21; E>1MeV).*

Run	Number of atoms [10^6]	Number of clusters	ND x 10^{22} [m^{-3}]	R_{eq} [nm]	Number of cluster core atoms	Global concentration [at. %]					Cluster concentration [at. %]					
						Si	Mn	Ni	P	Cu	Si	Mn	Ni	P	Cu	Fe
4596	0.7	1	4.6	1.31	100	0.50	1.11	0.74	0.007	0.042	5.0	8.0	11.0	4.0	0.0	72.0
4597	1.0	3	3.1	1.1	142	0.46	1.02	0.68	0.009	0.043	9.9	3.5	7.0	0.0	0.0	79.6
4600	9.0	32	10.5	1.4	2473	0.47	0.99	0.65	0.024	0.040	2.0	5.2	4.5	3.8	0.2	84.3
4648	2.8	2	2.2	1.4	293	0.50	1.10	0.73	0.038	0.044	4.8	5.1	9.6	0.0	0.3	79.9
4662L	6.6	-	-	-	-	0.47	1.17	0.72	0.027	0.047	-	-	-	-	-	-

Table 11. *APT experiments on CT RPV steel O neutron irradiated in BR2 at 290 °C up to the dose of 0.063 dpa (φt 4.38; E>1MeV).*

Run	Number of atoms [10^6]	Number of clusters	ND x 10^{22} [m^{-3}]	R_{eq} [nm]	Number of cluster core atoms	Global concentration [at. %]					Cluster concentration [at. %]					
						Si	Mn	Ni	P	Cu	Si	Mn	Ni	P	Cu	Fe
4545	0.9	8	25.0	1.3	323	0.66	1.12	0.80	0.039	0.063	1.2	7.7	6.5	6.8	0.6	75.5
4547	1.9	9	12.3	1.3	1165	0.59	1.06	0.77	0.058	0.061	2.2	5.9	4.2	3.4	0.1	82.9
4549	2.8	11	10.9	1.3	1140	0.60	0.99	0.75	0.065	0.055	1.8	4.0	3.8	4.8	0.5	84.2
4572	0.7	3	11.4	1.1	156	0.59	1.12	0.72	0.054	0.056	3.2	7.7	4.5	3.2	0.0	80.8
4574	2.0	7	9.8	1.0	296	0.51	1.04	0.73	0.066	0.053	1	8.8	2.7	8.4	0.0	78
4577	2.9	12	11.0	1.1	665	0.65	1.16	0.75	0.041	0.056	1.7	5.9	6.2	3.0	0.0	82.7

Table 12. *APT experiments on CT RPV steel W neutron irradiated in BR2 at 290 °C up to the dose of 0.061 dpa (φt 4.25; E>1MeV).*

Run	Number of atoms [10^6]	Number of clusters	ND x 10^{22} [m^{-3}]	R_{eq} [nm]	Number of cluster core atoms	Global concentration [at. %]					Cluster concentration [at. %]					
						Si	Mn	Ni	P	Cu	Si	Mn	Ni	P	Cu	Fe
4514	4.7	294	163	1.5	23149	0.54	1.05	1.67	0.028	0.309	4.2	7.8	12.7	0.4	6	67.2
4628	0.4	21	144	1.3	869	0.74	1.05	1.43	0.060	0.245	4.1	5.8	12.3	1.2	4	71
4629	0.8	66	194	1.5	5408	0.54	1.34	1.76	0.012	0.254	3.9	8.9	17.3	0.2	4.3	63.4
4629A	0.2	-	-	-	-	0.45	4.68	3.45	0.034	0.688	-	-	-	-	-	-
4650	0.8	48	133	1.4	2633	0.52	1.07	1.59	0.042	0.271	4.7	8.2	13.9	0.6	7.5	63.3
4821	1.0	73	188	1.2	3813	0.60	1.08	1.56	0.056	0.260	4.6	8.6	13.7	0.2	5.6	65.4

Appendix C

C.1 Point defect concentration calculations

Formation of solute clusters and precipitates by both irradiation enhanced and -induced processes is governed by the oversaturation of point defects under the effect of irradiation. The main parameters influencing the magnitude of radiation-induced segregation, such as vacancy and self-interstitial atom diffusion coefficients and concentrations, should be assessed. To evaluate the PD concentrations, the point defect balance equations for V an SIA should be solved [1]:

$$\frac{dC_v}{dt} = R_v - K_{iv}C_v^{at}C_i^{at} - K_{vs}C_v^{at}C_s^{at} \quad (1)$$

$$\frac{dC_i}{dt} = R_i - K_{iv}C_v^{at}C_i^{at} - K_{is}C_i^{at}C_s^{at} \quad (2)$$

where:

C_v^{at} – vacancy concentration [per atom];

C_i^{at} – interstitial concentration [per atom];

C_s^{at} – sink concentration [per atom];

R_v – vacancy production rate [$s^{-1}m^{-3}$];

R_i – SIA production rate [$s^{-1}m^{-3}$];

K_{iv} – vacancy-interstitial recombination rate [$s^{-1}m^{-3}$];

K_{vs} – vacancy-sink reaction rate [$s^{-1}m^{-3}$];

K_{is} – interstitial-sink reaction rate coefficient [$s^{-1}m^{-3}$].

Correlation between PD concentrations and other parameters, such as production and annihilation rates and different sinks strengths, is usually performed with the atomistic modelling. One of the most widespread methods is the atomistic kinetic Monte Carlo modelling [2-4].

During irradiation, the steady state of PD concentrations is achieved [1]. Results obtained by Martinez and co-workers with standard rate theory (SRT) for electron irradiation (T=327 °C, dose rate 10^{-9} dpa/s) predict that steady state is reached in ~10^{-2} seconds [2]. Soisson and co-workers predicted by AKMC simulations that the steady state is reached in a time between 1 and 10 seconds for neutron irradiation at 290 °C [3]. Regardless, it is correct to state that in comparison with the total irradiation time of materials in the present study of around 2 to 4 x 10^6 seconds, the steady state is reached almost immediately. Yet, not to contradict with the physics, let's assume that PD concentrations grow from equilibrium to the steady state

during the first 100000 seconds or ~0.001 dpa. In the steady state the number of created point defects equals to the number of annihilated by mutual recombination and at sinks ones. i.e. $\frac{dC_{i,v}}{dt} = 0$. Therefore, the equations 1 and 2 become:

$$0 = R_v - K_{iv}C_v^{at}C_i^{at} - K_{vs}C_v^{at}C_s^{at} \quad (3)$$

$$0 = R_i - K_{iv}C_v^{at}C_i^{at} - K_{is}C_i^{at}C_s^{at} \quad (4)$$

and, hence:

$$R_v = K_{iv}C_v^{at}C_i^{at} - K_{vs}C_v^{at}C_s^{at} \quad (5)$$

$$R_i = K_{iv}C_v^{at}C_i^{at} - K_{is}C_i^{at}C_s^{at} \quad (6)$$

From the atomistic modelling in the conditions of high sink strength k^2 ~10^{14} m^{-2} the recombination rate was evaluated to be negligible in comparison with the rate of annihilation on sinks $K_{iv}C_v^{at}C_i^{at} \ll K_{vs}C_v^{at}C_s^{at}$ and $K_{iv}C_v^{at}C_i^{at} \ll K_{is}C_i^{at}C_s^{at}$ [3]. Further, to simplify the calculations, the assumption is made - that at the steady state and high sink density condition the recombination equals to zero. i.e. $K_{iv}C_v^{at}C_i^{at} = 0$. Consequentially equations 5 and 6 become:

$$R_v = K_{vs}C_v^{at}C_s^{at} \quad (7)$$

$$R_i = K_{is}C_i^{at}C_s^{at} \quad (8)$$

The magnitude of PD annihilation rate is dependent on the speed (diffusion coefficient $D_{i,v}$ [m^2/s]) and the distance between sinks *L*. The latter is expressed by the sink strength $k_{i,v}^2 = {}^1/_{L^2}$ [m^{-2}].

$$k_v^2 C_v D_v = K_{vs}C_v^{at}C_s^{at} \quad (9)$$

$$k_i^2 C_i D_i = K_{is}C_i^{at}C_s^{at} \quad (10)$$

where $C_{i,v}$ is calculated per volume unit [m^{-3}] and the total sink strength $k_{i,v}^2$ is the sum of sink strengths of different sinks $k_{i,v}^2 = \sum_X k_X^2$. Typical sinks are dislocation lines, grain boundaries and point defect clusters. DLs and GBs are present in the non-irradiated materials and PDCs are formed under the neutron irradiation. The sink strength values are calculated in the following way [1-4]:

- $k_{GB}^2 \approx 12/d^2$ [m^{-2}], where *d* is the grain size, selected to be around 3x10^{-6} [m] for the ferrite laths in RPV steels [5];
- $k_{DL}^2 = \rho_{DL}$ [m^{-2}], the dislocation density of 10^{14} [m^{-2}], evaluated with X-Ray Diffraction measurements was selected;
- $k_C^2 = 8C_s/1.3a^2$ [m^{-2}]

where C_s is the cluster concertation per atom and a [m] is the lattice parameter [3]. $C_s = ND/Nb_{atoms}$, where ND is the number density [m^{-3}] and Nb_{atoms} is the number of atoms in 1 cubic meter ~8.49×10^{28} [m^{-3}]. The sink strength of point-like sinks is proportional to the number of sites per volume C_s/a^3 [m^{-3}] multiplied by the capture radius ~a [m], and hence $k_C^2 \propto C_s/a^2$. The 8/1.3 proportionally factor was evaluated with AKMC simulations for different PD capture radii and sink strengths [3].

The strain field distortion around DLs makes them the preferable sinks for SIAs, and the bias of 1.25 for SIA absorption by DLs is selected. Finally, combining equations 7 with 9 and 8 with 10, the further form is obtained:

$$R_v = (k_{DL}^2 + k_{GB}^2 + k_C^2) C_v D_v \quad (11)$$

$$R_i = (1.25k_{DL}^2 + k_{GB}^2 + k_C^2) C_i D_i \quad (12)$$

The PD production rate ($R_{i,v}$) was calculated taking into account the number of survived in-cascade recombination PDs, which equals to ~0.3 of NRT displacement values. The latter value was estimated by Molecular Dynamics calculations (MDCs) [6]. Also, it should be noted that some part of survived point defects could had formed small PD clusters. The ratio of free V was set to 0.78 and to 0.85 for SIA of survived in-cascade recombination PDs. These values were obtained by the Cluster Dynamics for Precipitation (CD-P) modelling of the neutron irradiation at 290 °C and a similar dose rate of 7.5 x 10^{-8} dpa/s [7]. Taking the latter two observations into account, the production rate of V and SIA equal to $R_v = 0.234R$ and $R_i = 0.255R$ respectivly. Where $R=G/ Nb_{atoms}$ [$s^{-1}m^{-3}$] and G is the dose rate in dpa/s.

Finally, the diffusion coefficients, dependant on the temperature and migration energy $D = D_0 exp\left(\frac{-E_{i,v}^m}{k_B T}\right)$, were obtained from the literature and equal to D_v = 4.5×10^{-12} [m^2/s], D_i = 5.7×10^{-9} [m^2/s] [2,3]. The PD concentration values were calculated with the following equations:

$$C_v = 0.234R \,/\, (k_{DL}^2 + k_{GB}^2 + k_C^2) D_v \quad (13)$$

$$C_i = 0.255R \,/\, (1.25k_{DL}^2 + k_{GB}^2 + k_C^2) D_i \quad (14)$$

The only unknown parameter is the sink strength of the PDCs. Unfortunately, these clusters cannot be identified with APT. Hence work around solute clusters, which had most probably formed on PDCs and also act PDs sinks, was performed. The selection of SCs as the sinks for PDs provides the ability to correlate the experimentally observed data (number density of solute clusters) with the PD concentration calculations.

Other important note is that ND of solute clusters evolves with time (∝ irradiation dose). To evaluate the tendencies of the ND evolution, the power trendlines for steels irradiated to more than one dose (E, F, I) were performed (Fig. 1). Since the number density of solute clusters increases with dose, the total sink strength also grows. The example of the calculated sink strength evolution is reported in figure 2. The step size is 0.001 dpa.

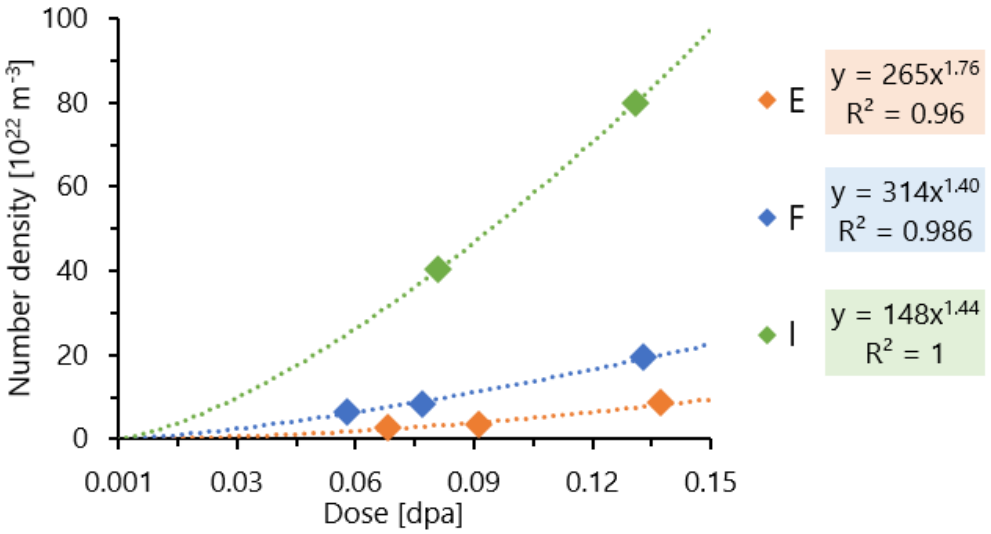

Figure 1. *Evolution of solute clusters number density as a function of irradiation dose. The equations for the trend lines are given in the legend.*

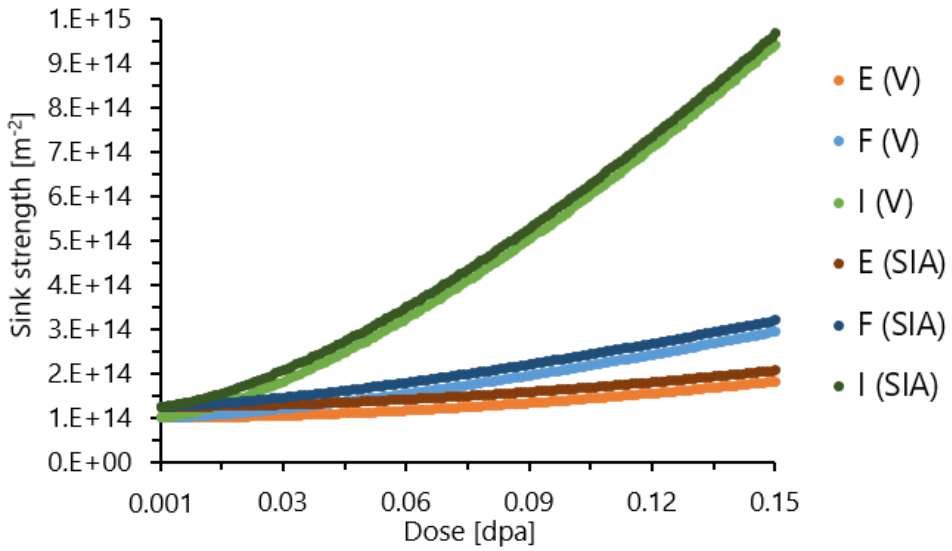

Figure 2. *Evolution of sink strength as a function of irradiation dose.*

Finally, even though the system is in the quasi-steady state, due to de evolution of the sinks strength, the PD concentrations evolves with time (Fig. 3).

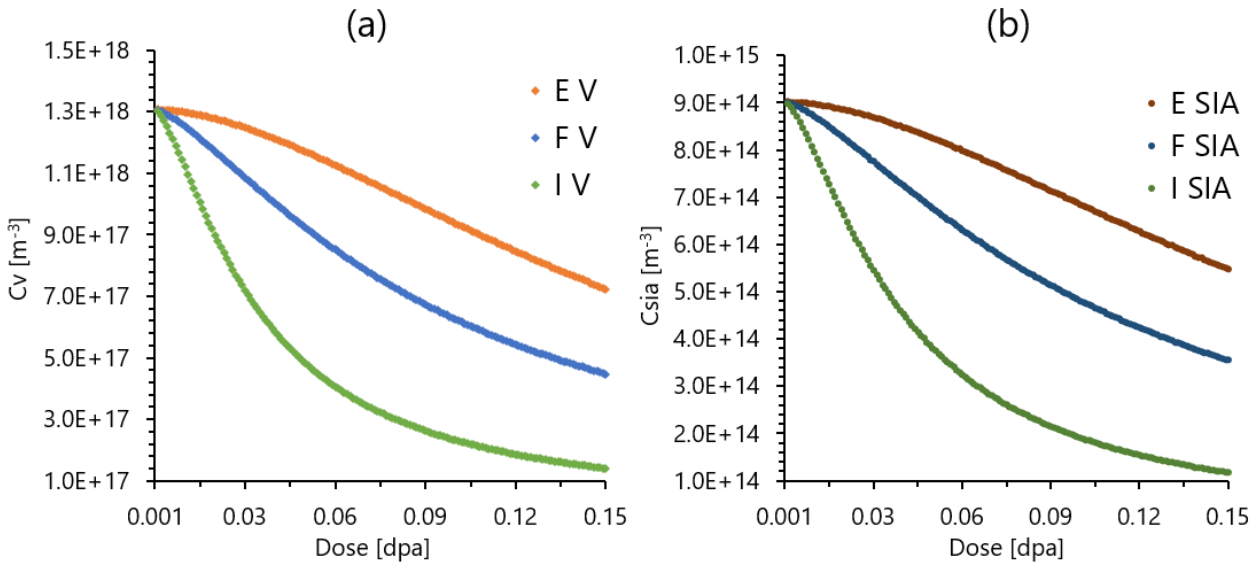

Figure 3. *Evolution of PD concentrations as a function of irradiation dose. (a) Vacancy concentration. (b) SIA concentration.*

The first observation is that in every steel vacancy concentration (~10^{17} m^{-3}) around three orders of magnitude larger than of SIAs (~10^{14} m^{-3}). Secondly, for both V and SIA, the concentrations are higher in steels where lower ND of solute clusters ($\propto$ sink strength) was measured.

Radiation-induced solute segregation is possible by the virtue of the solute and PD flux coupling. The positive coupling (drag) results in the redistribution of solutes in the material and segregation of latter on the sinks.

To evaluate the magnitude of solute segregation, a flux ($J_{i,v}$) of PDs towards sinks should be calculated first: $J_{i,v} = -D_{i,v}\nabla C_{i,v}$ [m/s], where $\nabla C_{i,v}$ is the concentration gradient. $\nabla C_{i,v} = C_{i,v}^{eq,at} - C_{i,v}^{at}/L$ [m^{-1}]. For the present case, the PD concentrations are presented per atoms [without unit], and not per volume [m^3]. The distance between sinks (L) was calculated from the sink strength in a following way: $L = \sqrt{1/k^2} = 1/k$. Equilibrium V and SIA concentrations are expected to be several orders of magnitude lower than at the quasi-steady state and can be neglected. Hence, $\nabla C_{i,v} = -C_{i,v}^{at}/L$. The obtained results are presented in figure 4.

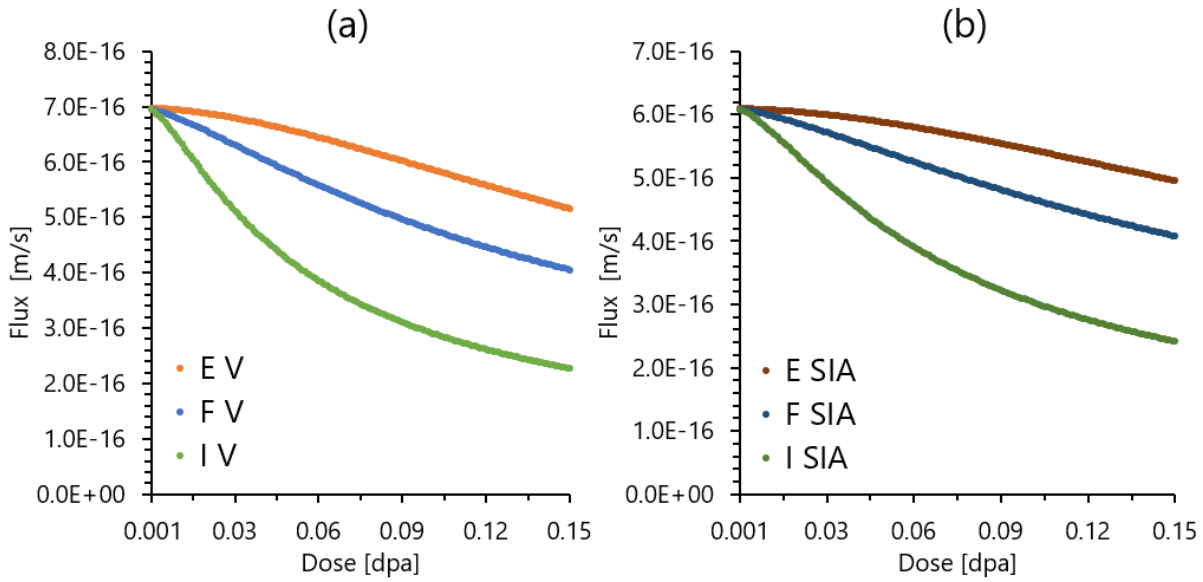

Figure 4. *PD flux as a function of irradiation dose. (a) Vacancy flux. (b) SIA flux.*

Even though the concentration of Vs is by several orders of magnitude larger than of SIAs, their fluxes are on the similar level of around 10^{-16} m/s. This is due to higher diffusion coefficient of the latter. The distance between sinks is lower in steels I and F, where higher number density of SC was measured. Yet, due to the lower PD concentration, the PD flux is also lower in steel I and F, than in steel E.

Additionally, from the obtained sink strength values, the ratio of Vs and SIAs annihilated on SC and DL was estimated (GBs are not included, since their sink strength is around two orders of magnitude lower than of DL). The results are reported in figures 5.a and 5.b as a ratio of annihilation of SCs over the annihilation on DLs: k_c^2/k_{DL}^2.

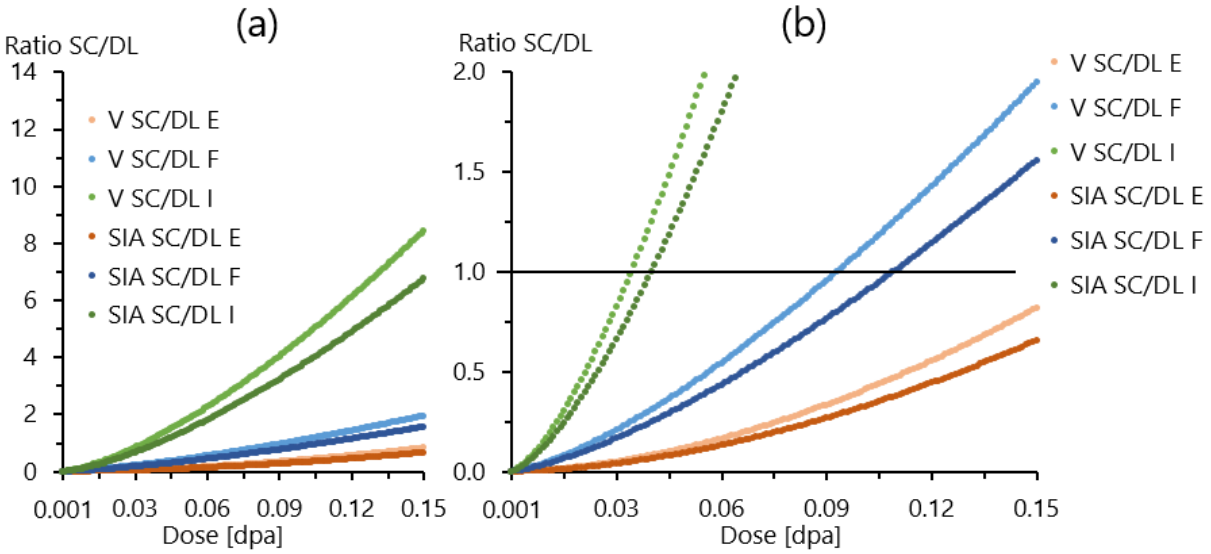

Figure 5. *(a) Ratio of SC over DL annihilation. (b) A close up of the figure 5.a. 1/1 line is also plotted.*

In every steel, at the early stages of irradiation, the dislocation lines are the preferable sinks for PD annihilation. With increase of SC number density, the sink strength grows and consequentially more PDs annihilate on the latter. In the case of steel I SC became the dominant sink at the dose of around 0.04 dpa. The same happened at around 0.10 dpa for steel F. In the case of steel E, even at 0.15 dpa, due to the lower SC number density, dislocation lines are still the dominant PD sink. Also, for a given dose, the ratio of V annihilation on solute clusters is larger than of SIAs in every steel.

Main conclusions are the following:

- SIA and V steady state concentrations are in a good agreement with the values predicted by the atomistic modelling [2,3];
- With increase of irradiation dose, the total sink strength increases due to formation of additional sinks, such as solute clusters;
- With increase of dose and sink strength, the quasi-steady state V and SIA concentrations decrease;
- With increase of irradiation dose, and consequentially of cluster number density in steels I and F (effectively sink strength), more SIAs started to annihilate on clusters. Contrary, in steel E majority of SIA goes towards DLs at every irradiation dose;
- Calculated PD concentrations and fluxes are sufficient for the RIS process.

References

1. G.S. Was. Fundamentals of Radiation Materials Science: Metals and Alloys. Springer, New York (2007). https://doi.org/10.1007/978-3-540-49472-0

2. E. Martínez, F. Soisson, M. Nastar. Journal of Nuclear Materials 539 (2020): 152233. https://doi.org/10.1016/j.jnucmat.2020.152233

3. F. Soisson, E. Meslin, O. Tissot. Journal of Nuclear Materials 508 (2018): 583-594. https://doi.org/10.1016/j.jnucmat.2018.06.015

4.F. Soisson, T. Jourdan. Acta Materialia 103 (2016): 870-881. https://doi.org/10.1016/j.actamat.2015.11.001

5. G. Monnet. Journal of Nuclear Materials 508 (2018): 609–27. https://doi.org/10.1016/j.jnucmat.2018.06.020

6. L. Malerba. Journal of Nuclear Materials 351 (2006): 28–38. https://doi.org/10.1016/j.jnucmat.2006.02.023

7. F. Christien, A. Barbu. Journal of Nuclear Materials 324 (2004): 90–96. https://doi.org/10.1016/j.jnucmat.2003.08.035

Appendix D

D.1 Embrittlement prediction models

Within the NRC Reg. Guide 1.99 rev.2 the temperature shift is calculated as [1]:

$$\Delta T_{41J} = [CF] \times \varphi t^{(0.28-0.1\log \varphi t)} \quad \text{(D.1)}$$

where *CF* is the chemical factor obtained from the table depending on the Cu and Ni bulk contents, and φt is neutron fluence in 10^{23} n/m^2 (or 10^{19} n/cm^2). The upper limit for Cu content is 0.4 wt.% and for Ni is 1.2 wt.%.

WR-C(5)R1 (or ASTM E900-15) equation the TTS is composed from two parts [2]:

$$TTS = TTS_1 + TTS_2 \quad \text{(D.2)}$$

$$TTS_1 = A\,\frac{5}{9}\,1.8943 \times 10^{-12} \varphi t^{0.5695} \left(\frac{1.8T_i + 32}{550}\right)^{-5.47} \left(0.09 + \frac{P}{0.012}\right)^{0.216} \left(1.66 + \frac{Ni^{8.54}}{0.63}\right)^{0.39} \left(\frac{Mn}{1.36}\right)^{0.3} \quad \text{(D.3)}$$

$$TTS_2 = \frac{5}{9}\,\max\,[\min\,(Cu;\,0.28) - 0.053; 0] \times M \quad \text{(D.4)}$$

$$M = B\,612.6 \left(\frac{1.8T_i + 32}{550}\right)^{-5.45} \left(0.1 + \frac{P}{0.012}\right)^{-0.098} \left(0.168 + \frac{Ni^{0.58}}{0.63}\right)^{0.73} \quad \text{(D.5)}$$

where T_i is the temperature degrees Celsius and φt is neutron fluence in n/m^3. The CT RPV steels were fabricated in the same way as commercial plates of A533B ASTM standard. Hence, A (1.080) and B (0.819) coefficients for plates were selected.

Within the EONY model the transition temperature shift is composed from matrix feature (MF) and Cu-rich precipitate (CRP) terms [3-5]:

$$TTS = MF + CRP \quad \text{(D.6)}$$

$$MF = A(1 - 0.001718T_i)(1 + 6.13P\,Mn^{2.47})\sqrt{\varphi t} \quad \text{(D.7)}$$

$$CRP = B(1 + 3.77Ni^{1.191})(Cu - 0.072 + 1.359[P - 0.008])^{0.668} g \quad \text{(D.8)}$$

$$g = \frac{1}{2} + \frac{1}{2}\tanh\left(\frac{\log_{10} \varphi t + 1.139Cu - 0.448Ni - 18.12}{0.629}\right) \quad \text{(D.9)}$$

A (1.56 x 10^{-7}) and B (128.2) coefficients for plates were selected. In the case of materials with Cu content below 0.072 wt. % (all steels apart from W), the *CRP* term equals to 0 and the total *TTS* corresponds only to the *MF* term (Eq. 7).

The FIS method is utilised to perform the embrittlement predictions on French and Belgian RPV materials of power reactors. The DBTT shift is calculated in the following way [3,6,7]:

$$\Delta TT = 15.4[1 + 35.7(P - 0.008) + 6.6(Cu - 0.08) + 5.8Ni^2Cu] \times \varphi t^{0.59} \qquad \text{(D.10)}$$

where *P*, *Cu* and *Ni* are the bulk solute concentrations in weight percentage, and φt is neutron fluence in 10^{23} n/m^2 (or 10^{19} n/cm^2). As we can already see from equation (10), P, Cu and Ni are expected to be the most detrimental solutes causing irradiation embrittlement of RPV steels, which correlates well with results obtained by APT where a strong effect of P, Cu and Ni on the solute cluster formation was observed.

With the older Japanese model JEAC4201-2004 the embrittlement is calculated as [8]:

$$\Delta T_{41J} = [-16 + 1210P + 215Cu + 77\sqrt{CuNi}] \times \varphi t^{(0.29 - 0.04 \log \varphi t)} \qquad \text{(D.11)}$$

where same as above, *P*, *Cu* and *Ni* are the bulk solute concentrations in weight percentage, and φt is neutron fluence in 10^{23} n/m^2 (or 10^{19} n/cm^2).

The DBTT shift predictions with various models as a function of the converted from the tensile test data embrittlement values are reported in figure 1.

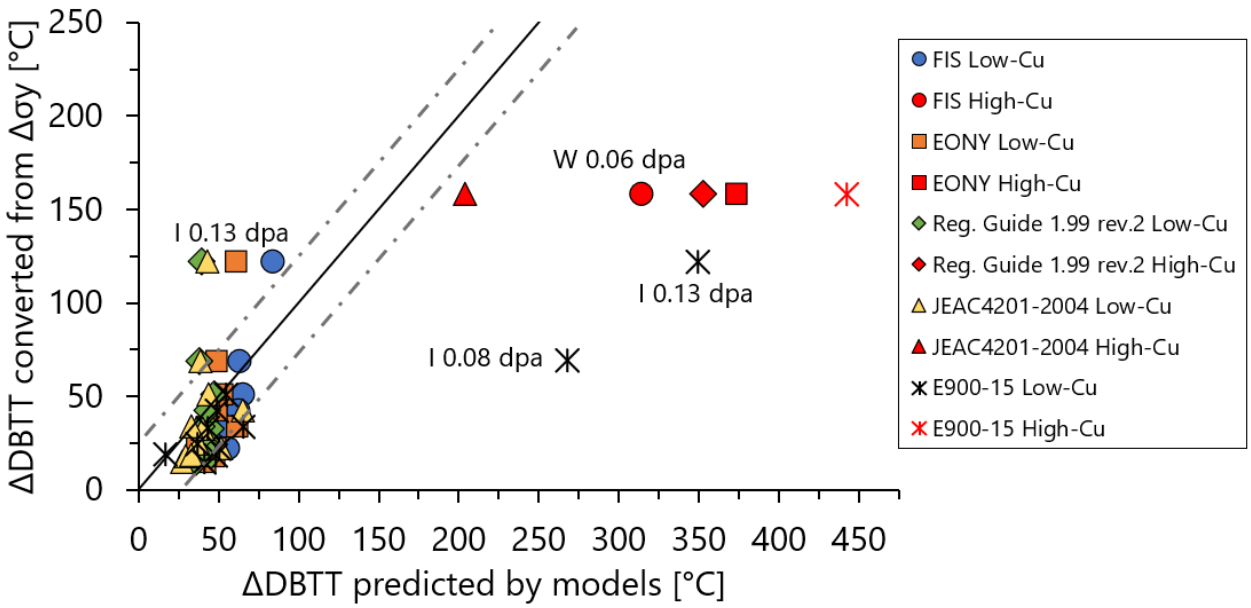

Figure 1. *Estimated embrittlement of the CT RPV steels. Estimated values are converted from the yield stress increase measured by tensile tests. Predicted values are calculated from the bulk chemical composition and accumulated dose. Uncertainty margin of around 25 °C was selected from literature [9].*

References

1. NRC Regulatory Guide 1.99 Revision 2, Task ME 305-4 (1988). https://www.nrc.gov/docs/ML0314/ML031430205.pdf

2. ASTM E900-15, Standard Guide for Predicting Radiation-Induced Transition Temperature Shift in Reactor Vessel Materials (2017). https://doi.org/10.1520/E0900-15

3. N. Soneda (Ed.). Irradiation Embrittlement of Reactor Pressure Vessels (RPVs) in Nuclear Power Plants. Elsevier (2015). https://doi.org/10.1016/C2013-0-17428-4

4. E. Eason, G.R. Odette, R.K. Nanstad, T. Yamamoto (Eds). A Physically Based Correlation of Irradiation-Induced Transition Temperature Shifts for RPV Steels. Report ORNL/TM-2006/530 (2007): 250. https://info.ornl.gov/sites/publications/files/Pub2592.pdf

5. E.D. Eason, G.R. Odette, R.K. Nanstad, T. Yamamoto. Journal of Nuclear Materials 433 (2013): 240–254. http://dx.doi.org/10.1016/j.jnucmat.2012.09.012

6. C. Brillaud, F. Hedin, B. Houssin. ASTM International (1987): 420-447. https://doi.org/10.1520/STP25666S

7. P. Todeschini, Y. Lefebvre, H. Churier-Bossennec, N. Rupa, G. Chas, C. Benhamou. Revision of the irradiation embrittlement correlation used for the EDF RPV fleet. Paper A084-T01 (2010)

8. N. Soneda, A. Nomoto. Journal of Engineering for Gas Turbines and Power 132 (2010): 102918. https://doi.org/10.1115/1.4001056

9. N. Castin, G. Bonny, M.J. Konstantinovic, A. Bakaev, F. Bergner, C. Courilleau, C. Domain, B. Gomez-Ferrer, J.M. Hyde, L. Messina, G. Monnet, M.I. Pascuet, B. Radiguet, M. Serrano, L. Malerba. Materials Science (2022). https://doi.org/10.48550/arXiv.2204.11441

Influence of the Bulk Chemical Composition on the Microstructure Evolution of Irradiated Chemically-tailored Nuclear RPV Steels

Abstract: Lifetime of the nuclear power plant (NPP) is limited by the embrittlement of the reactor pressure vessel steel (RPV) steel. One of the most important parameters determining the embrittlement is the bulk concentration of irradiation sensitive solutes.

A set of chemically-tailored (CT) steels with the tuned bulk solute contents were neutron irradiated at 290 °C in high flux BR2 reactor. To study the nanosized solute clusters the state of the art Atop Probe Tomography (APT) technique was utilised.

The results of this study show that:

- Solute clusters enriched in Mn, Ni, Si and to the less extent in Cu and P were observed in 11 out of 12 conditions. These clusters were formed inside the ferritic matrix, alongside dislocation lines and at low-angle grain boundaries (LAGBs);
- Addition of all solutes of interest results in the increase in solute cluster number density. The stronger effect was observed for Ni and Cu that of Mn and P. In addition, a positive synergy between Mn and Ni was evaluated;
- Measured by tensile testes irradiation hardening is well explained by the formation of solute clusters. Solute clusters are weak obstacles with an obstacle strength of around 0.14.

Key words: Nuclear Power, Reactor Pressure Vessel Steel, Atom Probe Tomography, Solute Clusters, Irradiation Hardening, Lifetime Extension

Effets des éléments Cu, P, Ni et Mn sur l'évolution de la microstructure d'aciers irradiés

Résumé : La durée de vie d'un réacteur nucléaire à eau pressurisée (REP) peut être limitée par le durcissement et la fragilisation sous irradiation de l'acier de la cuve du réacteur. Un des paramètres importants influençant l'évolution des propriétés mécaniques de l'acier de cuve sous irradiation est la composition chimique de ce dernier, en particulier les teneurs en éléments réputés fragilisant, tels que Mn, Ni, Si, Cu et P.

Dans cette thèse, un ensemble d'aciers de compositions chimiques contrôlées, permettant d'isoler les effets du Mn, du Ni, du Cu et du P et les synergies entre ces éléments, a été irradié aux neutrons à une température de 290 °C dans le réacteur expérimental BR2. L'évolution de la microstructure sous irradiation à été étudiée par sonde atomique tomographique. Les microstructures d'irradiation ont été comparées à des résultats d'essais de traction réalisés au SCK.CEN.

Les résultats de cette étude montrent que :

- Des amas nanométriques de solutés enrichis en Mn, Ni, Si et dans une moindre mesure en Cu et P sont observés après irradiation. Ces amas se situent dans la matrice ferritique, le long des lignes de dislocation et aux joints de grains;
- L'augmentation de la teneur initiale en solutés réputés fragilisant entraîne une augmentation de la densité numériques d'amas de solutés. L'effet le plus fort est observé pour le Ni et le Cu. De plus, une synergie positive entre Mn et Ni a été mise en évidence;
- La variation de la limite d'élasticité due à l'irradiation s'explique bien par la formation des amas de solutés en considérant ces amas comme des obstacles faibles (force d'obstacle d'environ 0,14).

Mots clés : Acier des cuves de réacteurs nucléaires, Vieillissement, durée de vie, Techniques d'analyses de hautes résolutions